

NORTHWESTERN UNIVERSITY

**High-Resolution Analysis of Adsorbate-Induced GaAs(001)
Surface Structures and Strain in Buried III-V Semiconductor
Heterolayers by X-Ray Standing Waves**

A DISSERTATION

SUBMITTED TO THE GRADUATE SCHOOL
IN PARTIAL FULFILLMENT OF THE REQUIREMENTS

for the degree of
DOCTOR OF PHILOSOPHY

Field of Materials Science and Engineering

By

Tien-Lin Lee

EVANSTON, ILLINOIS

December 1999

© Copyright by Tien-Lin Lee 1999
All Rights Reserved

ABSTRACT

High-Resolution Analysis of Adsorbate-Induced GaAs(001) Surface Structures and Strain in Buried III-V Semiconductor Heterolayers by X-Ray Standing Waves

Tien-Lin Lee

The GaAs(001) surface has been of great interest due to its technological importance and rich surface structures. Despite considerable experimental and theoretical investigations, the detailed structure of a number of GaAs(001) surface reconstructions are still under debate. Recently the growth of coherently strained 3-dimensional islands and short-period superlattices composed of III-V semiconductors has become a new challenge for developing the next generation of electronic and optical devices. Since the vertical dimensions of these structures are typically 2 - 3 monolayers, the studies of adsorbate-induced compound semiconductor surfaces and the strain in buried monolayers can directly lead to a better understanding and control of the growth of these highly lattice-mismatched systems.

In this work, a series of high-resolution in situ measurements using the x-ray standing wave (XSW) technique were carried out to characterize the bonding geometries of the GaAs(001) surfaces upon the submonolayer adsorption of Sb and In. For the Sb-

terminated surface, the XSW analysis supports the formation of a stable (2x4) structure with 0.5 ML of Sb dimerized on the GaAs(001) surface. The XSW measured Sb dimer bond length agreed well with previous theoretical calculations. Several existing models are compared and only one of them is found to be consistent with the XSW measurements. However, for the In-terminated GaAs(001) (4x2) surface, the XSW analysis shows that In occupies an unexpected adsorption site and disagrees with previous models that predict the formation of In dimers. From this a new structural model is proposed that best explains the present XSW results and previous STM observations for this surface. In addition, XSW analysis was directly used to measure the vertical strain in monolayers of InGaAs buried in GaAs(001) and InAsSb buried in InSb(111). The results were compared with the macroscopic continuum elasticity theory and a microscopic description based on random-cluster calculations using a valence-force field. Finally, the dynamical diffraction theory necessary for calculating the x-ray standing wave field generated by a single crystal epitaxial thin film is derived and applied to the polarity determination of a ferroelectric thin film.

Thesis Adviser: M.J. Bedzyk
Department of Materials Science and Engineering
Northwestern University
Evanston, IL 60208

ACKNOWLEDGEMENTS

I would like to take this opportunity to first thank my thesis advisor, Prof. Michael J. Bedzyk, for introducing me to the exciting fields of x-ray and surface physics, and also for his constant guidance and support.

I consider myself very fortunate to also have the chance of working with Jorg Zegenhagen (Max-Planck-Institut, Stuttgart) and Joseph C. Woicik (NIST). The discussions with them have always been inspiring and their help has made my thesis research more fruitful.

I would like to thank every member in our group at Northwestern University for their help. In particular, I would like to give my great appreciation to Yonglin Qian and Paul Lyman for their instruction in operating beamline X15A at the National Synchrotron Light Source and other advice and assistance.

I would like to express my deep gratitude to Prof. S.A. Barnett, Prof. B.W. Wessels, M. Pillai, G. Labanda, S.C. Theiring, J. Mirecki Millunchick, J.G. Pellegrino,(NIST) and B.O. Fimland (Norwegian Institute of Technology) for their assistance in preparing samples (or substrates) and to L. Thompson and P.M. Baldo in performing RBS measurements at ANL.

I am grateful for the help and instruction from Hoydoo You (ANL) during the x-ray diffraction measurements at beamline X6B at the NSLS. I am also grateful for the

technical assistance given by the staff scientists and engineers of the BESSRC CAT and the DND CAT at the Advanced Photon Source.

This work was supported by the U. S. Department of Energy under contract No. W-31-109-ENG-38 to Argonne National Laboratory, contract No. DE-AC02-76CH00016 to the National Synchrotron Light Source at Brookhaven National Laboratory, and by the National Science Foundation under contracts No. DMR-9632593 to MJB and No. DMR-9632472 to the MRC at Northwestern University.

Finally I would like to thank my family for their encouragement and support. I dedicate this thesis to my parents.

TABLE OF CONTENTS

ABSTRACT	iii
ACKNOWLEDGEMENTS	v
LIST OF TABLES	x
LIST OF FIGURES	xi
Chapter 1 Introduction	1
Chapter 2 X-Ray Standing Wave Technique	5
2.1 Introduction	5
2.2 Generalized dynamical theory of x-ray	5
2.2.1 Total field intensity	6
2.2.2 Recursion formulae	8
2.2.3 Takagi-Taupin theory	12
2.2.4 Boundary conditions (Bragg case), dispersion surfaces and deviation parameter	21
2.2.5 Solutions to Takagi-Taupin equations for perfect slabs	27
2.3 XSW analysis	34
2.4 Primary extinction and evanescent-wave emission	36
2.5 Simulations and experimental results: PbTiO ₃ thin film XSW	41
Chapter 3 Experimental	52
3.1 X15A (NSLS)	52
3.2 5ID-C and 12ID-D (APS)	55

Chapter 4 Reconstructions of Clean GaAs(001) Surface	65
4.1 Introduction	65
4.2 Electron counting model	67
4.3 Reconstructions of GaAs(001) surface	72
4.3.1 (2×4)/c(2×8)	73
4.3.2 (4×2)/c(8×2)	92
4.3.3 c(4×4)	95
4.3.4 (n×6)	97
4.4 Clean surface preparation	97
 Chapter 5 High-Resolution Structural Analysis of Sb-Terminated GaAs(001)-(2×4) Surface	 100
5.1 Introduction	100
5.2 Background information	100
5.3 Surface preparation	102
5.4 XSW results and discussions	106
5.4.1 Sb-Sb dimer bond length and dimer height	106
5.4.2 Sb coverage	112
5.4.3 α_2 and β_2 models	114
5.4.4 δ_2 model	118
5.5 Summary	122
 Chapter 6 Indium-Induced GaAs(001) (4×2)/c(8×2) Reconstruction	 123
6.1 Introduction	123
6.2 Indium adsorption on GaAs(001): Background information	123
6.2.1 InAs(001) clean surface	124
6.2.2 Initial growth of InAs on GaAs(001)	129
6.2.3 Surfactant-mediated growth of InAs on GaAs(001)	131

6.2.4 In-terminated GaAs(001) (4×2)/c(8×2)	133
6.3 Experimental results	140
6.3.1 LEED and Auger	140
6.3.2 XSW measurements	144
6.4 Discussions	154
6.4.1 XSW analysis: (4×2)/c(8×2)	154
6.4.2 Structural model for GaAs(001):In (4×2)/c(8×2)	162
6.4.3 XSW analysis: Streaky (4×1)	167
6.5 Summary	169
Chapter 7 Strains and Lattices Distortions in Buried Heterolayers	171
7.1 Introduction	171
7.2 Strains in GaAs(001)/InGaAs	172
7.3 In-plane structures of GaAs(001)/InGaAs probed by off-normal XSW measurements	192
7.4 Strain-induced cap displacement: An x-ray evanescent- wave emission measurement	199
7.5 Strains in InSb(111)/InAsSb	204
Chapter 8 Summary	221
REFERENCES	225
Appendix A Strains in Pseudomorphic Heterolayers of Cubic Materials	243

LIST of TABLES

3.1	Calculated Bragg angles θ_B , Darwin widths ω , d-spacing d_H and the slope $\Delta\lambda/\Delta\theta$ for the Si(111), (004) and (008) reflections at 12.00 keV.	64
5.1	Theoretical and experimental values of the structural dimensions for the Sb dimers on different surfaces [see Figure 5.5(a)].	111
6.1	The calibrated In coverages (Θ_{In}), annealing temperatures (T_{anneal}), LEED patterns and the results of the XSW analysis of the four GaAs(001) samples (S1 through S4) used in the present study.	147
6.2	The calculated coherent positions based on the Resch-Esser's model and the hollow site H in Figure 6.15(c) compared with the XSW results from sample S2.	160
7.1	Results of the (004) XSW measurements. The coherent fractions f_{004} and coherent positions P_{004} were determined by χ^2 fit of Eq. (2.72) to the data. The theoretical values of ϵ_{\perp} and P_{004} were obtained by applying Eq. (7.1) and Eq. (7.2) for A and B, respectively, using calibrated x values.	175
7.2	XSW results of the (004) measurements on sample D through G ($E_{\gamma} = 6.8$ keV).	193
7.3	Results of the off-normal XSW measurements ($E_{\gamma} = 6.9$ keV).	193
7.4	Result of the (004) XSW measurements and calculated escape depths Z_2 at $\alpha_u = 2^{\circ}, 3^{\circ}, 4^{\circ}$ and 10° .	200
7.5	XSW results of the (111) and (022) As K measurements ($E_{\gamma} = 12.8$ keV). The "P ₁₁₁ theory" was based on the non-cluster Keating calculation (Figure 7.18).	208

LIST OF FIGURES

2.1	The schematic of a multilayer structure composed of a substrate and N layers of films to illustrate how the recursion formulae can be derived.	9
2.2	Transformation of a real space lattice vector from \mathbf{a}_0 to \mathbf{a} due to a displacement field $\mathbf{u}(\mathbf{r})$ induced by a small deformation of the lattice.	16
2.3	The σ and π polarization vectors for the incident and the diffracted waves.	16
2.4	The miscut angle ϕ of a surface. The value of ϕ is defined to be positive in this picture.	22
2.5	Two sets of internal and external Ewald spheres satisfying a Bragg condition for a reflection \mathbf{H} .	22
2.6	Selection of a tie point (F) on the dispersion surfaces by the boundary condition and the geometrical interpretation of the dispersion parameters .	25
2.7	Reflection and transmission amplitude ratios for the \mathbf{H} and $-\mathbf{H}$ reflections of a slab.	30
2.8	Boundary conditions for the \mathbf{H} and $-\mathbf{H}$ reflections of a slab.	30
2.9	(a) The calculated angular dependence for the escape depth (Z_2) and the surface intensity ($I_{s,2}$) for As $L\alpha$ emission (1.282 keV) from GaAs. (b) The calculated angular dependence of the penetration depth of the primary x-ray for the GaAs(004) reflection at $E_\gamma = 6.00$ keV.	37
2.10	The PbTiO_3 perovskite unit cells of the up and down polarization states. The atomic coordinates are listed below.	42
2.11	The calculated (a) rocking curve, (b) the real and imaginary parts and (c) the phase of the D-field amplitude ratio at the surface for bulk SrTiO_3 (001) reflection at 13.5 keV.	44
2.12	(a) The D-field amplitude ratio, (c) the incident D-field intensity and (d) the total D-field intensity at the Ti site calculated at various depths z for the PbTiO_3 (001) reflection (13.5 keV) of 400 \AA PbTiO_3 (polarized up) on SrTiO_3 (001). (b) shows the phase of the D-field amplitude ratio at the	45

	surface.	
2.13	The total D-field intensities at the Pb site near the PbTiO ₃ (001) reflection for a 415.6 Å PbTiO ₃ (polarized up) thin film at various depths z.	48
2.14	XSW data and best fits for the reflectivity and (a) Pb L and (b) Ti K fluorescence yields for 400 Å PbTiO ₃ on SrTiO ₃ (001).	49
3.1	Top view of the multi-chamber UHV system at beamline X15A at the NSLS (it is currently located at the 12ID-D undulator station of the BESSRC CAT at the APS).	53
3.2	Simulated fluorescence yields for the GaAs(004) reflection at 7.00 keV for various coherent positions P to demonstrate how the standing wave field moves with respect to a diffraction plane.	54
3.3	A float chart describing the structure of the XSW data acquisition program used at 5ID-C/APS.	56
3.4	Typical experimental setup at the APS for open-air XSW measurements using bulk Bragg reflections.	57
3.5	Block diagram of the electronic systems at the 5ID-C undulator station of the DND CAT at the APS.	59
3.6	A picture of the multi-chamber UHV system shot right after its installation at the 12ID-D hutch of the BESSRC CAT at the APS.	61
3.7	(a) A DuMond diagram considering the Si(111), (004) and (008) reflections at 12.00 keV. (b) and (c) are a comparison in DuMond diagrams between scanning a Si sample [(b)] and scanning a Si(004) channel cut [(c)].	63
4.1	The crystal structure of bulk GaAs.	65
4.2	The ideally bulk terminated GaAs(001) surface.	66
4.3	Energy-level diagrams for GaAs in the bulk (a) and at the surface (b), based on linear combinations of Ga and As atomic orbitals.	68
4.4	Filled and empty dangling bonds predicted by the electron counting model in an As- (a) and a Ga- (b) terminated GaAs(001) surface.	71

4.5	The structural models proposed by Chadi for the GaAs(001) (2×4) reconstruction with (a) 3 As dimers in the first layer and (b) two As dimers in the first layer and the third dimer in the third layer.	77
4.6	The GaAs(001) c(2×8) unit cells constructed from (a) the three-dimer and (b) the two-dimer (2×4) models proposed by Chadi (see Figure 4.5).	78
4.7	The structural models for the GaAs(001) (2×4) (a) α , (b) β and (c) γ phases proposed by Farrell and Palmström based on the relative intensities of the RHEED fractional peaks.	81
4.8	The relaxed structural models for the GaAs(001) (2×4) (a) α , (b) β and (c) β_2 phases based on theoretical calculations.	83
4.9	The GaAs(001) (2×M) unit cell containing D As dimers and (M – D) dimer vacancies.	87
4.10	The charge distributions based on the electron counting model for the GaAs(001) (2×4) (a) β and (b) β_2 structures.	87
4.11	(a) The structural model of the GaAs(001) (2×4) β_2 surface with kinks in the As dimer rows. (b) The energy-level diagram near the GaAs(001) surface showing the band bending induced by doping and surface states.	91
4.12	The structural models proposed for the GaAs(001) (4×2) reconstruction by (a) Frankel et al. (β), (b) Biegelsen et al. (β_2), (c) Skala et al. and (d) Moriarty et al..	94
4.13	The structural models proposed for the GaAs(001) c(4×4) reconstruction with dimer blocks containing (a) 3 As dimers ($\Theta_{\text{as}} = 1.75$ ML) and (b) 2 As dimers ($\Theta_{\text{as}} = 1.5$ ML).	96
5.1	Some of the LEED patterns commonly observed on the clean GaAs(001) surface prepared by thermal annealing of an As capped substrate: (a) c(4×4), (b) (1×6) and (c) (3×6)/(6×6).	103
5.2	Comparison between the (a) As- and (b) Sb-stabilized (2×4) LEED patterns. The Sb-stabilized (2×4) surface was annealed at 505 °C.	104
5.3	Auger spectra of the GaAs(001) surface (a) before and (b) after the As protective layer was thermally desorbed and (c) after the adsorption of about 0.8 ML of Sb.	105

5.4	The GaAs(001):Sb-(2×4) experimental XSW data (filled circles) and the best fits (solid lines) for the normalized Sb L fluorescence yields and the reflectivities R versus the incident angle θ for the GaAs (a) (004) and (b) the (022) Bragg reflections.	107
5.5	The (a) [110] and (b) [100] projections of an Sb-terminated GaAs(001) surface.	109
5.6	Proposed structural models for the Sb-stabilized GaAs(001) (2×4) surface with one and three Sb dimers per unit cell.	113
5.7	The top and the $[\bar{1}\bar{1}0]$ side views of two different GaAs(001):Sb-(2×4) models. Both models have two Sb dimers per unit cell ($\Theta_{\text{Sb}} = 0.5$ ML).	115
5.8	The (111) XSW data (filled circles) and the best fits (solid lines) for the normalized Sb L fluorescence yield and the GaAs(111) reflectivity R. The dashed line is the calculated Sb fluorescence yields for $\Delta x = 0.4$ Å in Figure 5.7, while the best-fit solid line corresponds to $\Delta x = 0$.	117
5.9	The top and the $[\bar{1}\bar{1}0]$ side views of the δ_2 model for the GaAs(001):Sb-(2×4) surface proposed by Schmidt and Bechstedt.	119
5.10	Calculated (022) (solid curve) and (111) (dashed curve) coherent fractions based on Eq. (5.7) and (5.8), respectively, for the δ_2 model.	121
6.1	Structural models proposed for the InAs(001) As-rich (2×4) surface by Yamaguchi and Horikoshi (a)(b) and for the InAs(001) In-rich (4×2) surface by Ohkouchi and Ikoma and by Kendrick <i>et al.</i> (c).	125
6.2	The energy-level diagram near the (001) surfaces of (a) n-type and (b) p-type InAs.	127
6.3	Filled-state STM images measured by Resch-Esser <i>et al.</i> of the GaAs(001):In (4×2) surfaces with approximately (a) 0.25 and (b) 0.5 ML of In. (c) shows the same surface of (b) over a larger area. Each set of figures contains a 3D image (bottom). All the images were obtained from J. Zegenhagen.	134
6.4	The c(8×2) models proposed for the GaAs(001):In surface by Resch-Esser <i>et al.</i> based on STM for In coverages (a) below and (b) above 0.25 ML.	137

6.5	Two (4×2) models proposed for the GaAs(001):In surface by Xue <i>et al.</i> based on STM.	138
6.6	(a) A typical Auger spectrum measured on an In-terminated GaAs(001) surface. (b) In coverage of a GaAs(001):In surface measured as a function of the annealing temperature.	141
6.7	A series of LEED patterns of the In-terminated GaAs(001) surface recorded at two different beam energies during the annealing experiment depicted in Figure 6.6(b).	142
6.8	Typical x-ray fluorescence spectra from the (004) and (022) XSW scans measured from a GaAs(001):In surface.	145
6.9	The (004), ($\bar{1}11$) and (111) XSW experimental data and analysis for sample S1.	148
6.10	The (004) and ($\bar{1}11$) XSW data and analysis for sample S2.	149
6.11	The (022) and (111) XSW data and analysis for sample S2.	150
6.12	The (004) and (022) XSW data and analysis for sample S3.	151
6.13	The (004) and (022) XSW data and analysis for sample S4 annealed at 420 °C.	152
6.14	The (004) and (022) XSW data and analysis for sample S4 annealed at 450 °C.	153
6.15	(a) - (c) The [110], [$0\bar{1}0$] and [$\bar{1}\bar{1}0$] projected views of various symmetric sites (A – H) on the unreconstructed GaAs(001) surface. (d) Possible adsorption sites on the GaAs(001) surface.	156
6.16	Calculated In fluorescence yields (dashed lines) based on Resch-Esser's model [Figure 6.4(a)] compared with the present XSW measurements for sample S2 for (a) the (022) reflection and (b) the (111) reflection.	158
6.17	(a) The proposed (4×2)/c(8×2) model based on the present XSW analysis and the previous STM studies for the GaAs(001):In surface with an In coverage of 0.25 ML. (b) A (4×1) model constructed by changing the termination of the bare surface in the trenches from Ga dimers in (a) to As dimers.	164

7.1	The (004) XSW data and the theory (solid lines) for the normalized In L fluorescence yields and the GaAs(004) reflectivity R versus incident angle θ for (a) samples A and B and (b) sample C.	176
7.2	The [110] projected side view depiction of a pseudomorphically grown 1 ML $\text{In}_x\text{Ga}_{1-x}\text{As}$ buried heterostructure.	178
7.3	The 42-atom cluster and the surrounding 46 medium atoms used in the present calculation for 1ML $\text{In}_x\text{Ga}_{1-x}\text{As}$ buried in GaAs(001).	181
7.4	The calculated vertical positions with respect to the nearest substrate (004) As plane for (a) the In atoms and (b) the As atoms right below the $\text{In}_x\text{Ga}_{1-x}$ layer. The measured positions A, B and C in (a) are from the present XSW experiment. The data point S is the statistically averaged value of the In P_{004} positions for $x = 1.0$ in Ref. 9, 10, and 11 of Chapter 7.	184
7.5	The calculated compositional dependence of the variation of the second nearest neighbor As-As distance for the As atoms right below and above the $\text{In}_x\text{Ga}_{1-x}$ layer.	186
7.6	The calculated (a) In-As and Ga-As bond lengths L and (b) As-In-As and As-Ga-As bond angles ϕ in the $\text{In}_x\text{Ga}_{1-x}\text{As}$ ML as functions of the In concentration x (solid lines).	188
7.7	The (111) (top) and ($\bar{1}\bar{1}1$) (bottom) XSW data and the best fits (solid lines) for the normalized In L fluorescence yields and reflectivity (R) versus the incident angle (θ) for samples A and B.	194
7.8	(a) [$1\bar{1}0$] and (b) [110] projected side views of a pseudomorphically grown 1 ML $\text{In}_x\text{Ga}_{1-x}\text{As}$ buried heterostructure.	196
7.9	00L (top, solid lines), 11L (bottom, solid lines) and $\bar{1}\bar{1}L$ (bottom, dots) rod scans at 8.00 keV for samples C through G.	198
7.10	The experimental XSW data and the best fits for the normalized As L fluorescence yields at $\alpha_u = 2^\circ$ and 10° and the GaAs(004) reflectivity (R) versus the incident angle (θ). The sample was a ML of InAs grown on a GaAs(001) substrate and capped with 25 Å of GaAs.	202

7.11	The experimental XSW data and the best fits for the normalized As $K\alpha$ fluorescence yields and the InSb(111) reflectivity (R) versus the incident angle (θ) for samples W1 and W2.	206
7.12	The experimental XSW data and the best fits for the normalized As $K\alpha$ fluorescence yields and the InSb(022) reflectivity (R) versus the incident angle (θ) for samples W1 and W2.	207
7.13	The in-plane and out-of-plane geometries for the polarization-dependent EXAFS measurements.	209
7.14	EXAFS measured absorption coefficients $\mu(E)$ for the InAs standard and for sample W2-2 at the in-plane and out-of-plane geometries.	209
7.15	The [01-1] view of an InSb(111)/1 ML InAsSb/InSb heterostructure.	211
7.16	(a) The As K EXAFS $\chi(k)$ and (b) the magnitudes of the Fourier transform of the k-weighted EXAFS, $k\chi(k)$, for the InAs standard and for the in-plane and out-of-plane measurements of sample W2-2.	213
7.17	(a) Comparisons of the Fourier-filtered first-shell contributions with $k\chi(k)$ and (b) the best fits to the Fourier-filtered first-shell data for the in-plane and out-of-plane measurements of sample W2-2.	214
7.18	(a) Comparison between the P_{111} calculated based on continuum elasticity theory (dots) and the non-cluster Keating calculation (solid lines) for the As in the buried monolayer and the In at the lower InAsSb/InSb interface.	216
7.19	(a) The $\text{InAs}_j\text{Sb}_{4-j}$ cluster with the medium atoms used for the present random-cluster calculation. (b) Calculated In-As and In-Sb bond lengths in a strained $\text{InAs}_x\text{Sb}_{1-x}$ layer (solid lines) and unstrained bulk $\text{InAs}_x\text{Sb}_{1-x}$ (dashed lines).	218
A.1	The stress tensor notation.	225

Chapter 1 Introduction

The GaAs(001) surface has been of great interest due to its technological importance and rich surface structures. Despite considerable experimental and theoretical investigations, the detailed structures of a number of the reconstructions are still under debate. Recently the growth of coherently strained 3-dimensional islands and short-period superlattices composed of III-V semiconductors has become a new challenge for developing the next generation of electronic and optical devices. The studies of adsorbate-induced compound semiconductor surfaces and the strain in heterolayers can directly lead to a better understanding and control of the growth of highly lattice-mismatched systems. I therefore carried out in this thesis work a series of high-resolution measurements using the x-ray standing wave technique to characterize the bonding geometries of the GaAs(001) surface upon the adsorption of Sb and In as well as the local lattice distortions in strained buried monolayers.

In the following chapters, I first discuss the principle of the x-ray standing wave technique in Chapter 2. The dynamical diffraction theory for x-rays is described in Section 2.2. Towards the end of my thesis work I was involved in developing a new structural probe for determining the polarization state of a ferroelectric thin film using the x-ray standing waves generated by the film. Since this requires an understanding of Takagi-Taupin dynamical theory, and since no comprehensible description of this theory (particularly for the application in the standing wave technique) is available, I introduce

the dynamical theory following Takagi and Taupin's approach. This leads to results of more general applications. Examples of theoretical simulations and experimental data are presented at the end for a ferroelectric thin film. It is shown that the conventional, Ewald and von Laue's approach, which is what most of this thesis work is based on, can be described as a special case of this more general theory.

In Chapter 3 we discuss the experimental setup for the x-ray standing wave measurements. The x-ray experiments reported in this thesis were conducted at Brookhaven National Laboratory and Argonne National Laboratory using synchrotron radiation. As we have been increasingly using the newly constructed x-ray source at Argonne National Laboratory, I have more descriptions of the standing wave setups used there.

In Chapter 4 I review the background information for the GaAs(001) clean surface. First there is an introduction to the electron counting model for semiconductor surfaces. It explains the fundamental surface structures of the III-V surfaces based on simple electronic and energetic considerations. I then discuss a number of surface reconstructions observed for GaAs(001), including both the structural and electronic properties. I put emphasis on the As-rich (2×4) reconstruction due to the extensive previous investigations and its technological importance. However, the (4×2) surface is more relevant to the study in Chapter 6. I describe the procedure for preparing a clean GaAs(001) surface at the end of Chapter 4.

Chapters 5 and 6 describe the results of *in-situ* studies of adsorbate structures on the GaAs(001) surface. In Chapter 5 I discuss the measurements for the coverage and the

dimer bonding geometry of the GaAs(001): Sb (2×4) surface. I compare our measurements with theoretical calculations and six existing structural models. It is found that one, and only one, of these models is consistent with our experimental. In Chapter 6 I describe investigations of the surface structure of the In-induced GaAs(001) (4×2)/c(8×2) reconstruction. Our x-ray standing wave measurements suggest an unexpected In adsorption site. I also discuss the possible surface Ga and As structures based on high-resolution scanning tunneling microscopy images from our collaborators. We propose a c(8×2) unit cell to best explain the experimental observations. A general review of InAs(001) surface structures, the growth of InAs on GaAs(001) and related issues are given at the beginning of this chapter to outline the motivation and to also help understand the In-induced (4×2)/c(8×2) reconstruction.

In Chapter 7 I include our XSW results for the measurements of strain in buried III-V monolayer heterolayers. The expansion or contraction of buried III-V layers is directly measured by the x-ray standing waves and compared with continuum elasticity theory and random-cluster calculations using the Keating valence force field. I first discuss the case of one monolayer of InGaAs buried in GaAs(001). Based on our studies we conclude with a simple microscopic picture describing the bond-bending-induced local lattice distortions of a strained (001) layer, which leads to the macroscopic behavior described by continuum elasticity theory. For a (111)-oriented film, a more complicated picture associated with a bond length split due to symmetry considerations has been predicted by a random cluster calculation. However, our x-ray standing wave measurements and extended x-ray absorption fine structure studies of InAsSb

monolayers buried in InSb(111) are inconsistent with the theoretical calculations. We also show the results of x-ray standing wave measurements using off-normal reflections and the evanescent wave emission effect. We briefly summarize this thesis work in Chapter 8.

Chapter 2 X-Ray Standing Wave Technique

2.1 Introduction

In this chapter I introduce the x-ray standing wave (XSW) technique based on the generalized dynamical theory developed by Takagi [1] and Taupin [2], which was initially derived for treating deformed crystals, but recently has been applied more extensively to diffraction studies of thin film structure [17]. This is due to the advantage that the theory can be expressed explicitly as a pair of partial differential equations with respect to the depth z . The understanding of this theory has led to the prediction of a new structural probe using the standing wave field generated by Bragg reflections of thin films. The feasibility of this technique has been demonstrated experimentally by a number of research groups [3 - 9]. The classical dynamical theory, which forms the theoretical foundation of this thesis work and is applicable mainly to semi-infinite perfect crystals, will be shown to be a special case of the more general theory. A review of the conventional x-ray standing wave method can be found in Ref. 10.

2.2 Generalized Dynamical Theory of x-ray

The difference between the dynamical and the kinematical diffraction theories lie in the fact that the former takes into account multiple scattering, which becomes a dominant effect for strong reflections such as those used for XSW measurements. Several different approaches have been developed for dynamical calculations. Complete

historical and theoretical reviews of the various dynamical theories for x-ray can be found in Ref. 11 – 15. Most of the theoretical studies were focused on deriving the scattered intensity at the surface (i.e., the reflectivity). For the XSW technique, we need to also calculate the total field intensity inside a crystal.

2.2.1 Total field intensity

In the XSW method, atomic positions are probed by monitoring their emission of the secondary photons or electrons while spatially scanning the XSW field through the lattice. Based on the electrical dipole approximation of the photoelectric effect [10, 16], the yields of the emitted fluorescence and photoelectrons, or the cross section of the photoelectric effect, are proportional to the total field intensity at the center of the probed atom. We hence first derive the total internal D-field intensity within the two-beam approximation.

Consider an incident and a Bragg-diffracted plane waves traveling along \mathbf{k}_0 and \mathbf{k}_H , respectively,

$$\begin{aligned} \mathcal{D}_0 &= \mathbf{D}_0 e^{2\pi i[\nu t - \mathbf{k}_0 \cdot \mathbf{r}]} \\ \mathcal{D}_H &= \mathbf{D}_H e^{2\pi i[\nu t - \mathbf{k}_H \cdot \mathbf{r}]} \end{aligned} \quad (2.1)$$

where \mathbf{H} is a reciprocal lattice vector of the diffracting crystal. \mathbf{D}_0 and \mathbf{D}_H are the D-field amplitudes of the incident and scattered waves. ν is the photon frequency. For the

internal wave vectors \mathbf{k}_0 and \mathbf{k}_H the conservation of momentum or Bragg's law requires that

$$\mathbf{k}_H = \mathbf{k}_0 + \mathbf{H}. \quad (2.2)$$

The internal wave vectors can be related to the external wave vectors \mathbf{K}_0 and \mathbf{K}_c through proper boundary conditions at the surface. \mathbf{K}_0 and \mathbf{K}_H are real vectors with an amplitude $|\mathbf{K}_0| = |\mathbf{K}_H| = K = 1/\lambda$, where λ is the wavelength of the x-ray, while \mathbf{D}_0 , \mathbf{D}_H , \mathbf{k}_0 and \mathbf{k}_H are in general complex vectors.

The total field intensity can be expressed as

$$\begin{aligned} |\mathcal{D}|^2 &= |\mathcal{D}_0 + \mathcal{D}_H|^2 = \left| e^{-2\pi i \mathbf{k}_0 \cdot \mathbf{r}} (D_0 \hat{\mathbf{e}}_0 + D_H \hat{\mathbf{e}}_H e^{-2\pi i \mathbf{H} \cdot \mathbf{r}}) \right|^2 \\ &= |D_0|^2 e^{-4\pi \text{Im}(\mathbf{k}_0) \cdot \mathbf{r}} \left\{ 1 + \left| \frac{D_H}{D_0} \right|^2 + 2 \hat{\mathbf{e}}_0 \cdot \hat{\mathbf{e}}_H \text{Re} \left[\frac{D_0^* D_H}{|D_0|^2} e^{-2\pi i \mathbf{H} \cdot \mathbf{r}} \right] \right\}, \end{aligned} \quad (2.3)$$

where we have applied Eq. (2.2) and defined $\mathbf{k}_0 = \mathbf{k}_0' - i\mathbf{k}_0''$. $\hat{\mathbf{e}}_0$ and $\hat{\mathbf{e}}_H$ are the unit vectors along \mathbf{D}_0 and \mathbf{D}_H . If we define the polarization factor $P = \hat{\mathbf{e}}_0 \cdot \hat{\mathbf{e}}_H$ and the D-field

amplitude ratio $X_H = \frac{D_H}{D_0}$, and used the fact that $\frac{D_0^* D_H}{|D_0|^2} = \frac{D_H}{D_0} = X_H$, Eq. (2.3) can be

further reduced to

$$|\mathcal{D}|^2 = |D_0|^2 e^{-4\pi \text{Im}(\mathbf{k}_0) \cdot \mathbf{r}} \left\{ 1 + |X_H|^2 + 2P |X_H| \cos[\nu - 2\pi \mathbf{H} \cdot \mathbf{r}] \right\}, \quad (2.4)$$

where ν is the phase of $X_{\mathbf{H}}$ (i.e., the phase difference between the incident and the scattered waves).

Eq. (2.4) indicates that to calculate the total internal D-field intensity $|\mathcal{D}|^2$ at a position \mathbf{r} inside a crystal, we need to know (1) the D-field amplitude ratio $X_{\mathbf{H}}$ at \mathbf{r} and (2) the incident D-field intensity $|\mathcal{D}_0|^2 e^{-4\pi\mathbf{k}_0 \cdot \mathbf{r}} = |\mathcal{D}_0|^2$ at \mathbf{r} . It will be shown in the following discussion that the factor $e^{-4\pi\mathbf{k}_0 \cdot \mathbf{r}}$ carries the information regarding the attenuation of the primary beam.

2.2.2 Recursion formulae

In this section we discuss how to calculate $X_{\mathbf{H}}$ and $|\mathcal{D}_0|^2$ for a multilayer structure. We follow the argument used by Bartels *et al.* [17] to develop a set of recursion formulae, which are the most desirable form for dynamical calculations for a layered system. These formulae consider noncentrosymmetric crystals and misoriented interfaces.

Figure 2.1 shows the schematic of a multilayer structure composed of a substrate and N layers of films. It is assumed that the structure is homogeneous within each layer.

To help the discussion proceed, we define the modified D-field amplitudes to be

$D_0 = \mathcal{D}_0 e^{-2\pi\mathbf{k}_0 \cdot \mathbf{r}}$ and $D_{\mathbf{H}} = \mathcal{D}_{\mathbf{H}} e^{-2\pi\mathbf{k}_0 \cdot \mathbf{r}}$ to include attenuation. Notice that

$\frac{D_{\mathbf{H}}}{D_0} = \frac{\mathcal{D}_{\mathbf{H}}}{\mathcal{D}_0} = X_{\mathbf{H}}$. In Figure 2.1 we are interested in calculating $X_{\mathbf{H}}$ and D_0 at point A,

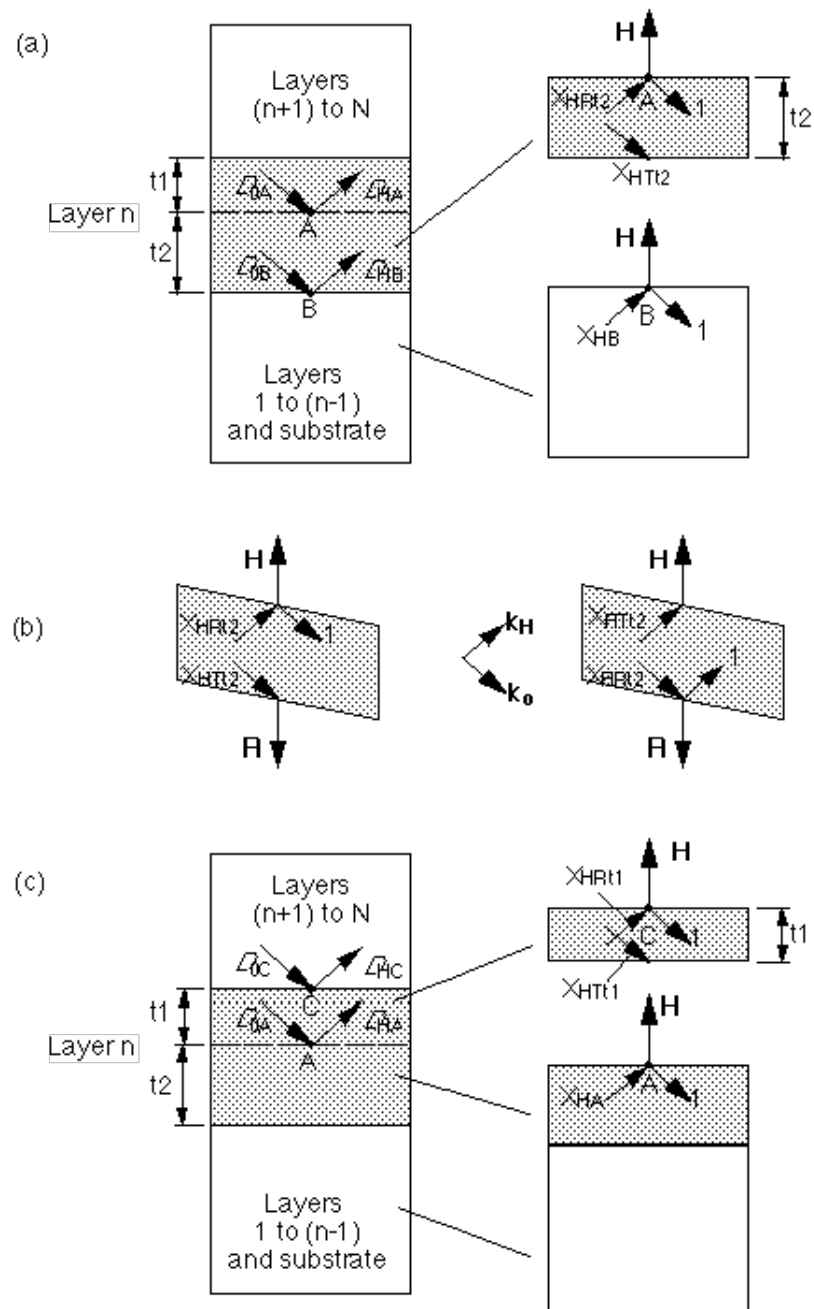


Figure 2.1 The left-hand sides of (a) and (c) show the schematic of a multilayer structure composed of a substrate and N layers of films. On the right-hand side the structure is divided into two parts in two different ways to illustrate how the recursion formulae can be derived. (b) depicts all the amplitude ratios for a film with miscut.

which is located inside the n th layer and t_1 below the $n/(n+1)$ interface [or t_2 above the $(n-1)/n$ interface].

Figure 2.1(a) shows the quantities we need to calculate $X_{\mathbf{H}\mathbf{A}}$. We assume that we already know (1) the transmission ($X_{\mathbf{H}\mathbf{T}t_2}$) and reflection ($X_{\mathbf{H}\mathbf{R}t_2}$) amplitude ratios of the \mathbf{H} reflection for a slab of thickness t_2 of the n th layer material, (2) the transmission ($\bar{X}_{\mathbf{H}\mathbf{T}t_2}$) and reflection ($\bar{X}_{\mathbf{H}\mathbf{R}t_2}$) amplitude ratios of the $\bar{\mathbf{H}}$ reflection for the same slab, and (3) the (reflection) amplitude ratio ($X_{\mathbf{H}\mathbf{B}}$) for the \mathbf{H} reflection at the surface of a semi-infinite crystal composed of the substrate and the first $(n-1)$ layers. $X_{\mathbf{H}\mathbf{T}t_2}$ is defined to be the ratio between the modified D-field amplitudes at the bottom and the top surfaces traveling in the \mathbf{k}_0 direction. For $\bar{X}_{\mathbf{H}\mathbf{T}t_2}$ and $\bar{X}_{\mathbf{H}\mathbf{R}t_2}$ we consider the incident beam arriving at the bottom surface along the $\mathbf{k}_{\mathbf{H}}$ direction and the scattered beam traveling along the \mathbf{k}_0 direction [Figure 2.1(b)]. This is required by the two-beam approximation (i.e., only two wave vectors are considered). It also implies that $\bar{X}_{\mathbf{H}\mathbf{T}t_2}$ ($\bar{X}_{\mathbf{H}\mathbf{R}t_2}$) are in general different from $X_{\mathbf{H}\mathbf{T}t_2}$ ($X_{\mathbf{H}\mathbf{R}t_2}$) due to miscut and noncentrosymmetry of the films.

The following set of linear equations of $D_{0\mathbf{A}}$, $D_{\mathbf{H}\mathbf{A}}$, $D_{0\mathbf{B}}$ and $D_{\mathbf{H}\mathbf{B}}$ can be derived by considering multiple diffraction in Figure 2.1(a)

$$D_{\mathbf{H}\mathbf{A}} = D_{0\mathbf{A}}X_{\mathbf{H}\mathbf{R}t_2} + D_{\mathbf{H}\mathbf{B}}\bar{X}_{\mathbf{H}\mathbf{T}t_2}, \quad D_{0\mathbf{B}} = D_{0\mathbf{A}}X_{\mathbf{H}\mathbf{T}t_2} + D_{\mathbf{H}\mathbf{B}}\bar{X}_{\mathbf{H}\mathbf{R}t_2}, \quad D_{\mathbf{H}\mathbf{B}} = X_{\mathbf{H}\mathbf{B}}D_{0\mathbf{B}}, \quad (2.5)$$

which can be combined into a single equation by eliminating all the D 's

$$X_{\text{HA}} = \frac{X_{\text{HRt2}} + X_{\text{HB}}(X_{\text{HTt2}}\bar{X}_{\text{HTt2}} - X_{\text{HRt2}}\bar{X}_{\text{HRt2}})}{1 - X_{\text{HB}}\bar{X}_{\text{HRt2}}}. \quad (2.6)$$

Eq. (2.6) is the expression for calculating the amplitude ratio at any location inside a multilayer. The recursion nature of Eq. (2.6) is clear: The value of X_{HA} obtained at the $n/(n+1)$ interface becomes the X_{HB} that we need for calculating X_{HA} in the $(n+1)$ layer. The other four complex quantities in Eq. (2.6), which are associated with the slab of thickness t_2 , have to be calculated individually based on Takagi-Taupin theory at each point. The recursion process starts with the substrate and advances upwards through each layer until it reaches point A.

Using the similar approach we can derive a general expression for $D_0 = D_0 e^{-2\pi k_0'' r}$.

In Figure 2.1(c) we consider a slab of thickness t_1 and a semi-infinite crystal terminated at surface A. If we already know X_{HTt1} , X_{HRt1} , \bar{X}_{HTt1} and \bar{X}_{HRt1} , which are defined in a similar way and can be calculated from Takagi-Taupin theory, we can derive the following algebraic relationship between D_{0A} and D_{0C}

$$D_{0A} = D_{0C} X_{\text{HTt1}} + D_{\text{HA}} \bar{X}_{\text{HRt1}} = D_{0C} X_{\text{HTt1}} + D_{0A} X_{\text{HA}} \bar{X}_{\text{HRt1}}, \quad (2.7)$$

which leads to

$$D_{0A} = \frac{D_{0C} X_{\text{HTt1}}}{1 - X_{\text{HA}} \bar{X}_{\text{HRt1}}}. \quad (2.8)$$

Eq. (2.8) implies that, due to the dependence of D_{0A} on D_{0B} , the recursion process for calculating D_{0A} needs to start at the surface of the multilayer and then proceed layer by layer down to point A. Since X_{HA} appears in the right hand side of Eq. (2.8), the computing strategy would be to carry out the calculation for X_{HA} [Eq. (2.6)] first.

With the recursion formulae the problem we are trying to solve has been simplified, with respect to dynamical calculations, from dealing with an arbitrary multilayer system to considering just a single slab. We next discuss the generalized dynamical theory - Takagi-Taupin theory.

2.2.3 *Takagi-Taupin theory*

In this section we first compare briefly the differences between the classical (based on Ewald [18] and von Laue [19]) and the generalized (based on Takagi [1] and Taupin [2]) dynamical theories. We then derive the latter following the argument used in Ref. 20. More discussions regarding Takagi-Taupin theory can be found in Ref. 12 and 21 – 24.

In Ewald and von Laue's approach the dynamical theory was developed by solving Maxwell's equations in a medium described by a perfectly periodic complex dielectric function κ . Based on the classical dipole oscillator model [11, 25] the electric susceptibility χ of a periodic medium can be described by a Fourier sum over the reciprocal lattice as

$$\chi(\mathbf{r}) = \kappa - 1 = -\Gamma \sum_{\mathbf{g}} F_{\mathbf{g}} e^{-2\pi i \mathbf{g} \cdot \mathbf{r}}, \quad (2.9)$$

where \mathbf{g} 's are the reciprocal lattice vectors, $\Gamma = \frac{r_e \lambda^2}{\pi V_{uc}}$, $r_e = \frac{e^2}{mc^2}$ and V_{uc} the unit cell volume. $F_{\mathbf{g}} = \int_{V_{uc}} \rho_e(\mathbf{r}) e^{2\pi i \mathbf{g} \cdot \mathbf{r}} d\mathbf{r}$ is the structure factor [26]. The solution near a Bragg reflection to the Maxwell's equations employing the periodic dielectric function Eq. (2.9) is assumed to be

$$\mathbf{D}(\mathbf{r}, t) = e^{2\pi i \mathbf{k}_0 \cdot \mathbf{r}} \sum_{\mathbf{g}} \mathbf{D}_{\mathbf{g}} e^{-2\pi i \mathbf{k}_{\mathbf{g}} \cdot \mathbf{r}} = e^{2\pi i \mathbf{k}_0 \cdot \mathbf{r}} \sum_{\mathbf{g}} \mathbf{D}_{\mathbf{g}} e^{-2\pi i \mathbf{g} \cdot \mathbf{r}}, \quad (2.10)$$

where $\mathbf{k}_{\mathbf{g}} = \mathbf{k}_0 + \mathbf{g}$. Eq. (2.10) has the form of a Bloch function. Notice that the coefficients $\mathbf{D}_{\mathbf{g}}$ are constant vectors due to the translational symmetry along the surface normal for a semi-infinite perfect crystal, i.e., the part of the crystal below any point \mathbf{r} is still a semi-infinite crystal.

Takagi-Taupin theory was originally derived for predicting the intensity of dynamical diffraction from a slightly deformed crystal. Consider that the deformation of the lattice has transformed a vector \mathbf{r}_0 into a new vector \mathbf{r} . We can define a displacement field \mathbf{u} as $\mathbf{u}(\mathbf{r}) = \mathbf{r} - \mathbf{r}_0$. The electric susceptibility for the deformed lattice become

$$\chi(\mathbf{r}) = -\Gamma \sum_{\mathbf{g}} F_{\mathbf{g}} e^{-2\pi i \mathbf{g} \cdot [\mathbf{r} - \mathbf{u}(\mathbf{r})]}. \quad (2.11)$$

The transformation $\mathbf{r}_0 = \mathbf{r} - \mathbf{u}(\mathbf{r})$ will convert Eq. (2.11) back into Eq. (2.9).

To find a possible solution, as we did in Eq. (2.10) for the classical theory, we need to construct a new reciprocal space for the deformed crystal. Consider three vector $\mathbf{a}_0 = \mathbf{r}_{a0} - \mathbf{r}_0$ defined in a perfect lattice (Figure 2.2). After a deformation of the lattice the three vectors become

$$\mathbf{a} = \mathbf{r}_a - \mathbf{r} = [\mathbf{r}_{a0} + \mathbf{u}(\mathbf{r}_a)] - [\mathbf{r}_0 + \mathbf{u}(\mathbf{r})] = \mathbf{a}_0 + \mathbf{u}(\mathbf{r} + \mathbf{a}) - \mathbf{u}(\mathbf{r}). \quad (2.12)$$

If we assume $|\mathbf{a}| \ll |\mathbf{r}|$, or a macroscopic deformation, we can express $\mathbf{u}(\mathbf{r} + \mathbf{a})$ as

$\mathbf{u}(\mathbf{r} + \mathbf{a}) = \mathbf{u}(\mathbf{r}) + \mathbf{a} \left(\frac{\partial \mathbf{u}}{\partial \mathbf{r}} \right)$. Eq. (2.12) thus implies that

$$\mathbf{a} = \mathbf{a}_0 \left\{ 1 + \left(\frac{\partial \mathbf{u}}{\partial \mathbf{r}} \right) \right\}, \quad (2.13)$$

where $\left(\frac{\partial \mathbf{u}}{\partial \mathbf{r}} \right)$ is nothing but the strain tensor $\varepsilon_{ij} = \left(\frac{\partial u_i}{\partial r_j} \right)$. If \mathbf{a}_i 's are the real-space basis

vectors for the deformed crystal, the corresponding reciprocal basis vectors can be

defined as $\mathbf{b}_j \cdot \mathbf{a}_i = \delta_{ij}$, and Eq. (2.13) would imply that $\mathbf{b}_j = \left\{ 1 - \left(\frac{\partial \mathbf{u}}{\partial \mathbf{r}} \right) \right\} \mathbf{b}_{0j}$. Therefore, in

general, a deformed reciprocal lattice can be constructed on the basis of the perfect

reciprocal lattice as

$$\mathbf{g}(\mathbf{r}) = \left\{ 1 - \left(\frac{\partial \mathbf{u}}{\partial \mathbf{r}} \right) \right\} \mathbf{g}_0 = \mathbf{g}_0 - \begin{pmatrix} \partial \mathbf{u} / \partial x \\ \partial \mathbf{u} / \partial y \\ \partial \mathbf{u} / \partial z \end{pmatrix} \mathbf{g}_0 = \mathbf{g}_0 - \nabla(\mathbf{g}_0 \cdot \mathbf{u}), \quad (2.14)$$

where the subscript 0 denotes vectors for perfect crystals. Based on this new vector system, a simple equation, expressed in the form of a modified Bloch function, can be used as the assumed solution to the Maxwell's equations containing the dielectric function Eq. (2.11)

$$\mathbf{D}(\mathbf{r}, t) = e^{2\pi i \nu t} \sum_{\mathbf{g}_0} \mathbf{D}_{\mathbf{g}_0}(\mathbf{r}) e^{-2\pi i (\mathbf{k}_{\mathbf{g}_0} \cdot \mathbf{r} - \mathbf{g}_0 \cdot \mathbf{u})}. \quad (2.15)$$

Applying the momentum operator $-i\hbar\nabla$ to the \mathbf{g}_0 -th component wave in Eq. (2.15) we have $-i\hbar\nabla e^{-2\pi i (\mathbf{k}_{\mathbf{g}_0} \cdot \mathbf{r} - \mathbf{g}_0 \cdot \mathbf{u})} = -2\pi\hbar \left[\mathbf{k}_{\mathbf{g}_0} - \nabla(\mathbf{g}_0 \cdot \mathbf{u}) \right] e^{-2\pi i (\mathbf{k}_{\mathbf{g}_0} \cdot \mathbf{r} - \mathbf{g}_0 \cdot \mathbf{u})}$, which suggests that

$$\mathbf{k}_{\mathbf{g}} = \mathbf{k}_{\mathbf{g}_0} - \nabla(\mathbf{g}_0 \cdot \mathbf{u}) = \mathbf{k}_0 + \mathbf{g}_0 - \nabla(\mathbf{g}_0 \cdot \mathbf{u}) = \mathbf{k}_0 + \mathbf{g} \quad (2.16)$$

can be considered as the true wave vector for the \mathbf{g}_0 -th component wave. Due to the deformation as well as the possible finite dimensions of the crystal the coefficients \mathbf{D} in (2.15) are not constants any more.

We now derive the Takagi-Taupin equations [20]. We start with solving Maxwell's equations

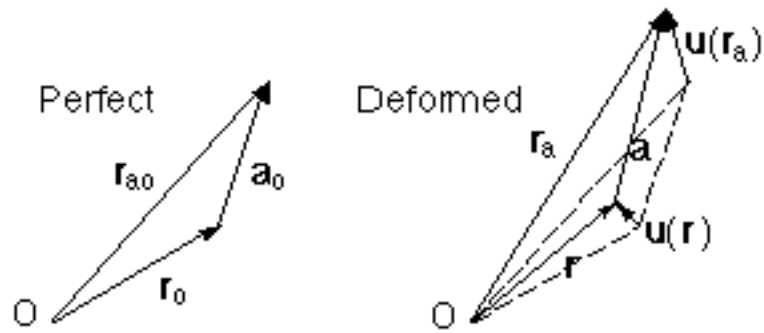


Figure 2.2 Transformation of a real space lattice vector from \mathbf{a}_0 to \mathbf{a} due to a displacement field $\mathbf{u}(\mathbf{r})$ induced by a small deformation of the lattice.

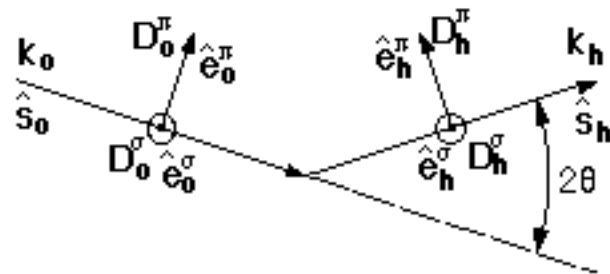


Figure 2.3 The σ and π polarization vectors for the incident and the diffracted waves.

$$\begin{cases} \nabla \times \mathbf{E} = -\frac{1}{c} \frac{\partial \mathbf{H}}{\partial t} \\ \nabla \times \mathbf{H} = \frac{1}{c} \frac{\partial \mathbf{D}}{\partial t} \end{cases} \quad (2.17)$$

using Eq. (2.11) and (2.15). The equations in (2.17) can be combined into a single equation [27]

$$\nabla^2 \mathbf{D} - \frac{1}{c^2} \frac{\partial^2 \mathbf{D}}{\partial t^2} + \nabla \times \nabla \times (\chi \mathbf{D}) = 0. \quad (2.18)$$

The three terms in (2.18) can be derived individually as the following [28]

$$\frac{\partial^2 \mathbf{D}}{\partial t^2} = -4\pi^2 v^2 e^{2\pi i v t} \sum_{\mathbf{g}_0} \mathbf{D}_{\mathbf{g}_0}(\mathbf{r}) e^{-2\pi i (\mathbf{k}_{\mathbf{g}_0} \cdot \mathbf{r} - \mathbf{g}_0 \cdot \mathbf{u}(\mathbf{r}))}, \quad (2.19)$$

$$\nabla^2 \mathbf{D} = -e^{2\pi i v t} \sum_{\mathbf{g}_0} \left\{ 4\pi i (\mathbf{k}_{\mathbf{g}} \cdot \nabla) \mathbf{D}_{\mathbf{g}_0} + 4\pi^2 (\mathbf{k}_{\mathbf{g}} \cdot \mathbf{k}_{\mathbf{g}}) \mathbf{D}_{\mathbf{g}_0} \right\} e^{-2\pi i (\mathbf{k}_{\mathbf{g}_0} \cdot \mathbf{r} - \mathbf{g}_0 \cdot \mathbf{u})}, \quad (2.20)$$

$$\nabla \times (\chi \mathbf{D}) = -\Gamma e^{2\pi i v t} \sum_{\mathbf{g}_0} \left\{ e^{-2\pi i (\mathbf{k}_{\mathbf{g}_0} \cdot \mathbf{r} - \mathbf{g}_0 \cdot \mathbf{u})} (\nabla - 2\pi i \mathbf{k}_{\mathbf{g}}) \times \sum_{\mathbf{q}_0} \mathbf{D}_{\mathbf{q}_0} F_{\mathbf{g}_0 - \mathbf{q}_0} \right\}, \quad (2.21)$$

$$\nabla \times \nabla \times (\chi \mathbf{D}) = 4\pi^2 \Gamma e^{2\pi i v t} \sum_{\mathbf{g}_0} \left\{ e^{-2\pi i (\mathbf{k}_{\mathbf{g}_0} \cdot \mathbf{r} - \mathbf{g}_0 \cdot \mathbf{u})} \sum_{\mathbf{q}_0} F_{\mathbf{g}_0 - \mathbf{q}_0} \mathbf{k}_{\mathbf{g}} \times (\mathbf{k}_{\mathbf{g}} \times \mathbf{D}_{\mathbf{q}_0}) \right\}. \quad (2.22)$$

Substituting (2.19), (2.20) and (2.22) into (2.18) we have

$$\sum_{\mathbf{g}_0} \left\{ 4\pi i (\mathbf{k}_g \cdot \nabla) \mathbf{D}_{\mathbf{g}_0} + 4\pi^2 \left[(\mathbf{k}_g \cdot \mathbf{k}_g) - \left(\frac{v}{c} \right)^2 \right] \mathbf{D}_{\mathbf{g}_0} - 4\pi^2 \Gamma \sum_{\mathbf{q}_0} F_{\mathbf{g}_0 - \mathbf{q}_0} \mathbf{k}_g \times (\mathbf{k}_g \times \mathbf{D}_{\mathbf{q}_0}) \right\} e^{-2\pi i (\mathbf{k}_{\mathbf{g}_0} \cdot \mathbf{r} - \mathbf{g}_0 \cdot \mathbf{u})} = 0 \quad (2.23)$$

Let us define $\hat{\mathbf{s}}_g$ and $\hat{\mathbf{e}}_{\mathbf{g}_0}$ to be the unit vectors of \mathbf{k}_g and $\mathbf{D}_{\mathbf{g}_0}$, respectively. Since $\hat{\mathbf{s}}_g \perp \hat{\mathbf{e}}_{\mathbf{g}_0}$ [29], $\mathbf{D}_{\mathbf{g}_0}$ can be decomposed as $\mathbf{D}_{\mathbf{q}_0} = (\mathbf{D}_{\mathbf{q}_0} \cdot \hat{\mathbf{s}}_g) \hat{\mathbf{s}}_g + (\mathbf{D}_{\mathbf{q}_0} \cdot \hat{\mathbf{e}}_{\mathbf{g}_0}) \hat{\mathbf{e}}_{\mathbf{g}_0}$. We can then make the following simplification [30]

$$\begin{aligned} \mathbf{k}_g \times (\mathbf{k}_g \times \mathbf{D}_{\mathbf{q}_0}) &= (\mathbf{D}_{\mathbf{q}_0} \cdot \mathbf{k}_g) \mathbf{k}_g - (\mathbf{k}_g \cdot \mathbf{k}_g) \mathbf{D}_{\mathbf{q}_0} = |\mathbf{k}_g|^2 (\mathbf{D}_{\mathbf{q}_0} \cdot \hat{\mathbf{s}}_g) \hat{\mathbf{s}}_g - (\mathbf{k}_g \cdot \mathbf{k}_g) \mathbf{D}_{\mathbf{q}_0} \\ &= -|\mathbf{k}_g|^2 (\mathbf{D}_{\mathbf{q}_0} \cdot \hat{\mathbf{e}}_{\mathbf{g}_0}) \hat{\mathbf{e}}_{\mathbf{g}_0} + (|\mathbf{k}_g|^2 - \mathbf{k}_g \cdot \mathbf{k}_g) \mathbf{D}_{\mathbf{q}_0} \approx -|\mathbf{k}_g|^2 (\mathbf{D}_{\mathbf{q}_0} \cdot \hat{\mathbf{e}}_{\mathbf{g}_0}) \hat{\mathbf{e}}_{\mathbf{g}_0} \end{aligned} \quad (2.24)$$

Therefore, for each reciprocal lattice vector \mathbf{g}_0 in (2.23) we have:

$$i(\mathbf{k}_g \cdot \nabla) \mathbf{D}_{\mathbf{g}_0} + \pi \left[(\mathbf{k}_g \cdot \mathbf{k}_g) - K^2 \right] \mathbf{D}_{\mathbf{g}_0} + \pi \Gamma \sum_{\mathbf{q}_0} F_{\mathbf{g}_0 - \mathbf{q}_0} |\mathbf{k}_g|^2 (\mathbf{D}_{\mathbf{q}_0} \cdot \hat{\mathbf{e}}_{\mathbf{g}_0}) \hat{\mathbf{e}}_{\mathbf{g}_0} = 0, \quad (2.25)$$

where $K = v/c = 1/\lambda$. (2.25) can be further simplified by applying the two-beam approximation, which requires that the indices \mathbf{g}_0 and \mathbf{q}_0 can only be $\mathbf{0}$ or a reciprocal lattice vector \mathbf{h}_0 . For the σ polarization state ($\mathbf{D}_{\mathbf{q}_0} \cdot \hat{\mathbf{e}}_{\mathbf{g}_0} = D_{\mathbf{q}_0}$, Figure 2.3) and $\mathbf{g}_0 = \mathbf{0}$ (2.25) becomes

$$i(\mathbf{k}_0 \cdot \nabla)D_0^\sigma + \pi[(\mathbf{k}_0 \cdot \mathbf{k}_0) - K^2]D_0^\sigma + \pi\Gamma(F_0|\mathbf{k}_0|^2 D_0^\sigma + F_{\mathbf{h}_0}|\mathbf{k}_0|^2 D_{\mathbf{h}_0}^\sigma) = 0$$

or

$$i(\mathbf{k}_0 \cdot \nabla)D_0^\sigma + \pi[(\mathbf{k}_0 \cdot \mathbf{k}_0) - (K^2 - \Gamma F_0|\mathbf{k}_0|^2)]D_0^\sigma + \pi\Gamma F_{\mathbf{h}_0}|\mathbf{k}_0|^2 D_{\mathbf{h}_0}^\sigma = 0. \quad (2.26)$$

First we notice that by definition (2.14) $\mathbf{k}_0 = \mathbf{k}_{0_0}$, i.e., deformation has no effect on the incident wave vector. We thus drop the subscript 0 denoting perfect crystals for the incident beam. Second, based on Ref. 26 the average complex amplitude of the internal wave vector is $\mathbf{k} = K\left(1 - \frac{1}{2}\Gamma F_0\right)$. We can make the approximation [31]

$$K^2 - \Gamma F_0|\mathbf{k}_0|^2 \approx K^2 - \Gamma F_0 k^2 = k^2(1 + \Gamma F_0) - \Gamma F_0 k^2 = k^2. \quad (2.27)$$

We now define the dispersion parameter for the incident wave vector

$$\xi_0 = \frac{(\mathbf{k}_0 \cdot \mathbf{k}_0) - k^2}{2k} \quad (2.28)$$

and (2.26) reduces to

$$i(\hat{\mathbf{s}}_0 \cdot \nabla)D_0^\sigma + 2\pi\xi_0 D_0^\sigma + \pi k \Gamma F_{\mathbf{h}_0} D_{\mathbf{h}_0}^\sigma = 0. \quad (2.29)$$

For $g_0 = h_0$ (2.25) becomes

$$i(\mathbf{k}_h \cdot \nabla)D_{\mathbf{h}_0}^\sigma + \pi[(\mathbf{k}_h \cdot \mathbf{k}_h) - K^2]D_{\mathbf{h}_0}^\sigma + \pi\Gamma(F_{\mathbf{h}_0}|\mathbf{k}_h|^2 D_0^\sigma + F_0|\mathbf{k}_h|^2 D_{\mathbf{h}_0}^\sigma) = 0. \quad (2.30)$$

Through the similar argument, we have

$$i(\hat{\mathbf{s}}_h \cdot \nabla)D_{h_0}^\sigma + 2\pi\xi_h D_{h_0}^\sigma + \pi k \Gamma F_{h_0} D_0^\sigma = 0, \quad (2.31)$$

where $\xi_h = \frac{(\mathbf{k}_h \cdot \mathbf{k}_h) - k^2}{2k}$ is the dispersion parameter for the scattered wave vector. For

the π polarization state (Figure 2.3) $\mathbf{D}_{q_0} \cdot \hat{\mathbf{e}}_{g_0} = D_{q_0} (\hat{\mathbf{e}}_{q_0} \cdot \hat{\mathbf{e}}_{g_0}) = \begin{cases} D_{q_0} & \text{if } \mathbf{q}_0 = \mathbf{g}_0 \\ D_{q_0} \cos 2\theta_B & \text{if } \mathbf{q}_0 \neq \mathbf{g}_0 \end{cases}$.

(2.25) reduces to

$$i(\hat{\mathbf{s}}_0 \cdot \nabla)D_0^\pi + 2\pi\xi_0 D_0^\pi + \pi k \Gamma F_{h_0} \cos 2\theta_B D_{h_0}^\pi = 0 \text{ for } \mathbf{g}_0 = \mathbf{0}, \quad (2.32)$$

$$\text{and } i(\hat{\mathbf{s}}_h \cdot \nabla)D_{h_0}^\pi + 2\pi\xi_h D_{h_0}^\pi + \pi k \Gamma F_{h_0} \cos 2\theta_B D_0^\pi = 0 \text{ for } \mathbf{g}_0 = \mathbf{h}_0. \quad (2.33)$$

By combining the results from the two polarization states we obtain the Takagi-Taupin equations

$$i\lambda(\hat{\mathbf{s}}_0 \cdot \nabla)D_0 = -2\pi\lambda\xi_0 D_0 + \pi\chi_{h_0} P D_{h_0} \quad (2.34)$$

$$\text{and } i\lambda(\hat{\mathbf{s}}_h \cdot \nabla)D_{h_0} = \pi\chi_{h_0} P D_0 - 2\pi\lambda\xi_h D_{h_0}, \quad (2.35)$$

where we have applied the approximation $\Gamma F_{g_0} k_i \approx -\chi_{g_0} / \lambda$ and defined the polarization

$$\text{factor } P = \begin{cases} 1 & \text{for } \sigma \text{ polarization} \\ \cos 2\theta_B & \text{for } \pi \text{ polarization} \end{cases}.$$

2.2.4 Boundary conditions (Bragg case), dispersion surfaces and deviation parameter

Before we can solve (2.34) and (2.35) for either a slab or a semi-infinite crystal, it is necessary to examine the boundary conditions at the surface, from which the two dispersion parameters ξ_0 and ξ_h can be calculated.

Since we are only interested in perfect lattices [$\mathbf{u}(\mathbf{r}) = 0$], we omit all the subscript 0 in the following discussion. The D-field amplitudes D_0 and D_h are expected to be only functions of z due to the possible finite crystal dimensions in this direction. The left-hand side of (2.34) and (2.35) can be thus reduced to (Figure 2.4) $(\hat{\mathbf{s}}_0 \cdot \nabla)D_0 = \sin(\theta + \phi) \frac{dD_0}{dz}$ and $(\hat{\mathbf{s}}_h \cdot \nabla)D_h = -\sin(\theta - \phi) \frac{dD_h}{dz}$. The Takagi-Taupin equations become

$$i\lambda\gamma_0 \frac{dD_0}{dz} = -2\pi\lambda\xi_0 D_0 + \pi\chi_h^* P D_h \quad (2.36)$$

and

$$i\lambda\gamma_h \frac{dD_h}{dz} = \pi\chi_h P D_0 - 2\pi\lambda\xi_h D_h, \quad (2.37)$$

where $\gamma_0 = \sin(\theta + \phi)$, $\gamma_h = -\sin(\theta - \phi)$, and ϕ is the miscut angle.

To have a geometrical interpretation of the dispersion parameters ξ_0 and ξ_h , we first apply the following approximation

$$\xi_0 = \frac{(\mathbf{k}_0 \cdot \mathbf{k}_0) - k^2}{2k} = \frac{\left((\mathbf{k}_0 \cdot \mathbf{k}_0)^{1/2} + k \right) \left((\mathbf{k}_0 \cdot \mathbf{k}_0)^{1/2} - k \right)}{2k} \approx (\mathbf{k}_0 \cdot \mathbf{k}_0)^{1/2} - k. \quad (2.38)$$

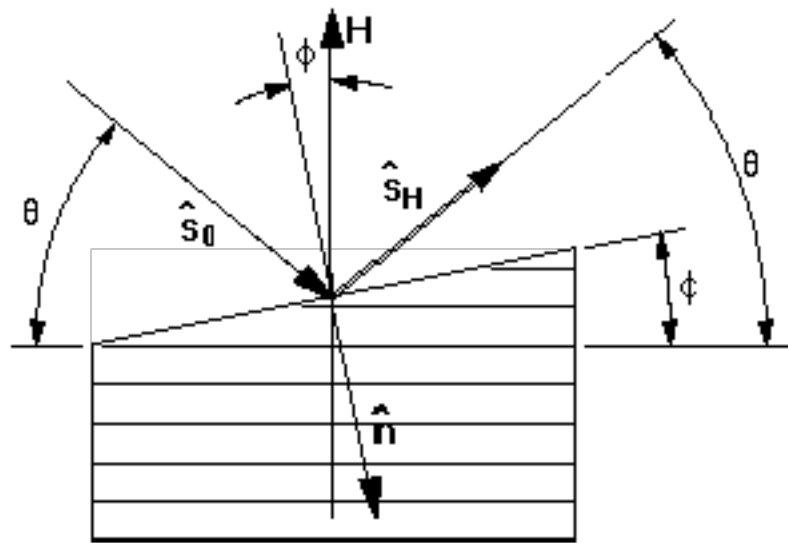


Figure 2.4 The miscut angle ϕ of a surface. The value of ϕ is defined to be positive in this picture.

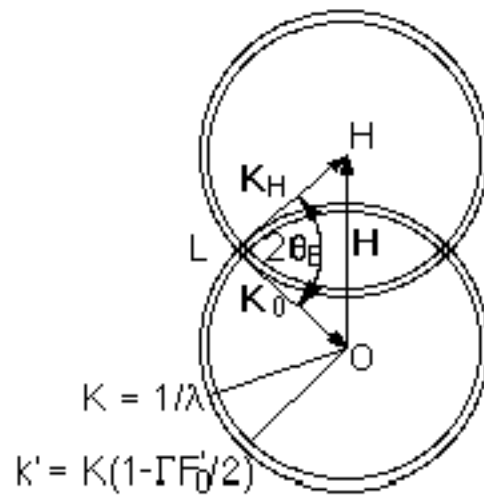


Figure 2.5 Two sets of internal and external Ewald spheres satisfying a Bragg condition for a reflection H .

Similarly,
$$\xi_0 = \frac{(\mathbf{k}_h \cdot \mathbf{k}_h) - k^2}{2k} \approx (\mathbf{k}_h \cdot \mathbf{k}_h)^{1/2} - k . \quad (2.39)$$

We then plot the internal and external Ewald spheres with the wave vectors under a Bragg condition in Figure 2.5. Notice that in the wavelength range of x-ray the internal Ewald sphere is only about 10^{-5} smaller than the external sphere. Figure 2.6 (a) shows a magnification of Figure 2.5 around the intersections between the incidence and the diffraction spheres. Based on (2.38) and (2.39) the amplitude of the true internal wave vector \mathbf{k}_0 (\mathbf{k}_h) will deviate from the average value $(1-\Gamma F_0/2)/\lambda$ by ξ_0 (ξ_h) in the vicinity of a Bragg reflection. We indicate the real parts of the two dispersion parameters in Figure 2.6(a). For semi-infinite perfect crystals, since D_0 and D_h are constants, the Takagi-Taupin equations (2.36) and (2.37) reduce to the simpler form described by the classical dynamical theory

$$-2\pi\lambda\xi_0 D_0 + \pi\chi_h P D_h = 0 \quad (2.40)$$

and
$$\pi\chi_h P D_0 - 2\pi\lambda\xi_h D_h = 0, \quad (2.41)$$

which have non-trivial solutions for D_0 and D_h only if

$$\begin{vmatrix} -2\pi\lambda\xi_0 & \pi\chi_h P \\ \pi\chi_h P & -2\pi\lambda\xi_h \end{vmatrix} = 0, \quad \text{or} \quad \xi_0 \xi_h = \frac{1}{4\lambda^2} P^2 \chi_h \chi_h . \quad (2.42)$$

(2.42) defines two hyperbolic surfaces near a Bragg reflection called the dispersion surfaces [the dashed lines in Figure 2.6(a)].

When a set of plane waves travel across a surface, the internal and external waves are expected to have the same amplitude and frequency, i.e., $D_{0e}e^{2\pi i\mathbf{K}_0 \cdot \mathbf{r}} + D_{he}e^{2\pi i\mathbf{K}_h \cdot \mathbf{r}} = D_0e^{2\pi i\mathbf{k}_0 \cdot \mathbf{r}} + D_h e^{2\pi i\mathbf{k}_h \cdot \mathbf{r}}$. This implies (a) $D_{0e} = D_0$ and $D_{he} = D_h$, and (b) $\mathbf{K}_0 \cdot \mathbf{r} = \mathbf{k}_0 \cdot \mathbf{r}$ and $\mathbf{K}_h \cdot \mathbf{r} = \mathbf{k}_h \cdot \mathbf{r}$. Since \mathbf{r} lies in the surface, (b) further implies that

$$\mathbf{k}_0 = \mathbf{K}_0 - \frac{q_0}{\lambda} \hat{\mathbf{n}} \quad \text{and} \quad \mathbf{k}_h = \mathbf{K}_h - \frac{q_h}{\lambda} \hat{\mathbf{n}}, \quad (2.43)$$

where $\hat{\mathbf{n}}$ is the surface normal. (2.43) states that the internal wave vectors can only differ from their external wave vectors by a vector parallel to the surface normal [Figure 2.6(a)]. The quantities $q_0 = q_0' + iq_0''$ and $q_h = q_h' + iq_h''$ are complex. Their real parts are shown in Figure 2.6(a) as $\frac{q_0'}{\lambda} \hat{\mathbf{n}} = \overline{DF}$ and $\frac{q_h'}{\lambda} \hat{\mathbf{n}} = \overline{GF}$. (2.43) also suggests that

$$\mathbf{k}_0' = \mathbf{K}_0 - \frac{q_0'}{\lambda} \hat{\mathbf{n}}, \quad \mathbf{k}_0'' = \frac{q_0''}{\lambda} \hat{\mathbf{n}}, \quad \mathbf{k}_h' = \mathbf{K}_0 + \mathbf{H} - \frac{q_0'}{\lambda} \hat{\mathbf{n}} \quad \text{and} \quad \mathbf{k}_h'' = \frac{q_0''}{\lambda} \hat{\mathbf{n}}.$$

Therefore, for a Bragg diffraction from a perfect crystal, once the external incident angle is given [D in Figure 2.6(a)], the boundary condition (2.43) will select a tie point (F) on the dispersion surface [32], which determines the dispersion parameters and thus the internal wave vectors.

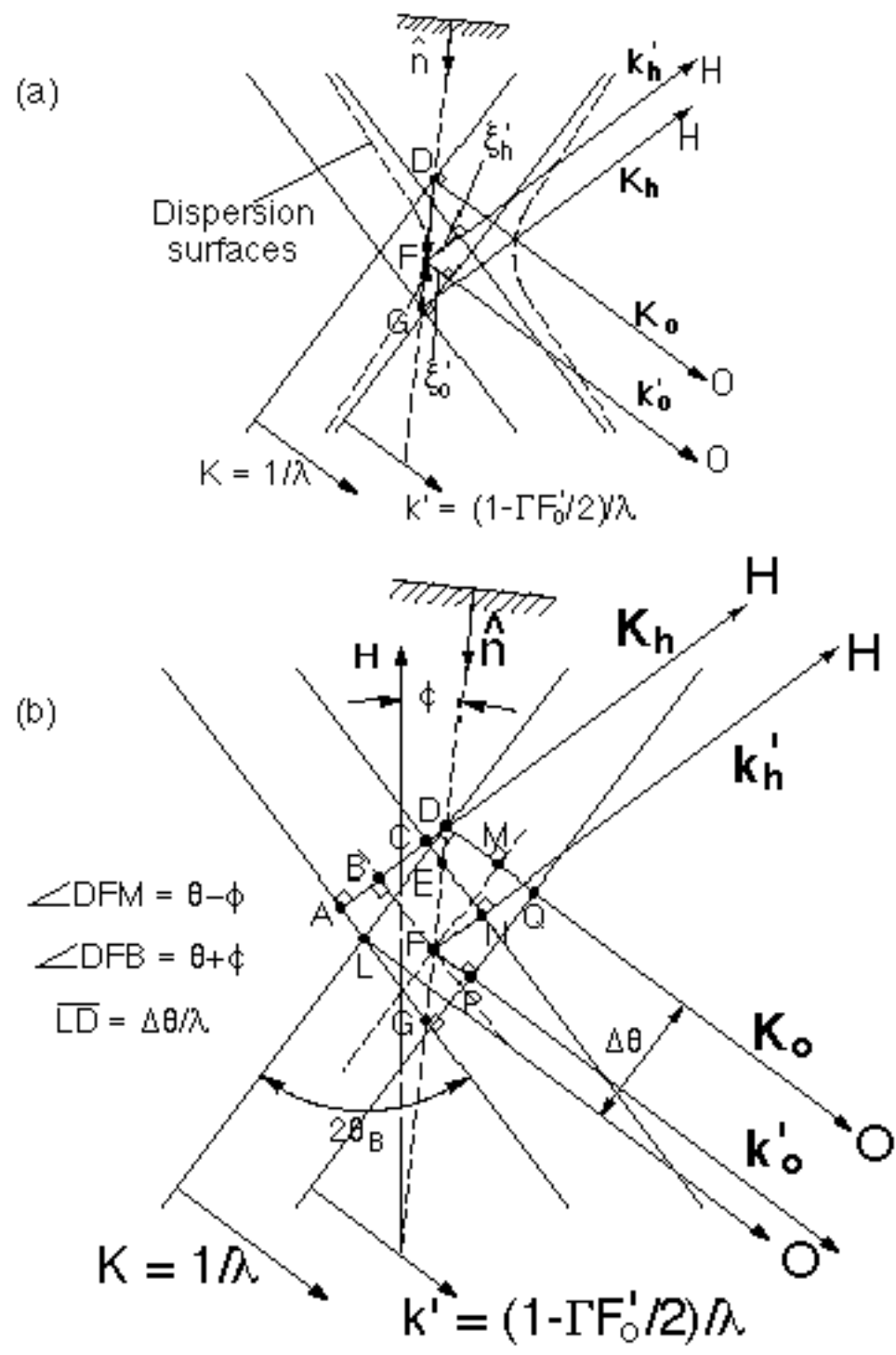


Figure 2.6 Selection of a tie point (F) on the dispersion surfaces by the boundary condition and the geometrical interpretation of the dispersion parameters (see text).

It is possible to relate the dispersion parameters to the measurable quantities such as γ_0 , γ_h , θ_B and $\Delta\theta = \theta - \theta_B$ [Figure 2.6(b)]. Based on (2.38) the imaginary part of ξ_0 can be expressed as

$$\begin{aligned}\xi_0'' &= \text{Im}\left\{\left[(\mathbf{k}_0' - i\mathbf{k}_0'') \cdot (\mathbf{k}_0' - i\mathbf{k}_0'')\right]^{1/2} - k\right\} \approx \text{Im}\left[\left((k_0')^2 - i2\frac{q_0''}{\lambda}\hat{\mathbf{n}} \cdot \mathbf{k}_0'\right)^{1/2} - k\right] \\ &\approx \text{Im}\left[k_0' \left(1 - \frac{i}{\lambda} \frac{q_0''}{k_0'} \gamma_0\right) - \frac{1}{\lambda} \left(1 - \frac{1}{2} \Gamma F_0\right)\right] = \frac{1}{\lambda} \left(\frac{1}{2} \Gamma F_0'' - q_0'' \gamma_0\right).\end{aligned}\quad (2.44)$$

Similarly
$$\xi_h'' = \frac{1}{\lambda} \left(\frac{1}{2} \Gamma F_0'' - q_0'' \gamma_h\right). \quad (2.45)$$

The expressions for the real parts of ξ_0 and ξ_h can be derived geometrically [Figure 2.6(b)]

$$\xi_0' = \overline{FP} = \overline{MQ} = \overline{DQ} - \overline{DM} = \frac{1}{\lambda} \left(\frac{1}{2} \Gamma F_0' - q_0' \gamma_0\right) \quad (2.46)$$

$$\xi_h' = \overline{FN} = \overline{BC} = \overline{AC} - \overline{AB} = \overline{AC} - \overline{AD} + \overline{BD} = \frac{1}{\lambda} \left(\frac{1}{2} \Gamma F_0' - \Delta\theta \sin 2\theta_B - q_0' \gamma_h\right) \quad (2.47)$$

(2.44) – (2.47) imply that
$$\xi_0 = \frac{1}{\lambda} \left(\frac{1}{2} \Gamma F_0 - q_0 \gamma_0\right) \quad (2.48)$$

and
$$\xi_h = \frac{1}{\lambda} \left(\frac{1}{2} \Gamma F_0 - \Delta\theta \sin 2\theta_B - q_0 \gamma_h\right). \quad (2.49)$$

Therefore we have
$$\gamma_h \xi_0 - \gamma_0 \xi_h = \frac{\gamma_h}{\lambda} \left[P \left(\left[b \chi_h \chi_{\bar{h}} \right]^{1/2} \right) \right] \eta, \quad (2.50)$$

Where
$$\eta = \frac{b \Delta \theta \sin 2\theta_B - \chi_0 (1 - b) / 2}{\left[P \left(\left[b \chi_h \chi_{\bar{h}} \right]^{1/2} \right) \right]} \quad (2.51)$$

and $b = \frac{\gamma_0}{\gamma_h}$. η is the so-called deviation parameter. The expression (2.50) will be used in solving Takagi-Taupin equations in Section 2.2.5. It can be shown that geometrically $\gamma_h \xi_0' - \gamma_0 \xi_h' = \gamma_0 \gamma_h \overline{GE}$ in Figure 2.6(b).

2.2.5 Solutions to Takagi-Taupin equations for perfect slabs

In this section we solve the Takagi-Taupin equations for a perfect slab of thickness t (Figure 2.7). Semi-infinite perfect crystals can then be treated as a special case as t approached infinity. As we need for applying Eq. (2.6) and (2.8), we first derive the expressions for $X_{\text{HR}t}$ and $X_{\text{HT}t}$, and then consider $\overline{X}_{\text{HR}t}$ and $\overline{X}_{\text{HT}t}$.

The boundary conditions [(2.43), (2.50) and (2.51)] discussed in Section 2.2.4 for the internal and external wave vectors are still valid here, but the dispersion surfaces are

undefined for a slab because $dDh/dz \neq 0$ in (2.37) and the determinant
$$\begin{vmatrix} -2\pi\lambda\xi_0 & \pi\chi_{\bar{h}}P \\ \pi\chi_hP & -2\pi\lambda\xi_h \end{vmatrix}$$

can not be zero in this case.

To make the derivation more concise, we introduce two complex quantities $D_0' = D_0 e^{-2\pi i \xi_0 / \gamma_0}$ and $D_h' = D_h e^{-2\pi i \xi_0 / \gamma_0}$. Using them and the expression (2.50) we convert the Takagi-Taupin equations (2.36) and (2.37) to

$$i\lambda\gamma_0 \frac{dD_0'}{dz} = \pi\chi_{\bar{h}} P D_h' \quad (2.52)$$

and

$$i\lambda\gamma_h \frac{dD_h'}{dz} = \pi\chi_h P D_0' - 2\pi|P| \left(\frac{\chi_h \chi_{\bar{h}}}{|b|} \right)^{1/2} \eta D_h'. \quad (2.53)$$

We separate the two variables D_0' and D_h' into two second-order equations

$$\gamma_0 \gamma_h \lambda^2 \frac{d^2 D_j'}{dz^2} - 2\pi i \lambda |P| \left(|\gamma_0 \gamma_h| \chi_h \chi_{\bar{h}} \right)^{1/2} \eta \frac{dD_j'}{dz} + \pi^2 P^2 \chi_h \chi_{\bar{h}} D_j' = 0, \quad j = \mathbf{0}, \mathbf{h}. \quad (2.54)$$

Solving (2.54) is straightforward. The solutions are expected to have the following form:

$$D_j' = C_{j1} e^{\alpha_{\pm} z} + C_{j2} e^{\alpha_{\mp} z}, \quad j = \mathbf{0}, \mathbf{h} \quad (2.55)$$

where

$$\alpha_{\pm} = -\frac{\pi i |P|}{\lambda} \left(\frac{\chi_h \chi_{\bar{h}}}{|\gamma_0 \gamma_h|} \right)^{1/2} \left(\eta \pm \sqrt{\eta^2 - 1} \right). \quad (2.56)$$

To solve the constants C in (2.55) we apply the boundary conditions at both the top and the bottom surfaces of the slab (Figure 2.7), i.e., $D_0'(z=0) = 1$ and $D_h'(z=t) = 0$.

The solutions are

$$X_{HRt} = D_h|_{z=0} = \frac{i\pi P \chi_h}{\lambda |\gamma_h|} \left(\frac{1 - e^{(\alpha_+ - \alpha_-)t}}{\alpha_+ e^{(\alpha_+ - \alpha_-)t} - \alpha_-} \right) \quad (2.57)$$

and

$$X_{HTt} = D_0|_{z=t} = D_0|_{z=0} e^{-2\pi k_0'' t} = \frac{(\alpha_+ - \alpha_-)}{\alpha_+ e^{-\alpha_+ t} - \alpha_- e^{-\alpha_- t}} e^{2\pi i \xi_0' t / \gamma_0} e^{-2\pi k_0'' t}. \quad (2.58)$$

Since $k_0'' = \frac{q_0''}{\lambda} = \frac{-1}{\gamma_0} \left(\frac{\chi_0''}{2\lambda} + \xi_0'' \right)$ [(2.43) and (2.44)], we have

$$X_{HTt} = \frac{(\alpha_+ - \alpha_-)}{\alpha_+ e^{-\alpha_+ t} - \alpha_- e^{-\alpha_- t}} e^{2\pi \left(i \xi_0' + \frac{\chi_0''}{2\lambda} \right) t / \gamma_0}. \quad (2.59)$$

For semi-infinite crystals, $t \rightarrow \infty$ and $\lim_{t \rightarrow \infty} \text{Re}(\alpha_+ - \alpha_-)t = \pm\infty$. Using the fact that

$$\alpha_+ \alpha_- = -\frac{\pi^2 P^2}{\lambda^2} \frac{\chi_h \chi_{\bar{h}}}{|\gamma_0 \gamma_h|} \quad \text{we have from (2.57)}$$

$$X_{HR\infty} = -\frac{i\pi P \chi_h}{\lambda |\gamma_h|} \frac{1}{\alpha_{\pm}} = \frac{i\lambda \gamma_0}{\pi P \chi_{\bar{h}}} \alpha_{\pm} = \frac{|P|}{P} \sqrt{|b|} \left(\frac{\chi_h}{\chi_{\bar{h}}} \right)^{1/2} \left(\eta \pm \sqrt{\eta^2 - 1} \right), \quad (2.60)$$

which agrees with the classical dynamical theory [11].

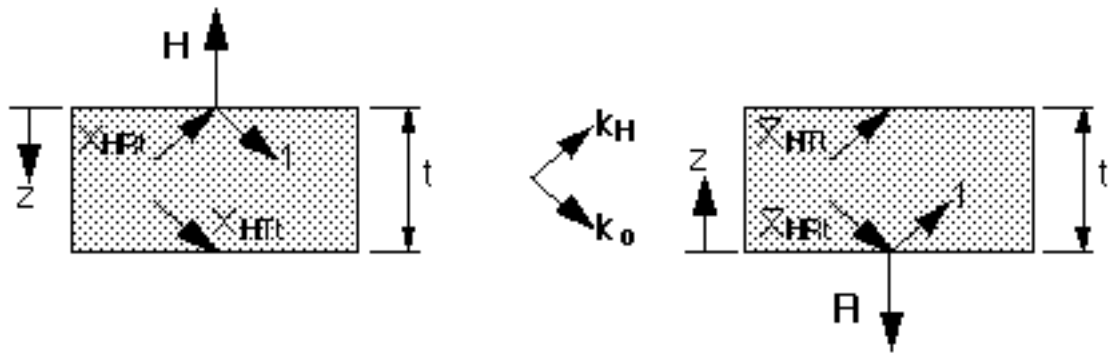


Figure 2.7 Reflection and transmission amplitude ratios for the \mathbf{H} and $-\mathbf{H}$ reflections of a slab. Notice that z is defined to point at the opposite directions for these two cases.

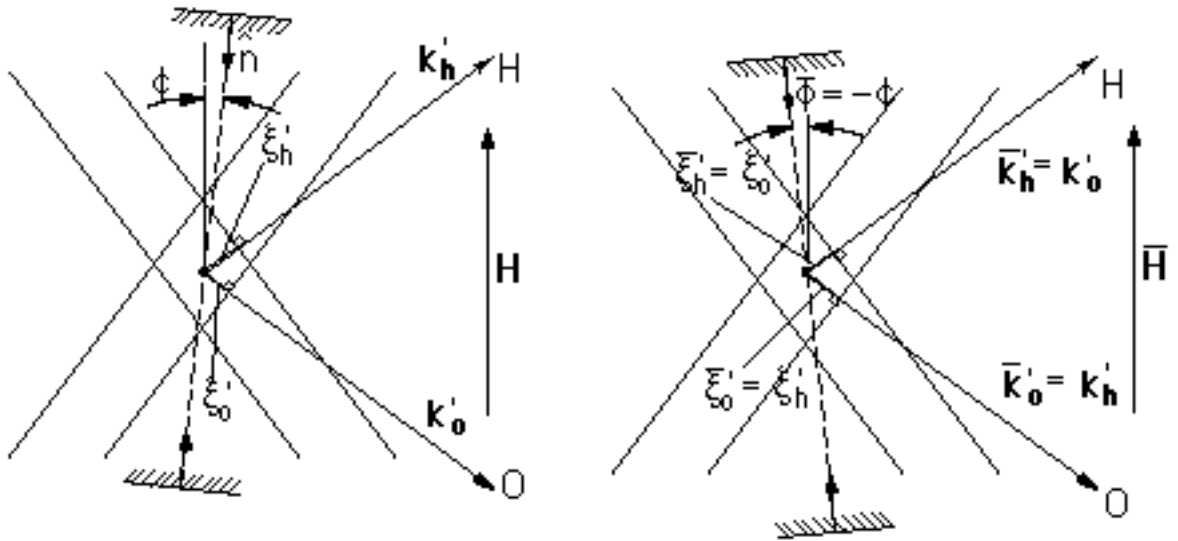


Figure 2.8 Boundary conditions for the \mathbf{H} and $-\mathbf{H}$ reflections of a slab. The same tie point is selected owing to the requirement of the two-beam approximation.

We consider next the expressions for \bar{X}_{HRt} and \bar{X}_{HTt} . Here we need to utilize the dispersion parameter we discussed in Section 2.2.4. As we mentioned in 2.2.2, \bar{X}_{HRt} and \bar{X}_{HTt} are the reflection and transmission amplitude ratios associated with the incident wave vector $\bar{\mathbf{k}}_0 = \mathbf{k}_h$ entering from the bottom surface of the slab (Figure 2.7). Since the miscut angle is $\bar{\phi} = -\phi$ for this case [Figure 2.1(a) and 4], the direction cosines of the incident and the diffracted beams become $\bar{\gamma}_0 = -\gamma_h$ and $\bar{\gamma}_h = -\gamma_0$ ($\because \bar{b} = 1/b$). Therefore, in principle, $\bar{X}_{\text{HRt}} \neq X_{\text{HRt}}$ and $\bar{X}_{\text{HTt}} \neq X_{\text{HTt}}$. However, since the two-beam approximation considers two (and only two) wave vectors at any time, the boundary conditions at the bottom surface of the slab for the back scattering should lead to the same tie point selected by the \mathbf{H} reflection (Figure 2.8). This implies $\bar{\xi}_0 = \xi_h$ and $\bar{\xi}_h = \xi_0$. Therefore, the Takagi-Taupin equations (2.36) and (2.37) become

$$-i\lambda\gamma_h \frac{d\bar{D}_0}{dz} = -2\pi\lambda\xi_h\bar{D}_0 + \pi\chi_h P\bar{D}_h \quad (2.61)$$

and

$$-i\lambda\gamma_0 \frac{d\bar{D}_h}{dz} = \pi\chi_h P\bar{D}_0 - 2\pi\lambda\xi_0\bar{D}_h. \quad (2.62)$$

We again introduce two new complex quantities $\bar{D}_0' = \bar{D}_0 e^{2\pi i \xi_0 / \gamma_0}$ and $\bar{D}_h' = \bar{D}_h e^{2\pi i \xi_0 / \gamma_0}$, which, together with (2.50), convert (2.61) and (2.62) to:

$$-i\lambda\gamma_h \frac{d\bar{D}_0'}{dz} = \pi\chi_h P\bar{D}_h' - 2\pi|P| \left(\frac{\chi_h \chi_h}{|b|} \right)^{1/2} \eta \bar{D}_0' \quad (2.63)$$

and
$$-i\lambda\gamma_0 \frac{d\bar{D}_h'}{dz} = \pi\chi_h P \bar{D}_0'. \quad (2.64)$$

(2.63) and (2.64) are equivalent to the following two second-order equations

$$\gamma_0\gamma_h\lambda^2 \frac{d^2\bar{D}_j'}{dz^2} + 2\pi i\lambda |P| \left(\frac{|\gamma_0\gamma_h\chi_h\chi_h}{|\gamma_0\gamma_h|} \right)^{1/2} \eta \frac{d\bar{D}_j'}{dz} + \pi^2 P^2 \chi_h \chi_h \bar{D}_j' = 0, \quad j = \mathbf{0}, \mathbf{h}. \quad (2.65)$$

The general solutions of (2.65) have the form $\bar{D}_j' = \bar{C}_{j1} e^{\bar{\alpha}_+ z} + \bar{C}_{j2} e^{\bar{\alpha}_- z}$ with $j = \mathbf{0}, \mathbf{h}$, where

$$\bar{\alpha}_\pm = -\frac{\pi i |P|}{\lambda} \left(\frac{\chi_h \chi_h}{|\gamma_0 \gamma_h|} \right)^{1/2} \left(-\eta \pm \sqrt{\eta^2 - 1} \right) = -\alpha_\mp \quad (2.65)$$

Applying the same boundary conditions at the surfaces we have

$$\bar{X}_{HRt} = \bar{D}_h|_{z=0} = \frac{i\pi P \chi_h}{\lambda \gamma_0} \left(\frac{1 - e^{(\alpha_+ - \alpha_-)t}}{\alpha_+ e^{(\alpha_+ - \alpha_-)t} - \alpha_-} \right) \quad (2.66)$$

and
$$\bar{X}_{HTt} = \bar{D}_0|_{z=t} = \bar{D}_0|_{z=t} e^{2\pi k_h t} = \frac{(\alpha_+ - \alpha_-)}{\alpha_+ e^{\alpha_+ t} - \alpha_- e^{\alpha_- t}} e^{-2\pi i \xi_0 t / \gamma_0} e^{2\pi k_h t}. \quad (2.67)$$

Notice that $\mathbf{k}_h \cdot \mathbf{r} = -k_h z$ (Figure 2.7) for this case. Since $k_h = \frac{q_0}{\lambda} = -\frac{1}{\gamma_0} \left(\frac{\chi_0}{2\lambda} + \xi_0 \right)$

[(2.43) and (2.45)], we have

$$\bar{X}_{\text{HT}t} = \frac{(\alpha_+ - \alpha_-)}{\alpha_+ e^{\alpha_+ t} - \alpha_- e^{\alpha_- t}} e^{-2\pi \left(i\xi_0 + \frac{\chi_0''}{2\lambda} \right) t / \gamma_0}. \quad (2.68)$$

One small problem is that the expressions for the transmission amplitude ratios (2.59) and (2.68) both contain the real part of the dispersion parameter ξ_0' in the exponents. The calculation of ξ_0 is unavailable due to the fact that the dispersion surfaces are unknown. However, first, in Eq. (2.8) our real interest is to be able to calculate the intensity $|D_{0A}|^2$, rather than D_{0A} . Second, in using Eq. (2.6), what we really need is the product of (2.59) and (2.68), which can be expressed as

$$X_{\text{HT}t} \bar{X}_{\text{HT}t} = \frac{(\alpha_+ - \alpha_-)^2}{(\alpha_+ e^{-\alpha_- t} - \alpha_- e^{-\alpha_+ t})(\alpha_+ e^{\alpha_+ t} - \alpha_- e^{\alpha_- t})}, \quad (2.69)$$

where ξ_0' has been cancelled out. Therefore, we have solved, without knowledge of the dispersion surfaces, the Takagi-Taupin equations for a perfect slab.

To calculate the reflection amplitude for the semi-infinite substrate, either (2.60) or (2.57) with a thickness t much larger than the x-ray extinction depth can be used. However, using (2.57) can avoid the possible programming problem caused by the “ \pm ” sign choice in (2.60). Once the reflection amplitude for the substrate is known, the total field in the films can be calculated by using (2.4) and the recursion formulae (2.6), (2.8) with the dynamical calculations of (2.57), (2.59), (2.66) and (2.69).

2.3 XSW analysis

In this section we briefly discuss how the structural information can be extracted from an XSW analysis. A more complete description is available in Ref. 10 and 16.

We first consider the structural analysis for adsorbates and buried thin layers. In this case the atoms we try to locate are either on the surface or distributed over a range in depth that is much smaller than the extinction length of the primary beam. We can thus ignore the exponential factor in (2.4). If we only consider using the XSW generated by the semi-infinite substrate, the amplitude ratio $|X_{\mathbf{H}}|^2$ in (2.4) can be replaced by the reflectivity R at the surface. Based on the dipole approximation, the total fluorescence yield for a fluorescent species j , which is proportional to the atom density of the fluorescent species and the total D-field intensity, can be expressed as

$$\begin{aligned} Y &= Y_{\text{OB}} \int_{V_{\text{uc}}} \rho_a^j(\mathbf{r}) [1 + R + 2\sqrt{R} \cos(\nu - 2\pi\mathbf{H} \cdot \mathbf{r})] d\mathbf{r} \\ &= Y_{\text{OB}} \left[1 + R + 2\sqrt{R} \int_{V_{\text{uc}}} \rho_a^j(\mathbf{r}) \cos(\nu - 2\pi\mathbf{H} \cdot \mathbf{r}) d\mathbf{r} \right], \end{aligned} \quad (2.70)$$

where $\rho_a^j(\mathbf{r})$ is the normalized atomic distribution function for the fluorescent species with all the atoms projected back into a bulk unit cell (i.e., $\int_{V_{\text{uc}}} \rho_a^j(\mathbf{r}) d\mathbf{r} = 1$) and Y_{OB} is the off-Bragg yield. Notice that in (2.70) only the cosine term varies rapidly over a unit cell. The reflectivity R is treated as a constant of z on this length scale. Eq. (2.70) can be reduced to

$$Y = Y_{\text{OB}} \left\{ 1 + R + 2\sqrt{R} \operatorname{Re} \left(e^{i\nu} \mathfrak{S}_{\mathbf{H}} \left[\rho_a^j(\mathbf{r}) \right] \right) \right\} \quad (2.71)$$

$$= Y_{\text{OB}} \left[1 + R + 2\sqrt{R} f_{\mathbf{H}} \cos(\nu - 2\pi P_{\mathbf{H}}) \right], \quad (2.72)$$

where $\mathfrak{S}_{\mathbf{H}}[\rho_a^j(\mathbf{r})] = \int_{V_{\text{uc}}} \rho_a^j(\mathbf{r}) e^{2\pi i \mathbf{H} \cdot \mathbf{r}} d\mathbf{r}$ is the \mathbf{H} th Fourier component of $\rho_a^j(\mathbf{r})$ in (2.71). In (2.72) $f_{\mathbf{H}} = |\mathfrak{S}_{\mathbf{H}}[\rho_a^j(\mathbf{r})]|$ and $2\pi P_{\mathbf{H}} = \operatorname{Arg} \left\{ \mathfrak{S}_{\mathbf{H}}[\rho_a^j(\mathbf{r})] \right\}$. $f_{\mathbf{H}}$ and $P_{\mathbf{H}}$ are commonly known as coherent fraction and coherent position. As described in (2.71) and (2.72), they are the amplitude and phase, respectively, of the \mathbf{H} th Fourier component of $\rho_a^j(\mathbf{r})$.

In a typical XSW measurement, R and Y are recorded simultaneously as functions of the incident angle θ through a Bragg peak. During the data analysis, the measured rocking curve is fitted with the dynamical theory (2.60) to determine the angular scale (i.e., θ_B). The agreement between the experimental and the theoretical rocking curve width and maximum reflectivity is crucial in the subsequent analysis of the yield. This relies on the high quality of the substrate crystal. Based on the best fit of the rocking curve, the fluorescence yield is then analyzed using (2.72) with Y_{OB} , $f_{\mathbf{H}}$ and $P_{\mathbf{H}}$ as the fitting parameters. The final structural determination requires further modeling and triangulation among several reflections. Detailed examples will be discussed in Chapter 5 – 7.

For XSW studies of bulk instead of monolayer structures, the differences in data analysis are that (a) the extinction effect of the primary beam needs to be considered and

(b) the probed atoms also become the atoms generating the probe (i.e., the XSW field). If we consider the extinction effect in (2.72) we will have

$$Y(\theta) = Y_{\text{OB}} \left[1 + R(\theta) + 2\sqrt{R(\theta)}f_{\text{H}} \cos(\nu(\theta) - 2\pi P_{\text{H}}) \right] L(\theta), \quad (2.73)$$

where $L(\theta)$ is the effective thickness accounting for the attenuation of both the primary x-ray field and the secondary fluorescent x-rays. We will have more discussion on (2.73) in Section 2.4.

2.4 Primary extinction and evanescent-wave emission

In this section we derive the effective thickness $L(\theta)$ in (2.73) for the XSW measurements collecting bulk fluorescence signals. We consider the attenuation effects for both the primary and secondary x-rays. These results will be applied to experiments using grazing emission angles.

We first consider the escape depth of fluorescent x-rays from atoms at and below the surface, which depend strongly on the take-off angle α . With a very small angle α one can dramatically reduce the depth probed by fluorescence. The gain in surface sensitivity originates from the evanescent-wave-emission effect demonstrated by Becker *et al.* [33] and Lee *et al.* [36]. As shown in the inset of Figure 2.9(a), emitted x-rays are refracted on their way out of the sample, just as if they were traveling into the sample along the reverse path. If the external angle α is at or below the critical angle α_c for total

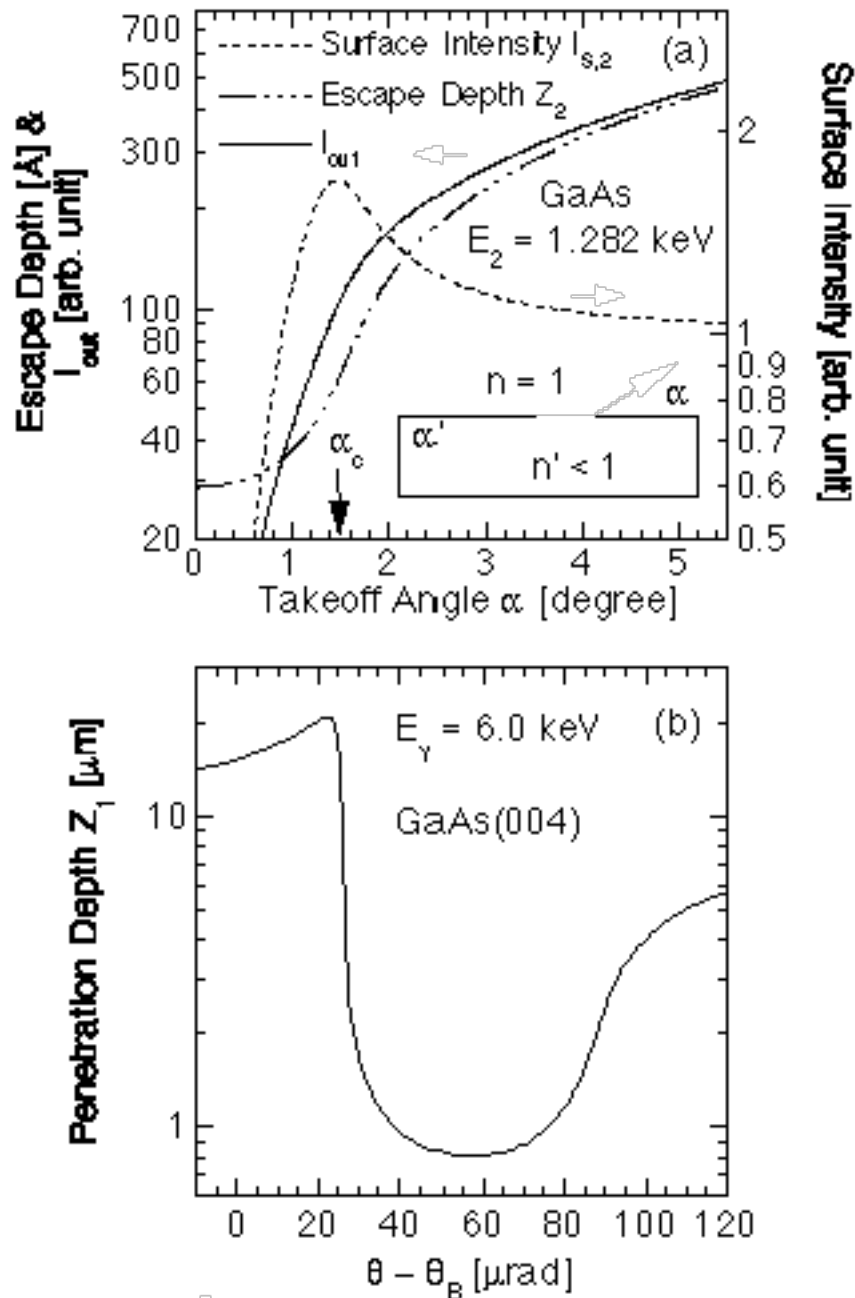


Figure 2.9 (a) The calculated angular dependence for the escape depth (Z_2) and the surface intensity ($I_{s,2}$) for As L α emission (1.282 keV) from GaAs. The intensity $I_{out}(\alpha) (= \int_0^\infty I_{out}(\alpha, z) dz)$ is obtained as the product of Z_2 and $I_{s,2}$ (see text). The inset shows the emission geometry for the secondary x-rays. (b) The calculated angular dependence of the penetration depth of the primary x-ray for the GaAs(004) reflection at $E_\gamma = 6.00$ keV. This shows the extinction effect.

external reflection, the real part of the internal angle α' vanishes. Thus for $\alpha < \alpha_c$ the emission is described by an evanescent wave with an exponentially damped depth measured in nanometers. According to the principle of microscopic reversibility, the optical theory used for describing the more easily visualized evanescent-wave-absorption effect can be directly used to calculate the evanescent-wave-emission effect. Therefore, the intensity I_{out} of a secondary x-ray from a depth z below the surface can be expressed as a function of takeoff angle α as:

$$I_{\text{out}}(\alpha, z) \propto I_{S,2}(\alpha) \cdot e^{-\mu_{z,2}(\alpha) \cdot z}, \quad (2.74)$$

where

$$I_{S,2}(\alpha) = 4 \left\{ 1 + \frac{|\xi(\alpha)|^2}{\sin^2 \alpha} + \frac{2 \operatorname{Re}(\xi(\alpha))}{\sin \alpha} \right\}^{-1} \quad \text{with } \xi(\alpha) = \sqrt{\sin^2 \alpha - 2(\delta + i\beta)}. \quad (2.75)$$

$I_{S,2}(\alpha)$ is the E-field intensity at the surface $|E(\alpha, z=0)/E_0|^2$ based on Fresnel theory. The subscript "2" is used to indicate that the calculations are performed at the secondary fluorescent x-ray energy. The optical constants δ and β are related to the index of refraction (n) of the specimen by the definition $n = 1 - \delta - i\beta$ (or $\delta = \Gamma F_0'/2$ and $\beta = \Gamma F_0''/2$). The exponential damping factor in Eq.(2.74) with

$$\mu_{z,2}(\alpha) = \frac{4\pi}{\sqrt{2}\lambda_2} \left\{ \left[(2\delta - \alpha^2)^2 + 4\beta^2 \right]^{1/2} + 2\delta - \alpha^2 \right\}^{1/2} \quad (2.76)$$

[34] accounts for the absorption and extinction of the emitted x-rays. Notice that

$I_{\text{out}}(\alpha, z)$ is simply the depth profile of the E-field intensity for an externally excited evanescent wave at this secondary energy. The same profile can not be easily obtained for an internally excited evanescent wave without applying the microscopic reversibility principle.

Figure 2.9(a) shows the surface intensity $I_{s,2}(\alpha)$ and the escape depth $Z_2(\alpha) = \mu_{z,2}(\alpha)^{-1}$ calculated from Eq.(2.74) and (2.75) for GaAs at As $L\alpha$ emission energy (1.282 keV). The surface intensity $I_{s,2}(\alpha)$ is zero at $\alpha = 0$, reaches its maximum at the critical angle $\alpha_c = \sqrt{2\delta} = 1.5^\circ$ and then approaches unity at high takeoff angles. For an externally excited evanescent wave, this variation corresponds to the inward motion of the first antinode of the standing wave created above the surface by total external reflection. Since the As L emission line is right above the Ga L_{III} edge (1.116 keV), the surface intensity maximum is suppressed by absorption ($I_{s,2}(\alpha_c) = 4$ without absorption). The escape depth $Z_2(\alpha)$, has a minimum value of 29 Å at $\alpha = 0^\circ$ followed by an abrupt rise at $\alpha = \alpha_c$. It eventually approaches $(\sin\alpha)/\mu_{0,2}$ for high takeoff angles, where $\mu_{0,2}$ is the normal absorption coefficient for GaAs. It is this drastic reduction in the escape depth occurring near the critical angle that makes this technique sensitive to the near surface atoms with the x-rays emitted deep below the surface unobservable by the fluorescence detector.

By including the attenuation factor $I_{\text{in}}(\theta, z)$ for the primary x-rays, we can express the θ and α dependence of the exponentially damped envelope of the standing wave amplitude as

$$y(\theta, \alpha, z) = I_{\text{in}}(\theta, z) \cdot I_{\text{out}}(\alpha, z) \propto I_{S,2}(\alpha) \cdot e^{-[\mu_{z,1}(\theta) + \mu_{z,2}(\alpha)]z}. \quad (2.77)$$

Based on dynamical diffraction theory [35] the effective linear absorption coefficient $\mu_{z,1}(\theta)$ in Eq.(2.77) is:

$$\mu_{z,1}(\theta) = \frac{\mu_{0,1}}{\sin \theta_B} \left[1 + \frac{F_{\mathbf{H}}''}{F_0''} \left(\frac{D_{\mathbf{H}}(\theta)}{D_0} \right)' + \frac{F_{\mathbf{H}}'}{F_0''} \left(\frac{D_{\mathbf{H}}(\theta)}{D_0} \right)'' \right], \quad (2.78)$$

where $\mu_{0,1}$ is the normal absorption coefficient for the primary x-ray and θ_B is the Bragg angle for the \mathbf{H} reflection. $D_{\mathbf{H}}(\theta)/D_0$ is the D-field amplitude ratio (2.60). $F_{\mathbf{H}}$ and F_0 are the structure factors for the \mathbf{H} and the zeroth order reflections. The notations prime and double prime used in Eq.(2.78) represent the real and the imaginary parts of complex quantities, respectively, and the subscript "1" is used to denote the primary beam. Physically, the first term in Eq.(2.78) corresponds to normal absorption. The second term corresponds to anomalous absorption, which accounts for the strengthening and diminishing of the photoelectric absorption due to the motion of the standing wave field with respect to the atomic planes. The last term accounts for the primary extinction effect. The penetration depth $Z_1(\theta) = \mu_{z,1}(\theta)^{-1}$ for the GaAs(004) reflection at $E_\gamma = 6.0$ keV is depicted in Figure 2.9(b). A minimum Z_1 (or extinction depth) of $0.8 \mu\text{m}$ can be found at the center of the rocking curve. This is about 200 times greater than the minimum escape depth for the evanescent wave emission effect described in Figure 2.9(a).

With the angular and depth distribution of the fluorescence yield described by Eq.(2.77), the total yield observed by the detector [Eq.(2.73)] can be obtained through the integration of Eq.(2.77) over z and α , which gives the effective thickness $L(\theta)$ as:

$$L(\theta) = \int_{\alpha_1}^{\alpha_u} \int_0^{\infty} y(\theta, \alpha, z) dz d\alpha = \frac{1}{L_{OB}} \int_{\alpha_1}^{\alpha_u} \frac{I_{s,2}(\alpha)}{\mu_{z,1}(\theta) + \mu_{z,2}(\alpha)} d\alpha, \quad (2.79)$$

where the constant L_{OB} is an integration factor which normalizes $L(\theta)$ to unity at the off-Bragg (OB) condition where $R(\theta) = 0$ and $\mu_{z,1}(\theta) = \mu_{0,1}/\sin\theta_B$. The necessity of the integration over takeoff angle α in Eq.(2.79), which must be carried out numerically, depends on the instrumental resolution of angle α or the width $\Delta\alpha = \alpha_u - \alpha_1$, and the center position α_0 of $\Delta\alpha$. It can be avoided and replaced with its integrand calculated at α_0 if α_0 is far above the critical angle α_c or if $\Delta\alpha$ is small compared to α_c . This can be understood by plotting the integrand $I_{s,2}(\alpha) / [\mu_{z,1}(\theta) + \mu_{z,2}(\alpha)] \approx I_{s,2}(\alpha)/\mu_{z,2}(\alpha)$ as a function of α . This is plotted as the $I_{out}(\alpha)$ curve in Figure 2.9(a).

An example using (2.79) to measure the strain induced GaAs cap displacement of 1 ML InAs buried in GaAs(001) will be discussed in Chapter 7.

2.5 Simulations and experimental results: *PbTiO₃ thin film XSW*

We tested out the above dynamical theory by performing XSW measurements on a $PbTiO_3(001)$ thin film. The details of the experimental setup and the background

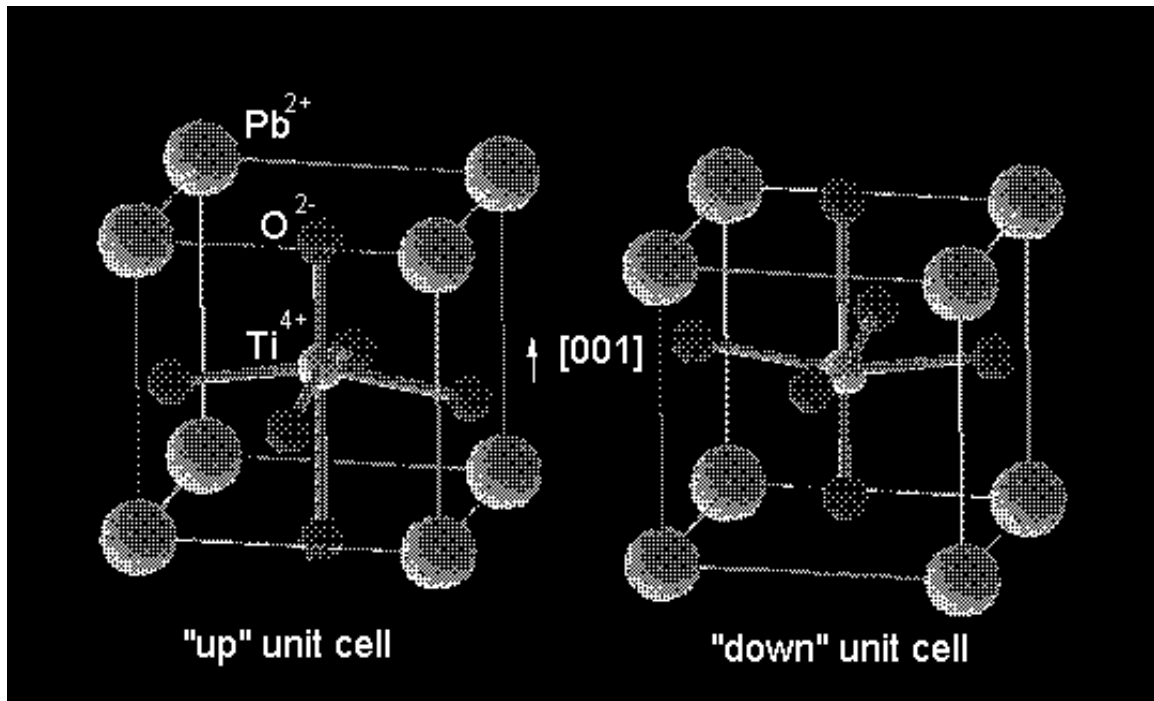


Figure 2.10 The PbTiO_3 perovskite unit cells of the up and down polarization states. The atomic coordinates are listed below.

SrTiO_3	Cubic, $a = b = c = 3.905 \text{ \AA}$ $\text{Sr} = 0,0,0;$ $\text{Ti} = 1/2,1/2,1/2$ $\text{O} = 1/2,1/2,0; 1/2,0,1/2; 0,1/2,1/2$
PbTiO_3 (up)	Tetragonal, $a = b = 3.905 \text{ \AA}, c = 4.156 \text{ \AA}$ $\text{Pb} = 0,0,0.1159;$ $\text{Ti} = 1/2,1/2,0.5769$ $\text{O} = 1/2,1/2,0; 1/2,0,1/2; 0,1/2,1/2$
PbTiO_3 (down)	Tetragonal, $a = b = 3.905 \text{ \AA}, c = 4.156 \text{ \AA}$ $\text{Pb} = 0,0,-0.1159;$ $\text{Ti} = 1/2,1/2,0.4231$ $\text{O} = 1/2,1/2,0; 1/2,0,1/2; 0,1/2,1/2$

information will be report elsewhere [9]. Here we place our emphasis on the theoretical part of the XSW simulations and data analysis.

Bulk PbTiO_3 is known to be a ferroelectric material with the perovskite structure. By displacing the Pb and Ti cations relative to the O^{2-} sublattice, the unit cell can exhibit either up or down polarization, as depicted in Figure 2.10. This results in the coexistence of small up and down domains in bulk PbTiO_3 crystal. However, it has been demonstrated recently that single crystal ferroelectric thin films can be grown with a film thickness well below the typical bulk domain size. It is therefore possible to use the standing wave field generated by a PbTiO_3 thin film, or thin-film XSW, to determine the polarization of the film.

A sample with a 400 Å thick PbTiO_3 film grow by metal-organic chemical vapor deposition (MOCVD) on a $\text{SrTiO}_3(001)$ substrate was used in this measurement. The XSW experiment was carried out using the 5ID-C undulator station at the DND CAT at the Advanced Photon Source (APS). The $\text{PbTiO}_3(001)$ reflection was employed to generate the standing wave field. The Pb L and Ti K fluorescence yields were recorded at incident energies of 13.5 keV and 8.00 keV, respectively. To measure the Ti position in the film, we reduced the emission take-off angle α_u to about 0.5° using a fluorescence slit to eliminate the Ti K signal from the SrTiO_3 substrate.

Figure 2.11(a) shows the calculated rocking curve ($|X_H|^2$) as a function of q for a semi-infinite $\text{SrTiO}_3(001)$ substrate at $E_\gamma = 13.5$ keV, where $q = 4\pi\sin\theta/\lambda$ is the momentum transfer normal to the surface. The calculation was based on Eq. (2.57) with a thickness $t = 100$ μm. It can be shown that the classical dynamical theory (2.60)

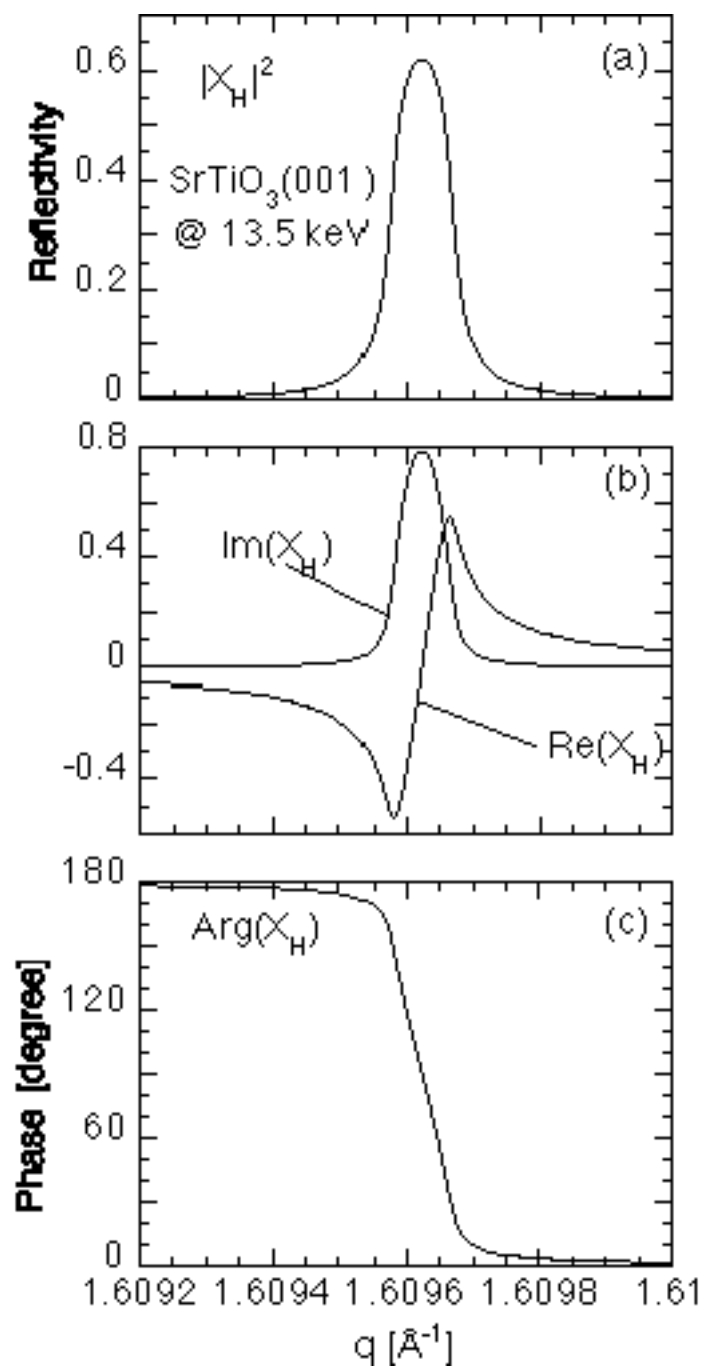


Figure 2.11 The calculated (a) rocking curve, (b) the real and imaginary parts and (c) the phase of the D-field amplitude ratio at the surface for bulk $\text{SrTiO}_3(001)$ reflection at 13.5 keV.

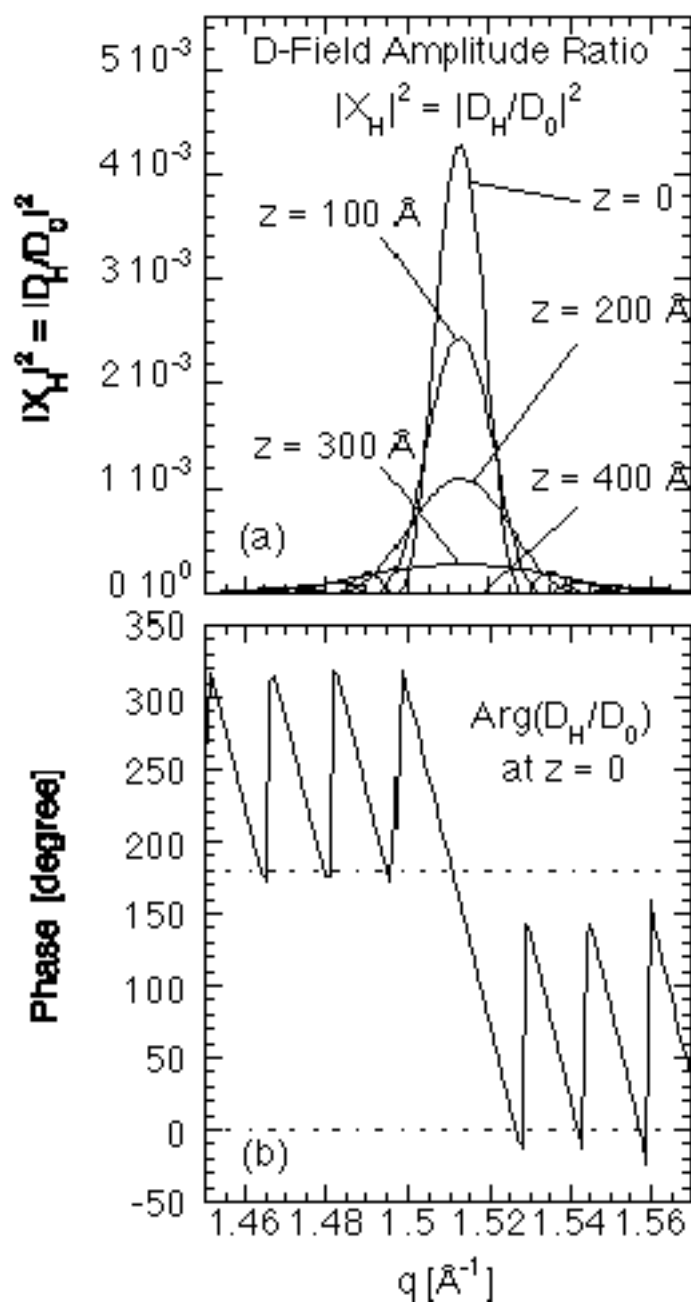


Figure 2.12 (a) The D-field amplitude ratio, (c) the incident D-field intensity and (d) the total D-field intensity at the Ti site calculated at various depths z for the PbTiO_3 (001) reflection (13.5 keV) of 400 \AA PbTiO_3 (polarized up) on SrTiO_3 (001). (b) shows the phase of the D-field amplitude ratio at the surface.

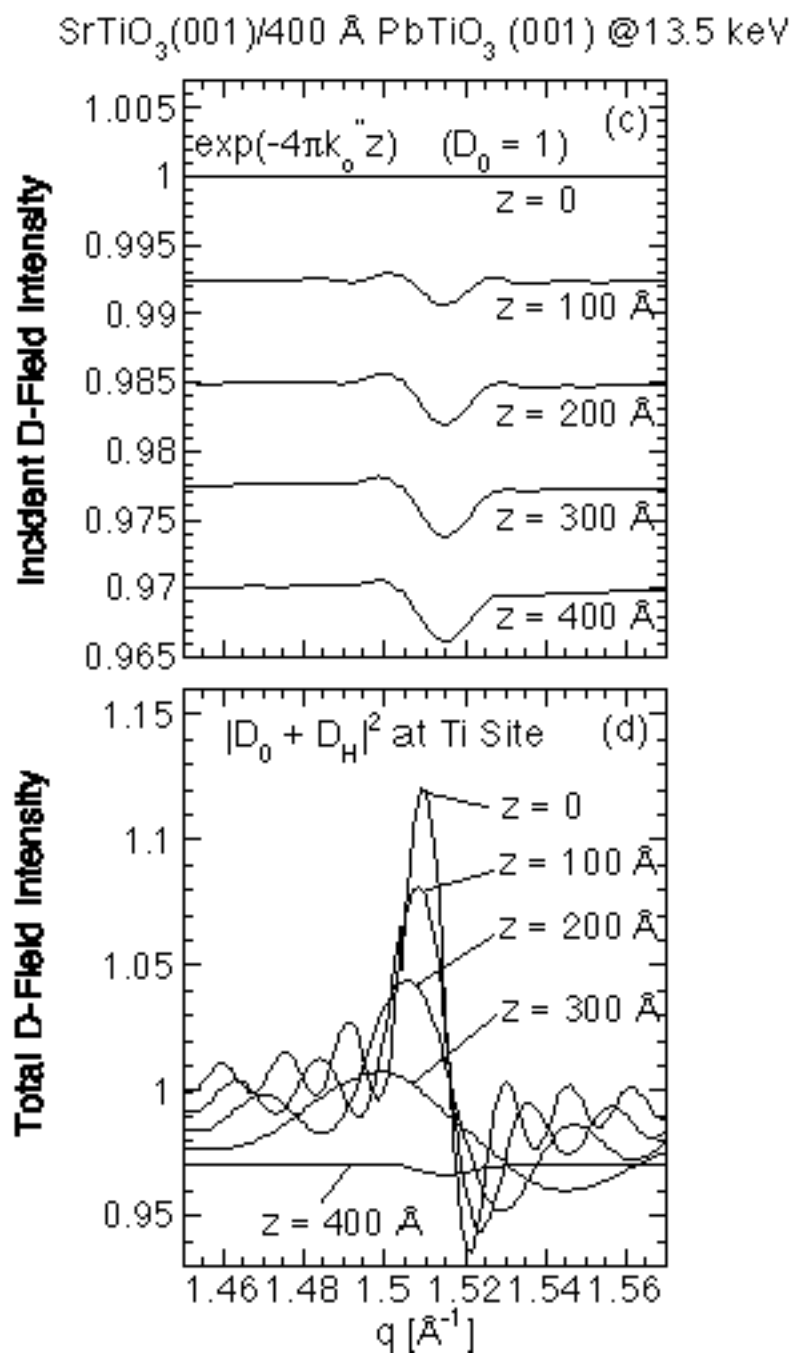


Figure 2.12 (Continued)

predicts the same rocking curve. Figure 2.11(b) and (c) show the real part, imaginary part and the phase of X_H . The 180° phase shift of X_H through the Bragg peak in Figure 2.11(c) leads to an inward movement of the nodes and antinodes of the standing waves. Notice that X_H is independent of z in this case.

Figure 2.12 shows the results of the calculations performed at an incident energy of 13.5 keV for a 400 Å thick PbTiO_3 film of up polarization state on a $\text{SrTiO}_3(001)$ substrate. In Figure 2.12(a) we calculate the reflectivity curves ($|X_H|^2$) for the $\text{PbTiO}_3(001)$ reflection at various depths z . Both the reflected intensity and the modulation frequency depend strongly on z . Figure 2.12(b) shows the phase of X_H calculated at the surface. It indicates that the phase shift is more than 180° over the Bragg region. In Figure 2.12(c) we calculate the incident D-field intensity $|D_0|^2 = |D_0|^2$ at various depths. The primary extinction effect near the $\text{PbTiO}_3(001)$ reflection is evident even within 400 Å below the surface. It can be proved that away from the Bragg angle in Figure 2.12(c) the incident field intensity approaches to $e^{-\mu_0 z / \gamma_0}$, where $\mu_0 = 2\pi\Gamma F'' / \lambda$ is the normal absorption coefficient of the film. Figure 2.12(d) shows the total D-field intensity calculated at the Ti site as a function of z . It suggests that in order to account for the total fluorescence yield correctly it is necessary to integrate the total D-field intensity over the entire film thickness. This is not only because of the extinction effect of the primary beam, as is the case for a semi-infinite crystal, but also the result of strong dependence of $|X_H|^2$ on z .

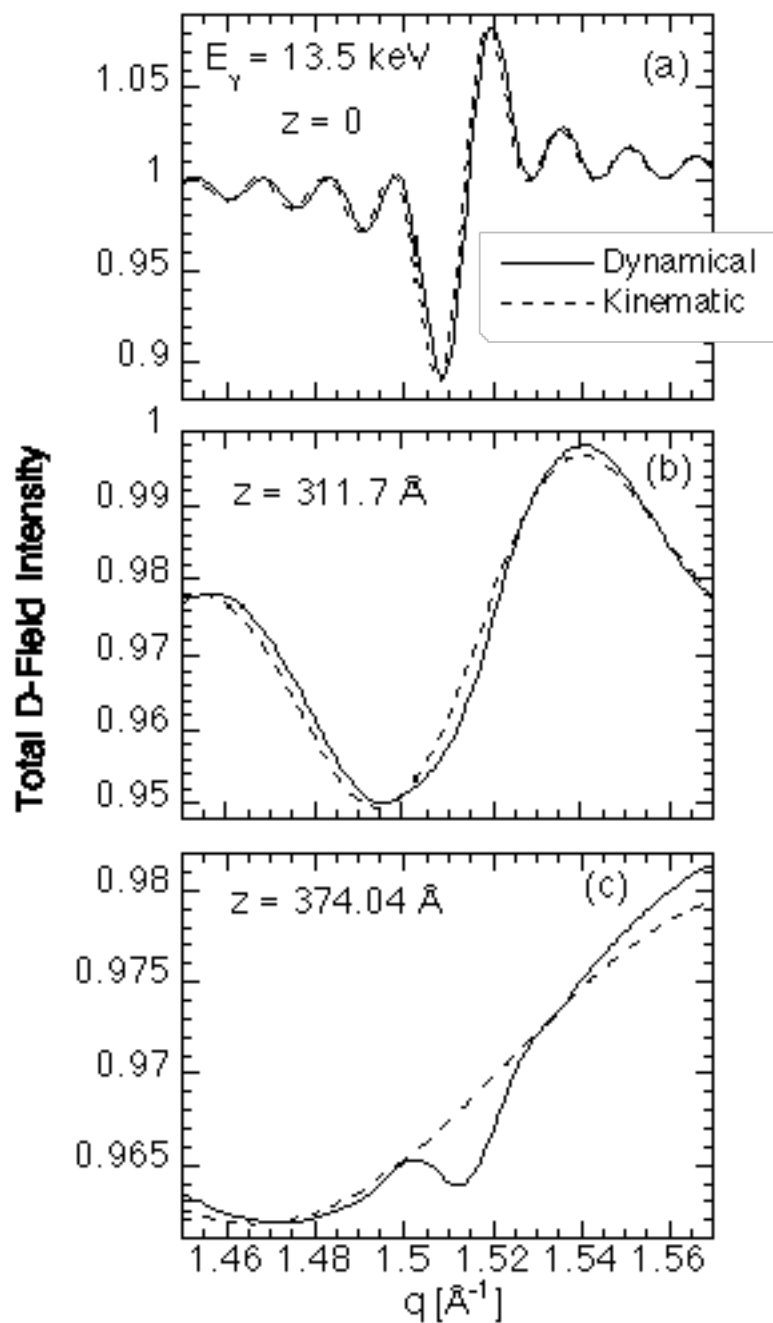


Figure 2.13 The total D-field intensities at the Pb site near the PbTiO_3 (001) reflection for a 415.6 \AA PbTiO_3 (polarized up) thin film at various depths z . The solid curves are calculated based on the dynamical theory developed in this work. The dashed curves are based on a kinematical approach (2.80).

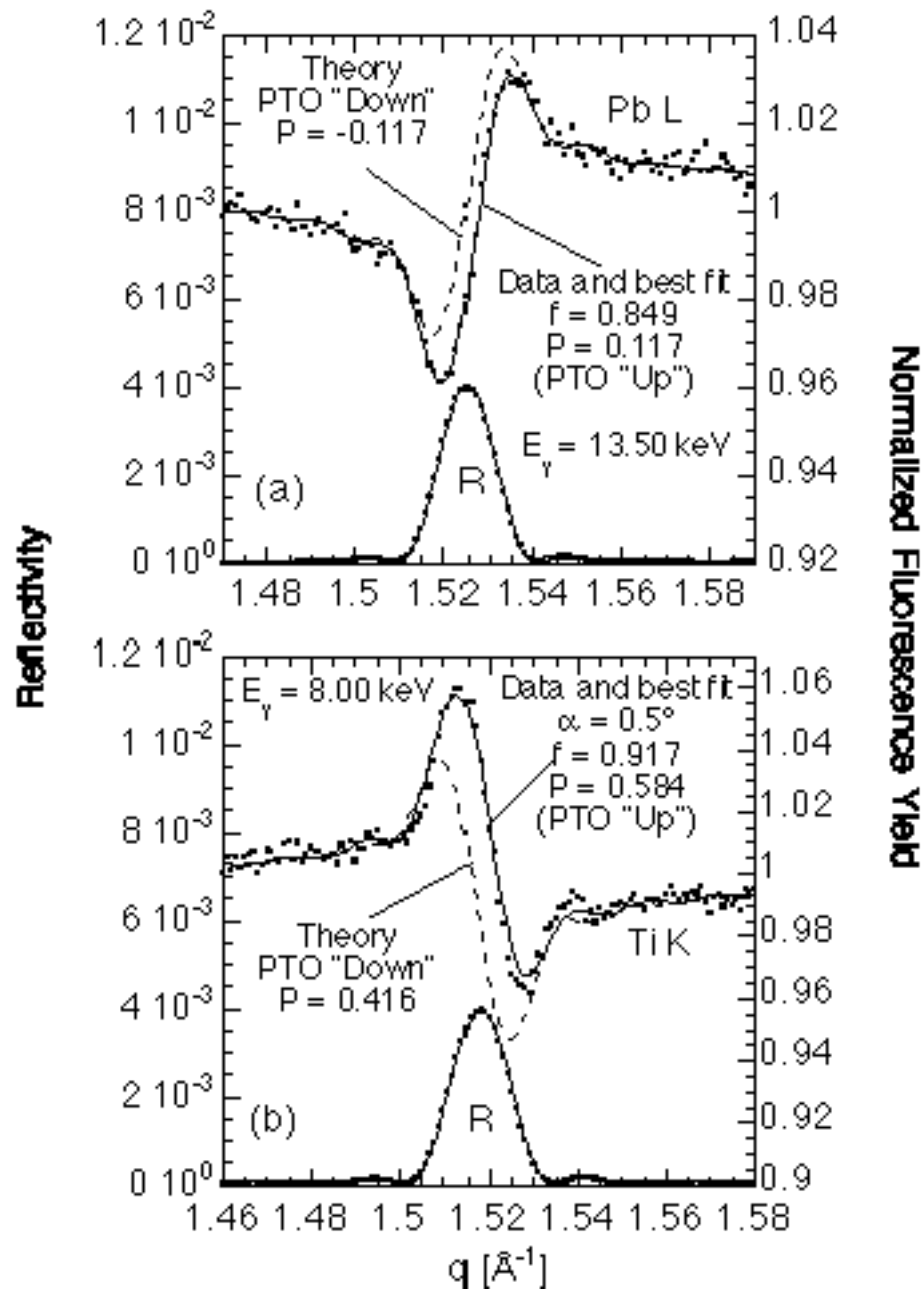


Figure 2.14 XSW data and best fits for the reflectivity and (a) Pb L and (b) Ti K fluorescence yields for 400 Å PbTiO₃ on SrTiO₃(001). The measurements were carried out at 13.5 keV for (a) and 8.00 keV for (b). The data was fitted with the dynamical theory derived in this work. The best fits showed that the PTO film carried a single “up” polarization state.

We next compare the present dynamical calculation with the kinematic theory. Figure 2.13 shows the total D-field intensities calculated at the Pb site for various depths z around the PbTiO_3 (001) reflection for a 415.6 Å thick, free standing PbTiO_3 film of up polarization. The solid curves are based on the dynamical theory derived in this work. The dashed curves are based on a kinematic approach, where in Eq. (2.4) we replace $4\pi K_0$ by μ_0/γ_0 and use the following formula for X_H

$$X_H(N, q) = \frac{i4\pi r_e}{a^2 q} F(q) \frac{1 - e^{-cN(iq + \frac{4\pi\mu_0}{\lambda q})}}{1 - e^{-c(iq + \frac{4\pi\mu_0}{\lambda q})}}. \quad (2.80)$$

In (2.80) a and c are the lattice constants, and N is the number of unit cells along the c axis (i.e., $z = 415.6 - Nc$). This comparison shows that the kinematic theory is able to render the correct phase for the D-field amplitude ratio, but it does not predict the intensity correctly close a Bragg reflection due to the extinction effect. The use of dynamical theory for a thin-film XSW analysis becomes more necessary as the film thickness increases.

We now discuss the experimental results in Figure 2.14. Figure 2.14(a) show the data and best fit of the reflectivity and Pb L fluorescence yield. In fitting the fluorescence data, four free parameters were used: Y_{BO} , f , P and a surface miscut angle ϕ , but the PbTiO_3 lattice used for the structure factor calculation was fixed by the bulk atomic coordinates listed in Figure 2.10 for the “up” polarization state (i.e., the fitting

process was not self-consistent). However, the Pb coherent position determined from the best fit (0.117) showed excellent agreement with the bulk position (0.116). No good fit can be attained if we fixed the structure factor using the bulk coordinates of the “down” polarization state. Based on this observation and the high coherent fraction (0.849) we concluded that the lattice of this 400 Å thick, as-grown PbTiO₃ film was perfectly aligned to exhibit a single up polarization state. Also shown in Figure 2.14(a) is the theoretical Pb fluorescence yield curve for the down state (dashed line). This demonstrates the sensitivity of this measurement. The results based on a more rigorous fitting procedure, as discussed in Section 2.3, will be reported in Ref. 9.

Figure 2.14(b) shows the Ti data and the best fit. Since the take-off angle α_u was below the critical angle for PbTiO₃ at the Ti K energy, the contribution to the Ti yield from the SrTiO₃ substrate was ignored (i.e., the more complicated analysis described in Section 2.4 was unnecessary). This measurement confirmed that the film was in a single up polarization state. Notice that (a) the modulation of the Ti fluorescence yield is nearly 180° out of phase from that of the Pb yield and (b) the Ti (001) XSW measurement shows greater contrast between the up and down polarization states.

Chapter 3 Experimental

3.1 X15A (NSLS)

Most of the XSW measurements in this thesis work were conducted at bending magnet beamline X15A of the National Synchrotron Light Source (NSLS) at Brookhaven National Laboratory (BNL). The beamline is equipped with a double-crystal monochromator for tuning and scanning the incident x-ray energy, a slit and ion chamber systems for defining the beam size and monitoring the beam intensity, as well as a Huber two-circle diffractometer including a reflectivity and a solid-state fluorescence detector systems for open-air XSW and low-angle reflectivity measurements. The optics of the beamline is also capable of x-ray extended absorption fine structure (EXAFS) experiments.

For *in situ* XSW and EXAFS measurements there was a multi-chamber ultra high vacuum (UHV) system behind the Huber 2-circle diffractometer. The UHV facility (base pressure $\sim 9 \times 10^{-11}$ torr) consisted of a molecular beam epitaxy (MBE) system coupled with a LEED/AES chamber and an XSW/EXAFS chamber, allowing sample preparation and *in situ* surface characterization. Figure 3.1 shows the top view of the UHV system. A more detailed description and the operational procedures of the X15A beamline and the UHV facility can be found in Ref. 1 and 2.

A typical XSW measurement at X15A consists of simultaneously recording the fluorescence spectra and the reflectivity from a sample while scanning the double-crystal

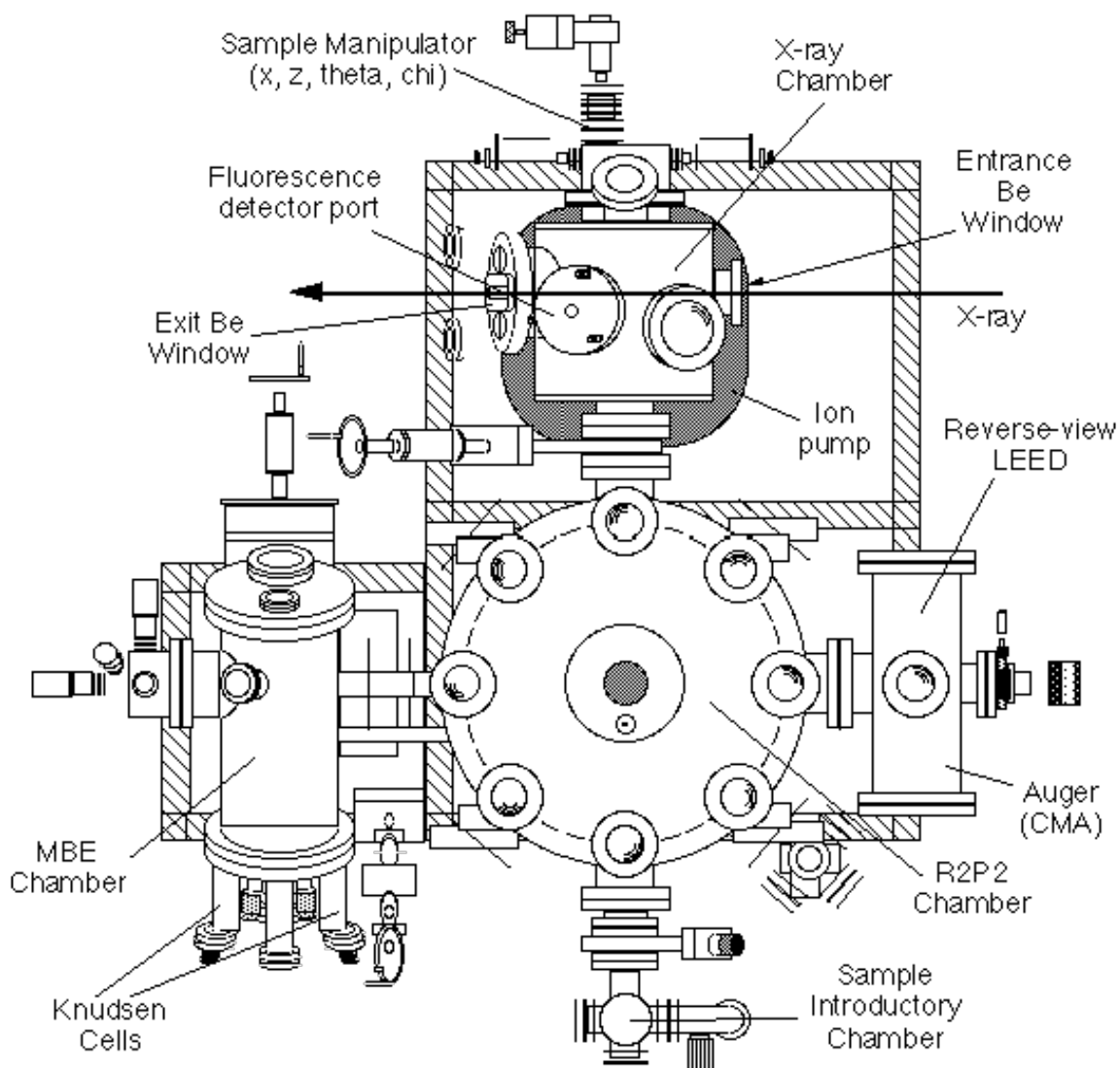


Figure 3.1 Top view of the multi-chamber UHV system at beamline X15A at the NSLS (it is currently located at the 12ID-D undulator station of the BESSRC CAT at the APS).

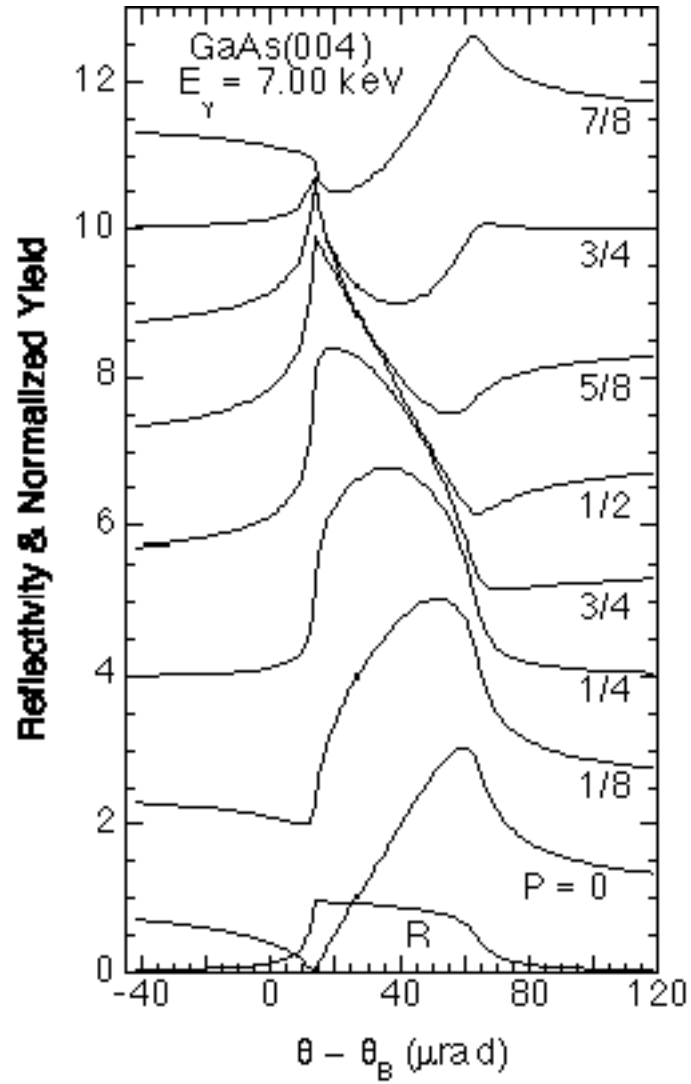


Figure 3.2 Simulated fluorescence yields for the GaAs(004) reflection at 7.00 keV for various coherent positions P (see Section 2.3) to demonstrate how the standing wave field moves with respect to a diffraction plane. The coherent fractions f are all equal to one.

monochromator in energy through a hkl Bragg reflection of the sample substrate. This eV-wide scan causes the standing wave to phase shift by 180° [Figure 2.11(c)] and move inward by one-half of the d-spacing relative to the hkl diffraction planes. This movement induces a characteristic modulation of the fluorescence yield depending on the position of the fluorescent atoms with respect to the hkl diffraction planes (Figure 3.2). The flow chart in Figure 3.3 illustrates the structure of the XSW data acquisition program (a SPEC macro).

3.2 5ID-C and 12ID-D (APS)

As the Advanced Photon Source (APS) at Argonne National Laboratory (ANL) becomes operational, we are increasingly using this third-generation synchrotron to take advantage of the more brilliant and collimated x-ray beam. Parts of the experiments that will be discussed in Chapter 6 (XSW) and Chapter 7 (EXAFS) were conducted at the 12ID-D undulator station of the Basic Energy Sciences Synchrotron Radiation Center (BESSRC) Collaborative Access Team (CAT) and at the 5ID-C undulator station of the DuPont-Northwestern-Dow (DND) CAT, respectively, at the APS.

In Figure 3.4 we show a typical XSW experimental setup at the APS. The undulator is an insertion device composed of a linear array of magnets with alternating polarities. The electrons circulating inside the synchrotron ring are forced to undergo a rapid horizontal oscillation while passing through the undulator. The radiation given off in successive oscillations can interfere constructively. This leads to approximately 100-eV wide spikes in the radiation spectrum, which are typically 10^3 times more intense than

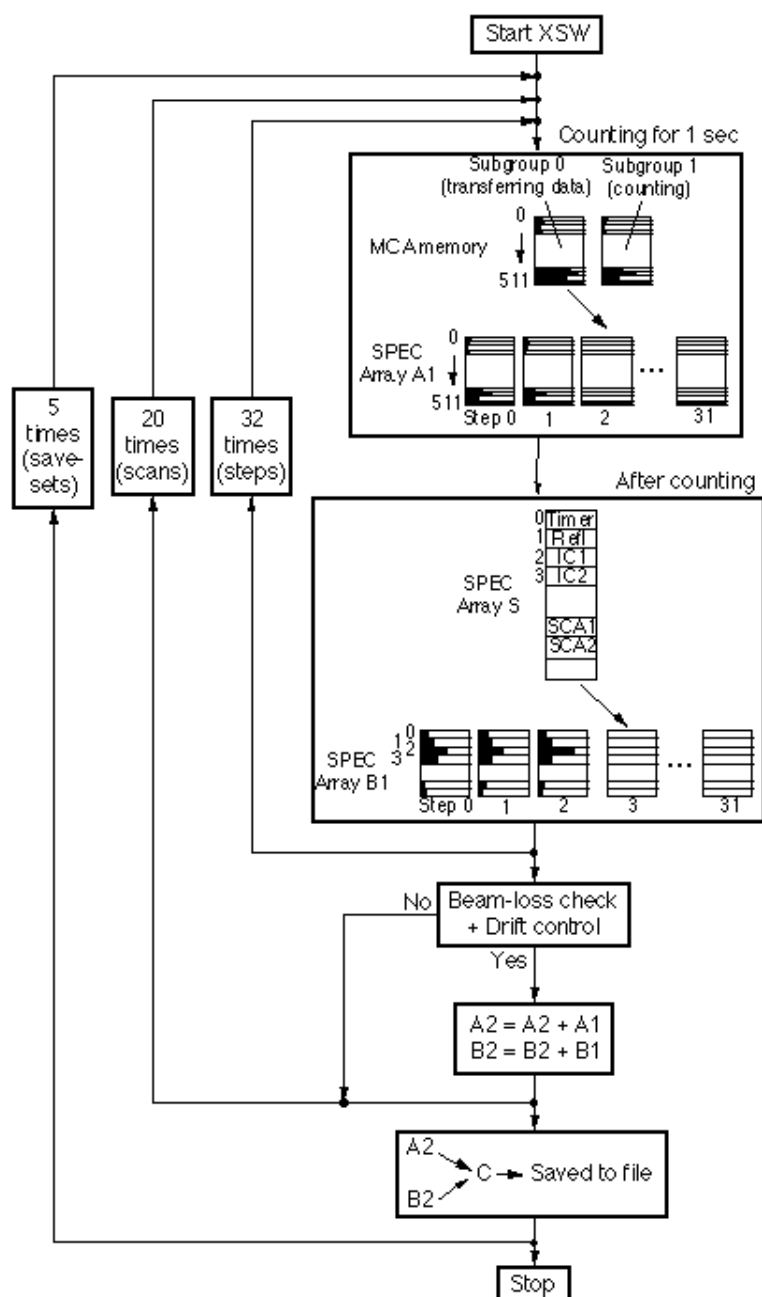


Figure 3.3 A flow chart describing the structure of the XSW data acquisition program used at 5ID-C/APS. In this example the XSW measurement is set to count for 1 second at each step. There are 32 steps per rocking curve scan, 20 scans per saveset and totally 5 savesets. The multi-channel analyzer (MCA) is set up to have 512 channels per subgroup. Two MCA subgroups (0 and 1) are used alternately for acquiring the spectra.

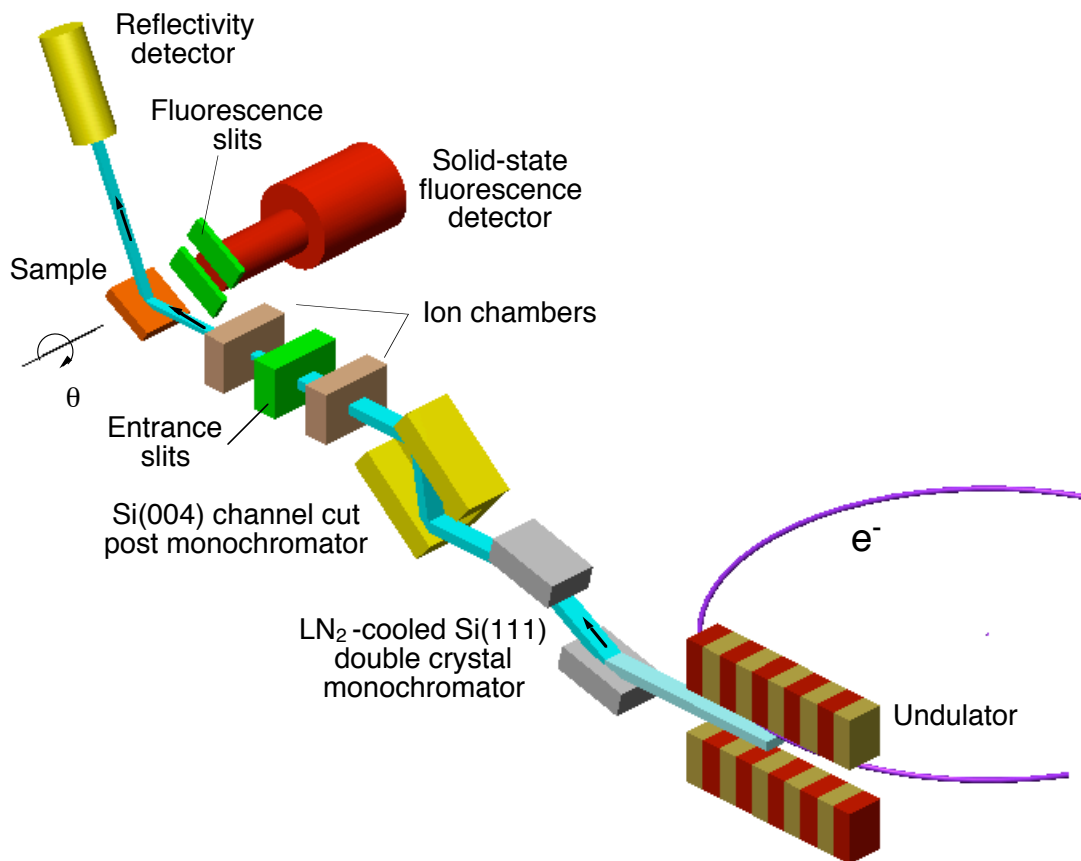


Figure 3.4 Typical experimental setup at the APS for open-air XSW measurements using bulk Bragg reflections.

the flux of a bending magnet beamline. The peaks in the undulator spectrum can be conveniently tuned in energy by adjusting the undulator gap. Due to the high power density of the undulator beam, the Si(111) double-crystal beamline monochromator is cooled by liquid nitrogen. For an XSW measurement utilizing bulk Bragg reflections, a Si(004) channel cut (post monochromator) is often added to further reduce the energy width ΔE of the incident x-ray and thus increase the precision of the measurement. The fluorescence slits shown in the figure are for the purpose of limiting the emission takeoff angle, which can be crucial if surface sensitivity is required (see Section 2.4, 2.5 and 7.4). We have been scanning the angles of the sample stages (driven by micro-stepping motors) during the XSW experiments at the APS, even though scanning energy is also possible. For an EXAFS measurement the channel cut, fluorescence slits and reflectivity detector are removed. The energy scans are achieved by scanning the LN₂-cooled Si(111) monochromator and the undulator gap simultaneously.

The electronic systems at the 5ID-C station are illustrated by the block diagram in Figure 3.5. Two computers running LINUX operating system are involved. The one inside the x-ray hutch is installed with all the necessary interface adapters and x-ray diffraction software (SPEC), controlling data acquisition and more than 40 stepping motors driving the diffractometers, optical table, slits and post-monochromator stage. Beamline users control their experiments from the computer outside the x-ray hutch through the local network and X Window system. The communications between SPEC and all the devices are conducted mostly through the VME crate and the CAMAC crate. The VME crate contains a number of stepping motor controllers (B) and a 16-channel

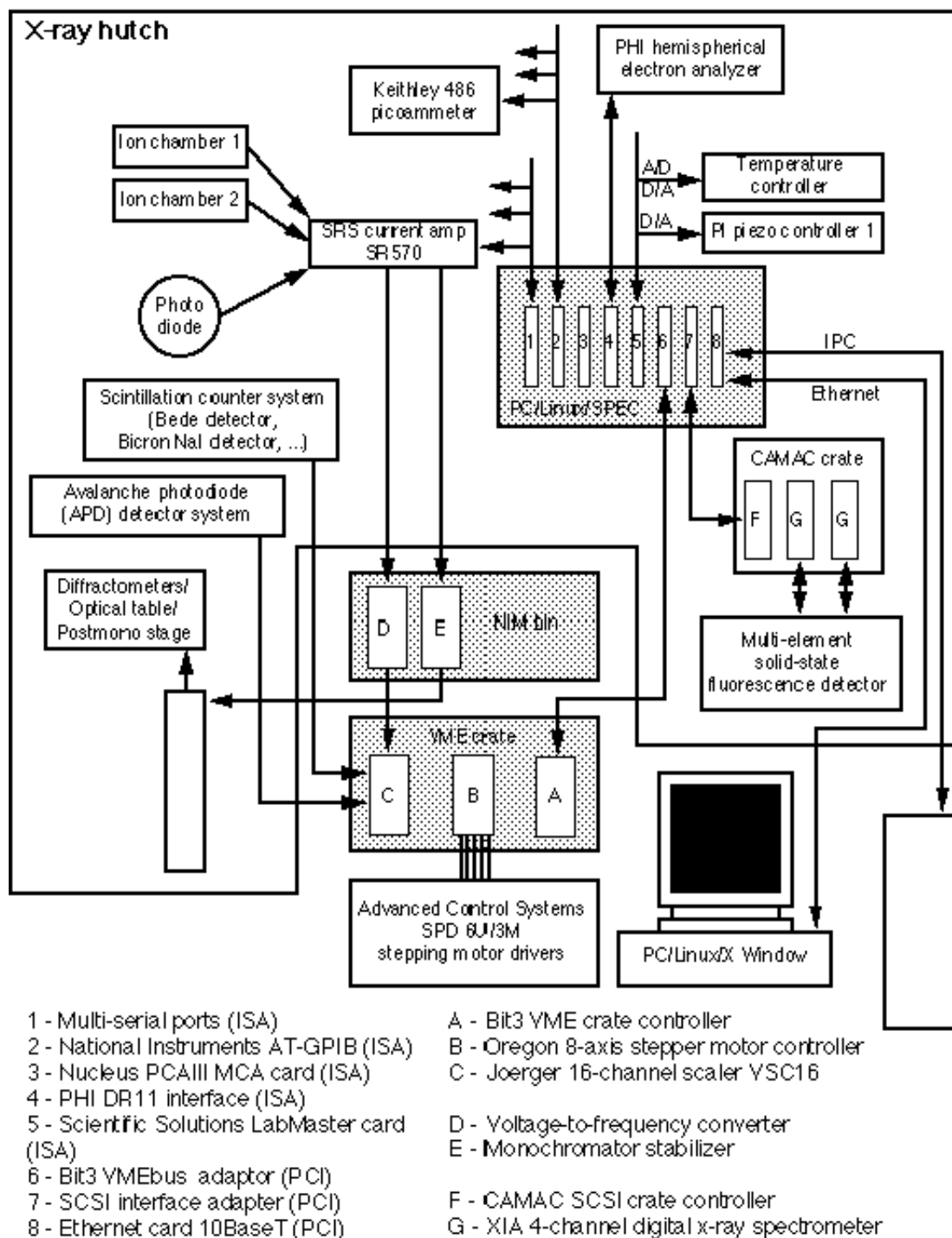


Figure 3.5 Block diagram of the electronic systems at the 5ID-C undulator station of the DND CAT at the APS.

scaler (C). The logical pulses from most of the detector systems are finally counted by the 16-channel scaler. The CAMAC crate has two digital x-ray spectrometer modules (G), which are in charge of the data acquisition from a multi-element solid-state fluorescence detector. Multiple RS232 ports and digital-analog converters are also available on the computer inside the hutch for serial and analog devices. The LN₂-cooled Si(111) monochromator is currently controlled by DND software. Direct control of the LN₂-cooled Si(111) monochromator from the SPEC at the 5IDC station can be achieved through the Interprocess Communication (IPC) over the network.

In October 1997 the multi-chamber UHV system at beamline X15A at the NSLS was moved from BNL to the BESSRC CAT at the APS. The system was reinstalled in the 12ID-D undulator station in June 1998 (Figure 3.6). Currently the μ rad-resolution incident angle scans for the XSW measurements using bulk reflections are accomplished by scanning the tilt of the entire 1800-lb UHV system with a custom designed supporting platform.

In principle scanning the sample and scanning the monochromator (i.e., the energy) are equivalent for an XSW measurement. However, with the greater source distance at the APS (e.g., roughly 70 m at the 12ID-D station) and the possibility of using a small beam to allow dynamical diffraction from an imperfect bulk crystal (e.g., SrTiO₃), the divergence of the incident beam is often determined by the vertical entrance slit size. This changes slightly the optical considerations as compared with the situation at the NSLS. Table 3.1 lists the theoretical Darwin widths (or the intrinsic rocking width) ω for

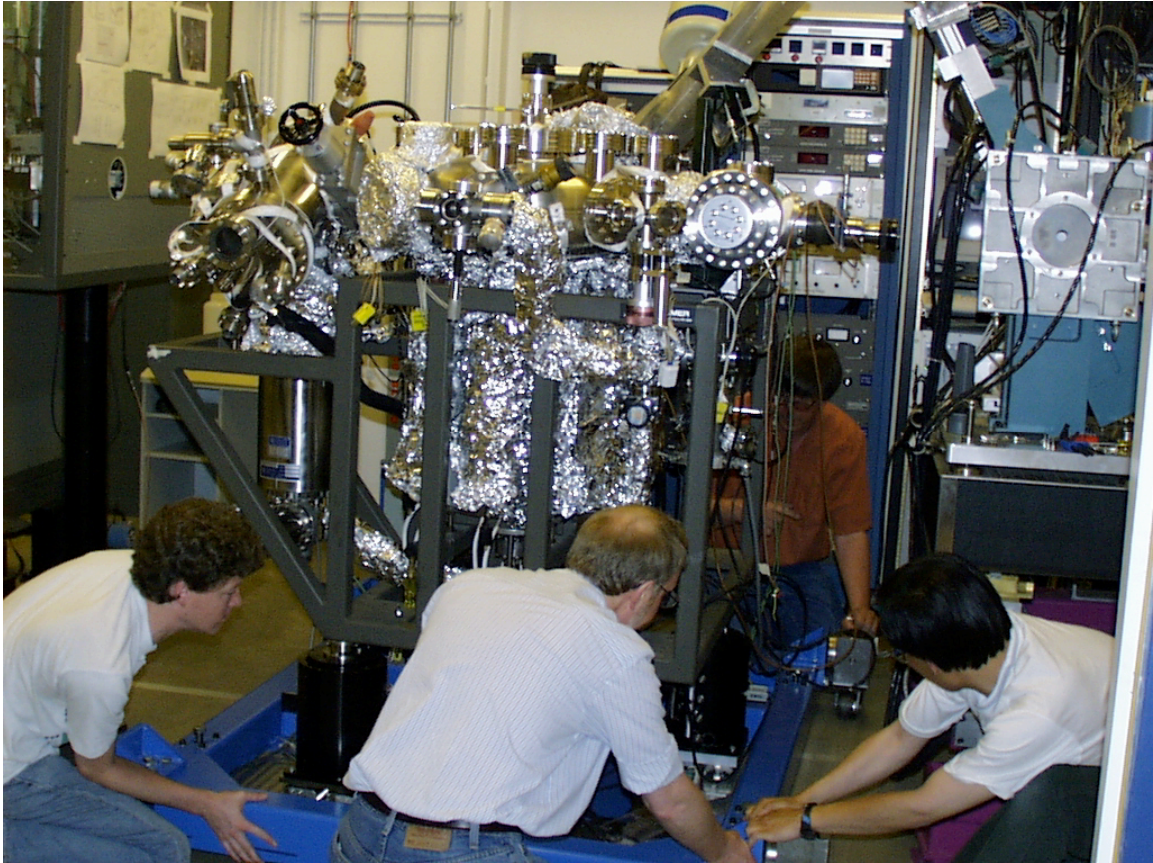


Figure 3.6 A picture of the multi-chamber UHV system shot right after its installation at the 12ID-D hutch of the BESSRC CAT at the APS. The UHV system rested on a custom-designed supporting platform. The four persons in the picture are (left to right) Paul Lyman, Alexander Kazimirov, Mike Bedzyk and myself. The picture was shot by Osami Sakata.

the (111), (004) and (008) reflections of Si at 12.00 keV based on the following equation deduced from (2.51):

$$\omega = \frac{2\Gamma F_{\mathbf{H}}'}{\sqrt{|\mathbf{b}|} \sin(2\theta_{\mathbf{B}})} \quad (3.1)$$

Figure 3.7(a) shows the DuMond diagram considering the three reflections. The x axis denotes the incident angle θ in μrad and the y axis is the wavelength in 10^{-6} \AA . The stripes represent the conditions where a Bragg diffraction is allowed by the dynamical theory. The slopes of the stripes can be estimated by Bragg's law as

$$\frac{\Delta\lambda}{\Delta\theta} = 2d_{\mathbf{H}} \cos\theta_{\mathbf{B}}. \quad (3.2)$$

Therefore, the slope is completely determined by the d-spacing $d_{\mathbf{H}}$ of the reflection. Also shown in Figure 3.7(a) are the diffraction-allowed areas restricted by the APS source divergence (11 μrad) and a 100- μm vertical entrance slit size at a source distance of 50 m (without considering the source size). The overlaps between these conditions with a Si(004) channel cut are indicated by the shaded and dark areas. Figure 3.7(b) and (c) show the difference between scanning a Si sample [(b)] and scanning a Si(004) channel cut (the post-monochromator) [(c)] for the sample (111) reflection considering only the angular restrictions by the entrance slits. It is clear in Figure 3.7(c) that due to the d-

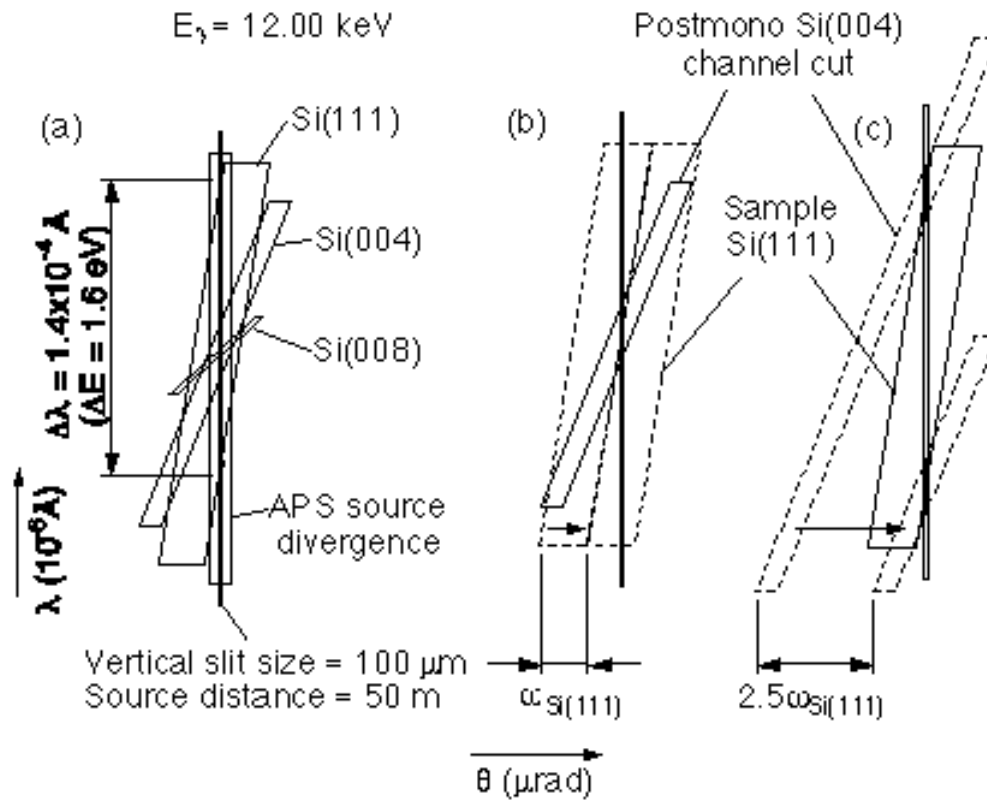


Figure 3.7 (a) A DuMond diagram considering the Si(111), (004) and (008) reflections at 12.00 keV. Also shown are the angular ranges due to the APS source divergence (11 μrad) and a 100- μm vertical slit size (2 μrad). (b) and (c) are a comparison in DuMond diagrams between scanning a Si sample [(b)] and scanning a Si(004) channel cut (the post-monochromator) [(c)] for measuring the sample (111) reflection with a 100- μm vertical slit size.

spacing mismatch between the (111) and (004) reflections, scanning the Si(004) channel cut will measure a sample rocking curve width of $(\Delta\lambda/\Delta\theta)_{\text{Si}(111)}/(\Delta\lambda/\Delta\theta)_{\text{Si}(004)} = 2.5$ times that of $\omega_{\text{Si}(111)}$, while scanning the Si(111) sample in this case yields the correct width. Since the intersection of the vertical slits and the Si(004) channel cut is very small in the wavelength direction, it is unnecessary to eliminate the dispersion due to the d-spacing mismatch by changing the post-monochromator crystal to match the d-spacing of the sample.

Table 3.1 Calculated Bragg angles θ_B , Darwin widths ω , d-spacing d_H and the slope $\Delta\lambda/\Delta\theta$ for the Si(111), (004) and (008) reflections at 12.00 keV [see Eq. (3.1) and (3.2)]

Si ($E_\gamma = 12$ keV)	θ_B (deg)	ω (μrad)	d_H (\AA)	$\Delta\lambda/\Delta\theta$ (\AA)
(111)	9.48	22	3.14	6.19
(004)	22.36	10	1.36	2.52
(008)	49.55	3.5	0.68	0.88

Chapter 4 Reconstructions of Clean GaAs(001) Surface

4.1 Introduction

The interest in studying semiconductor surfaces and interfaces originated from the desire for understanding the physics behind the rectifying behavior of metal-semiconductor contacts, which has been widely applied in power rectification based on cupreous oxide since the beginning of this century [1]. With the remarkable advances made in ultra-high vacuum and thin film growth technologies in the past fifty years, surfaces and interfaces of semiconductors as well as many other materials can now be studied in well-controlled environments using probes with atomic resolution and sub-monolayer sensitivity. Research of this kind has led not only to a better understanding of the fundamental properties of solid surfaces but also to possibilities of synthesizing novel nanometer-scale heterostructures for future applications.

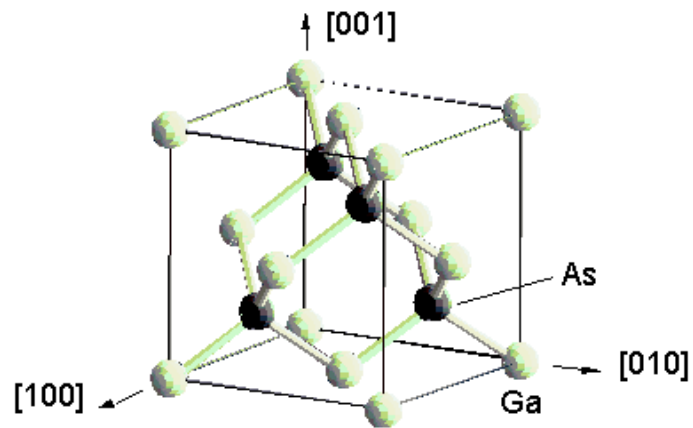


Figure 4.1 The crystal structure of bulk GaAs. The cubic unit cell contains 4 Ga and 4 As atoms.

GaAs has a zinc-blende crystal structure (Figure 4.1). In the [001] direction the GaAs lattice is constructed by stacking alternately Ga and As atomic planes with a separation of $d_{004} = 1.41 \text{ \AA}$. The [001] axis therefore represents a polar direction. The Ga-As chemical bond is primarily covalent with a slight ionic character. The band gap of GaAs is direct with an energy of 1.42 eV at room temperature [2]. The electron mobility of doped bulk GaAs is $8500 \text{ cm}^2/\text{Vs}$ at room temperature [2]. This is more than five times higher than that of Si. The direct band gap and high electron mobility have made GaAs an important semiconductor material for manufacturing optoelectronic devices, high-speed transistors and telecommunication devices.

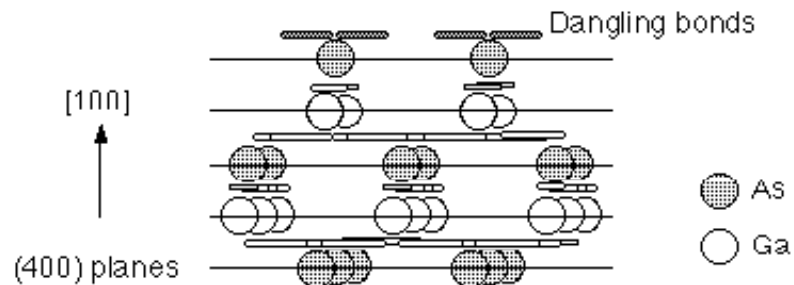


Figure 4.2 The ideally bulk terminated GaAs(001) surface.

When a semiconductor free surface is created, the ideal bulk termination is energetically unstable due to the highly directional covalent bonds broken at the surface (Figure 4.2). The surface energy can be reduced through relaxation and reconstruction. The former involves slight displacements of the near surface atoms from their bulk positions (primarily along the surface normal direction), but the surface lattice retains the

lateral periodicity of the bulk. The latter involves more severe alteration of the ideal structure. It is characterized by the reduction of the surface symmetry, which usually results from the formation of new chemical bonds and surface defects. The GaAs(110) surface, for example, was found to be only relaxed [3]. However, a number of rather complicated reconstructions have been observed for the GaAs(001) surface. In either case unique surface electronic states are present due to the termination of bulk symmetry.

4.2 Electron counting model

As pointed out by Duke [4], semiconductor surface reconstructions are, in general, driven by two dominant factors: saturation of chemical bonding and surface charge neutrality. For a compound semiconductor, these usually imply that the surface has a different stoichiometry from the bulk, which in turn adds a great complexity to the surface structure determination. Efforts have been made by several groups [4 - 9] since the 1970s to establish general rules for surface reconstruction of compound semiconductors. In proposing structural models for a surface, these rules can serve as simple tests for finding the most stable configuration among the competing candidates, before highly sophisticated theoretical calculations are carried out. They also help explain why certain features are commonly observed on these surfaces.

Figure 4.3(a) shows schematically the successive steps for constructing the energy states of bulk GaAs through linear combinations of atomic orbitals [6, 10]. Beginning with the atomic 4s and 4p levels of Ga and As, linear combinations of s and p wave

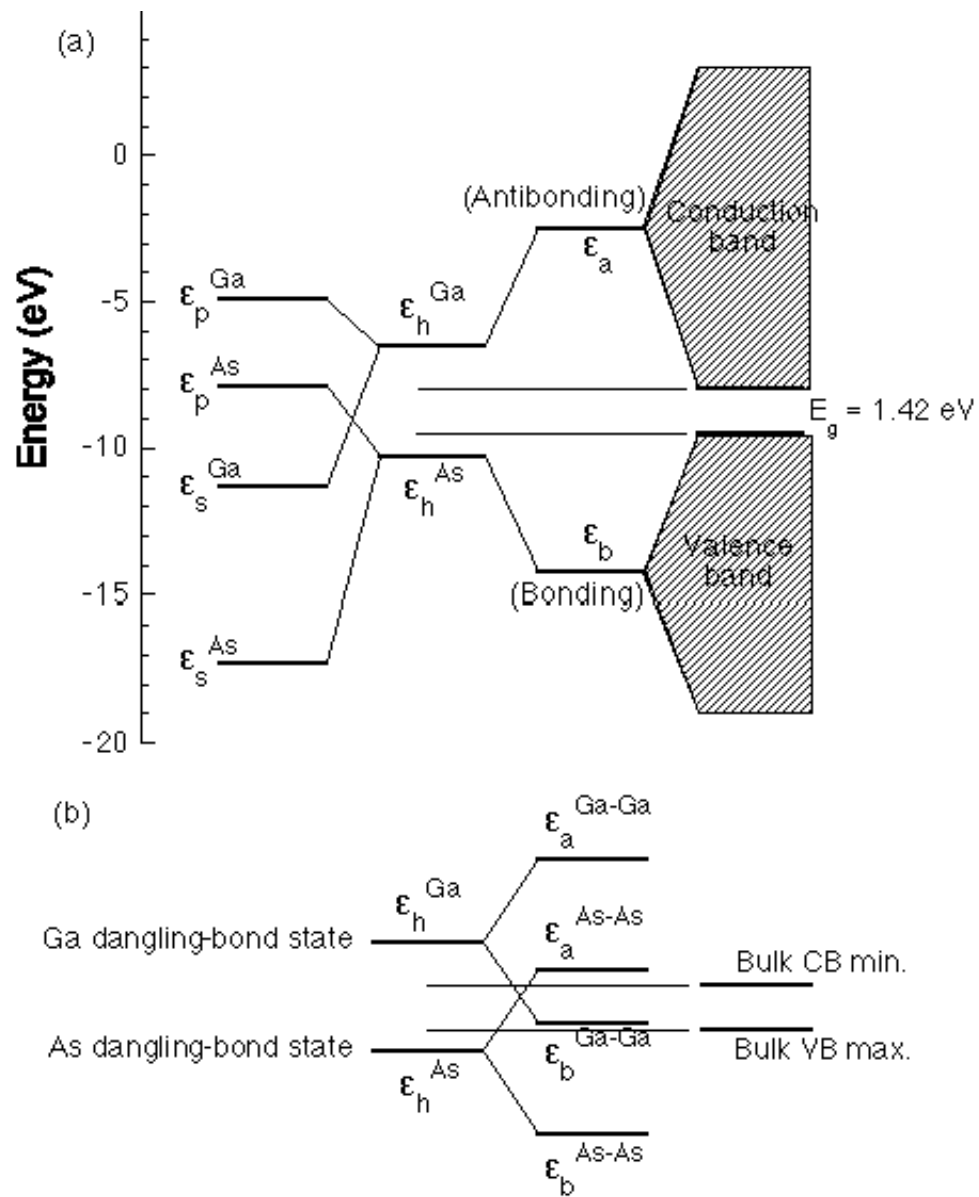


Figure 4.3 Energy-level diagrams for GaAs in the bulk (a) and at the surface (b), based on linear combinations of Ga and As atomic orbitals (see Ref. 10).

functions create the highly directional sp^3 hybrid orbitals (ϵ_h^{Ga} and ϵ_h^{As}), which determine the tetrahedral bonding geometry of the crystal. As the atoms are brought together, the wave functions of two adjacent Ga and As sp^3 states overlap, and a further linear combination of them leads to the formation of the bonding (ϵ_b) and antibonding states (ϵ_a). A Ga-As chemical bond is then formed by filling the bonding state with two valence electrons and keeping the antibonding state empty. In this process the total energy is reduced drastically in comparison with the energy levels of the hybrid orbitals for isolated Ga and As atoms. Finally, the bonding and antibonding states broaden into the valence band and conduction band, respectively, as the volume of the GaAs lattice increases.

The electronic structure and bonding geometry at a semiconductor surface are generally far more complicated than those in the bulk. The termination of a lattice interrupts the bulk translational symmetry. As shown in Fig. 4.2, the creation of an ideal bulk-terminated GaAs(001) surface reduces the coordination number from 4 to 2 for each surface atom. This leaves behind two broken bonds per atom on the surface called dangling bonds, each containing only one unpaired electron (or more rigorously speaking, $5/4$ and $3/4$ electrons for As and Ga termination, respectively). The energy levels of these dangling bonds can be estimated from those of the sp^3 hybrid orbitals for isolated Ga and As. The number of dangling bonds, and thus the surface energy, can be reduced if the atoms on the surface form chemical bonds with their second nearest neighbors in the surface plane. This leads to the dimerization of the surface. The bonding and antibonding states for these Ga-Ga and As-As dimers should be, again, linear

combinations of the atomic sp^3 hybrid orbitals for Ga and As, respectively, as suggested in Fig. 4.3(b).

For the hybrid orbitals that do not form bonds on the surface, Fig. 4.3(b) shows that the sp^3 energy level of Ga is above the conduction-band minimum of bulk GaAs, and the sp^3 energy level of As is below the bulk valence-band maximum. Therefore, a semiconducting surface can be achieved if all the As dangling-bond states are filled and all the Ga dangling-bond states are empty. Any partially filled dangling-bond orbital, on the other hand, would lead to a metallic surface. However, a semiconducting termination is energetically more favorable to the formation of dimer structures. This can be explained by a theory developed by Peierls [11] in 1930, which states that a one-dimensional lattice with a metallic electronic structure is unstable and will turn semiconducting through a distortion of the lattice (Peierls distortion). Since the (001)-oriented semiconductor surfaces are usually characterized by chains of dimers parallel to the $[\bar{1}10]$ or the $[110]$ directions, which have a one-dimensional nature, Peierls' finding is applicable here.

Using the above argument, Pashley [7] concluded that the stable reconstructions of semiconductor surfaces correspond to those electronic structures where the dangling-bond states in the valence band are completely filled by all available electrons and the dangling-bond states in the conduction band are left empty (Figure 4.4). Apparently, this requirement can only be satisfied by certain surface compositions. The significance of this so-called electron counting model is therefore that it can be used to determine the allowable stoichiometries of compound semiconductor surfaces. Moreover, for a given

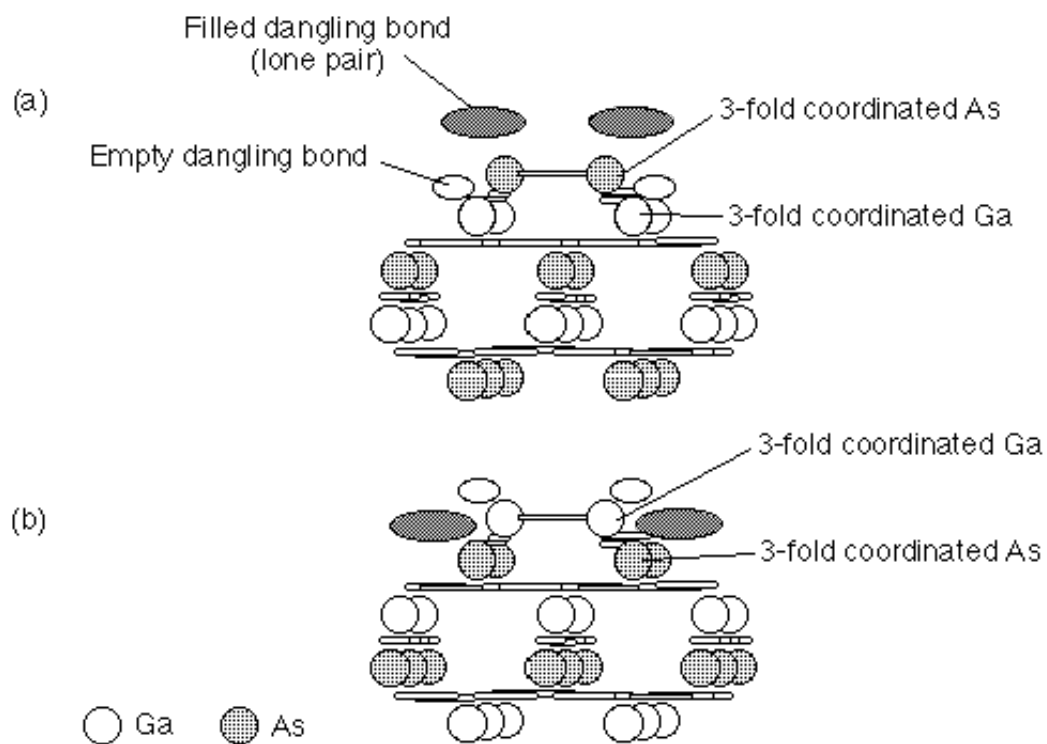


Figure 4.4 Filled and empty dangling bonds predicted by the electron counting model in an As- (a) and a Ga- (b) terminated GaAs(001) surface.

composition, this model implies that in the surface layer each 3-fold-coordinated electropositive atom will have to give up one (or 3/4) electron back to a 3-fold-coordinated electronegative atom. This charge transfer is important in maintaining an electrically neutral surface. For a polar surface such as the GaAs(001) surface, depending on whether it is terminated with As or Ga, positive or negative charges can be accumulated in the top layer if the surface remains unreconstructed. This is due to the fact that the Ga-As bond is slightly ionic. It can be shown that the surfaces with stoichiometries satisfying the electron counting rule will be automatically neutral. This provides another physical explanation for why semiconductor surfaces reconstruct. The application of the electron counting model will be demonstrated for the GaAs(001) $(2\times 4)/c(2\times 8)$ reconstruction in Section 4.3.2.

4.3 Reconstructions of GaAs(001) surface

A variety of reconstructions have been observed on clean GaAs(001) surfaces. The structures of these reconstructions strongly depend on surface stoichiometry, which is determined by preparation conditions such as substrate temperature and As and Ga partial pressures. More than five different GaAs(001) phases have been reported under ultra-high vacuum conditions, ranging from the most As-rich $c(4\times 4)$ to the most Ga-rich (4×6) reconstruction. Owing to the complexity introduced by the uncertainty of surface composition and the ionic nature of the Ga-As bond, the detailed structures of some of the reconstructions are still under debate, despite considerable experimental and theoretical investigations of this system. Therefore, new evidence is needed to clear up

the controversy. It is expected that the complete determination of the GaAs(001) surface structures will continue to be a subject of wide interest in the future.

In the following sections we briefly review some of the observed reconstructions and the proposed models for the GaAs(001) surface with special emphasis on the $(2\times 4)/c(2\times 8)$ structure.

4.3.1 $(2\times 4)/c(2\times 8)$

Among all the known GaAs(001) surface reconstructions, the $(2\times 4)/c(2\times 8)$ is perhaps the most important and intensively studied one. For most optical and electronic devices fabricated on GaAs(001) substrates using molecular beam epitaxy, growth is usually started with this surface structure.

Earlier studies [12 - 18] of the GaAs(001) surface focused on finding the dependence of the various surface symmetries on the Ga and As coverages. It was observed that the GaAs(001) surface exhibited a $(2\times 4)/c(2\times 8)$ symmetry over a wide temperature range between 400 and 650 °C, depending on the Ga and As impingement rates [12, 16]. Compared to the other (001) reconstructions, it appeared that the formation of this structure was preferred at a lower substrate temperature for a constant As flux, or a higher As flux at a fixed substrate temperature. The $(2\times 4)/c(2\times 8)$ termination was therefore characterized as the As-stabilized surface. Several studies [12 - 16] using reflection high-energy electron diffraction (RHEED) demonstrated that the $2\times$ period is parallel to the $[\bar{1}10]$ direction, which is consistent with the direction of the

As dangling bonds, and the $\times 4$ period is parallel to the [110] direction. The first attempt to interpret the $(2\times 4)/c(2\times 8)$ symmetry was made by Cho [16]. He suggested that the $2\times$ period observed in the RHEED pattern was due to dimerization of the surface As atoms, in analogy to the Si(001) (2×1) reconstruction. Due to the difficulty in data analysis, during 1970s and early 1980s RHEED was mainly used to establish surface symmetries and monitor MBE growth. Most of the information from RHEED studies on semiconductor surfaces remained qualitative.

The As coverage of the $(2\times 4)/c(2\times 8)$ surface has been characterized by Auger electron spectroscopy (AES) [17 - 19], photoemission spectroscopy (PES) [18, 20 - 22] and high-resolution electron-energy-loss spectroscopy (HREELS) [23]. By normalizing the intensity ratios between the As (~ 31 eV) and Ga (~ 55 eV) MNN Auger peaks measured on a GaAs(001) surface to the ratio measured on a (110) cleaved surface, Drathen et al. [17] determined the As coverage for the $(2\times 4)/c(2\times 8)$ reconstruction to be 0.6 ML. Later in a PES investigation, Bachrach et al. [20, 21] obtained a slightly higher As coverage ($7/8$ ML) for the same reconstruction by measuring the area ratio between Ga and As 3d core level peaks. In a more recent HREELS study of the vibrational spectra of chemisorbed atomic H on the GaAs(001) surface, Frankel et al. [23] showed that both As-H and Ga-H species were present on the $(2\times 4)/c(2\times 8)$ surface. This finding suggested the presence of As dimer vacancies, which could expose the Ga dangling bonds in the second layer. Thus, it also ruled out the possibility for the $(2\times 4)/c(2\times 8)$ surface being terminated by a full ML of As dimers.

The electronic structure of the $(2\times 4)/c(2\times 8)$ surface has been probed by HREEL [24 - 26], work function measurements [18] and angle-resolved photoemission spectroscopy (ARPES) [22, 27]. The purpose of these studies was to identify the surface states associated with the As and Ga dangling bonds. Due to the complexity of the surface structure and the relatively weak surface emissions, consistency between experimental data was poor. Ludeke and Koma [25] measured the low energy electron energy loss spectra for a variety of the GaAs(001) reconstructions, including the polar $\{111\}$, (001) and nonpolar (110) surfaces. They located empty surface states at about 0.9 eV above the bulk valence band edge and filled surface states at 0.5 – 2 eV below the valence band edge. They attributed the former to the Ga dangling bonds and the latter to the As lone pairs. Massies et al. [19] measured the work function of the GaAs(001) surface using contact potential difference (CPD). For a given (001) surface structure, they found no significant work function changes between n and p type substrates, indicating that the Fermi level was pinned by a high density of empty and filled surface states. The CPD measurements carried out on different reconstructed surfaces showed that the work function had strong dependence on the surface stoichiometry and structure.

Using ARPES with synchrotron radiation, Larsen et al. [27] mapped out the surface energy band for the GaAs(001) $(2\times 4)/c(2\times 8)$ surface. They found that the surface states were mostly in the energy range between -3 eV and the valence band maximum with very weak energy dispersion. The origin of these surface states was examined theoretically by tight binding calculations. They concluded that the (2×4) surface contained asymmetric As dimers with an As coverage of one ML. However, the surface

stoichiometry of their model was inconsistent with the previous measurements [17, 20, 21], and the evidence in their APRES data supporting the buckling of the As dimer was rather unclear. Later Chiang et al. [22] reported another ARPES measurement on the same surface structure, as well as on several other reconstructed GaAs(001) surfaces. Their study showed that the Fermi level was 0.55 eV above the valence band maximum for all the reconstructions. In their angle-resolved measurements they found that only peaks related to transitions from the GaAs bulk valence bands were observed in their spectra, which suggested that transitions due to the surface states were relatively weak for the GaAs(001) surface, in contrast to the strong surface-state emission of Si and Ge surfaces.

Theoretical studies have been carried out since 1970s to predict the structural and electronic properties of compound semiconductor surfaces. Owing to lack of information about the atomic structures, earlier calculations [28 - 32] for the GaAs(001) surface electronic structures were conducted primarily assuming an ideal, unreconstructed (1×1) As or Ga termination. Mainly empirical methods such tight-binding approach were used because of limited computing power. It was first pointed out by Appelbaum et al. [28] that the minimum area for a reconstructed GaAs(001) unit cell to achieve a nonmetallic surface was four times the substrate (1×1) unit cell. This was based on the argument that for the (1×1) ideal surface each As (Ga) dangling bond contained 5/4 (3/4) electrons; four As (Ga) atoms per surface unit cell will provide an odd number of electrons, which eliminates the possibility of having half-filled surface bands. Later tight-binding energy-minimization calculations by Chadi et al. [31] and *ab initio* pseudopotential

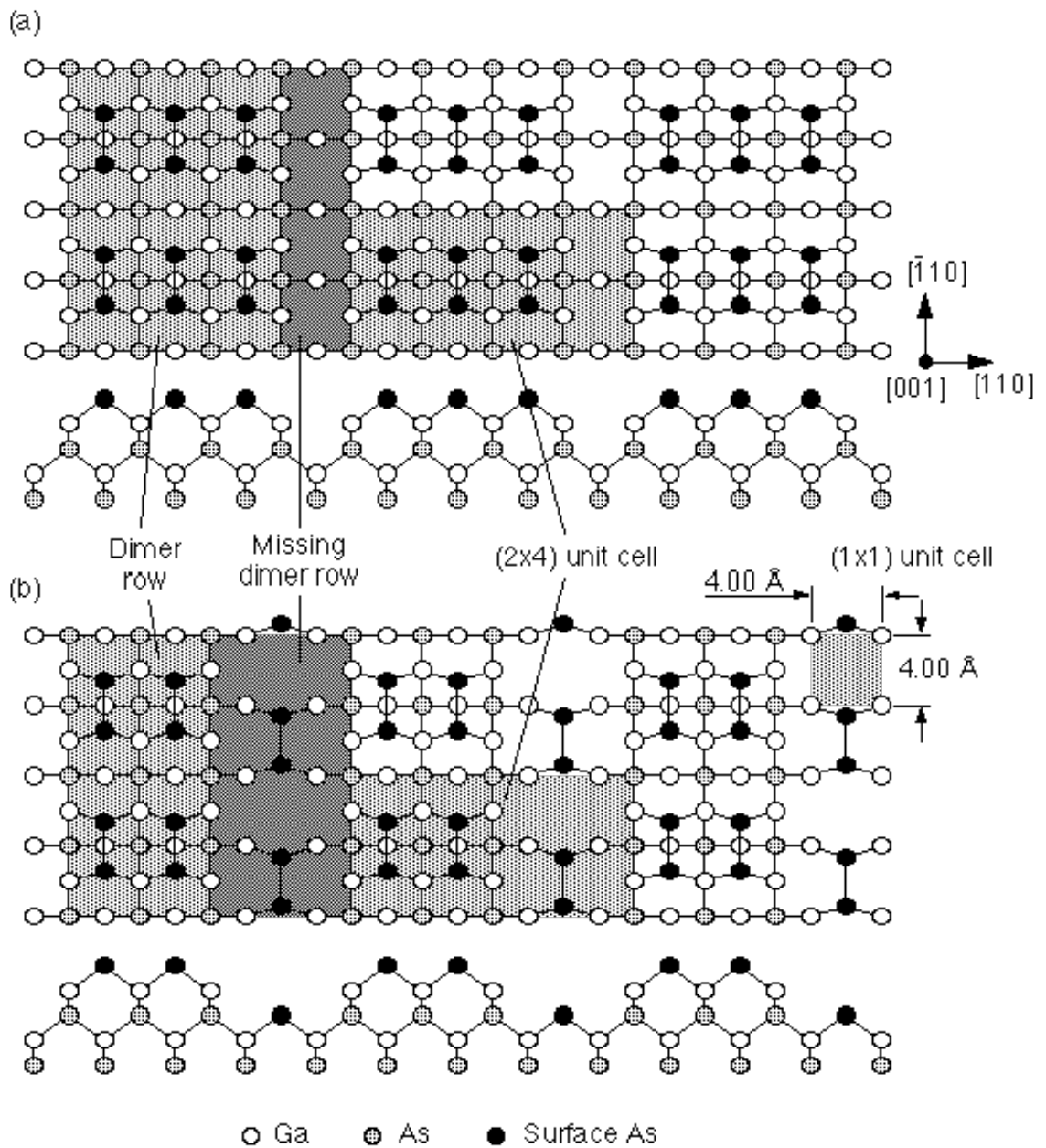


Figure 4.5 The structural models proposed by Chadi [33] for the GaAs(001) (2x4) reconstruction with (a) 3 As dimers in the first layer and (b) two As dimers in the first layer and the third dimer in the third layer.

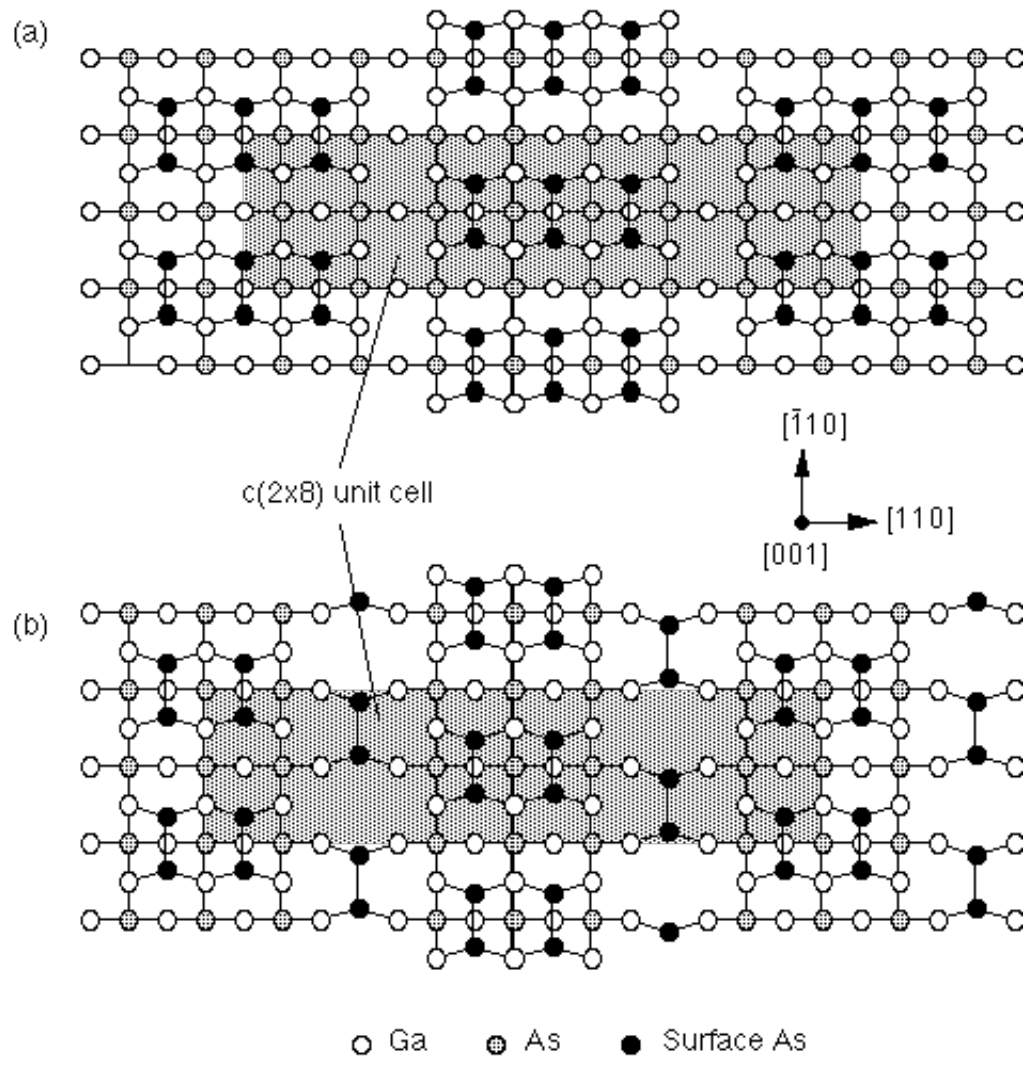


Figure 4.6 The GaAs(001) c(2x8) unit cells constructed from (a) the three-dimer and (b) the two-dimer (2x4) models proposed by Chadi (see Figure 4.5).

calculations by Ihm et al. [32] showed that the dimerization of As atoms on the GaAs(001) surface reduced the total energy by about 1 – 2 eV/dimer.

In an important article published in 1987, Chadi [33] evaluated theoretically a number of structural models for the GaAs(001) (2×4) surface. Based on his tight-binding-based total-energy calculations, he concluded that it was most likely that the surface contained three As dimers per unit cell. The two possible structures he considered are shown in Figure 4.5(a) and (b), each with an As coverage of 0.75 ML. The model in (a) has all three As dimers in the outermost layer, while the model in (b) has one of the As dimers in the third layer in the trench area (i.e., two As dimers and two missing dimers in the outermost layer). Chadi's calculations also indicated that the As dimers should be symmetric for these two (2×4) models. This was the first theoretical evidence suggesting that the ×4 symmetry along the [110] direction observed by LEED and RHEED was due to As dimer vacancies instead of asymmetric As dimers. The surface electronic states calculated by Chadi for this two models showed also good agreement with the ARPES measurement by Larsen et al. [27]. A c(2×8) unit cell can be constructed based on either of the two (2×4) models by shifting an As dimer row along the $[\bar{1}10]$ direction by a (1×1) lattice constant, as shown in Figure 4.6(a) and (b).

Significant progress in understanding the structures of the GaAs(001) surface came after the invention of scanning tunneling microscopy (STM) in 1982. The first STM image of the (2×4)/c(2×8) surface was published in 1988 by Pashley et al [34, 35]. Their micrographs showed that the surface can be characterized by bright blocks forming

bands parallel to the $[\bar{1}10]$ direction, which corresponded to the As dimer rows. These bands were 16 Å apart in the $[110]$ direction, leading to the four-fold spots observed in the LEED pattern. The width of the bands was estimated to be 12 Å, in good agreement with the missing dimer model in Figure 4.5(a). The bright blocks had a periodicity of 8 Å in the $[\bar{1}10]$ direction, corresponding to the two-fold spacing of the (2×4) unit cell. The $c(2\times 8)$ structure, resulting from the presence of antiphase boundaries (Figure 4.6), was also found on the surface. Their images over larger areas revealed islands made up of complete unit cells and elongated along the $[\bar{1}10]$ direction. In a later STM study, Biegelsen et al. [36] confirmed Pashley's observation. They showed in addition that the (2×4) surface tended to have unit cells with two As dimers and two missing dimers after annealed longer or at slightly higher temperature.

The dispute over the detailed atomic structures for the GaAs(001) (2×4) reconstruction had just begun. Farrell and Palmstrøm [37] reported surface stoichiometry studies using RHEED. They observed that the intensity of the $2/4$ th diffraction peak varied through three different stages as the surface was annealed from 500 to 600 °C at a constant As_4 flux while the RHEED pattern maintained essentially a (2×4) symmetry. They thus subdivided the (2×4) reconstruction into α , β and γ phases in order of decreasing annealing temperature, where the β phase showed equal intensity among all the fourfold fractional peaks and the α and γ phases had a relatively weak $2/4$ th order peak. Within in the kinematic approximation, they calculated the diffraction intensities for (2×4) unit cells with different number of As dimers and compared the

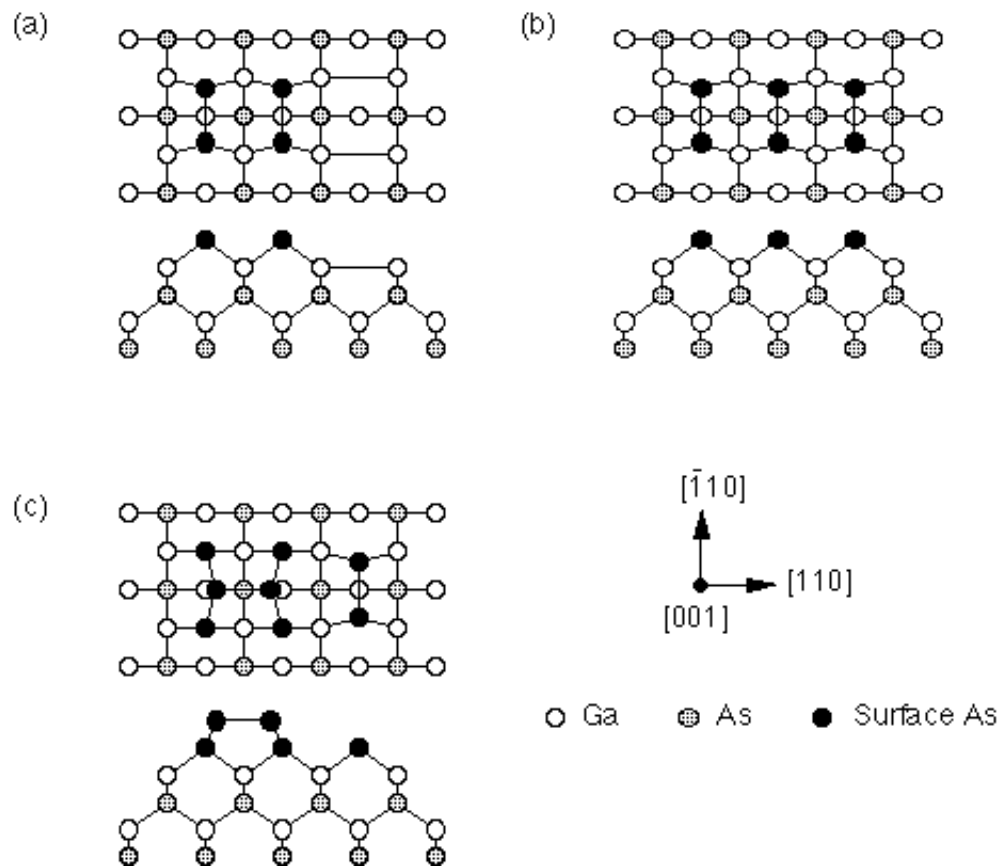


Figure 4.7 The structural models for the GaAs(001) (2×4) (a) α , (b) β and (c) γ phases proposed by Farrell and Palmström [37] based on the relative intensities of the RHEED fractional peaks.

result with the existing models [23, 33 – 35, 38]. They concluded that the α phase [Figure 4.7(a)] had two As-dimers per (2×4) unit cell in the top layer ($\theta_{\text{As}} = 0.5$ ML) with the exposed second-layer Ga atoms dimerized along the $[110]$ direction, as proposed by Harbison and Farrell [38]; the β phase [Figure 4.7(b)] had three As-dimers in the top layer ($\theta_{\text{As}} = 0.75$ ML), as proposed by Chadi [33] and by Harbison and Farrell [38]; while the γ phase was the β phase with additional As dimers adsorbed on top ($\theta_{\text{As}} > 0.75$ ML) [Figure 4.7(c)].

The first *ab initio* pseudopotential total-energy calculations applied to the GaAs(001) (2×4) surface using local density approximation were carried out by Ohno [39] and by Northrup and Froyen [40] in 1993. In both efforts the surface formation energies for various (2×4) structures were calculated as functions of the As or Ga chemical potential, which is directly related to the surface stoichiometry. Ohno's calculations showed that the threefold-coordinated Ga atoms in the two (2×4) models considered by Chadi (Figure 4.5) tended to relax significantly towards the As dimers [Figure 4.8(b) and (c)]. This relaxation broadened the surface energy gap, leading to complete charge transfer from the Ga dangling bonds to the As dangling bonds and thus a more stable structure. In addition, the formation energy for the β phase was found to be slightly lower than the two-As-dimer structure with a third dimer in the trench. Northrup and Froyen reported that under As-rich conditions a mixture of (2×4) - β and $c(4\times 4)$ phases (see section 4.3.3) would be energetically more favorable than forming a single phase of the (2×4) - γ structure proposed by Farrell and Palmstrøm [37]. Their

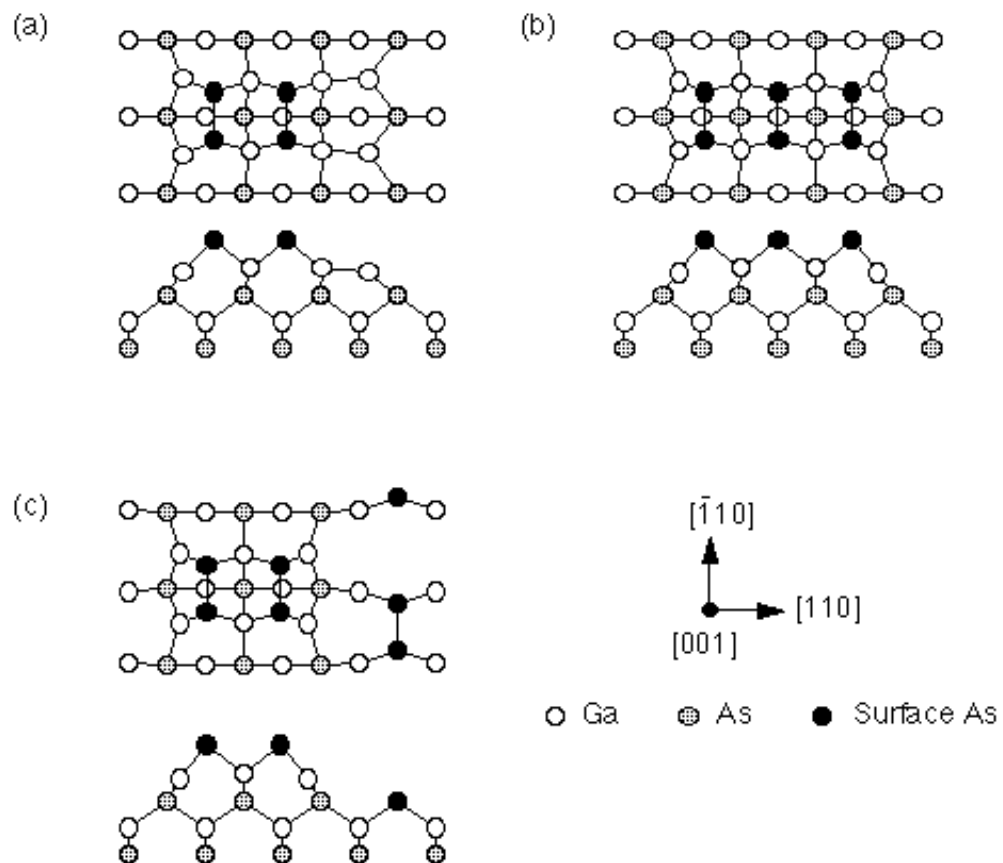


Figure 4.8 The relaxed structural models for the GaAs(001) (2x4) (a) α , (b) β and (c) β_2 phases based on theoretical calculations [39, 40, 48]. The calculations predicted severe relaxation for all the 3-fold coordinated Ga atoms, especially the atoms in the first two layers of the α structure (due to the formation of the Ga dimers).

calculations also showed that for the α phase [Figure 4.7(a)] the atoms in the first two layers were expected to undergo large lateral displacements along the [110] direction (0.4 – 1.2 Å) to accommodate the strain induced by the formation of the Ga dimers in the second layer [Figure 4.8(a)]. However, these two *ab initio* calculations reached opposite conclusions regarding the stability and the formation of the Ga dimers for the (2×4)- α phase.

In later *ab initio* calculations, Northrup and Froyen [8] included the two-As-dimer model depicted in Figure 4.5 proposed by Chadi [33], and referred to it as the β_2 phase. Since the β_2 structure can be constructed from the β phase by removing two As and two Ga atoms per (2×4) unit cell, it was expected that the difference between the surface formation energies of these two phases depended only on the sum of the As and Ga chemical potentials, which should be a constant under the condition of equilibrium with the bulk. Their calculation showed that the energy of the β_2 phase was, regardless of the value of the Ga (As) chemical potential, 0.05 eV per (1×1) unit cell lower than the β phase, contrary to Ohno's results. Based on their findings Northrup and Froyen ruled out the possibility for the β structure being a stable phase. This conclusion supported the two As dimers observed by several more recent STM studies [36, 41, 42]. In addition, they found that the presence of the lower-energy states introduced by the β_2 phase also made the chemical potential window extremely narrow for the α phase to be stable.

Further experimental evidences regarding the structures of the three different (2×4) phases were provided by Hashizume et al. [43, 44] based on STM and RHEED. Their

high-resolution STM images showed clearly that all three phases had two As dimers and two dimer vacancies in the outermost layer. However, the three phases were distinguishable in their domain sizes and depth profiles: The β phase tended to form larger domains containing no kinks; the depth measured by the STM tip in the dimer vacancy regions for the α phase was twice as deep as those for the β and γ phases; the γ phase was best characterized by the large open space (wider than 16 Å) separating the As dimer rows in the first layer. Their measured RHEED intensities of the fractional order peaks for the three phases agreed with the results reported by Farrell and Palmstrøm [37]. By comparing the measurements with dynamical RHEED calculations based on the previously proposed structures, they concluded with a unified model: The α phase should be the two-As-dimer model with Ga dimers in the second layer, as proposed by Harbison and Farrell [38] and later modified by Northrup and Froyen [40, Figure 4.8(a)]; the β phase should be the β_2 model proposed by Chadi [33, Figure 4.8(c)]; the γ phase was mainly a mixture of the β_2 structure and the $c(4\times 4)$ phase.

Most recently the detailed structure including atomic coordinates for the (2×4) - β phase was determined by Garreau et al. [45] using surface x-ray diffraction and by McCoy et al. [46] using RHEED. Theoretical values of the atomic positions were made also available based on *ab initio* pseudopotential calculations by Srivastava and Jenkins [47] and by Schmidt and Bechstedt [48, 49]. The experimental results showed excellent agreement with the theoretical calculations for the β_2 model. The As-As dimer bond length was found to be very close to the value in the bulk trivalent arsenic (2.51 Å).

Srivastava and Jenkins [47] reported that the bond length of the As dimers in the outermost layer should be about 0.1 \AA shorter than the one in the trench. They attributed the difference to the presence of both threefold and fourfold coordinated Ga atoms in the first layer.

We now apply the electron counting model to the (2×4) reconstruction, following the argument given by Pashley [7]. First, it is assumed that under the usual As-rich condition the GaAs(001) surface is terminated with As dimers, and those dimerized As atoms are the only As atoms that are threefold coordinated. This determines the $2 \times$ period of the unit cell. The introduction of each As dimer to the unit cell requires 14 valence electrons (two for the As-As dimer bond, eight for the four As-Ga bonds, and four for the two As dangling bonds). For a $(2 \times M)$ unit cell with D As dimers (Figure 4.9), if we consider only the first two surface layers, there will be $MN_{\text{Ga}} + 2DN_{\text{As}}$ valence electrons available, where $N_{\text{Ga}} = 3$ and $N_{\text{As}} = 5$ are the valencies for Ga and As. Here each Ga in the second layer contributes only half of its valence electrons to the surface. Equating the number of electrons available ($3M + 10D$) to the number of electrons needed ($14D$) per unit cell leads to $4D = 3M$. Therefore, the smallest unit cell satisfying the electron counting model is a (2×4) with 3 As dimers. Notice that in the above argument the use of the electron counting model takes place when we count two electrons for each As dangling bond and exclude all electrons from filling Ga dangling bonds (associated with threefold-coordinated Ga atoms). The immediate result from this

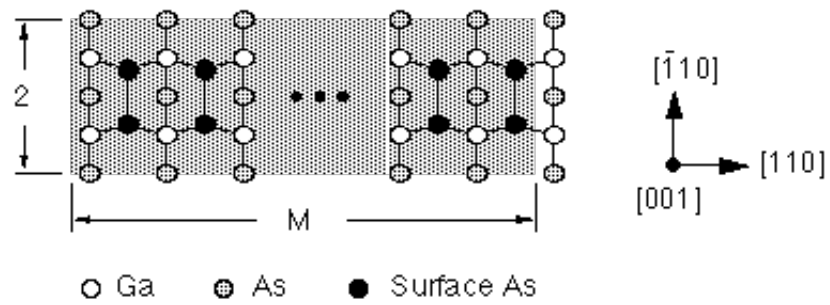


Figure 4.9 The GaAs(001) ($2 \times M$) unit cell containing D As dimers and $(M - D)$ dimer vacancies.

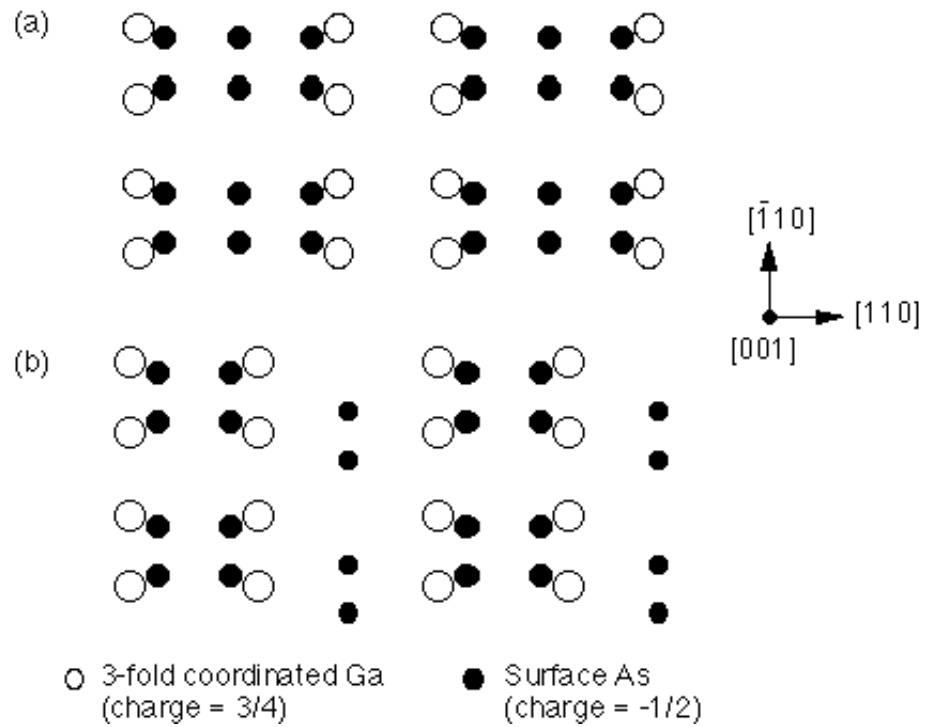


Figure 4.10 The charge distributions based on the electron counting model for the GaAs(001) (2×4) (a) β and (b) β_2 structures [8].

simple model is that it predicts the presence of As dimer vacancies. In other words, in order to stay semiconducting, the As-rich GaAs(001) surface has to develop a large unit cell to allow the formation of dimer vacancies, in contrast to the Si(001) and Ge(001) surfaces, where the same result is achieved by forming asymmetric Si and Ge dimers (Peierls distortion) in relatively small, (2×1) unit cells.

The above discussion showed that both β and β_2 structures are possible candidates for the (2×4) reconstruction. If we include Ga-Ga dimers in constructing the surface unit cell, it can be shown that the α model also satisfies the electron counting rule. To further discriminate energetically between the β and β_2 models, Northrup and Froyen [8] suggested that the electrostatic interactions between the cations and anions must be considered. In bulk GaAs, each Ga-As tetrahedral bond has 3/4 of an electron contributed from Ga and 5/4 of an electron contributed from As. On the (001) surface, however, each threefold-coordinated Ga atom (whose three nearest neighbors are all As for the β and β_2 structures) carries a charge of $3 - 3 \times 3/4 = +3/4$, and each threefold-coordinated (or dimerized) As atom carries a charge of $5 - 2 \times 5/4 - 3 = -1/2$ (the -3 accounts for the one electron in the dimer bond and the two in the dangling bond). The total charge of the (2×4) unit cell is zero. This charge transfer is one of the ways by which the reconstruction produces a semiconducting surface, as mentioned earlier. Figure 4.10 shows the charge distributions for the β and β_2 structures based on the above assignment. Northrup and Froyen have shown that the Madelung energy $E = 1/2 \sum q_i q_j / |\mathbf{R}_i - \mathbf{R}_j|$, which estimates the electrostatic energy of an assembly of ions with

locations R_i and charges q_i , is 0.05 eV per (1×1) unit cell lower for the β_2 structure than that for the β structure, in good agreement with their *ab initio* calculation. They eventually demonstrated that electrostatic interactions in general played an important role in determining the lowest-energy structures for compound semiconductor surfaces.

The electronic structures of the β_2 surface revealed by the *ab initio* calculations [47, 48] are actually far more complicated than what was described above by the simple electron counting model. Since atoms on a GaAs or Si surface have different coordination numbers and bonding geometry from those in their bulk, the surface dimer bonds, dangling bonds and even the bonds within a few layers below the surface are expected to have, to a certain extent, natures that differ from the bulk sp^3 orbitals. Depending on the bond angles around each surface atom, the hybrid orbitals on the surface, whose formation are based on new combinations of the atomic $|s\rangle$, $|p_x\rangle$, $|p_y\rangle$ and $|p_z\rangle$ states, can be much more s- or p-like. This so-called dehybridization process associated with semiconductor surface reconstructions was first explained by Harrison [5, 10, 50]. The *ab initio* calculations by Schmidt and Bechstedt [48] showed that for the β_2 phase the As dimers in the first and the third layers were bonded by the σ combination of the dehybridized As in-plane p orbitals as well as by the π combination of the dehybridized As dangling (p_z) orbitals (i.e., the As dangling bonds are involved in the formation of the As dimer bonds). This electronic structure is close to what was predicted by Kress et al. [51] for the diamond (001) (2×1) reconstruction, where the carbon dimers tended to form C=C double bonds. Another noticeable feature for the β_2

phase is the inward displacement of the threefold-coordinated Ga atoms towards the As dimer block [47, 48], which leads to a planar, sp^2 -like bonding geometry for these Ga atoms.

In addition to the contribution of the As and Ga dangling bonds, surface states of the GaAs(001) are also found to be associated with the surface defects. In a systematic study using STM and scanning tunneling spectroscopy (STS) by Pashley *et al.* [41, 52, 53], Si doped (n-type) GaAs layers of various thickness and doping levels were grown on undoped buffer layers. It was found that kinks in the dimer rows [Figure 4.11(a)] on the (2×4) surface act as acceptors. The kink density increased in proportion to the doping level and doped-layer thickness. As a result of the electron transfer from the Si donor states to the surface acceptor states associated with the kink sites, a space charge (or depletion) layer formed near the surface region. Their STS spectra measured on top of the As dimers revealed further evidence that the Fermi level was pinned at the midgap (i.e., half way between the surface valence and conduction band edges), which implies upward band bending at the surface [Figure 4.11(b)]. Interestingly, for p-type GaAs(001) [53], no defects associated with surface donor states were observed. At high p-doping level, the Fermi level was measured to be slightly above the valence band maximum, instead of being pinned at the midgap.

To sum up for the GaAs(001) $(2\times 4)/c(2\times 8)$ reconstruction, three sub-phases labeled α , β and γ (in order of increasing As coverage) have been observed based on the relative intensities of the RHEED fractional peaks. The currently accepted structural models are

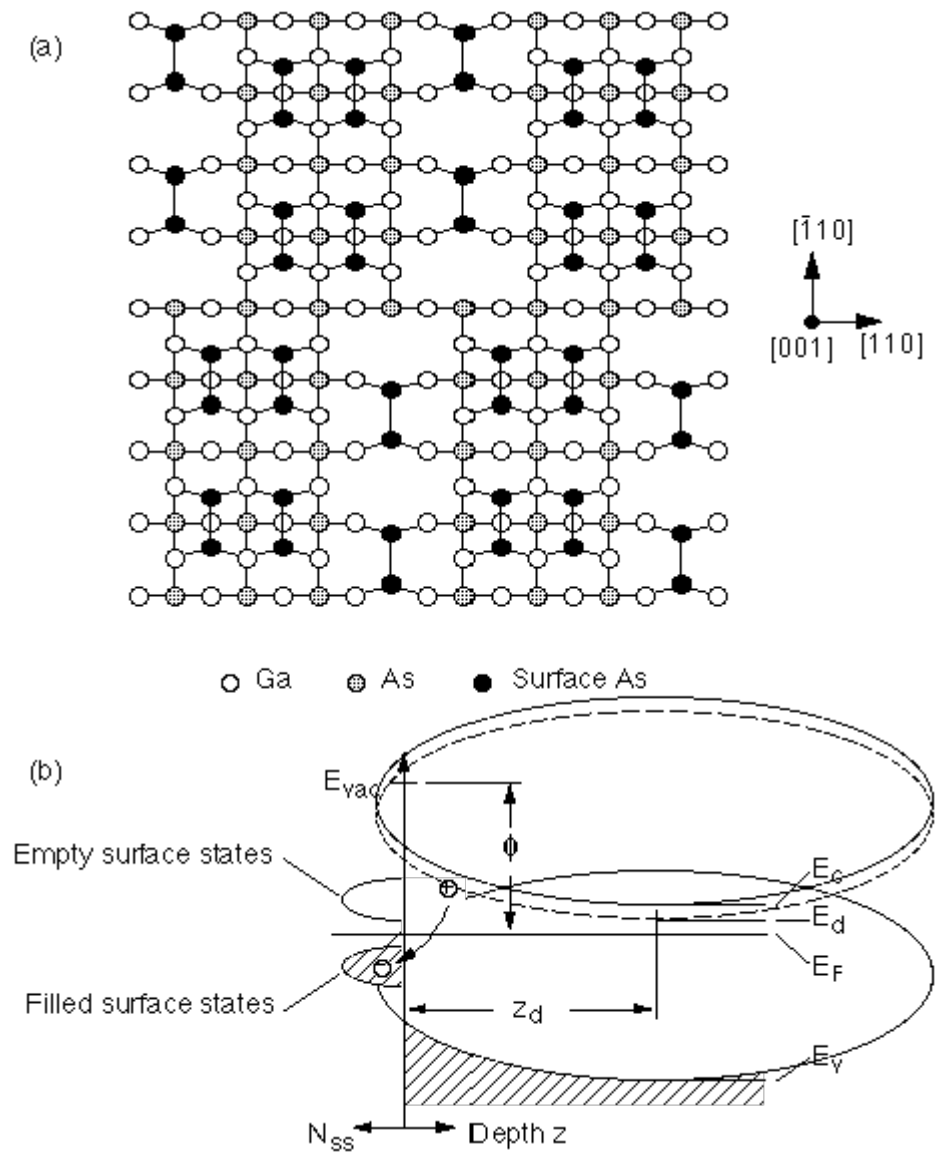


Figure 4.11 (a) The structural model of the GaAs(001) (2x4) β_2 surface with kinks in the As dimer rows. (b) The energy-level diagram near the GaAs(001) surface showing the band bending induced by doping and surface states. E_c and E_v are the conduction and valence band edges. E_d and E_F are the donor level and the Fermi level. ϕ and z_d are the work function and the thickness of the depletion layer.

as follows. The β phase is the most stable phase, which can be described by the β_2 structure [Figure 4.8(c)] proposed by Chadi. The α phase is either the relaxed two-As-dimer model having two Ga dimers in the second layer [Figure 4.8(a)] due to Northrup and Froyen (no direct experimental evidence reported for this structure so far), or just a disordered β_2 phase. The γ phase is a mixture of the β_2 and $c(4\times 4)$ phases.

4.3.2 $(4\times 2)/c(8\times 2)$

The (4×2) reconstruction is the Ga-rich counterpart of the (2×4) phase. However, it has drawn much less attention than the (2×4) surface has. STM images by Resch-Esser *et al.* [54] showed that, unlike the (2×4) As-rich surface, the (4×2) surface was relatively smooth, containing no kinks over terraces of large areas.

Structural models for the (4×2) surface were proposed primarily based on STM by analogies made with the better-known (2×4) surface, but the lack of direct understanding of the electronic structures for the Ga-rich surface has led to controversial conclusions. Using HREEL Frankel *et al.* [23] proposed a (4×2) model (later called the $(4\times 2)\beta$ phase) with three Ga dimers and one dimer vacancy per unit cell in the first layer [Figure 4.12(a)]. The first STM image of the (4×2) surface was reported by Biegelsen *et al.* [36]. The surface was characterized by bright rows parallel to the $[110]$ direction with a period of 16 \AA in the $[\bar{1}10]$ direction. The width of the bright rows was consistent with two dimers per unit cell. They thus attributed the bright feature to the Ga dimers and proposed a model later recognized as the $(4\times 2)\beta_2$ structure [Figure 4.12(b)], which is

similar to the $(2\times 4)\beta_2$ model. *Ab initio* calculations by Northrup and Froyen [40] showed that the $(4\times 2)\beta_2$ structure is energetically more stable than the $(4\times 2)\beta$ structure, as is the case between the $(2\times 4)\beta$ and $(2\times 4)\beta_2$ models.

High-resolution STM images reported by Skala et al. [55] further revealed that each bright row consisted of two separate straight lines, and the corrugation maxima in each line showed a $\times 1$ period along the $[110]$ direction. In addition, their images resolved four faint spots per (4×2) unit cell between the bright rows which exhibited a $\times 2$ period along the $[110]$ direction. They concluded that the $\times 1$ corrugations were due to the As dangling bonds and the bright rows corresponded to the dimer rows composed of one As dimer per (4×2) unit cell [Figure 4.12(c)]. The faint $\times 2$ spots were due to the Ga dimers in the second layer. However, this model was later challenged by Xue et al. [56] based on STM and *ab initio* calculations [57]. Their filled-state STM images for the (4×2) reconstruction were essentially identical to those reported by Skala et al., but they found the most plausible model to be the β_2 structure [Figure 4.12(b)]. They attributed the faint protrusions to the two Ga dimers per unit cell in the outermost layer and the bright protrusions to the As dangling bonds associated with the threefold-coordinated As atoms in the second layer. Therefore, the bright rows corresponded to the trench areas between the Ga dimer rows. Their calculations indicated that for each Ga dimer the charge density maximum occurred at the middle of the dimer bond. For the β_2 model, this suggested that the locations of the bright spots and the faint spots should be completely out of phase with respect to each other along the $[110]$ direction, which was

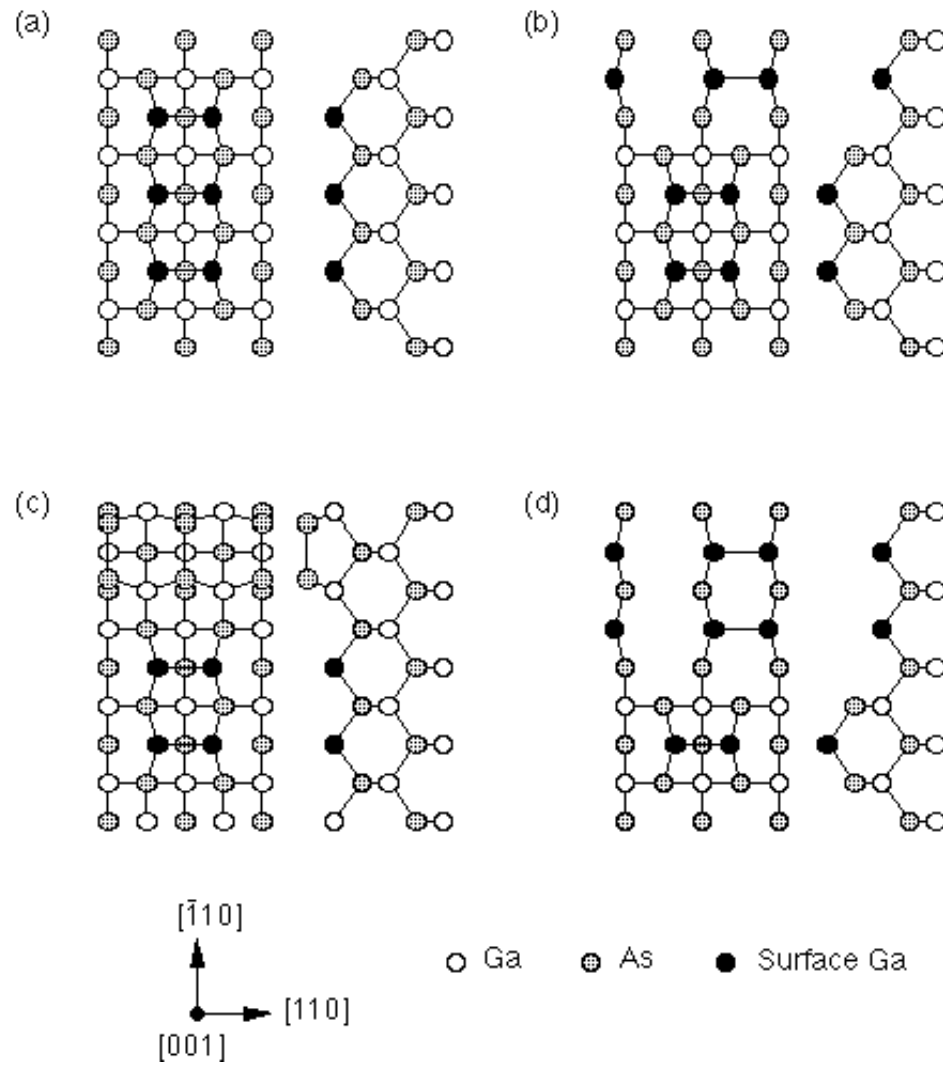


Figure 4.12 The structural models proposed for the GaAs(001) (4×2) reconstruction by (a) Frankel et al. (β) [23], (b) Biegelsen et al. (β2) [36], (c) Skala et al. [55] and (d) Moriarty et al. [59].

consistent with the STM images. Nevertheless, their argument also suggested that there should be only one faint spot every $\times 2$ period along the [110] direction, which failed to explain the two faint spots every $\times 2$ period revealed by their STM images.

Most recently Cerda *et al.* [58] evaluated the β , $\beta 2$ models and the one proposed by Skala using LEED I-V analysis. They found that the β structure yielded an agreement with their data significantly better than the other two models. Based on STM Moriarty *et al.* [59] proposed another (4×2) model [Figure 4.12(d)] with one Ga dimer in the first layer and two more in the third layer in the trench areas.

4.3.3 $c(4\times 4)$

The GaAs(001) $c(4\times 4)$ has been known as the As-saturated surface. Early PES studies by Larsen *et al.* [60] presented evidence that the As coverage of the $c(4\times 4)$ surface exceeded one ML and the reconstruction was due to the chemisorbed, excess As layer. In a study using temperature programmed desorption (TPD) and RHEED Sasaoka *et al.* [61] measured the As coverage of this surface to range between 1.28 and 1.61 ML. The STM images reported by Biegelsen *et al.* [36] revealed that the $c(4\times 4)$ symmetry was due to the arrangement of dimer blocks consisting of three As dimers. They proposed a structural model [Figure 4.13(a)] corresponding to an As coverage of 1.75 ML. Theoretical calculations by Northrup and Froyen [40] confirmed that under the most As-rich condition this $c(4\times 4)$ structure is energetically more stable than the $\beta 2(2\times 4)$ phase. The detailed bonding geometry was probed by surface x-ray diffraction

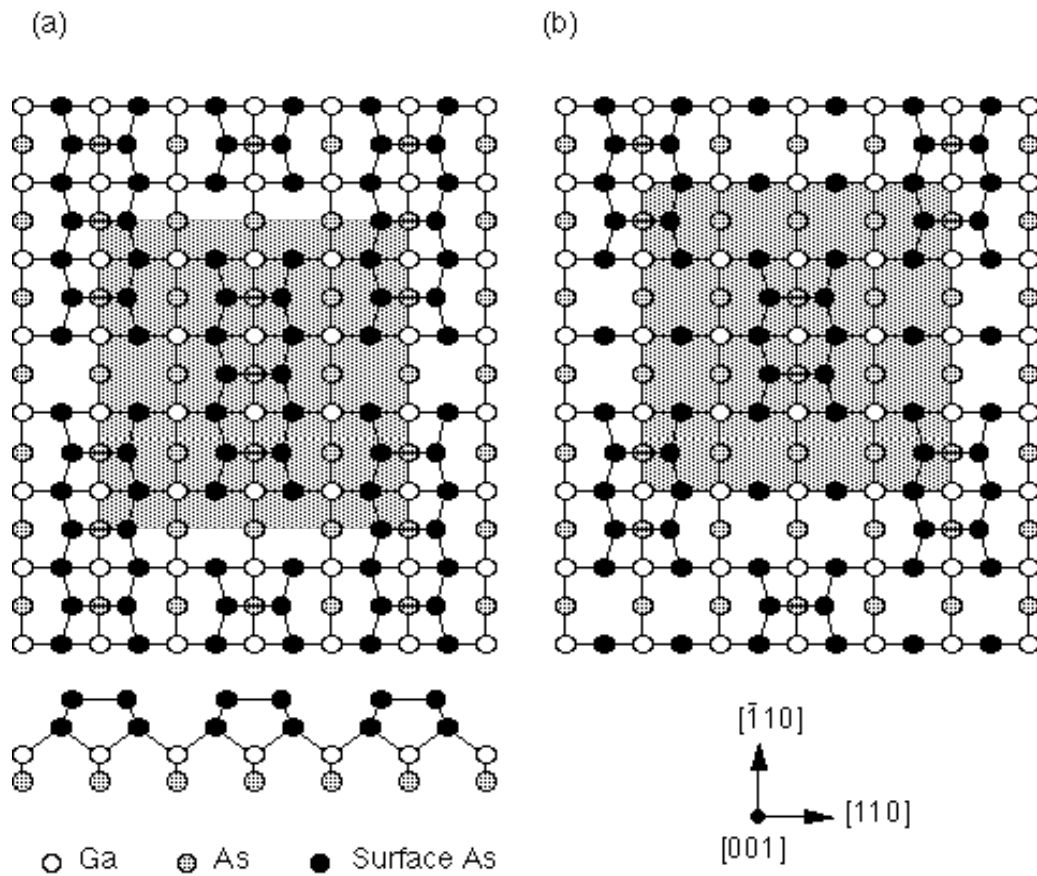


Figure 4.13 The structural models proposed for the GaAs(001) c(4x4) reconstruction with dimer blocks containing (a) 3 As dimers ($\Theta_{\text{as}} = 1.75$ ML) and (b) 2 As dimers ($\Theta_{\text{as}} = 1.5$ ML) [36, 62 - 64].

[62 - 64] and secondary-ion mass spectrometry (SIMS) [65]. The surface x-ray diffraction studies showed that the $c(4\times 4)$ reconstruction contained a mixture of dimer blocks with two [Figure 4.13(b)] and three As dimers, which accounted for the variation of the As coverage. It can be shown that the model with three As dimers satisfies the electron counting rule. However, the model with two (or even one [63]) As dimer per dimer block does not seem to be a stable structure due to the presence of twofold-coordinated As atoms in the second layer. More recent STM investigation by Avery *et al.* [66] concluded that the wide coverage range of the $c(4\times 4)$ surface was due to a varying number of As atoms missing from the six-atom dimer blocks, contrary to the model based on the x-ray diffraction studies.

4.3.4 ($n\times 6$)

A number of intermediate phases exhibiting ($n\times 6$) symmetries with $n = 1, 2, 3$ and 6 [36, 67 - 70] have been observed during the transition between the As-rich (2×4) and Ga-rich (4×2) reconstructions. The STM images of these surfaces were characterized by bright rows parallel to the $[\bar{1}10]$ direction separated by a period of 24 \AA in the $[110]$ direction, which accounts for the $\times 6$ symmetry revealed by LEED. The structures of these reconstructions are still under debate and are expected to be complicated due to the relatively large unit cell.

4.4 Clean surface preparation

High-quality GaAs(001) surfaces for *in situ* UHV studies are usually prepared by MBE growth [71], which involves thermally desorbing native oxides at > 580 °C in an As ambient, and the subsequent growth of an epitaxial layer of typically 0.2 to 2 μm at a temperature between 550 to 650 °C. The growth is stopped by closing the Ga shutter and followed by annealing the substrate (for about 5 to 10 minutes) in an As flux to allow the surface roughness to decrease and the surface reconstruction to recover [67]. Different reconstructions can be achieved by varying the annealing temperature and the As partial pressure (the phase diagram of the GaAs(001) surface structures can be found in Ref. 72). The growth mode, growth rate and surface symmetry in the above process are usually monitored by RHEED. The prepared surface is then ready for *in situ* characterization. Studies of this type require the samples to be transferable under UHV condition between the III-V MBE growth facility and the chamber equipped with surface analysis instruments.

For the situation where *in situ* measurements are unavailable, it has been demonstrated [73] that an amorphous As layer can be used to protect the GaAs surface from contamination during sample transfer through air. The growth of the As cap can take place after the formation of the (2×4) reconstruction is confirmed by RHEED at the end of the epilayer growth process. Due to the low sticking coefficient of As to itself, the GaAs substrate has to be held at more than 30 °C below room temperature to allow the As to condense [69, 73, 74]. To achieve a cap thickness of 1000 Å, which is necessary for preventing any contamination reaching the As-GaAs interface during ambient

storage of a few weeks to a few months, it usually takes several hours for the As cap to grow even with a LN₂-cooled sample manipulator [75]. Resch-Esser *et al.* [76] also reported that the use of As₂, instead of As₄, to grow the protective layer is crucial for preparing high-quality GaAs(001) surfaces, especially for the c(4×4) reconstruction.

Once the As-capped GaAs(001) substrate is under UHV again, the clean, reconstructed surface can be recovered by thermally desorbing the amorphous As layer. Prior to the removal of the As layer, the sample should be degassed at 250 °C (this removes the As₂O₃ layer at the surface [77]) to minimize the GaAs surface contamination that may happen during the decapping process. The As desorption occurs at 300 – 350 °C. Further annealing at 350 °C results in a c(4×4) LEED pattern, indicating an As-saturated surface. The (2×4) reconstruction can be obtained over a wide temperature range between 380 and 450 °C. Annealing at even higher temperatures leads to the (n×6) reconstructions and finally to the (4×2) Ga-rich surface. Several studies [54, 59, 76, 78] using STM and LEED have already shown that the quality of the decapped GaAs(001) (2×4) surface can be as good as those measured *in situ*. One drawback of this technique is that the structural transitions described above at various temperatures are essentially irreversible, and thus the substrates generally can not be used repeatedly, without the use of an As source.

Chapter 5 High-Resolution Structural Analysis of Sb-Terminated GaAs(001)-(2x4) Surface

5.1 Introduction

The precise locations of Sb atoms for the GaAs(001):Sb-(2 × 4) surface were measured by the x-ray standing wave (XSW) technique. The XSW results are consistent with symmetric Sb dimers, whose formation has recently been predicted by six competing models. The (004) and (022) XSW analysis determined the Sb dimer height and bond length to be 1.72 Å and 2.84 Å, respectively. The Sb coverage of the (2 × 4) reconstruction was measured by Rutherford backscattering to be 0.48 monolayers (ML). This coverage agrees with the three proposed structural models that have two Sb dimers per (2x4) unit cell and disagrees with the models that propose one or three Sb dimers. Finally, a (111) XSW measurement, which tested for lateral displacement of the Sb dimers in the [110] direction, was used to discriminate among the remaining three models.

5.2 Background information

The atomic arrangement at compound semiconductor surfaces and interfaces is closely related to the initial growth of the corresponding strained layer heterostructures. Such structures have potentially broad applications in telecommunication and high-speed electronic components. Scientifically, there has been a growing interest in the (001) III-V surfaces, arising from the abundant, strongly coverage-dependent surface structures. For GaAs(001), for instance, extensive investigations have been carried out, and the surface has been reported to exhibit various phases ranging from the most As-rich c(4 × 4) to the most Ga-rich (4 × 6) reconstruction, as reviewed in Chapter 4.

Recently, similar structures were observed by Madea *et al.* [1] on a Sb-terminated GaAs(001) surface. Their reflection high-energy electron diffraction (RHEED) study revealed a number of different phases, including a (2×4) pattern for annealing temperatures between 440° and 560° C. Their core-level photoelectron spectroscopy measurements suggested that this (2×4) reconstruction was formed by the surface Sb bonding to the underlying Ga after the desorption of As at the Sb/GaAs interface. Later, Esser *et al.* [2] performed a reflectance anisotropy spectroscopy (RAS) study combined with total-energy and tight-binding calculations. Their calculations rendered a Sb dimer bond length of 2.86 - 2.87 Å, and the RAS result was used in discriminating among several possible (2×4) models. Meanwhile, Moriarty *et al.* [3] reported a scanning tunneling microscopy (STM) investigation on a number of Sb-induced reconstructions on GaAs(001). Their study showed considerable differences in the structure and ordering of the Sb- and As-terminated GaAs(001) - (2×4) surfaces.

The bonding geometry of the Sb/GaAs(001) (2×4) surface was first addressed quantitatively by Sugiyama *et al.* [4] using back reflection x-ray standing waves (BRXSW). By monitoring the Sb 3d photoelectron yields through the GaAs (111) and $(\bar{1}\bar{1}\bar{1})$ Bragg reflections, they reported a Sb dimer height of 1.81 Å and a dimer bond length of 2.95 Å. These values are notably larger than other related measurements [5 - 7] and theoretical calculations [2] of Sb dimers on semiconductor surfaces.

Recently the detailed structural and electronic properties of this surface were evaluated theoretically by G.P. Srivastava and S.J. Jenkins [8] and by Schmidt and Bechstedt [9, 10] using first-principles pseudopotential calculations. They reported a Sb-Sb dimer bond length of 2.79 Å and 2.86 Å, respectively.

Herein, we report a conventional x-ray standing wave study of the GaAs(001):Sb- (2×4) surface. By measuring the Sb L fluorescence yields for the bulk GaAs (004) and

(022) reflections at a conventional Bragg geometry, we have a more direct measure of the dimer height and dimer bond length than that given by the $\{111\}$ BRXSW measurements. Our values are consequently a more accurate test for the theoretical calculations. In addition, we used a (111) XSW measurement (in combination with the (004) and (022)) to look for a lateral surface relaxation that was predicted in one of the surface models proposed by Esser *et al.* [2] and favored by their RAS results. We also determined the Sb coverage of the (2×4) surface using Rutherford backscattering spectrometry (RBS) and compared these results with the previously proposed (2×4) models, which vary in Sb coverage from 0.25 to 0.75 ML. The final synthesis of our measurements and analysis will be shown to be consistent with one and only one of the six competing models for this surface structure.

5.3 Surface preparation

The GaAs(001) substrate was prepared prior to the XSW measurement with a 1- μ m-thick homoepitaxial layer. The surface was then protected by an amorphous As layer for sample transfer in air. The XSW experiments were conducted at beamline X15A of the National Synchrotron Light Source at Brookhaven National Laboratory. After introduction into the MBE system, the GaAs substrate was first degassed at 250°C for about 45 minutes. The As protective layer was then removed by thermal desorption at 350°C, and a $c(4 \times 4)$ LEED pattern was observed [Figure 5.1(a)]. The As-rich $(2 \times 4)/c(2 \times 8)$ reconstructed surface was attained by annealing the sample further at 400 - 450°C [Figure 5.2(a)]. Sb was deposited from a Knudsen cell held at 420°C. The deposition rate was calibrated to be ~ 0.7 ML/min by measuring the Sb MNN Auger peak intensities from a Sb-terminated Si(001) surface which is known to have a saturated coverage at 0.8 ML [11]. To prepare the Sb-terminated GaAs(001) surface, ~ 4 ML of Sb was deposited

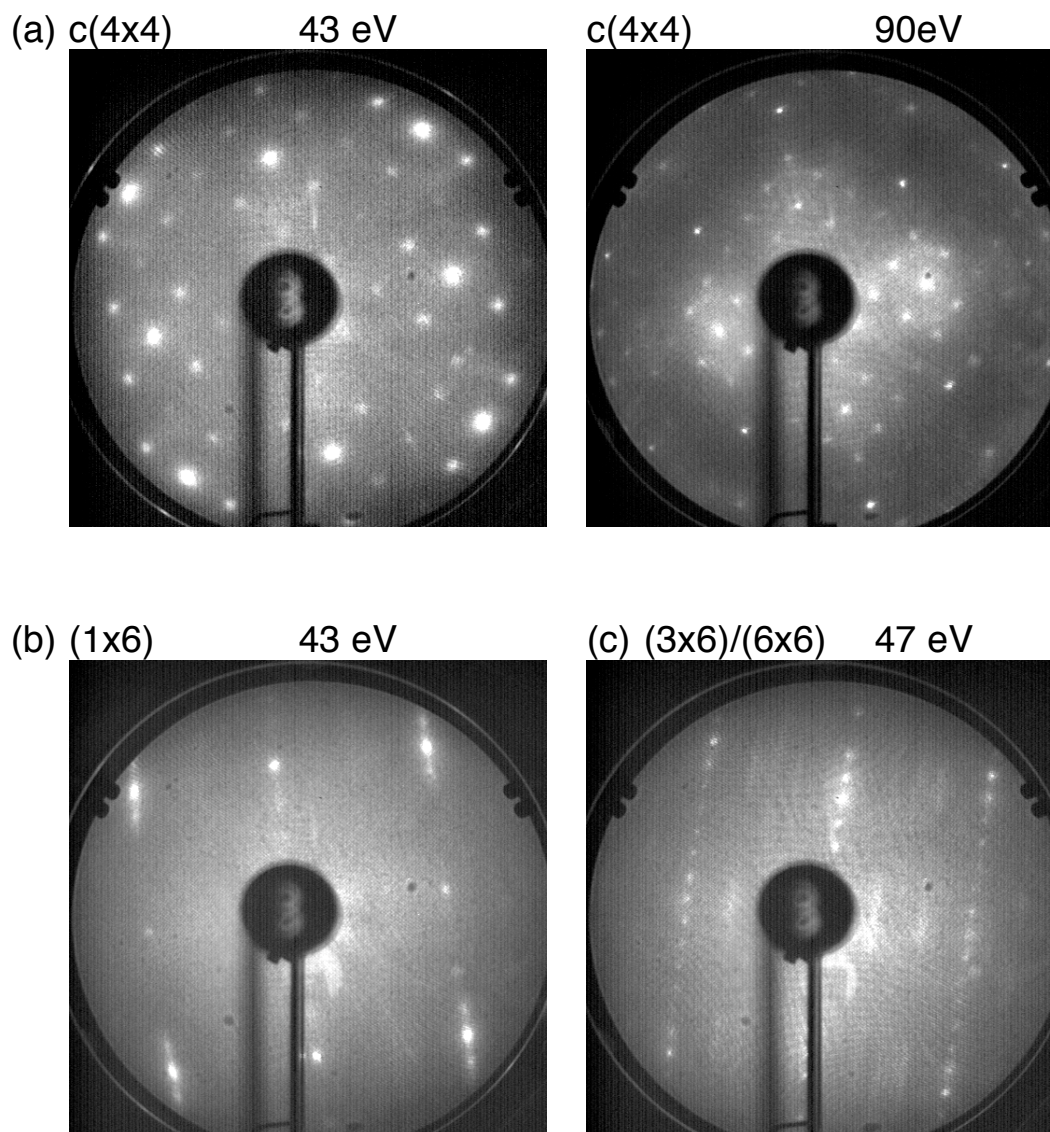
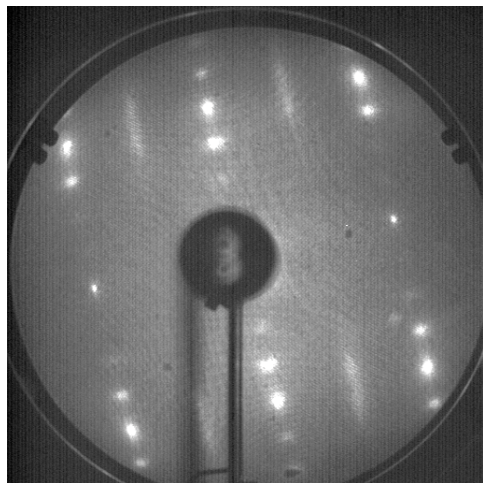
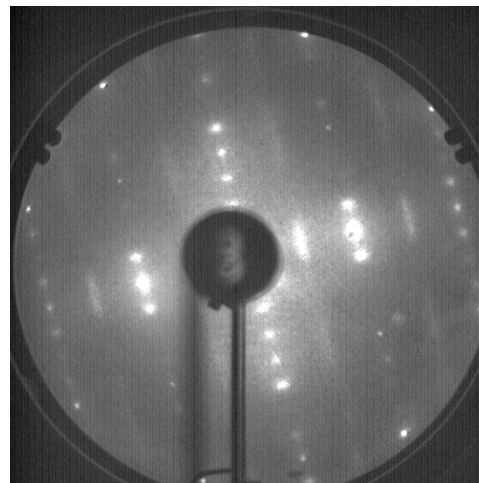


Figure 5.1 Some of the LEED patterns commonly observed on the clean GaAs(001) surface prepared by thermal annealing of an As capped substrate: (a) c(4x4), (b) (1x6) and (c) (3x6)/(6x6).

(a) (2x4) clean GaAs(001)
43 eV



87 eV



(b) (2x4) Sb stabilized GaAs(001)
42 eV

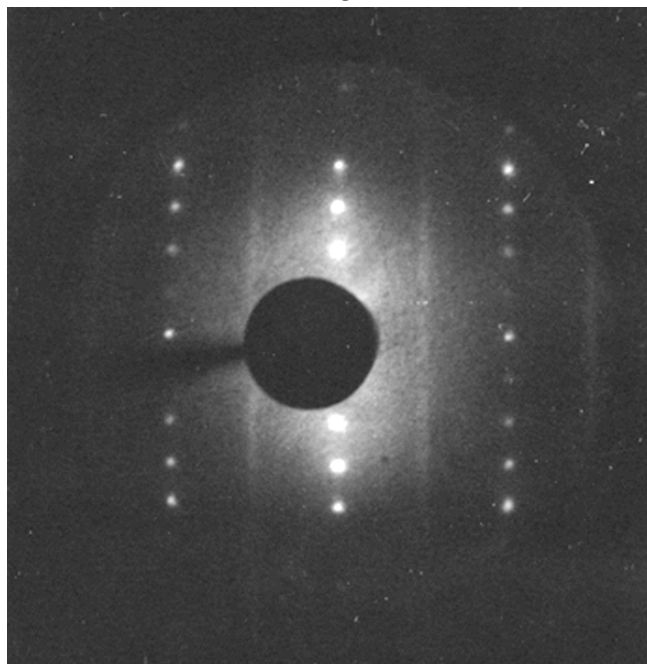


Figure 5.2 Comparison between the (a) As- and (b) Sb-stabilized (2x4) LEED patterns. The Sb-stabilized (2x4) surface was annealed at 505 °C.

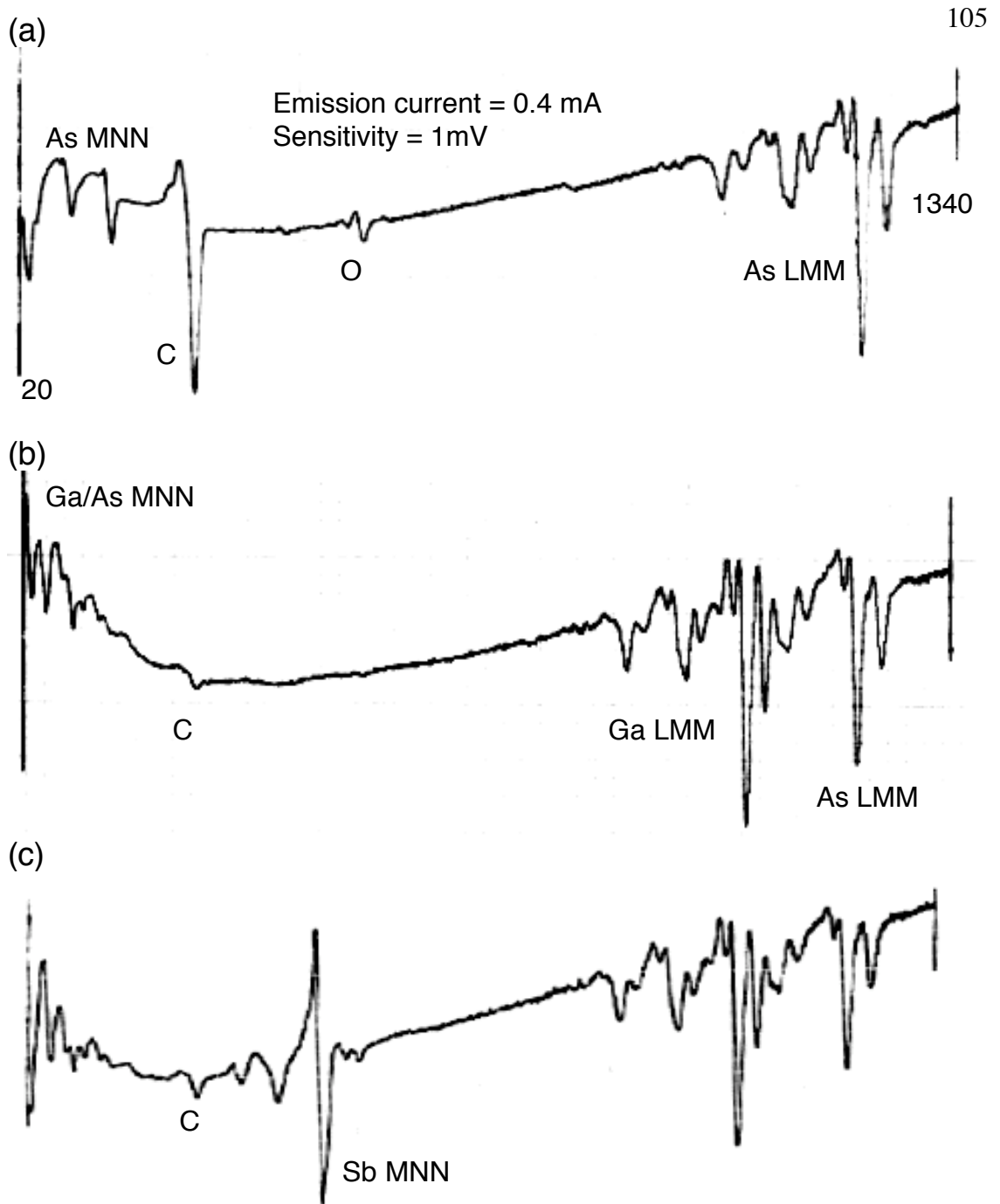


Figure 5.3 Auger spectra of the GaAs(001) surface (a) before and (b) after the As protective layer was thermally desorbed and (c) after the adsorption of about 0.8 ML of Sb.

with the substrate held at room temperature (RT), followed by a 20-minute anneal at 505°C. The LEED pattern showed a clear $(2 \times 4)/c(2 \times 8)$ reconstruction with streaky half-order spots along the [110] direction [Figure 5.2(b)]. The four-fold spots were much sharper than those from the As-rich clean surface, indicating a more highly ordered surface had developed upon the adsorption of Sb. This observation is consistent with the significantly lower density of kink sites on the Sb-terminated surface reported by STM [3]. Figure 5.1 shows some of the LEED patterns commonly observed on the clean GaAs(001) surface prepared from an As capped substrate. Figure 5.2 is a comparison between the As- and Sb-stabilized (2×4) LEED patterns. In Figure 5.3 we showed the Auger spectra recorded during the clean surface preparation and after the Sb adsorption.

5.4 XSW results and discussions

X-ray standing wave measurements were then used to triangulate the Sb atomic positions relative to the GaAs lattice. With an incident photon energy E_γ above the Sb L_{III} edge, the induced modulation of the Sb L fluorescence yield is monitored by a solid-state Si(Li) detector. To locate the Sb positions, we employed the GaAs (004) reflection at $E_\gamma = 7.60$ keV to directly measure the Sb dimer height (h'), and the (022) reflection at $E_\gamma = 7.00$ keV to deduce the dimer bond length L .

5.4.1 Sb-Sb dimer bond length and dimer height

Figure. 5.4(a) and (b) show the results of the (004) and (022) measurements. Based on χ^2 fits of Eq. (2.72) to the data, we determined the coherent fractions and the coherent positions to be $f_{004} = 0.68 \pm 0.02$, $P_{004} = 1.22 \pm 0.01$, $f_{022} = 0.45 \pm 0.01$ and $P_{022} = 1.10 \pm 0.01$.

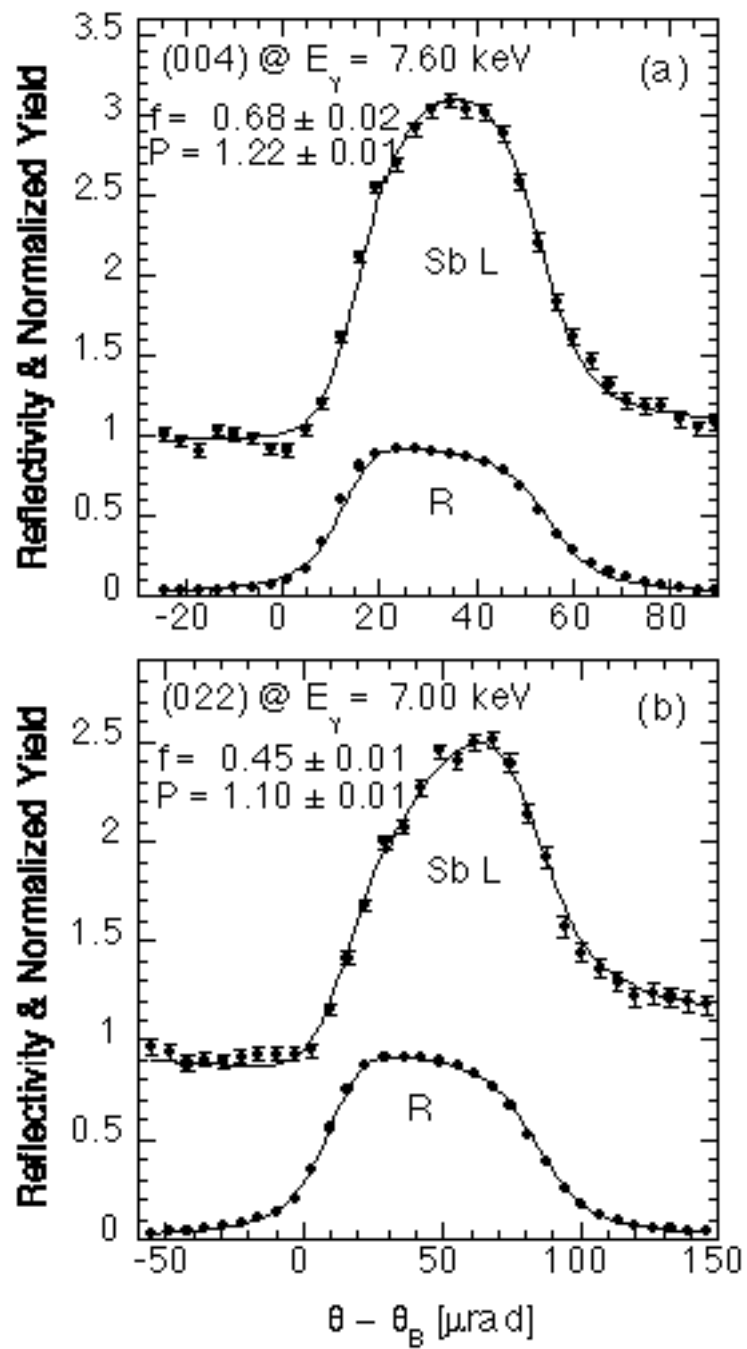


Figure 5.4 The GaAs(001):Sb-(2×4) experimental XSW data (filled circles) and the best fits (solid lines) for the normalized Sb L fluorescence yields and the reflectivities R versus the incident angle θ for the GaAs (a) (004) and (b) the (022) Bragg reflections.

If a symmetric Sb dimer model is assumed, the measured (004) coherent position can be directly related to the dimer height [Figure 5.5(a)] by

$$h' = P_{004} d_{004} \quad , \quad (5.1)$$

which locates the Sb dimer at $h' = 1.72 \pm 0.02 \text{ \AA}$ above the last bulk-extrapolated GaAs (004) atomic plane. When compared with the height of Sb dimers formed on a Si(001) surface, which has been measured previously by XSW [5] ($h' = 1.64 \text{ \AA}$) and by ion channeling [12] ($h' = 1.63 \text{ \AA}$), our result shows that h' is about 0.09 \AA higher for Sb on GaAs(001). This is consistent with the fact that Ga has a 0.09 \AA larger covalent radius ($r_{\text{Ga}} = 1.26 \text{ \AA}$, $r_{\text{Si}} = 1.17 \text{ \AA}$). In comparison, the determined Sb dimer height on GaAs(001) reported by Sugiyama *et al.* using BRXSW [4] ($h' = 1.81 \pm 0.02 \text{ \AA}$) is 5% larger than our measured value.

Notice that the measured coherent positions satisfy the following relationship:

$$P_{022} = (1 + P_{004})/2 \quad . \quad (5.2)$$

This meets the requirement for adatoms occupying two-fold symmetry related positions around the bridge site on a GaAs(001) surface [Figure 5.5(b)]. In addition, the fact that the measured coherent fraction f_{022} is significantly lower than f_{004} is also consistent with the Sb symmetric dimer model, since the positions of the dimerized Sb atoms in such a model are equivalent along the [004] direction [Figure 5.5(a)] but inequivalent along the [022] [Figure 5.5(b)]. To extract the Sb-Sb bond length L from the two measurements,

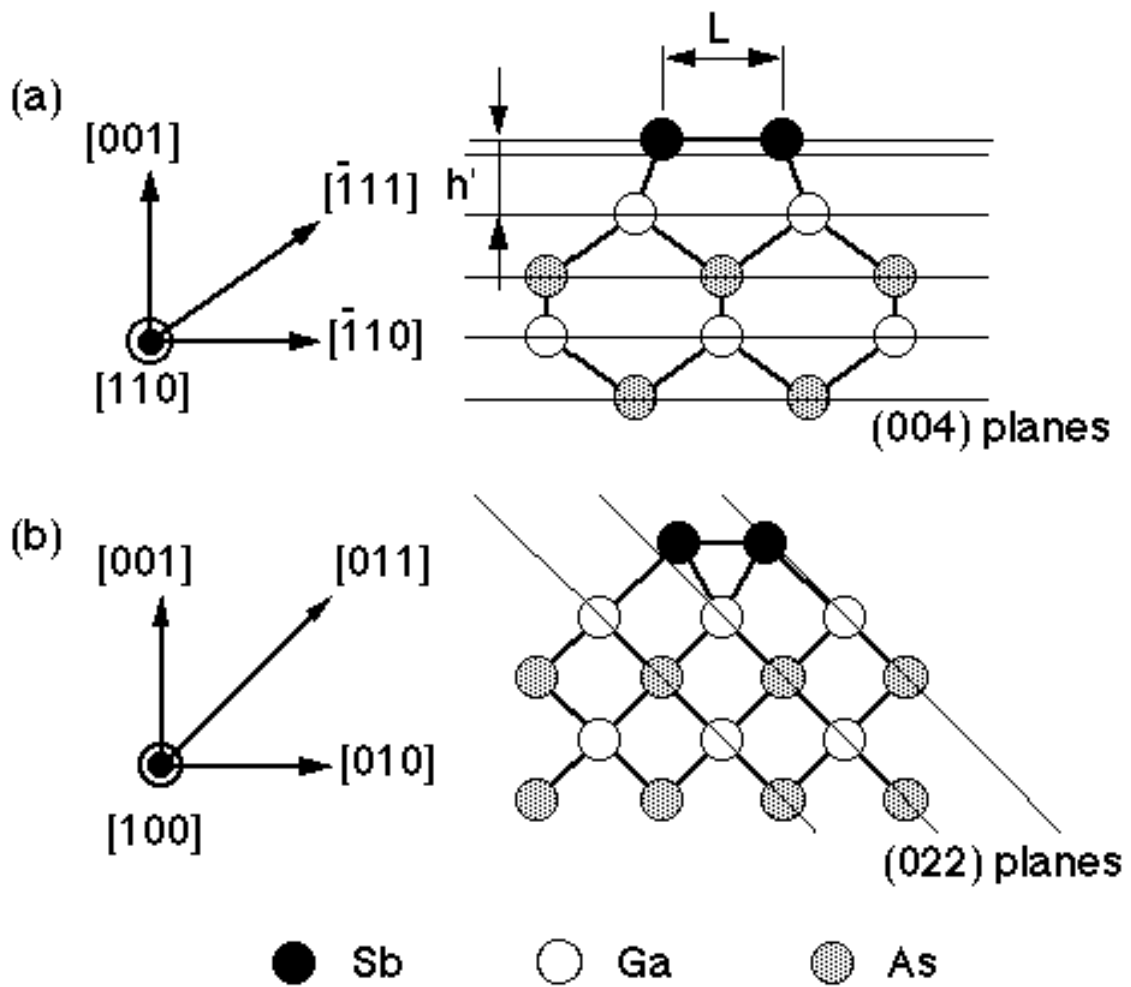


Figure 5.5 The (a) $[110]$ and (b) $[100]$ projections of an Sb-terminated GaAs(001) surface. The solid lines are the atomic planes for the different Bragg reflections. L is the Sb-Sb bond length. h' is the height of the Sb dimer relative to the unrelaxed GaAs(001) surface Ga planes.

the coherent fraction is decomposed into a product of three factors based on the convolution theorem [13]

$$f_{\mathbf{H}} = C a_{\mathbf{H}} D_{\mathbf{H}} , \quad (5.3)$$

where C is the fraction of adatoms at ordered positions, $D_{\mathbf{H}}$ is the adatom Debye-Waller factor, and $a_{\mathbf{H}}$ is the geometrical factor, accounting for the reduction of the coherent fraction due to multiple adatom positions along the \mathbf{H} direction. As illustrated in Figure 5.5, it can be shown that $a_{004} = 1$ and $a_{022} = |\cos(\pi L/2d_{022})|$. By combining the (004) and (022) results, the dimer bond length L can be determined as

$$L = \frac{2d_{022}}{\pi} \cos^{-1} \left(-\frac{f_{022}D_{004}}{f_{004}D_{022}} \right) . \quad (5.4)$$

At this point, we will make the simplifying approximation that the Sb adatoms have the same RT Debye-Waller B factor as reported for bulk GaAs ($B = 0.59 \text{ \AA}^2$) [14], and thus $D_{\mathbf{H}} = \exp(-B/2d_{\mathbf{H}}^2)$ will be estimated as $D_{004} = 0.86$ and $D_{022} = 0.93$. The two measurements therefore determine the Sb-Sb bond length through Eq. (5.4) to be $L = 2.84 \pm 0.05 \text{ \AA}$, which is in excellent agreement with the first-principles total energy calculations by Esser *et al.* [2] and by Schmidt and Bechstedt [9] ($L = 2.86 - 2.87 \text{ \AA}$). Our measured $L_{\text{Sb-Sb}}$ is also very close to the bond lengths of the Sb dimers formed on a GaAs(110) surface [7] ($L = 2.80 \text{ \AA}$) and on a Ge(001) surface [6] ($L = 2.90 \text{ \AA}$) reported by x-ray diffraction (XRD). While it is about 0.1 \AA longer than the Sb-Sb bond length of a Sb-terminated Si(001) surface measured by XSW [5] ($L = 2.75 \text{ \AA}$). The BRXSW study by

Sugiyama *et al.* [4], however, reported a Sb-dimer bond length of $2.95 \pm 0.06 \text{ \AA}$ on the GaAs(001) surface; note that this value is 4% larger than the present measurement, consistent with their report of a 5% larger value of h' .

Table 5.1 Theoretical and experimental values of the structural dimensions for the Sb dimers on different surfaces. L is the Sb dimer bond length. h' is the height of the Sb dimer relative to the surface GaAs (004) planes [see Figure 5.5(a)].

Substrate	Si(001)	Ge(001)	GaAs(110)	GaAs(001)	GaAs(001)	GaAs(001)
	XSW ^d	XRD ^e	XRD ^f	BRXSW ^g	Theory ^h	Present XSW
h' (Å)	1.64±0.02			1.81±0.02		1.72±0.02
L (Å)	2.75±0.06	2.90	2.80	2.95±0.06	2.86 - 2.87	2.84±0.05

^d Ref. 5

^e Ref. 6

^f Ref. 7

^g Ref. 4

^h Ref. 2 and 9

Since the thermal vibrational amplitude is normally larger for surface atoms, our extrapolated value of $L = 2.84 \text{ \AA}$ represents an upper bound on the true Sb dimer bond

length. Based on previous XSW measurements for As [15], Sb [5], and Bi [16] dimers on Si(001), we can reasonably approximate that the Sb thermal vibrational amplitude on GaAs(001) should be 0.15 Å. This value, which is 23% larger than that for bulk GaAs at RT, leads to a reduction in $L_{\text{Sb-Sb}}$ from 2.84 to 2.81 Å. This small reduction in $L_{\text{Sb-Sb}}$ is included within the quoted ± 0.05 Å error. We summarize our results in conjunction with other related measurements in Table 5.1.

5.4.2 Sb coverage

In addition to measuring the local bonding geometry of the Sb dimer, we also determined the Sb coverage Θ of the (2×4) surface using RBS. Major differences in Sb coverage can be found among the previously proposed (2×4) models: Maeda *et al.* [1] proposed a model (β_3) consisting of three Sb dimers per (2×4) unit cell, the theoretical calculations and RAS result by Esser *et al.* [2] were in favor of a (2×4) model (α_2) with two Sb dimers (and two Ga dimers) per unit cell, and the STM study by Moriarty *et al.* [3] suggested only one Sb dimer per unit cell (δ_1). Besides, Schmidt and Bechstedt [9] considered in their calculations three additional unit cells (δ_2 , β_{2_2} and β_{2_3}) containing both two and three Sb dimers. These six different (2×4) models correspond to Sb coverages of 0.75, 0.50 and 0.25 ML. Our RBS result showed that the same sample we studied with XSW was covered by 3.0×10^{14} Sb/cm², which is equivalent to 0.48 ML on a GaAs(001) surface ($1 \text{ ML} = 6.26 \times 10^{14} \text{ atoms/cm}^2$). By considering the ordered

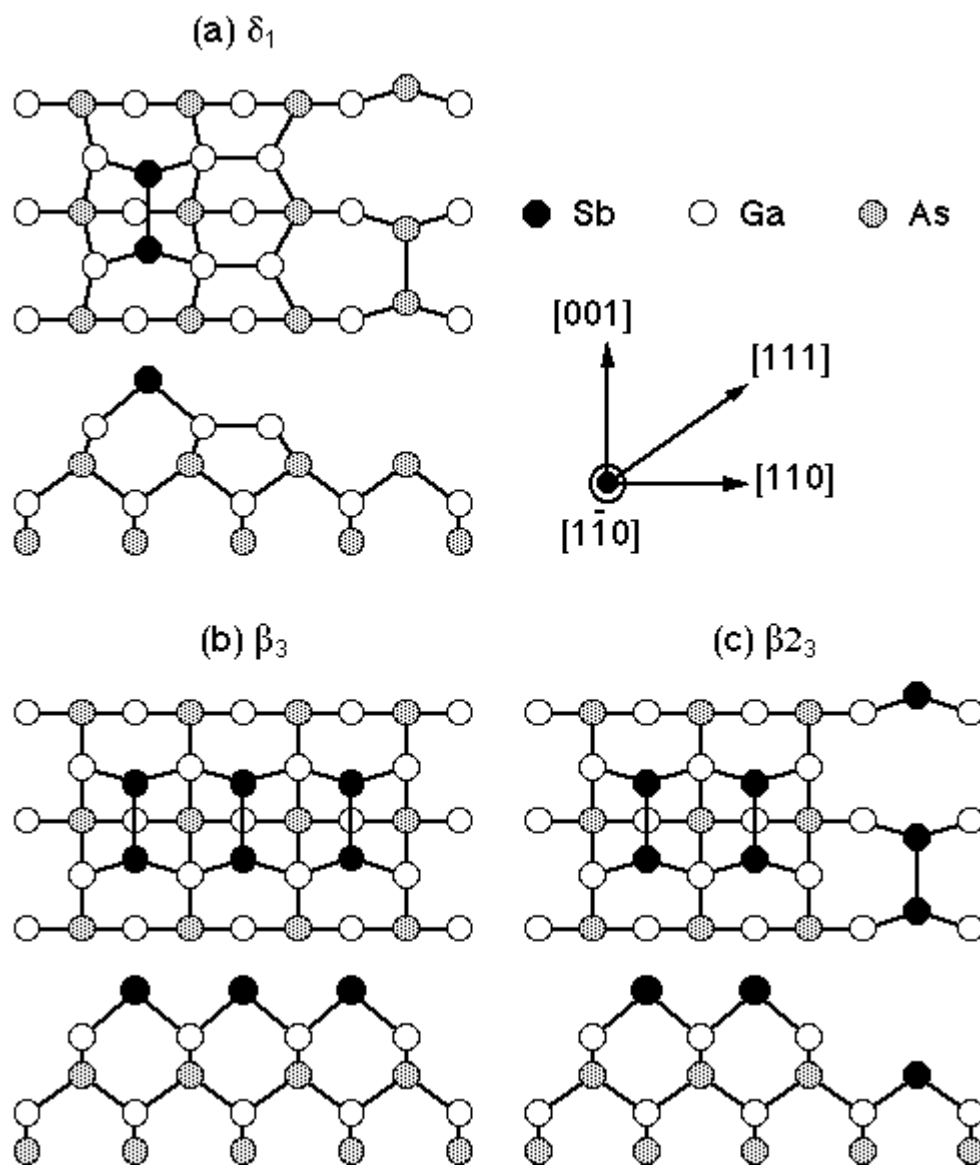


Figure 5.6 Proposed structural models for the Sb-stabilized GaAs(001) (2×4) surface with one and three Sb dimers per unit cell. (a) the δ_1 model ($\Theta_{\text{Sb}} = 0.25$ ML, Ref. 3 and 9), (b) the β_3 model ($\Theta_{\text{Sb}} = 0.75$ ML, Ref. 1 and 9) and (c) the β_{2_3} model ($\Theta_{\text{Sb}} = 0.75$ ML, Ref. 2 and 9).

fraction C measured from the (004) reflection of $C = f_{004}/D_{004} = 0.79$, we can obtain an ordered coverage of $C\Theta = 0.38$ ML. This value indicates that under the present growth condition the (2×4) ordered structure was formed by about 0.4 ML of Sb adatoms. This result is consistent with a surface composed predominantly of two Sb dimers per unit cell as proposed by Esser *et al.* [2] (α_2) and by Schmidt and Bechstedt [9] (β_{2_2} and δ_2). The ordered coverage of 0.4 ML rules out the possibility that the model proposed by Moriarty *et al.* [3] with one Sb dimer per unit cell (δ_1) is the only ordered structure on the (2×4) surface ($C\Theta \leq 0.25$ ML for this case). Figure 5.6 depicts the three proposed models having one and three Sb dimers (δ_1 , β_{2_3} and β_3).

5.4.3 α_2 and β_{2_2} models

In Esser's total-energy calculation [2] there are two different models considered which have two Sb dimers per (2×4) unit cell. They were also included later in the calculation by Schmidt and Bechstedt [9]. As illustrated in Figure 5.7, the α_2 model has two Ga dimers in the second layer, and the β_{2_2} model has one As dimer in the third layer. The former was based on the clean GaAs(001)- (2×4) α phase proposed by Farrell and Palmstrom [17], and the latter was based on the GaAs(001)- (2×4) model proposed by Chadi [18] (known as the β_2 phase). Energetically, these calculations show that the α_2 and β_{2_2} models are both stable (2×4) structures. The theoretical calculation by Northrup and Froyen [19] show that for the clean (2×4) α phase, the As and Ga atoms in the top

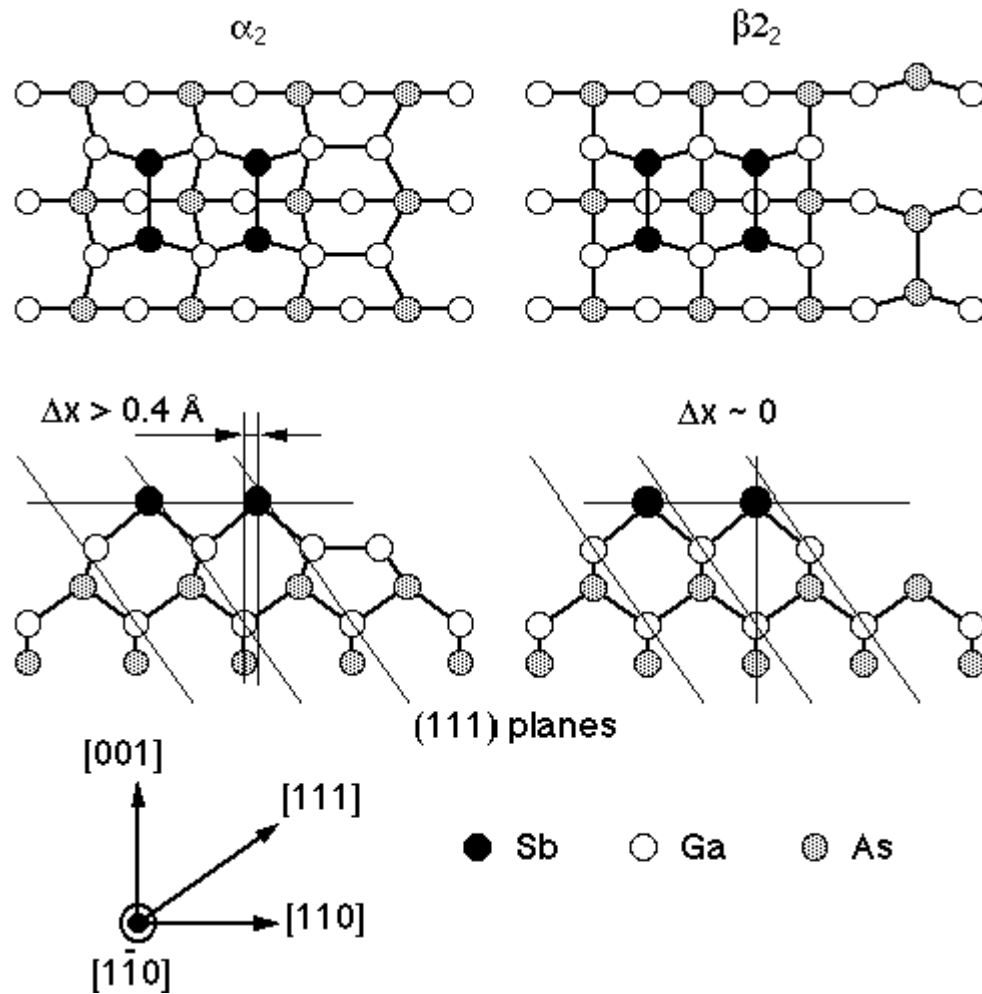


Figure 5.7 The top and the $[1\bar{1}0]$ side views of two different GaAs(001):Sb-(2x4) models (Ref. 2 and 9). Both models have two Sb dimers per unit cell ($\Theta_{\text{Sb}} = 0.5 \text{ ML}$). The β_2 model has two Ga dimers in the second layer and the α_2 model has one As dimer in the third layer. Δx in the α_2 model is the lateral shift of the Sb dimers along the $[110]$ direction relative to a bulk two-fold axis, in response to the strain induced by the formation of the Ga dimers.

two layers will undergo large lateral displacements (0.4 - 1.2 Å) in the [110] direction to allow the formation of the second-layer Ga-Ga dimers. A similar relaxation effect would be expected to occur on the Sb-terminated surface to accommodate the lateral strain if Sb and Ga dimers coexist in the top two layers, as illustrated in the α_2 model. Since the proposed displacement is perpendicular to the Sb-Sb dimer bonds, the standing wave generated by the (111) reflection would be most sensitive to this effect. Based on symmetry, the surface should be equally occupied by domains with Sb dimers shifted in the [110] and $[\bar{1}\bar{1}0]$ directions. Thus the distribution of Sb atoms from both domains, as projected into one unit cell, should remain centered along a bulk two-fold axis. Therefore

$$P_{111} = (P_{004} + 2)/4 , \quad (5.5)$$

which predicts $P_{111} = 0.81$ from our measured value for P_{004} . The proposed lateral relaxation of the surface in the α_2 model would broaden the Sb distribution along the [110] direction and lead to a lower (111) coherent fraction. We can calculate this reduction of f_{111} through Eq. (5.3) with the following formula for a_{111} :

$$a_{111} = \left| \cos \left(\frac{4\pi\Delta x}{\sqrt{6}d_{111}} \right) \right| . \quad (5.6)$$

Here we assume that all Sb dimers are shifted by the same amount, Δx (Figure 5.7), along the [110] in either direction. For the purpose of testing the two different models, we

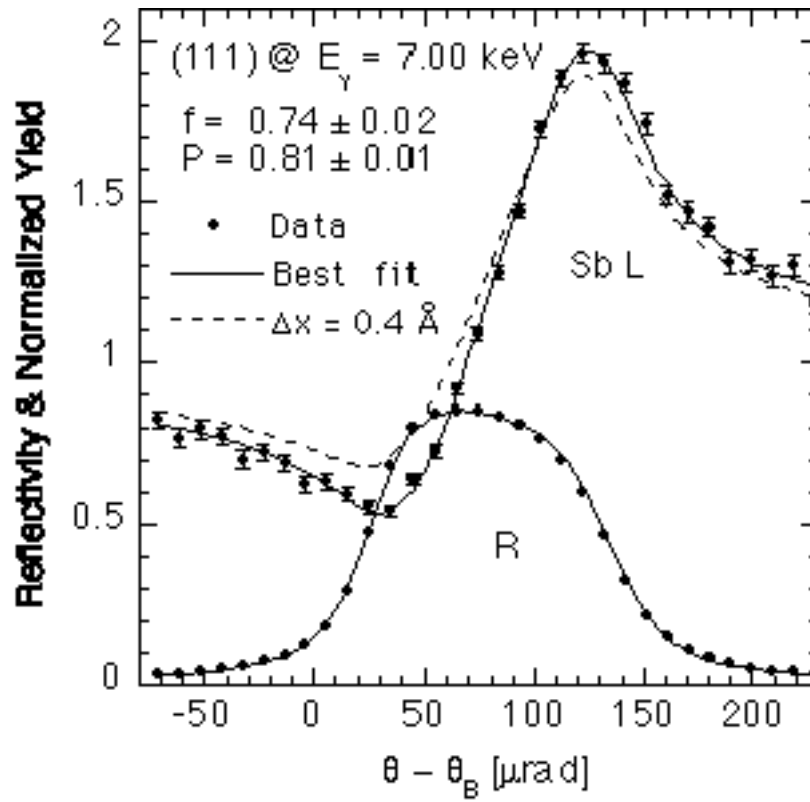


Figure 5.8 The (111) XSW data (filled circles) and the best fits (solid lines) for the normalized Sb L fluorescence yield and the GaAs(111) reflectivity R. The dashed line is the calculated Sb fluorescence yields for $\Delta x = 0.4 \text{ \AA}$ in Figure 5.7, while the best-fit solid line corresponds to $\Delta x = 0$.

estimated the displacement Δx in the α_2 model based on Schmidt and Bechstedt's calculation to be 0.4 \AA , which is also the lower bound of the lateral shifts calculated for the GaAs(001) (2×4) α phase reported in Ref. 19. This would reduce the (111) geometric factor to $a_{111} = 0.81$ and the coherent fraction to $f_{111} = CD_{111}a_{111} = 0.62$ (with $D_{111} = 0.97$). For the β_2 Model, the Sb dimers are close to the ideal positions ($\Delta x \approx 0$), therefore $a_{111} = 1$ and Eq. (5.3) renders $f_{111} = 0.77$.

Figure 5.8 shows the result of the (111) XSW measurement carried out at $E_\gamma = 7.00$ keV. The Sb coherent position (0.81 ± 0.01) agrees with the symmetry requirement of Eq. (5.5), while the measured coherent fraction (0.74 ± 0.02) implies $a_{111} \approx 1$ (or $\Delta x \approx 0$), in favor of the structural model without Ga dimers in the second layer (the β_2 model). The disagreement of our measurement with the α_2 model is evident in Figure 5.8 from the difference between the best fit curve (solid line) and the calculated curve for $\Delta x = 0.4 \text{ \AA}$ (dashed line).

5.4.4 δ_2 model

In this section we compare our XSW measurements with the δ_2 model proposed in Schmidt and Bechstedt's calculation. Figure 5.9 shows the structure of this model. It is constructed with one Sb dimer in the first layer, one Sb dimer in the third layer and two Ga dimers in the second layer, corresponding to a Sb coverage of 0.5 ML. Based on their calculated phase diagram, Schmidt and Bechstedt concluded that this model (together with

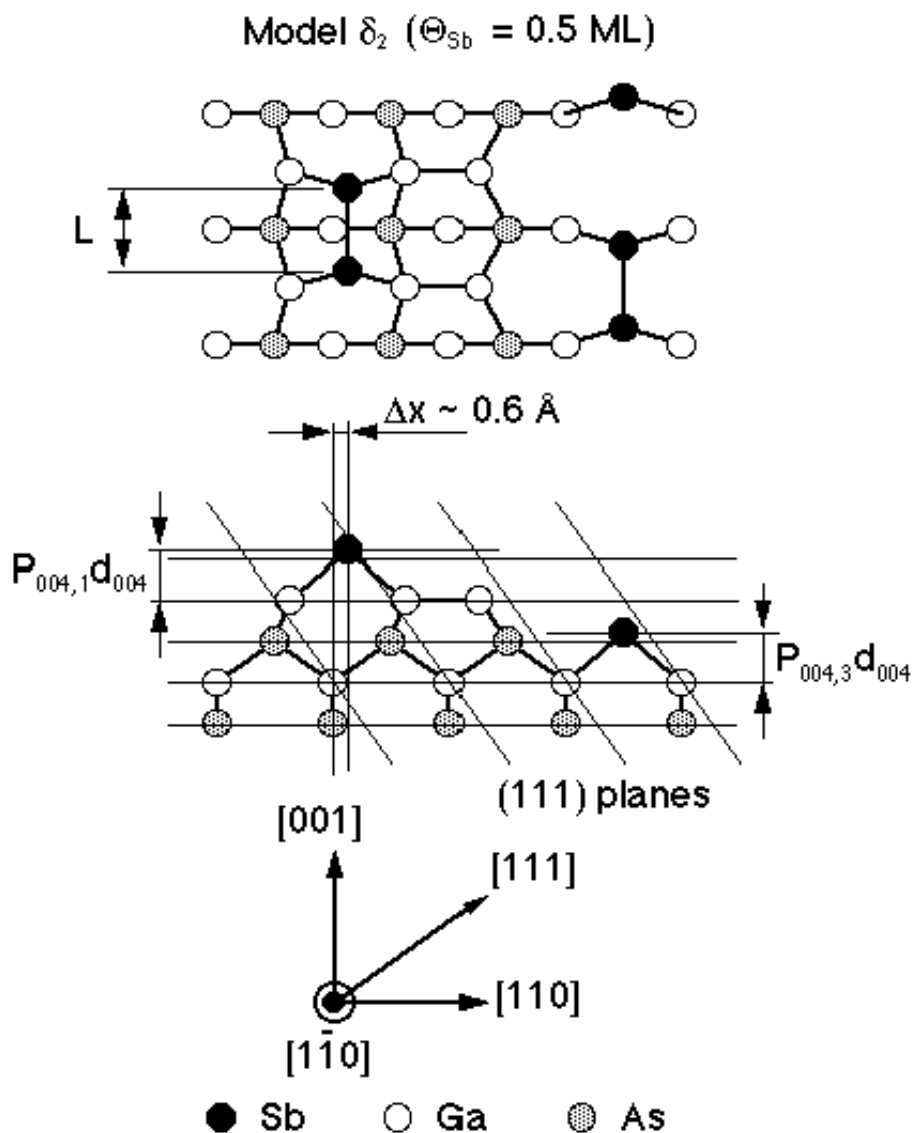


Figure 5.9 The top and the $[1\bar{1}0]$ side views of the δ_2 model for the GaAs(001):Sb- (2×4) surface proposed by Schmidt and Bechstedt [9]. It is constructed with one Sb dimer in the first layer, one Sb dimer in the third layer and two Ga dimers in the second layer ($\Theta_{\text{Sb}} = 0.5 \text{ ML}$). Δx is the lateral shift of the outermost Sb dimer along the $[110]$ direction relative to the bulk two-fold axis. Schmidt and Bechstedt's calculation suggested a Δx of about 0.6 \AA .

the δ_1 model) represented the structures actually observed in the experiments. However, the calculation suggested a lateral displacement Δx of approximately 0.6 Å for the outermost Sb dimer toward the second layer Ga atoms from the two-fold symmetry position, while almost no displacement for the Sb dimer in the third layer.

We now simulate the (022) and (111) coherent fractions for the δ_2 model based on the dimer geometry reported in Schmidt and Bechstedt's calculation. We first define the quantity $\Delta P_{004} = |P_{004,1} - P_{004,3}|$, where $P_{004,1}$ and $P_{004,3}$ are the (004) coherent positions for the Sb dimers in the first and third layers, respectively. It can be shown that the (004) geometric factor for this model is $a_{004} = \cos(\pi\Delta P_{004})$. Since the order fraction $C \leq 1$ in Eq. (5.3), from the XSW (004) measurement a_{004} must be greater than $f_{004}/D_{004} = 0.79$ and thus $\Delta P_{004} \leq 0.21$. Based on the structure in Figure 5.9, we can express a_{022} and a_{111} for the Sb atoms as

$$a_{022} = 0.5 \cos\left(\frac{\pi L}{2d_{022}}\right) \left\{ \left[\cos(\pi\Delta P_{004}) + \cos\left(\frac{\pi\Delta x}{d_{022}}\right) \right]^2 + \sin^2(\pi\Delta P_{004}) \right\}^{1/2} \quad (5.7)$$

$$\text{and} \quad a_{111} = 0.5 \left\{ \left[1 + \cos\left(\frac{\pi}{2}\Delta P_{004}\right) \cos\left(\frac{\pi\Delta x}{d_{022}}\right) \right]^2 + \sin^2\left(\frac{\pi}{2}\Delta P_{004}\right) \cos^2\left(\frac{\pi\Delta x}{d_{022}}\right) \right\}^{1/2}, \quad (5.8)$$

where $L = 2.87$ Å is the theoretical Sb dimer bond length (for both dimers). We plotted a_{022} and a_{111} in Figure 5.10 as functions of ΔP_{004} with $\Delta x = 0.6$ Å. It can be seen that

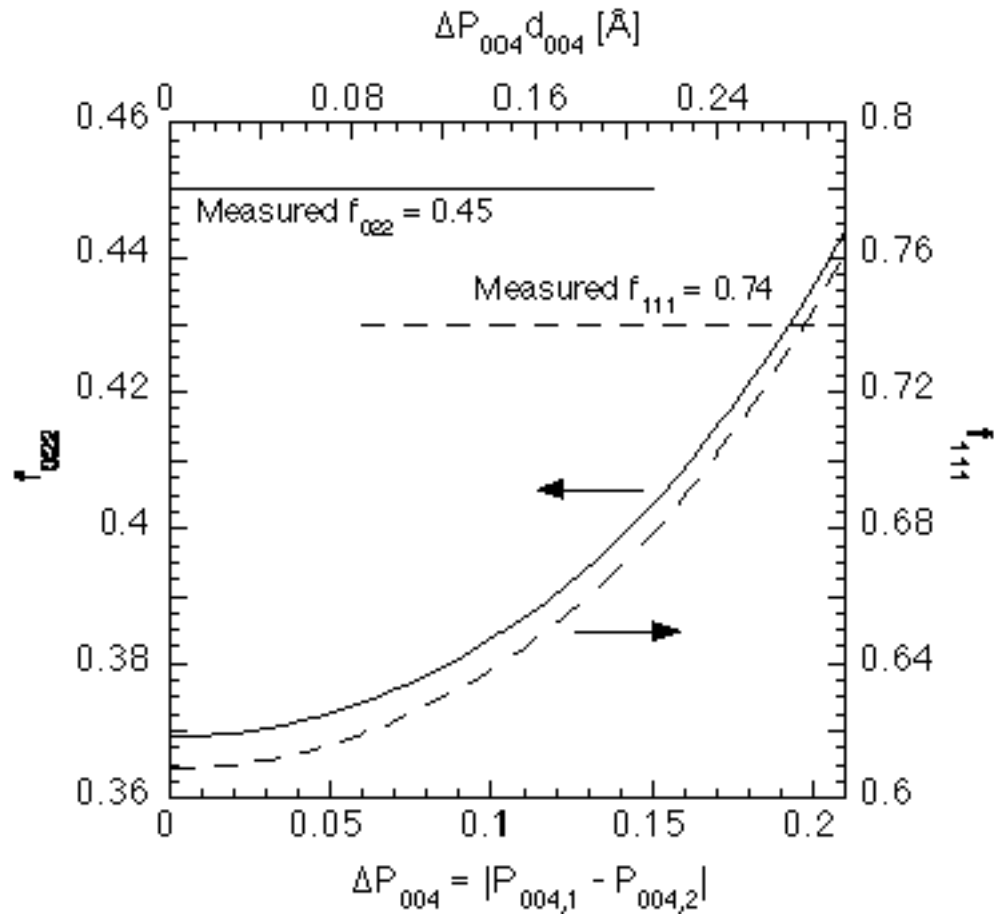


Figure 5.10 Calculated (022) (solid curve) and (111) (dashed curve) coherent fractions based on Eq. (5.7) and (5.8), respectively, for the δ_2 model. The straight solid and dashed lines indicate the XSW measured values. ΔP_{004} is the difference between the (004) coherent positions for the Sb dimers in the first and the third layers (Figure 5.9).

(5.7) and (5.8) will reproduce the experimental values ($a_{022} = 0.45$ and $a_{111} = 0.74$) only when ΔP_{004} is as large as 0.21. Since the δ_2 model agrees with our XSW measurements only for the extreme case ($\Delta P_{004} = 0.21$), and more importantly it corresponds to a height difference of $\Delta P_{004} d_{004} = 0.3 \text{ \AA}$ between the Sb dimers in the first and third layers, we conclude that our observed structure can not be described by the δ_2 model.

5.5 Summary

The GaAs(001):Sb-(2×4) surface prepared by MBE was studied by (004), (022) and (111) x-ray standing waves. All three XSW measurements are consistent with the formation of symmetric Sb dimers above the modified bridge site. The Sb dimer height was determined to be $h' = 1.72 \pm 0.02 \text{ \AA}$ above the bulk-like (004) Ga atomic plane. The Sb dimer bond length was measured to be $L = 2.84 \pm 0.05 \text{ \AA}$. Both values are in good agreement with previous theoretical calculations and other related measurements. The Sb coverage of the (2×4) reconstruction was determined by Rutherford backscattering to be 0.48 ML, consistent with surface models having two Sb dimers per (2×4) unit cell, and disagreeing with models (δ_1 , β_2 and β_3) having one and three Sb dimers per unit cell. Finally, the (111) measurement showed no lateral shift of the Sb dimers in the [110] direction. Our analysis strongly favors the (2×4) model with one As dimer in the third layer (the β_2 model) over the α_2 and δ_2 models.

Chapter 6 Indium-Induced GaAs(001) (4×2)/c(8×2) Surface

6.1 Introduction

Owing to the large lattice mismatch, GaAs/InAs has served as an ideal system for studies of the thermodynamics behind the epitaxial growth of highly strained heterostructures. It is known that two-dimensional (2D) growth of InAs on GaAs(001) can only occur during the nucleation of the first two monolayers. Recent investigations have shown that the planar growth is immediately followed by the formation of self-organized, coherent three-dimensional (3D) InAs islands, which has provided a practicable way for fabricating 0-dimensional quantum devices. For applications where 2D growth is more desirable, it was found that the 3D-island formation of InAs on the GaAs(001) can be delayed significantly under an In-rich growth condition. Despite this interesting behavior and potential applications, little has been known about the atomic structures at the initial growth stage of In or InAs on the GaAs(001). Previous STM observations showed that the In-induced GaAs(001) (4×2)/c(8×2) surface appeared to be well ordered. We therefore carried out XSW studies in conjunction with LEED and Auger analysis. In this chapter I present the experimental results and discuss possible structural models for this surface.

6.2 In adsorption on GaAs(001): Background information

Since it is expected that In forms InAs-like structure on the GaAs(001) surface, in

this section we first review what is known about the InAs(001) clean surface and the initial growth of InAs on the GaAs(001), followed by a discussion of the GaAs(001):In (4×2)/c(8×2) structures.

6.2.1 InAs(001) clean surface

The clean InAs(001) surface exhibits a variety of symmetries similar to GaAs(001). Experimental studies have observed the As-rich c(4×4) [1], (2×4) [2 – 8] and In-rich (4×2) [2, 4, 5, 7, 9] reconstructions. These surfaces were prepared either by growing an epitaxial layer using conventional MBE [2, 5] or by performing sputtering-annealing cycles [8, 9] on InAs(001) substrates. The reconstructions have been also observed on the clean surfaces prepared from As-protected InAs substrates [4, 6].

The As-rich (2×4) reconstruction has been studied by STM [3 - 7] and surface x-ray diffraction [8]. Yamaguchi and Horikoshi [4 - 6] showed that by annealing an As-capped InAs(001) substrate at 300 °C the (2×4) surface symmetry can be recovered. Their STM images revealed a highly uniform dimer-vacancy row structure, which was determined to be consistent with the β_2 model by Chadi [71], having two As dimers in the topmost layer [Figure 4.8(c) and 6.1(a)]. Annealing the (2×4) surface further at 340 °C caused the surface As to desorb and the subsequent STM images showed that the As dimer rows contained mainly a single As dimer. A new model [named (2×4) α_2 , Figure 6.1(b)], which has not been considered for the GaAs(001) (2×4) surface, was therefore proposed. The detailed bonding geometry of the InAs(001) (2×4) β_2 structure was recently

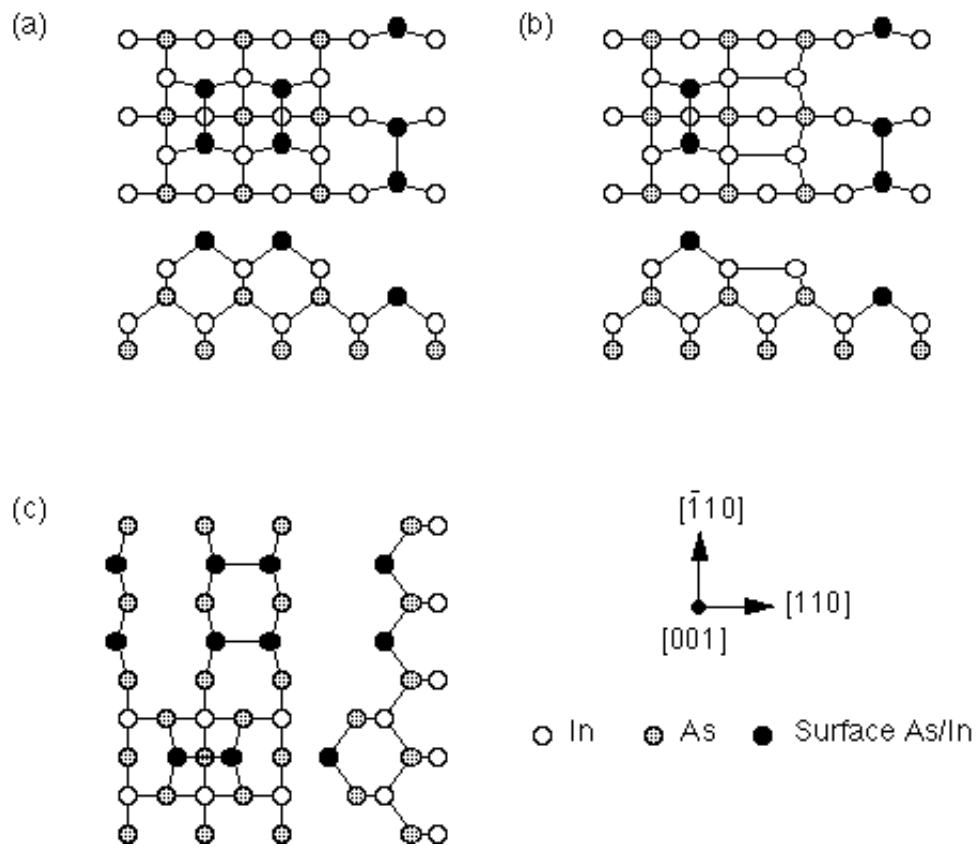


Figure 6.1 Structural models proposed for the InAs(001) As-rich (2×4) surface by Yamaguchi and Horikoshi [4] (a)(b) and for the InAs(001) In-rich (4×2) surface by Ohkouchi and Ikoma [7] and by Kendrick *et al.* [9] (c).

confirmed and determined using surface x-ray diffraction by Gothelid *et al.* [8].

The In-rich (4×2) reconstruction of the InAs(001) surface has been investigated by Ohkouchi and Ikoma [7] and by Kendrick *et al.* [9] using STM. Ohkouchi and Ikoma's filled-state images showed that the (4×2) surface was characterized by straight lines of about 4 Å wide parallel to the [110] direction separated by a spacing of approximately 17 Å. They attributed the straight lines to In dimer rows with a single dimer width. The empty-state STM images measured by Kendrick *et al.* further resolved the individual In dimer in the straight line and also revealed weak features in the trench areas. Both studies reached the same conclusion that the trench areas were terminated with two In dimers per (4×2) unit cell in the third layer [Figure 6.1(c)]. This (4×2)/c(8×2) model is essentially the same as the one proposed by Moriarty *et al.* [72] for the Ga-rich GaAs(001) (4×2) surface. It is interesting to point out that the high-resolution filled-state images of the InAs(001) (4×2) surface reported by Kendrick *et al.* [9] do not resemble exactly the images of the GaAs(001) (4×2) surface reported in Ref. 74 - 76.

Despite the similarities in surface symmetries, the InAs(001) and GaAs(001) surfaces were found to have different properties in several aspects. First, a number of studies [10 - 12] have shown that InAs tended to pin its Fermi level near the conduction band minimum at surfaces and interfaces. This implies a downward band bending and an electron accumulation (inversion) layer forming in the near-surface region for n-type (p-type) InAs (Figure 6.2). This charge accumulation at clean InAs surfaces has been measured by HREEL [10] and ARPES [11]. The former showed evidence that the

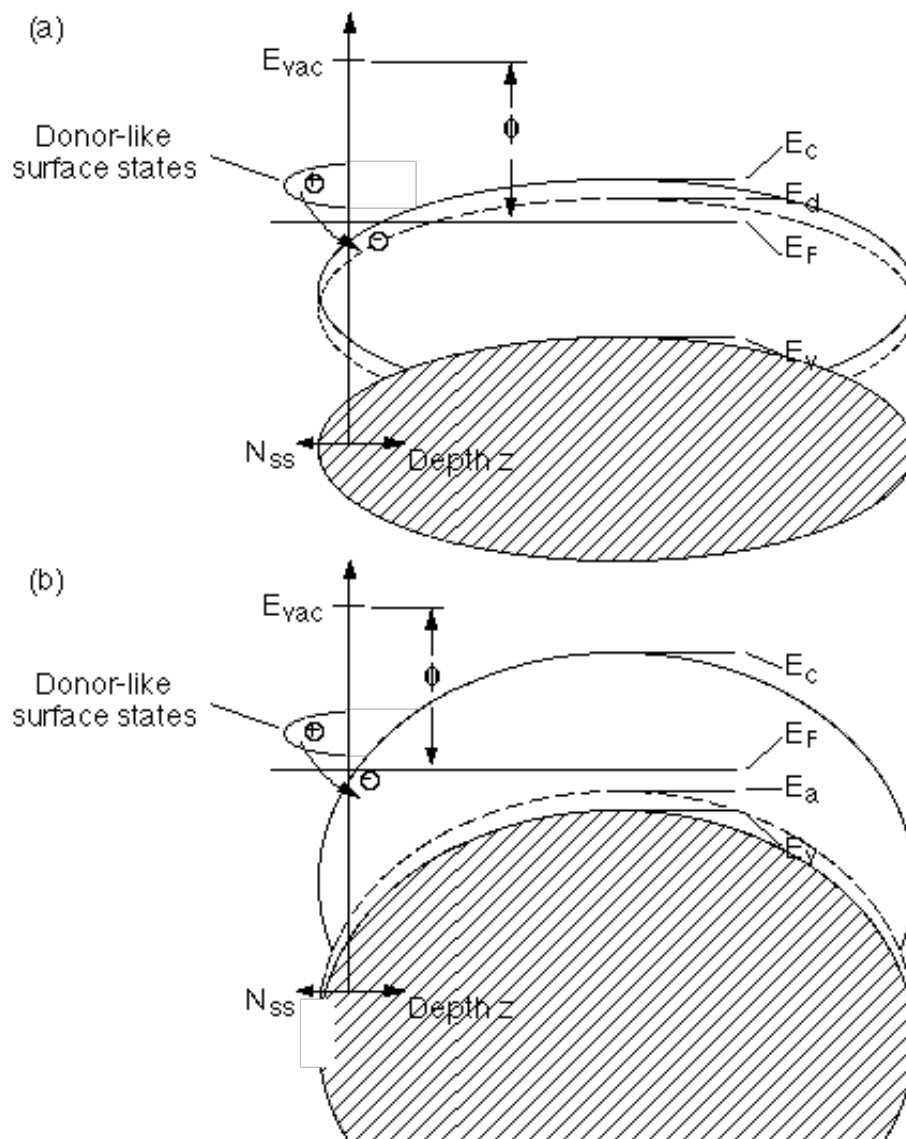


Figure 6.2 The energy-level diagram near the (001) surfaces of (a) n-type and (b) p-type InAs. It is found that the InAs(001) surface tended to pin its Fermi level near the conduction band minimum. E_c and E_v are the conduction and valence band edges. E_d , E_a and E_F are the donor level, acceptor level and the Fermi level, respectively. ϕ is the work function.

accumulation layer was induced by intrinsic donor-like surface states. However, in the recent STM studies by Yamaguchi and Horikoshi [4 - 6] no surface defect was found linked to the Fermi level pinning behavior of InAs, in contrast to the case of GaAs (see Section 3.3.1). Tersoff [13] pointed out based on elementary band structure considerations that this unusual behavior of InAs was due to the fact that its direct band gap (0.36 eV) was much narrower than its indirect band gap (1.21 eV). Because of the Fermi level pinning near the conduction band edge, almost all the metals make ohmic contacts with n-type InAs, while Schottky barriers can only form on p-type InAs [14].

Another difference between the InAs(001) and GaAs(001) surfaces lies in the structural transitions between the As-rich (2×4) and the Group-III-rich (4×2) reconstructions. By monitoring the RHEED specular reflectivity while annealing and cooling an InAs(001) surface under an As flux, Moison *et al.* [15] and later Yamaguchi and Horikoshi [2, 5, 16] observed that the surface structure evolved reversibly but abruptly between the (2×4) and the (4×2) phases through a hysteresis loop with a width of roughly 10 K, which has the character of a first-order phase transition. Similar measurements on the GaAs(001) surface [2, 5], on the other hand, showed that the (2×4)-(4×2) transition occurred reversibly and smoothly along a single path over several intermediate phases (see Section 4.3.4), indicating a higher order phase transition. Further investigations by STM [3 - 6] and Monte Carlo simulations [5, 16] found that these different transitions can be related to the strength of the lateral interactions between surface species and the As desorption behaviors at step edges.

6.2.2 Initial growth of InAs on GaAs(001)

InAs is a direct, narrow band gap semiconductor ($E_g = 0.36$ eV at RT [14]) with an electron mobility (33000 cm²/Vs [73]) more than 20 times higher than Si. When synthesized in conjunction with lattice-matched Sb-based compound semiconductors, InAs shows promising applications in fabricating high-speed transistors and electro-optical device in the infrared range [14].

Due to the 7% lattice mismatch with GaAs, InAs is often used in the form of ternary alloys (e.g., InGaAs and InAlAs) when grown on GaAs substrates. It has been shown that the growth of pure InAs on GaAs(001) can be described by the so-called Stranski-Krastanow [17] (SK) process, which involves a initial layer-by-layer growth followed by island formation. The critical thickness t_c , which is defined as the overlayer thickness beyond which the surface morphology favors energetically the formation of 3D islands over the 2D growth, was measured to be about 1.5 ML for InAs on GaAs(001) [18 - 20].

The reconstructions of the GaAs(001) surface upon InAs deposition was identified with coverages up to the critical thickness by Belk *et al.* [21, 22] using RHEED and STM and by Scholz *et al.* [23] using reflection anisotropy spectroscopy (RAS) and RHEED. Under As-stabilized growth conditions they observed that the surface exhibited a variety of symmetries including the $c(4\times 4)$, (1×3) , (2×3) and (2×4) , depending on the substrate temperature and the InAs coverage. The surface morphology within the 2D-growth regime was investigated by Bressler-Hill *et al.* [24, 25]. Their STM images showed that the InAs tended to form 2D islands elongated in the $[\bar{1}10]$ direction. The island size distribution in this direction was found to exhibit a scaling behavior [25]. In

the [110] direction, however, a preferred island size of approximately 40 Å was observed, independent of the InAs coverage. This anisotropic island shape was attributed to the different step edge reactivities and diffusion barriers along the $[\bar{1}10]$ and [110] directions, which are closely related to the reconstruction of the GaAs(001) surface. They also suggested that the preferred island size could be due to strain effects.

Beyond the critical thickness, Snyder *et al.* [26] have suggested, based on their STM and RHEED observations, that the strain energy in the heterolayer was relieved initially by forming coherent 3D islands prior to the nucleation of misfit dislocations. Ratsch and Zangwill [27] confirmed theoretically that coherent islands can be stable during a SK heteroepitaxial growth. In addition to the 2D-3D transition, Joyce *et al.* [28] showed evidence for the (In,Ga)As alloying during the growth of the InAs/GaAs heterostructure, which can not be fully described by the classic SK mode. Technologically, the formation of these self-organized, coherent 3D islands during the initial growth of highly strained systems opened up an opportunity for the realization of devices utilizing the 3D quantum-confinement effect. The studies of these so-called InAs quantum dots have become of great interest in the past five years. The electronic and optical properties of self-organized 2D and 3D InAs islands embedded in a GaAs matrix have been evaluated experimentally [29 - 33] and theoretically [34, 35], in search of the dependence on the island size distributions and facet orientations. Recently InAs-quantum-dot-based laser diodes [36 - 38], field effect transistors [39, 40] and infrared detectors [41] have been also demonstrated.

6.2.3 Surfactant-mediated growth of InAs on GaAs(001)

For the deposition of highly strained InGaAs on GaAs, the SK growth mode, as discussed above, was commonly observed under As-rich conditions. Since thermodynamically the modern thin-film growth processes normally occur far away from equilibrium, the growth mode and thus the ultimate surface morphology of the heterolayer depend strongly on the kinetic restrictions. It is generally understood that reducing the surface diffusion lengths of the adatoms can suppress the island formation, defer the 2D-3D transition and thus increase the critical thickness of the film [42 - 44]. These lead to the morphological change at interfaces that are desirable for improving the performance of a semiconductor layer structure.

In addition to employing low growth temperatures and high deposition rates, it has been found that such a kinetic limit can be imposed on the adatoms by introducing a surface-active foreign species (or surfactant) [45]. It was initially proposed that the role of surfactants was to modify the energetics in favor of 2D growth [45], owing to the fact that surfactants in general tend to passivate the surface and segregate at the growth front. Later studies [42, 43, 46] showed that, more importantly, surfactants altered the surface diffusion lengths of the growing materials, which determined the effect of a surfactant on the growth mode. It has been demonstrated that Bi, for example, can effectively change the growth mode and therefore be a surfactant for growing Si/Ge heterostructure [47], which has a lattice mismatch of 4% and a t_c of 3 - 4 ML [48].

It was reported by Schaffer *et al.* [49] using RHEED that by growing InAs under an In-stabilized condition onto an In-terminated GaAs(001) (4×2) surface the InAs layer

appeared to be coherently strained up to a thickness of 8 Å ($> t_c$). The unstrained bulk InAs in-plane lattice constant was measured only after the film thickness was over 2000 Å. Similar observations were reported by Munekata *et al.* [50]. Tournie and Ploog [51] later showed, in attempts to grow epitaxially strained InAs on $\text{Al}_{0.48}\text{In}_{0.52}\text{As}$ and GaAs, that by maintaining the (4×2) reconstruction at the growth front of the InAs layer, the growth of 3D islands was completely inhibited and the formation of misfit dislocations was delayed. They attributed the change of the growth mode to the kinetic limitations imposed on the As adatoms by the reactive In-terminated surface. They therefore considered the In atoms as a virtual surfactant (VS). The word “virtual” came from the fact that the growth modification here was driven mainly by the surface stoichiometry of the heterolayer itself, instead of the presence of a foreign species as in the cases of usual surfactant-mediated growths.

Further high-resolution transmission electron microscopy (HRTEM) analysis [44, 52] showed that different types of misfit dislocations had developed in the strained layers prepared by standard and VS-mediated MBE with thicknesses well beyond t_c . For VS-grown films, misfit dislocations were only detected at the InAs/GaAs interface and the InAs layers were essentially defect free. Photoluminescence measurements [53, 54] revealed superior optical properties of the VS-grown samples, which confirmed the high qualities of the InAs layers.

6.2.4 In-terminated GaAs(001) (4×2)/c(8×2)

Despite the intense scientific and technological interests in growing InAs/GaAs (either 2D layer or 3D island) heterostructure, very little has been known about the initial growth stage of this system, in particular the detailed atomic arrangements of the GaAs(001) surface after adsorption of a submonolayer of In or InAs.

STM studies of the In-terminated GaAs(001) (4×2) surface were first reported by Resch-Esser *et al.* [55]. The structure was prepared by depositing 0.2 to 1.6 ML of In on GaAs(001) (2×4) surfaces followed by annealing at 450 – 480 °C. Their STM image over a large area of the surface covered by 1.6 ML of In showed that the surface roughness was greatly reduced, i.e., the anisotropic 2D islands commonly observed on the GaAs(001) (2×4) surface disappeared completely. Their high-resolution filled-state images [Figure 6.3(a)] showed that for an In coverage of 0.25 ML the surface was characterized by straight lines parallel to the [110] direction separated by 16 Å, leading to the 4× period. The bright oval dots that composed the straight lines were, at least in some areas, evident and appeared to have the ×1 period along the lines. As the In coverage increased, the trench areas between the lines were gradually filled by bright round dots with a spacing of 8 Å along the $[\bar{1}10]$ direction until a latter-type pattern was completely formed at around a 0.5 ML coverage [Figure 6.3(b) and (c)]. For In coverages below 0.25 ML, the straight lines turned into broken rows. In addition, four faint corrugation maxima per (4×2) unit cell with roughly a 1×1 symmetry were clearly resolved in the trench areas. Based on this evidence they concluded that the low-

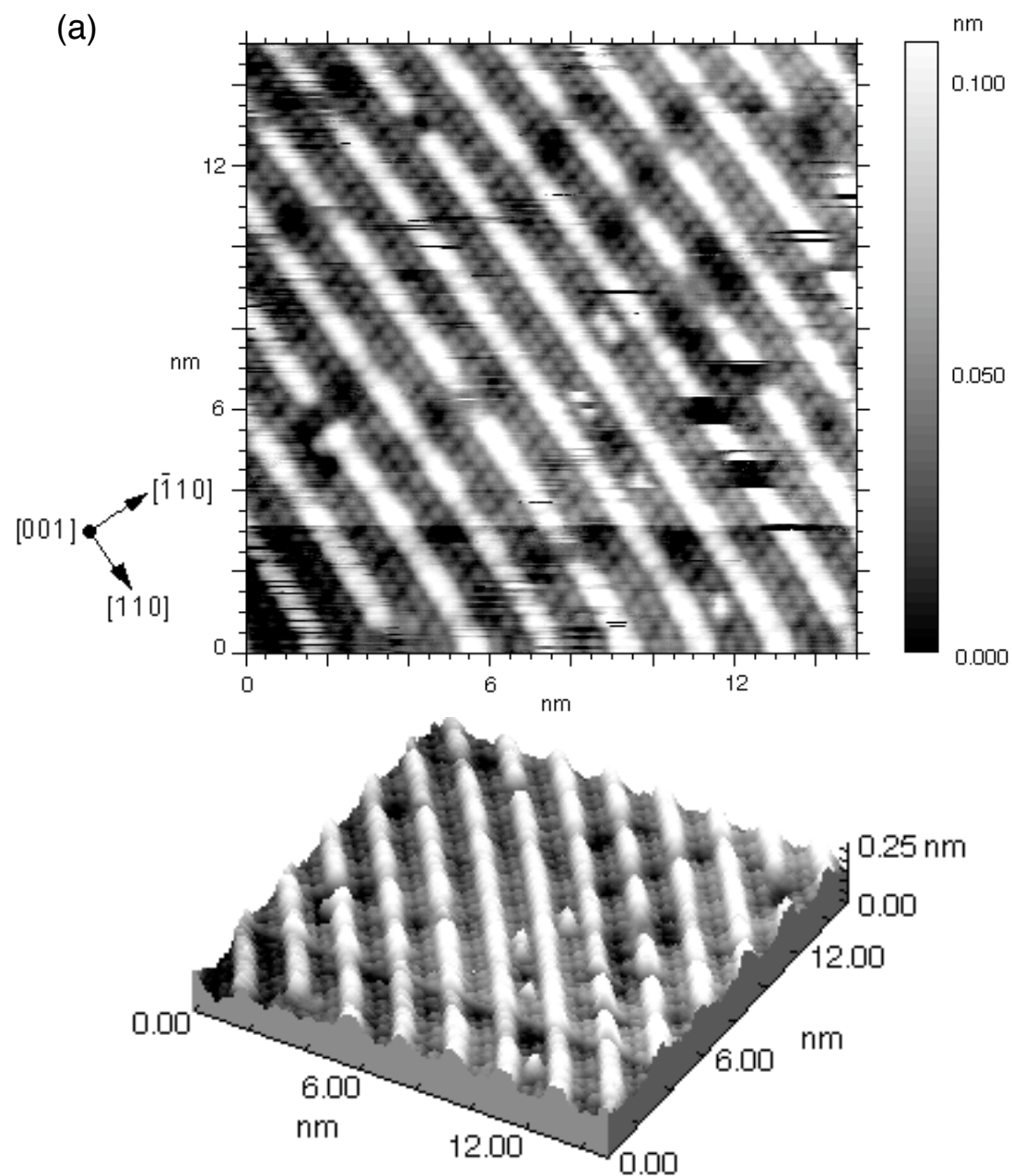


Figure 6.3 Filled-state STM images measured by Resch-Esser *et al.* [55] of the GaAs(001):In (4×2) surfaces with approximately (a) 0.25 and (b) 0.5 ML of In. (c) shows the same surface of (b) over a larger area. Each set of figures contains a 3D image (bottom). All the images were obtained from J. Zegenhagen.

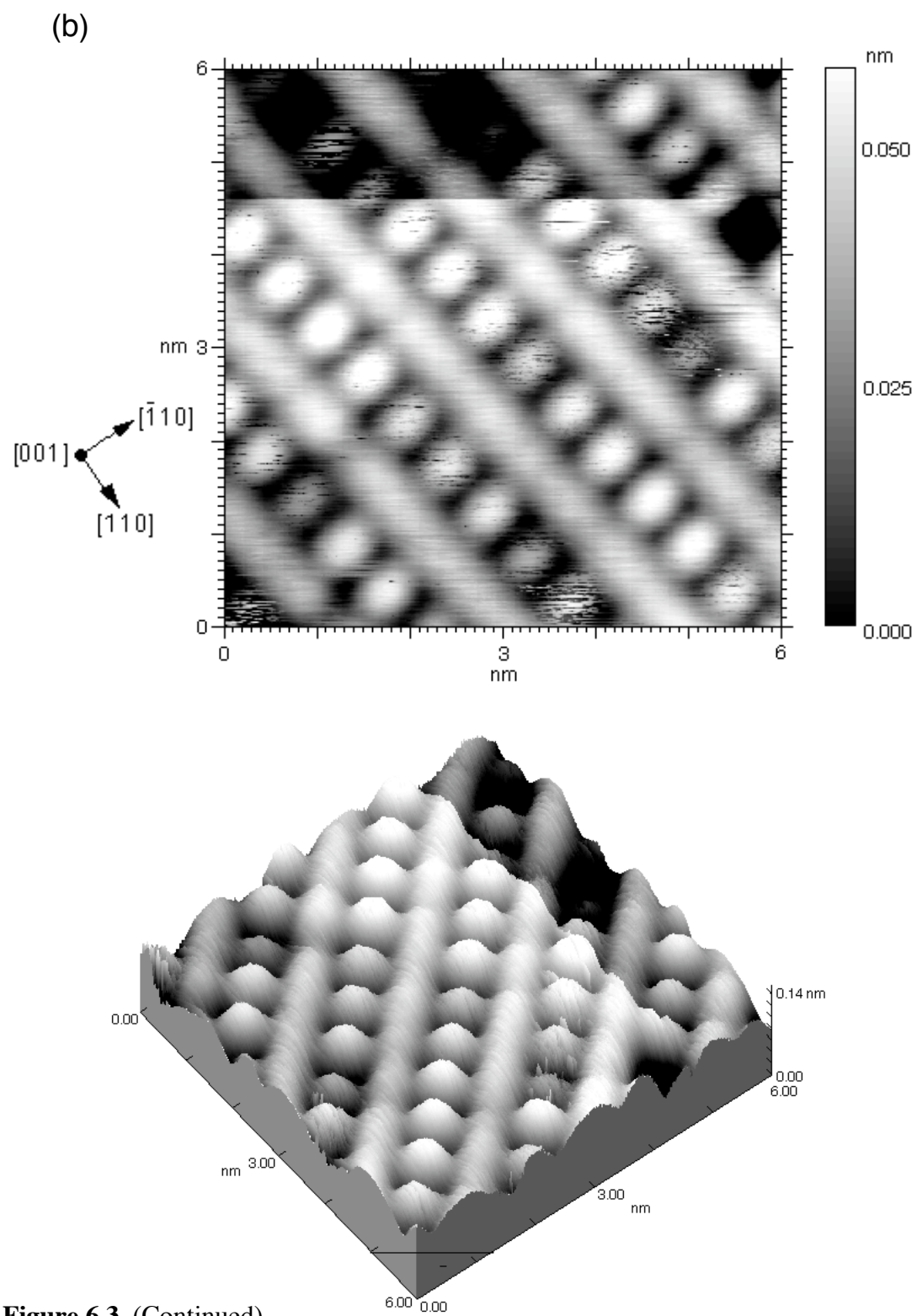
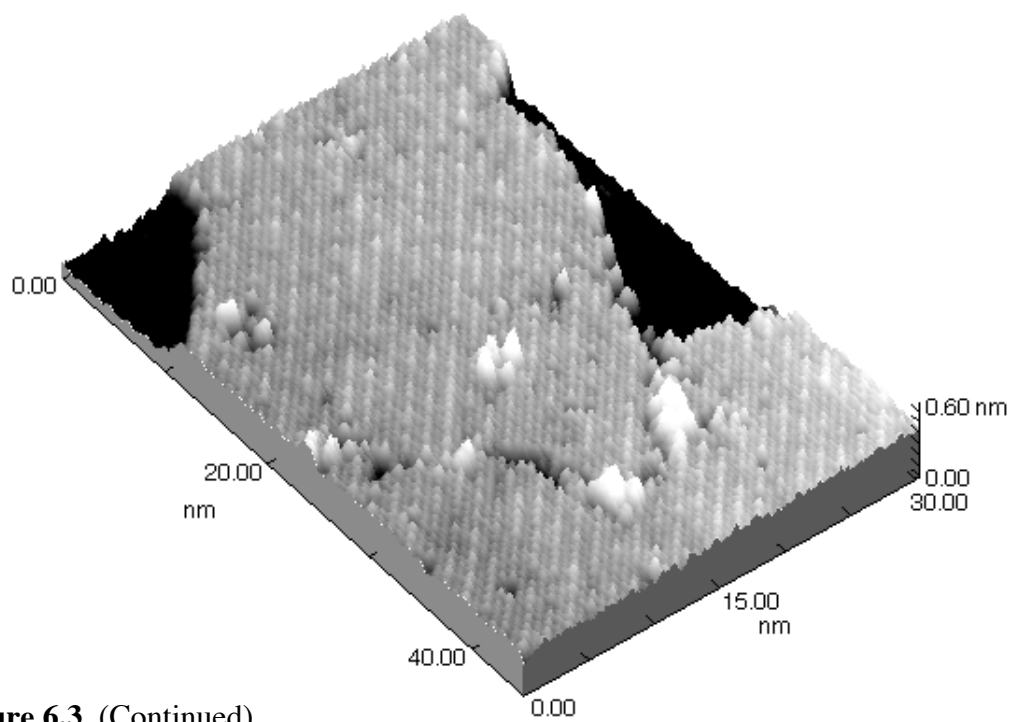
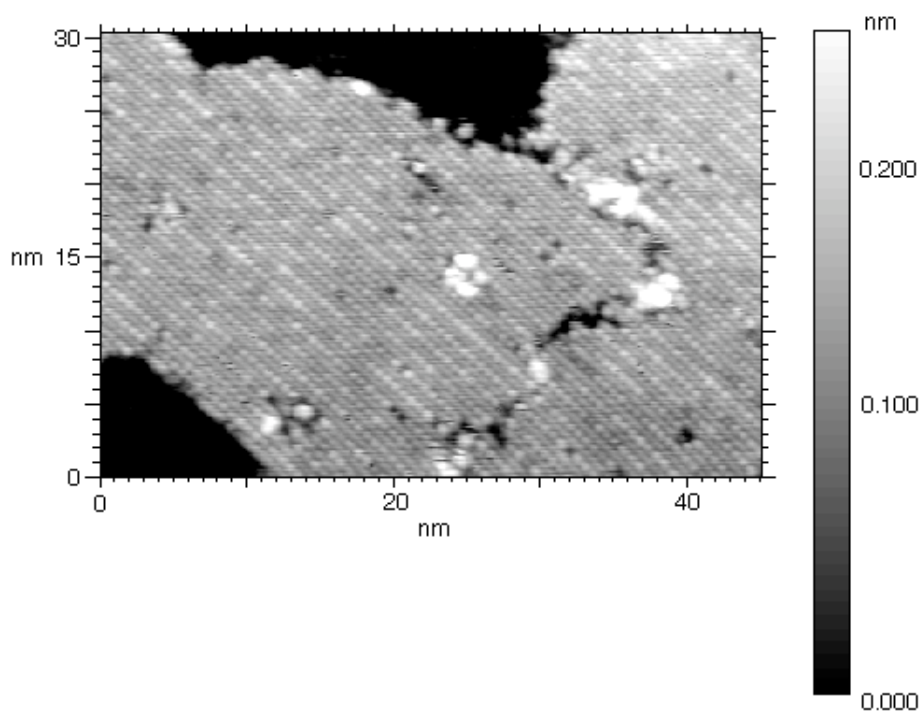


Figure 6.3 (Continued)

(c)

**Figure 6.3** (Continued)

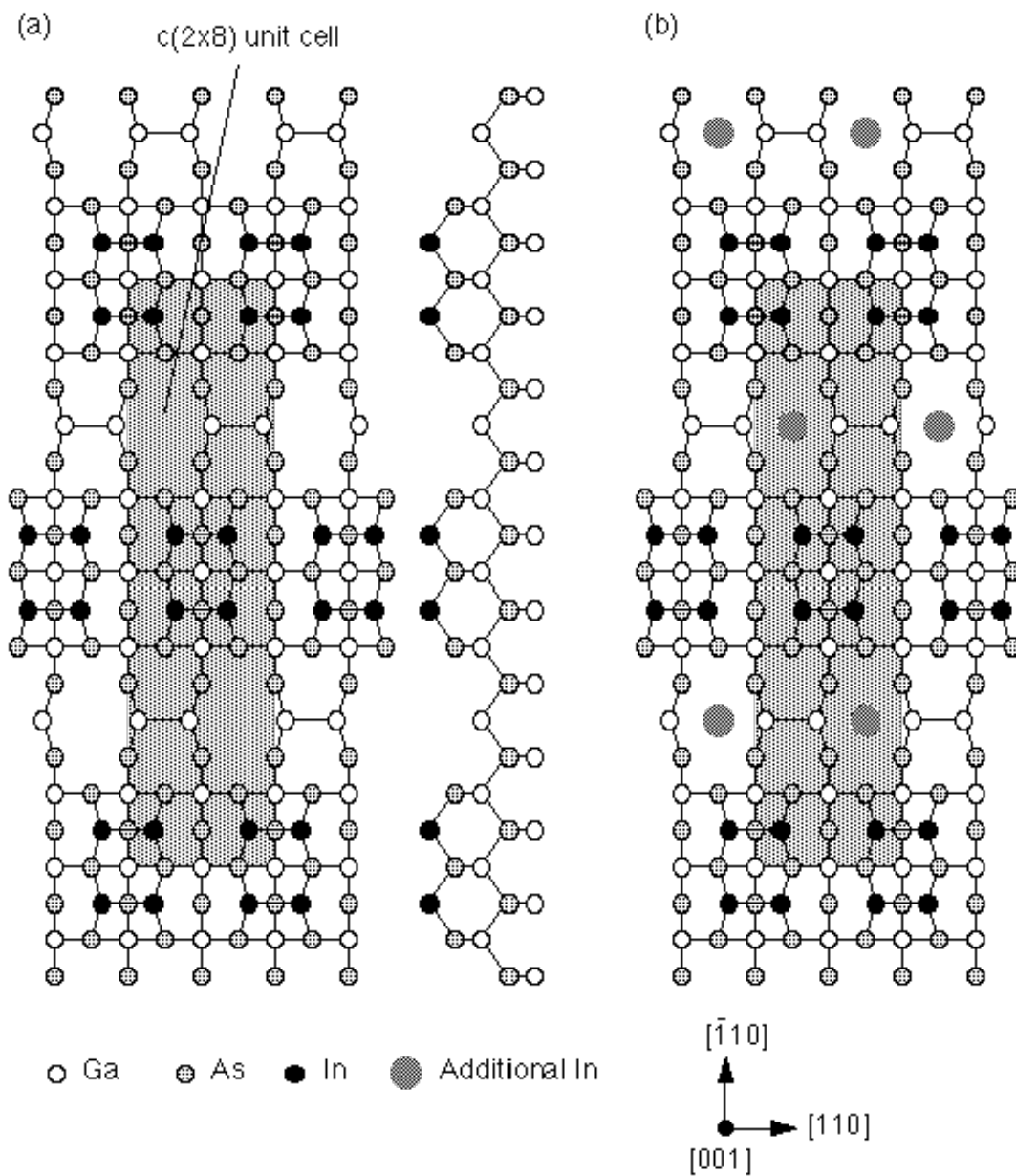


Figure 6.4 The $c(8 \times 2)$ models proposed for the GaAs(001):In surface by Resch-Esser *et al.* [55] based on STM for In coverages (a) below and (b) above 0.25 ML.

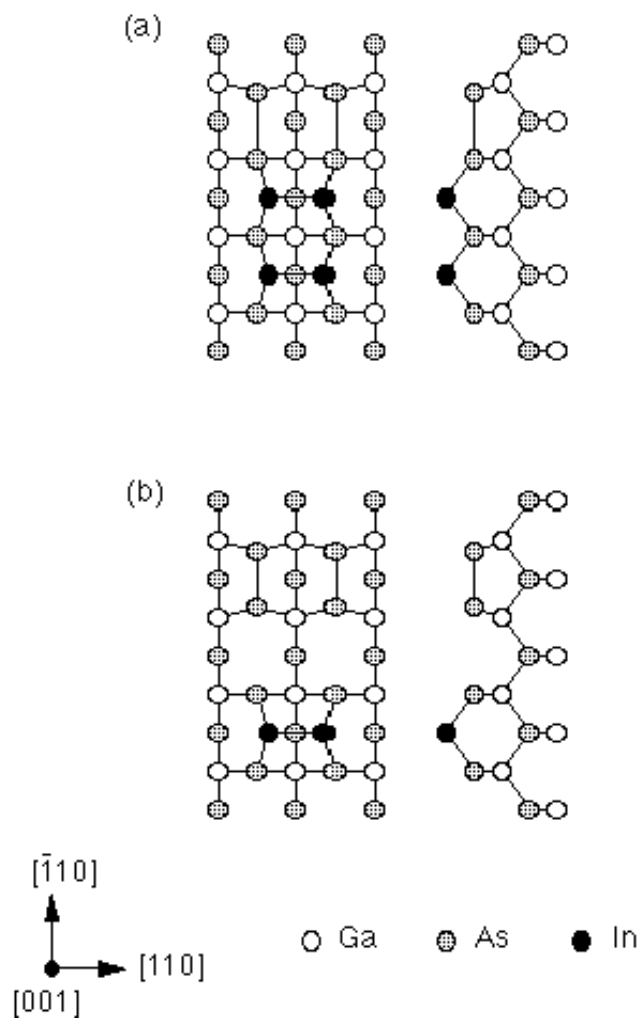


Figure 6.5 Two (4×2) models proposed for the GaAs(001):In surface by Xue *et al.* [57, 58] based on STM. Notice that they attributed the straight lines in the images to be the As dimer rows, in contrast to Resch-Esser's interpretation.

coverage surface can be described by a $c(8\times 2)$ structural model [Figure 6.4(a)] similar to the one proposed earlier by Biegelsen *et al.* [74] for the Ga-rich GaAs(001) (4×2) surface [Figure 4.12(b)]. The straight lines in the STM images were attributed to the two In dimers per unit cell in the first layer. The faint 1×1 spots in the trenches were assigned to the As dangling bonds in the second layer. For the high-coverage surface [Figure 6.4(b)] they introduced additional In in the trenches accounting for the bright round spots. Their Auger and reflectance anisotropy spectroscopy studies showed the presence of a threshold coverage at 0.5 ML [55, 56].

In a study of VS-type MBE growth of InAs on GaAs(001), Xue *et al.* [57, 58] reported STM images of the GaAs(001) surface covered by nominally 0.6 ML of In. Their filled-state images showed a fully developed ladder-type pattern, which resembled the one measured by Resch-Esser *et al.* [55] for an In coverage of 0.5 ML. The width of the straight lines in Xue's images appeared to be somewhat narrower. The filled-state image recorded at a less negative bias (-1.6V) clearly resolved the individual oval dots that formed the straight line. Each pair of adjacent dots was spaced by 4 Å in the [110] direction. They also were successful in obtaining an empty-state image, which showed a reversed contrast between the straight lines (darker) and the round dots in the trenches (brighter). Figure 6.5 show the two models proposed in their study for the (4×2) structure.

Behrend *et al.* [59] and Belk *et al.* [22] have reported high-resolution STM images of the (4×2) surfaces of 20 and 10 ML, respectively, of InAs deposited on GaAs(001)

under In-rich conditions. Interestingly, these images also exhibited ladder-type patterns, which looked remarkably like the patterns observed by Resch-Esser *et al.* [55] and Xue *et al.* [57, 58] for In coverages of about 1 ML prepared under less As-rich conditions. This ladder-type STM pattern therefore corresponds uniquely to the structure of an In-terminated InAs surface on GaAs(001).

6.3 Experimental results

6.3.1 LEED and Auger

Figure 6.6(a) shows a typical Auger spectrum measured on an In-terminated GaAs(001) surface. For this particular surface the In coverage was calibrated to be 0.4 ML. Figure 6.6(b) shows the In coverage, based on a RBS-calibrated In MNN/Ga LMM Auger peak ratio, measured as a function of the annealing temperature. The sample was cut from an As-protected GaAs(001) wafer and then mounted directly onto a Mo sample holder. The GaAs(001) (2×4) surface was initially deposited with approximately 0.4 ML of In at room temperature. The annealing temperatures were estimated based on a heating power versus sample temperature curve calibrated by a pyrometer. This Auger study showed that In desorption occurred at roughly 450 °C and the In adatoms can be completely removed from the GaAs(001) surface at above 500 °C.

Figure 6.7(a) shows the (2×4) LEED patterns of the clean GaAs(001) surface prepared at temperature T1. Figures 6.7 (b) – (e) show the corresponding LEED patterns of the In-terminated surface recorded at two different energies after being annealed at

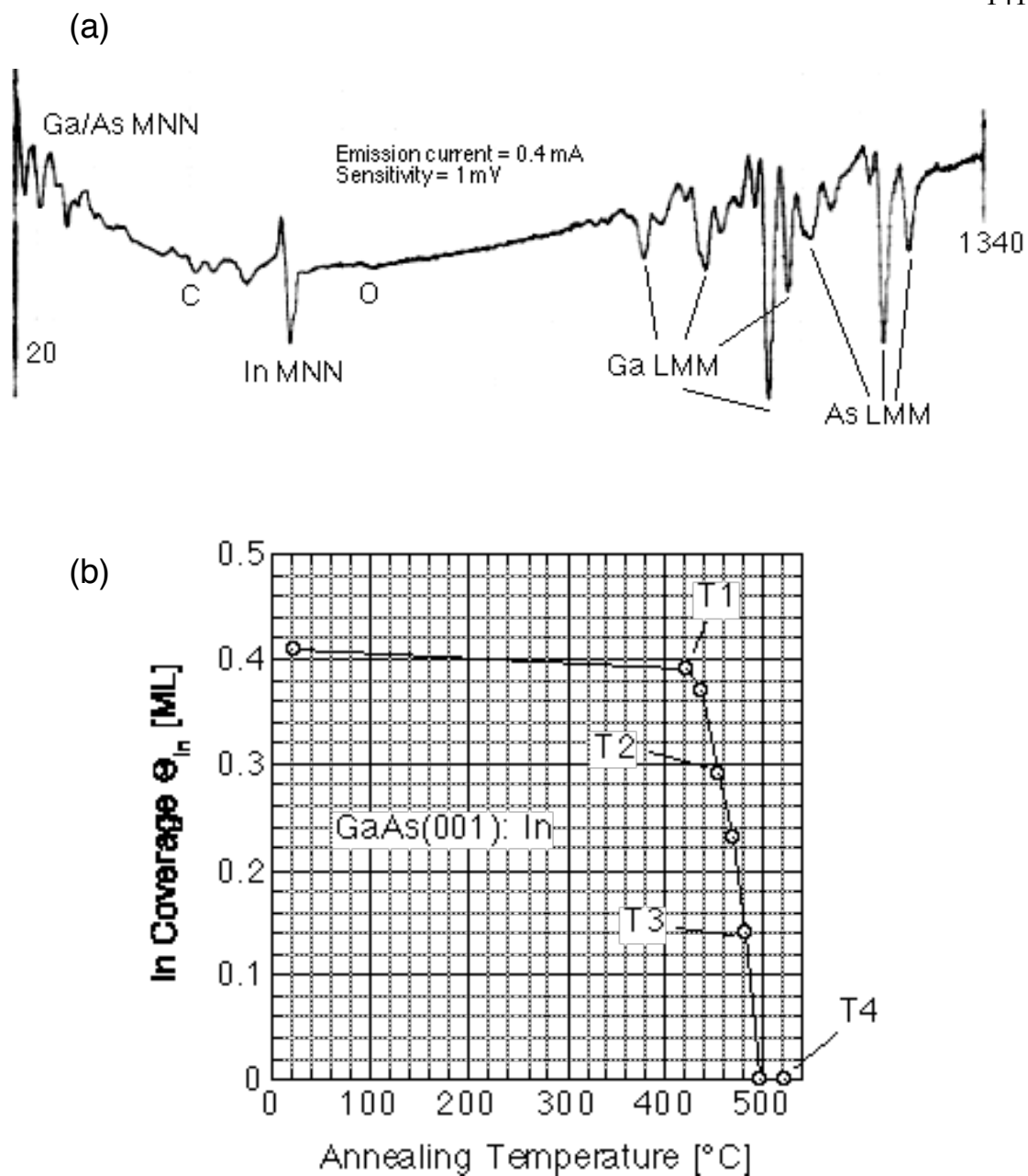


Figure 6.6 (a) A typical Auger spectrum measured on an In-terminated GaAs(001) surface. (b) In coverage of a GaAs(001):In surface measured as a function of the annealing temperature.

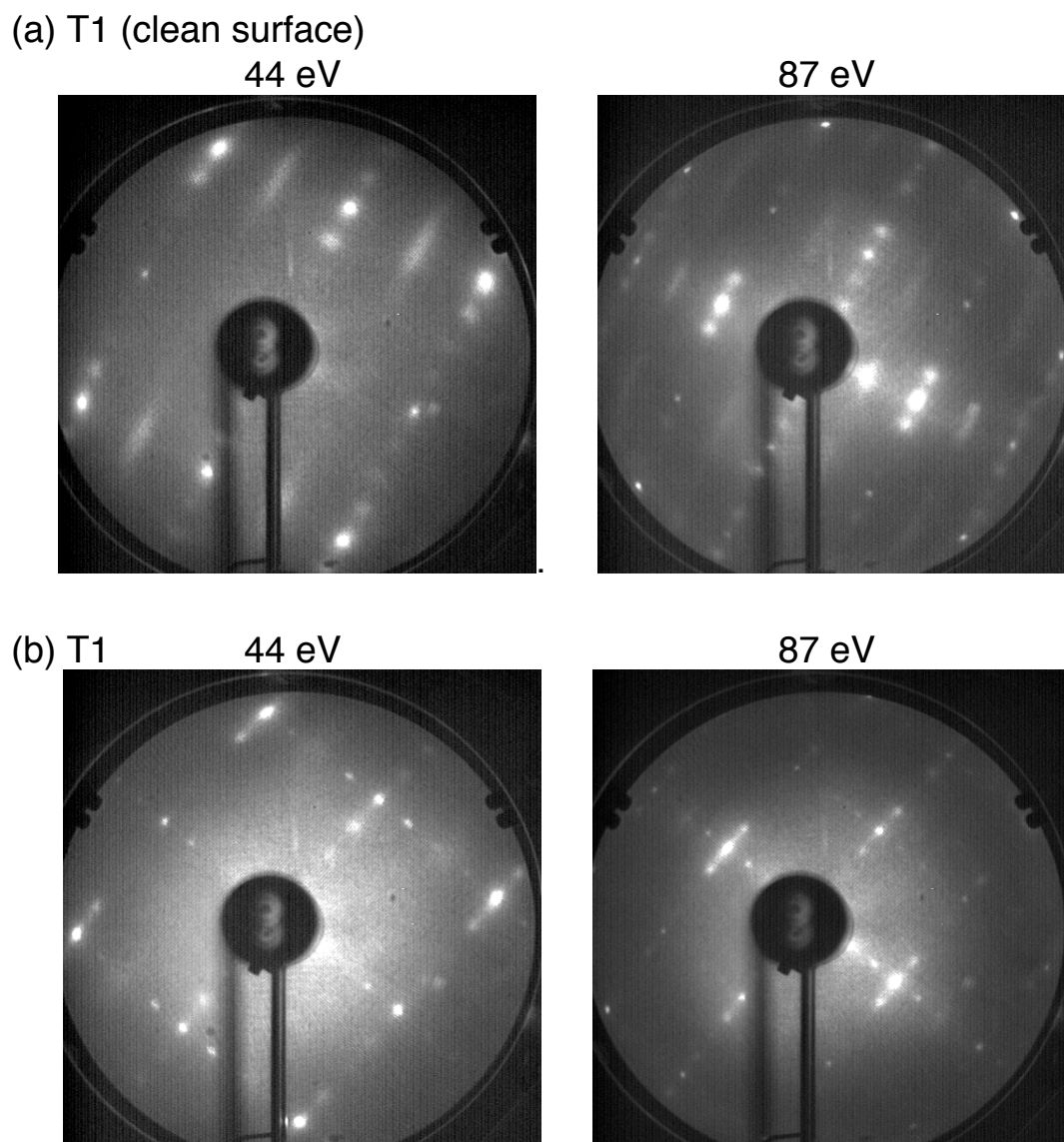


Figure 6.7 A series of LEED patterns of the In-terminated GaAs(001) surface recorded at two different beam energies during the annealing experiment depicted in Figure 6.6(b). (a) shows the LEED patterns of the clean surface annealed at T1 prior to the In deposition. (b) - (e) are the LEED patterns of the surface annealed at T1, T2, T3 and T4 following the initial deposition of roughly 0.4 ML of In.

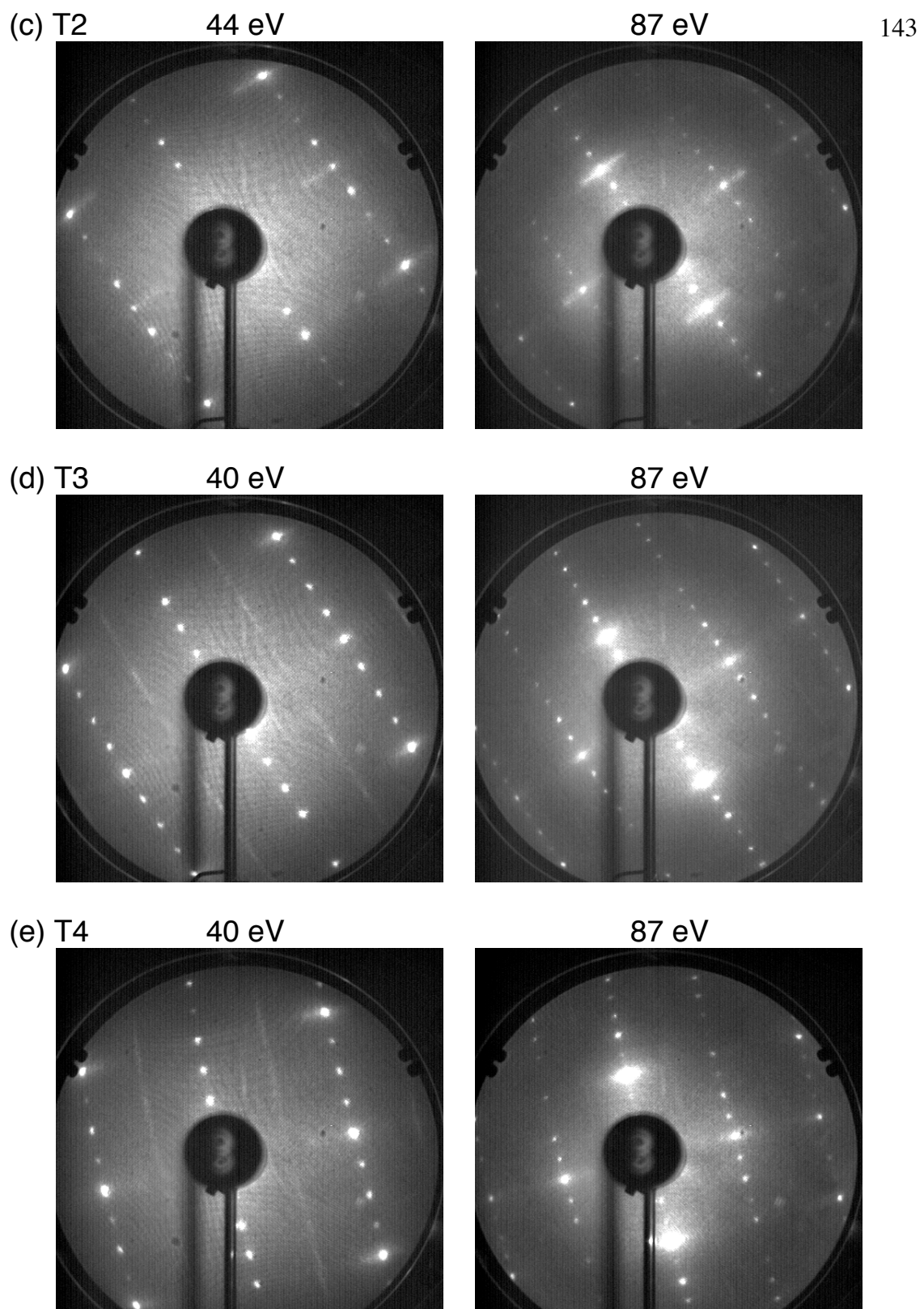


Figure 6.7 (Continued)

T1, T2, T3 and T4 in Figure 6.6(b). The surface exhibited a mixture of the (2×4) and (4×2) symmetries after being annealed at T1 (420 °C). Below T1 the LEED pattern remained (2×4) as was for the clean surface [56]. It transformed to a (4×1) pattern with short streaks along the [110] direction through the 1×1 spots as the temperature increased to T2 (450 °C). A sharp (4×2)/c(8×2) LEED pattern appeared at T3 (480 °C), indicating the completion of the (2×4)-(4×2) transition and the formation of a stable structure involving In adatoms. The LEED pattern remained essentially unchanged even after the In had completely desorbed at T4 (520 °C). It is expected that this final (4×2) surface was due to a Ga termination. It is interesting to note that the same Ga-rich (4×2) LEED pattern was not observed for a clean GaAs(001) surface during a similar annealing experiment up to 650 °C.

6.3.2 XSW measurements

The XSW measurements were conducted at beamline X15A of the National Synchrotron Light Source (NSLS) at Brookhaven National Laboratory and at undulator beamline 12ID-D (BESSRC) of the Advance Photon Source at Argonne National Laboratory. The experiments focused on solving the In-terminated surface structures for In coverages lower than 0.25 ML, in which case less complexity is expected based on the STM images [55].

Figure 6.8 shows typical x-ray fluorescence spectra recorded from an In-terminated GaAs surface using a Si(Li) solid-state detector during GaAs(004) and (022) XSW scans

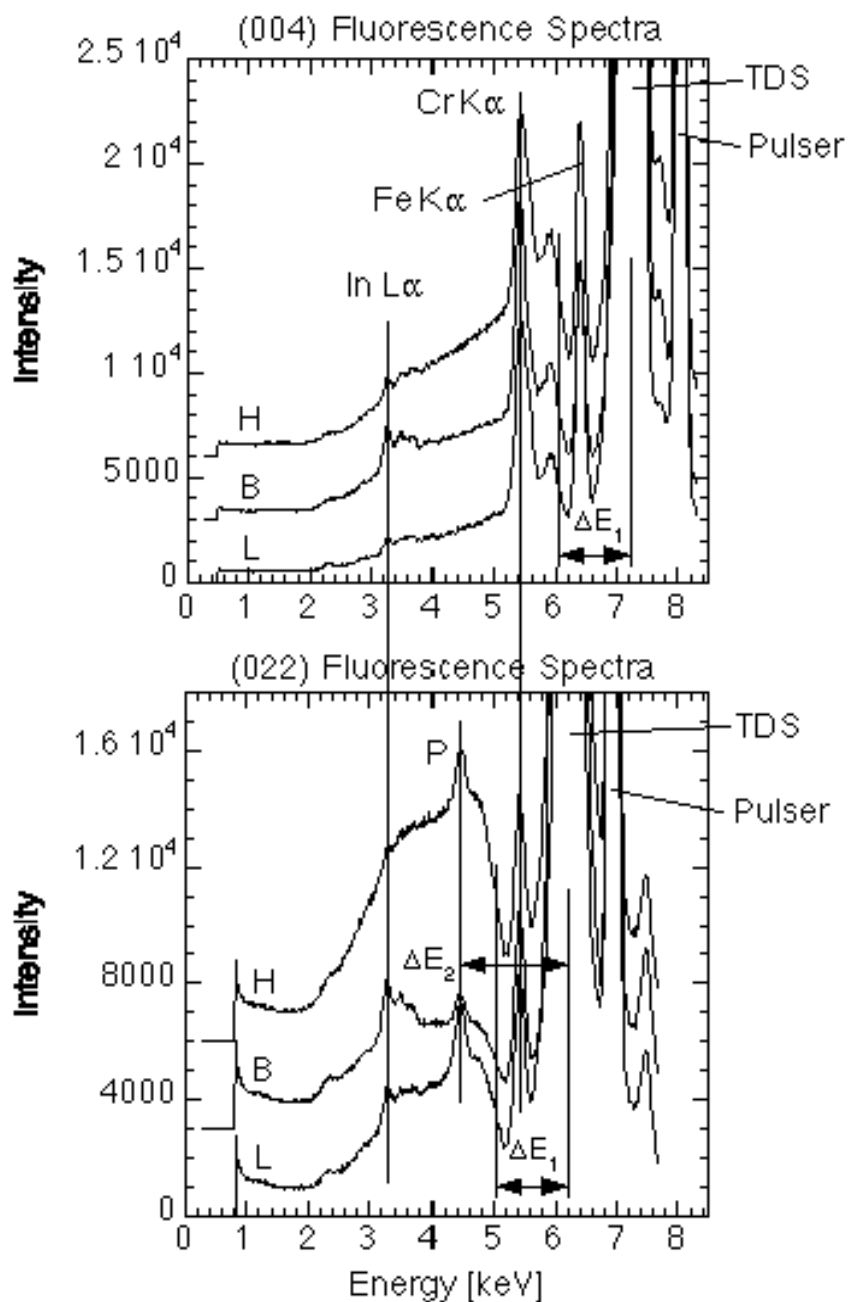


Figure 6.8 Typical x-ray fluorescence spectra from the (004) and (022) XSW scans measured from a GaAs(001):In surface. Three spectra are shown for each scan. The intensities were integrated over the incident angle for different ranges (see text). The incident beam energy E_γ was 7.3 keV for the (004) measurement and 6.2 keV for the (022) measurement.

at the NSLS. The three curves in each figure were the spectra integrated over angular ranges of the low-angle side (L) and the high-angle side (H) of the rocking curve as well as within the rocking curve (B). Angular modulations of the In L fluorescence intensities during the rocking curve scans are evident in the spectra. The high background levels around the In L peaks, which are more pronounced for the (022) scan due to the high takeoff angle of the fluorescence photons resulting from the experimental setup, exhibit a non-linear feature. This high background can be explained by an energy-loss process (Bremsstrahlung radiation) of the Ga and As L_{III} photoelectrons from the substrate, which leads to the characteristic edges about $\Delta E_1 = 1.2$ keV below the thermal diffuse scattering (TDS) peaks. The curvatures of the backgrounds below the edges were mainly caused by the absorption of the 0.005" Be window between the sample and the fluorescence detector [60].

Figures 6.9 - 14 show five sets of experimental XSW data (filled circles) and the best fits (solid lines) of the normalized In $L\alpha$ fluorescence yields to the data [Eq. (2.72)] and the reflectivities R versus the incident angles θ . The surfaces measured in these data sets were covered by 0.2 – 0.4 ML of In. All the In depositions were on the GaAs(001)(2 \times 4) reconstructed surface at room temperature followed by an anneal at elevated temperatures between 420 °C and 480 °C. The samples were prepared from As-protected GaAs(001) wafers (see Chapter 5) and attached using indium to Si substrates at 155 °C, which were then mounted onto Mo sample holders before being loaded into the UHV system. Table 6.1 summarizes the surface preparation conditions and the

Table 6.1 The calibrated In coverages (Θ_{In}), annealing temperatures (T_{anneal}), LEED patterns and the results of the XSW analysis of the four GaAs(001) samples (S1 through S4) used in the present study.

Sample	Θ_{In} (ML)	T_{anneal} (°C)	LEED	XSW H	Figure	f_{H}	P_{H}
S1*	0.3	480	(4×2)/	(004)	6.9(a)	0.60 ± 0.09	1.14 ± 0.02
			c(8×2)	($\bar{1}$ 11)	6.9(b)	0.57 ± 0.01	1.00 ± 0.01
				(111)	6.9(c)	0.28 ± 0.01	0.67 ± 0.01
S2*	0.2	480	(4×2)/	(004)	6.10(a)	0.46 ± 0.04	1.14 ± 0.02
			c(8×2)	($\bar{1}$ 11)	6.10(b)	0.59 ± 0.02	0.99 ± 0.02
				(111)	6.11(b)	0.37 ± 0.02	0.66 ± 0.02
				(022)	6.11(a)	0.43 ± 0.03	0.54 ± 0.02
S3*	0.4	450	(4×1)**	(004)	6.12(a)	0.37 ± 0.05	1.13 ± 0.02
				(022)	6.12(b)	0.03 ± 0.03	
S4 [#]	0.2	≤ 420	(2×4)	(004)	6.13(a)	0.55 ± 0.02	1.00 ± 0.01
				(022)	6.13(b)	0.33 ± 0.03	0.85 ± 0.01
S4 [#]	0.2	450	(4×1)**	(004)	6.14(a)	0.27 ± 0.03	0.96 ± 0.02
				(022)	6.14(b)	0.23 ± 0.03	0.65 ± 0.03

* Experiments were conducted at the NSLS/X15A.

[#] Experiments were conducted at the APS/12ID-D.

** The (4×1) pattern exhibited short streaks along the [110] direction through the 1×1 spots, similar to the one shown in Figure 6.7(c).

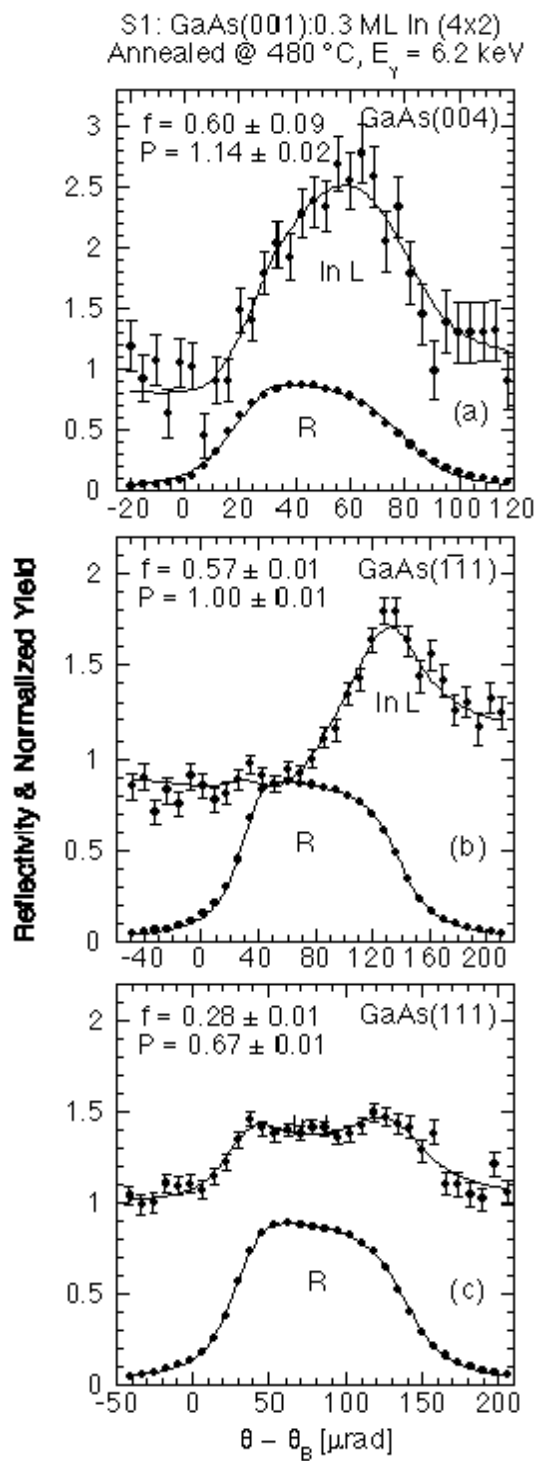


Figure 6.9 The (004), ($\bar{1}11$) and (111) XSW experimental data and analysis for sample S1.

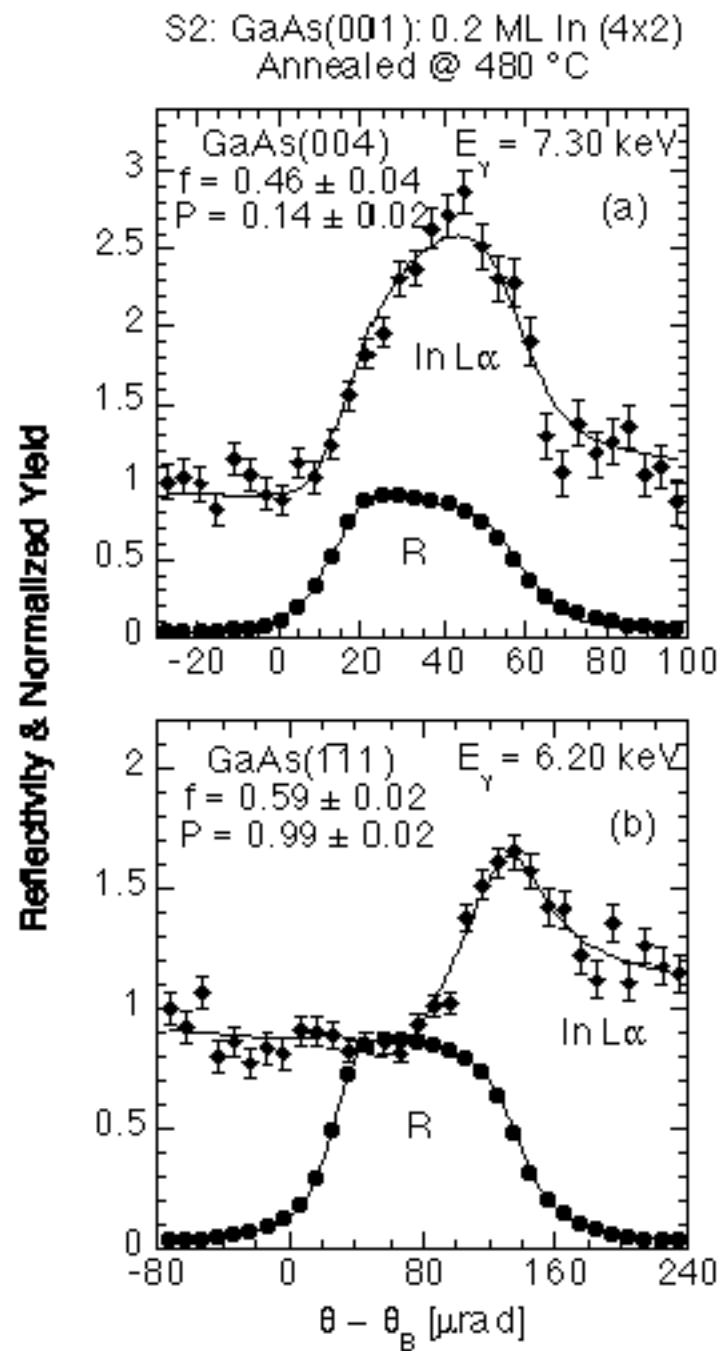


Figure 6.10 The (004) and ($\bar{1}\bar{1}1$) XSW data and analysis for sample S2.

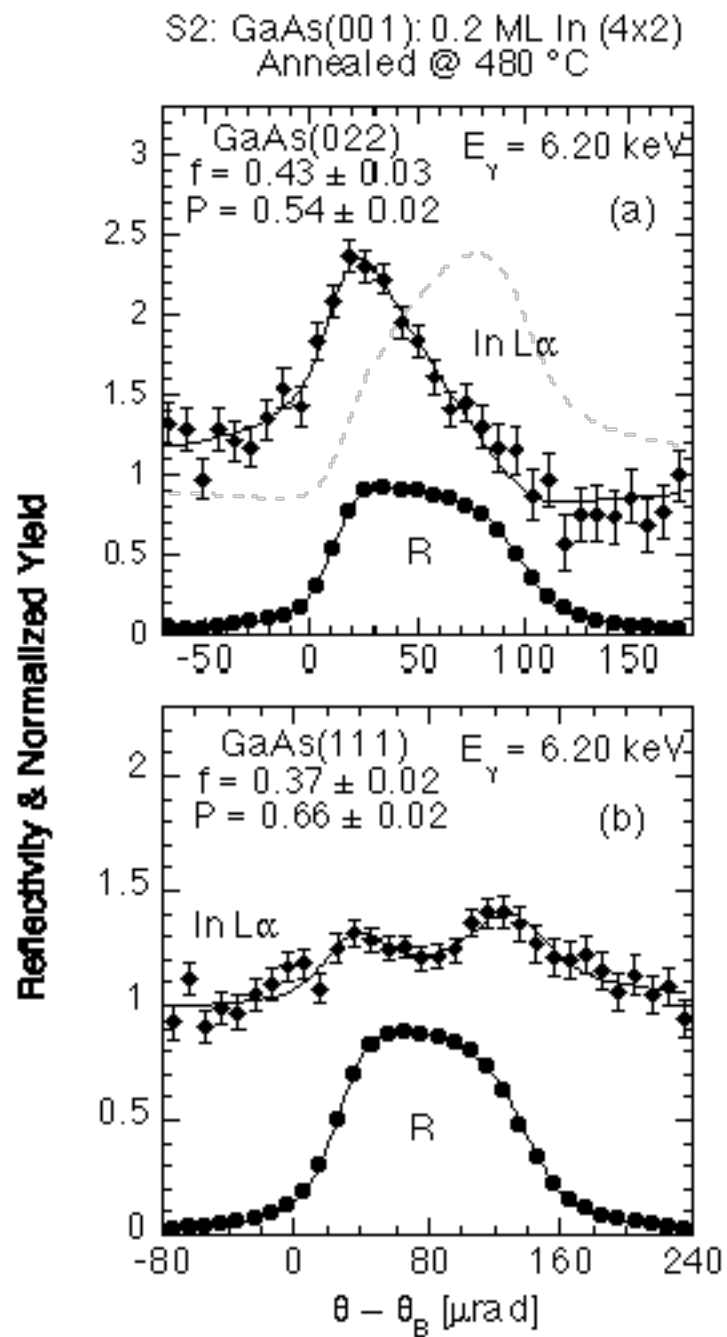


Figure 6.11 The (022) and (111) XSW data and analysis for sample S2.

S3: GaAs(001): 0.4 ML In Streaky (4x1)
Annealed @ 450 °C

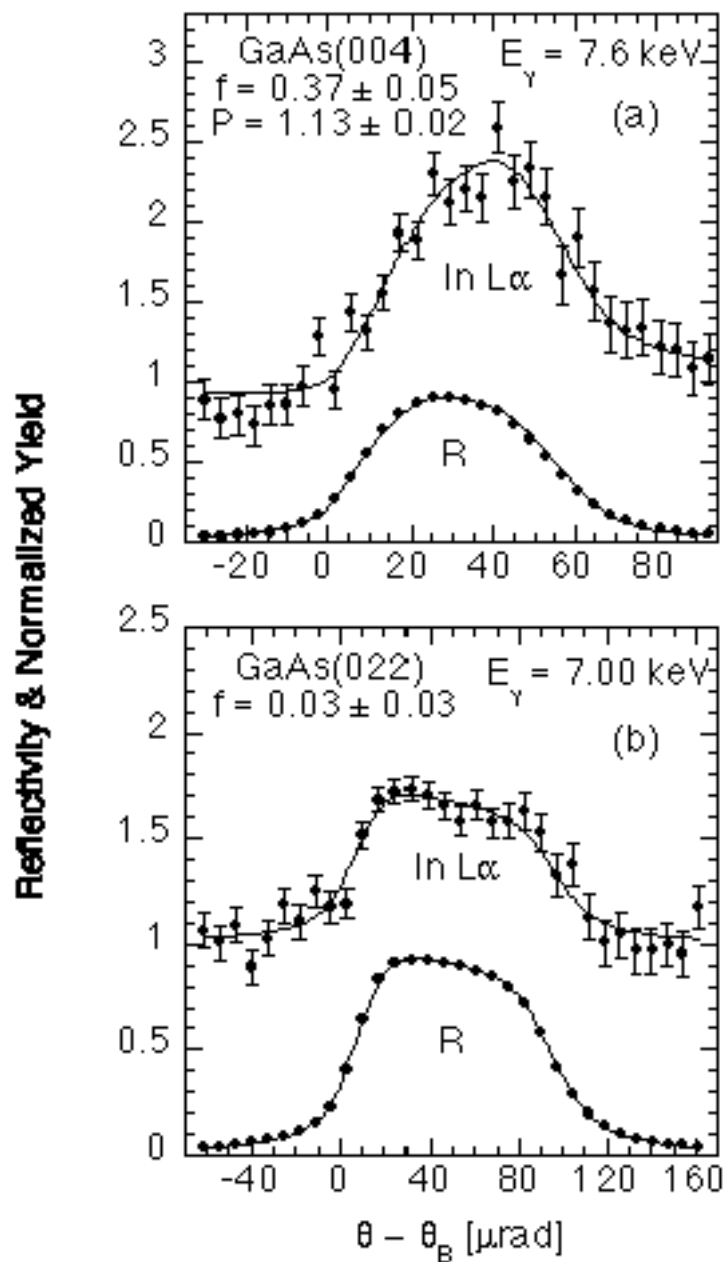


Figure 6.12 The (004) and (022) XSW data and analysis for sample S3.

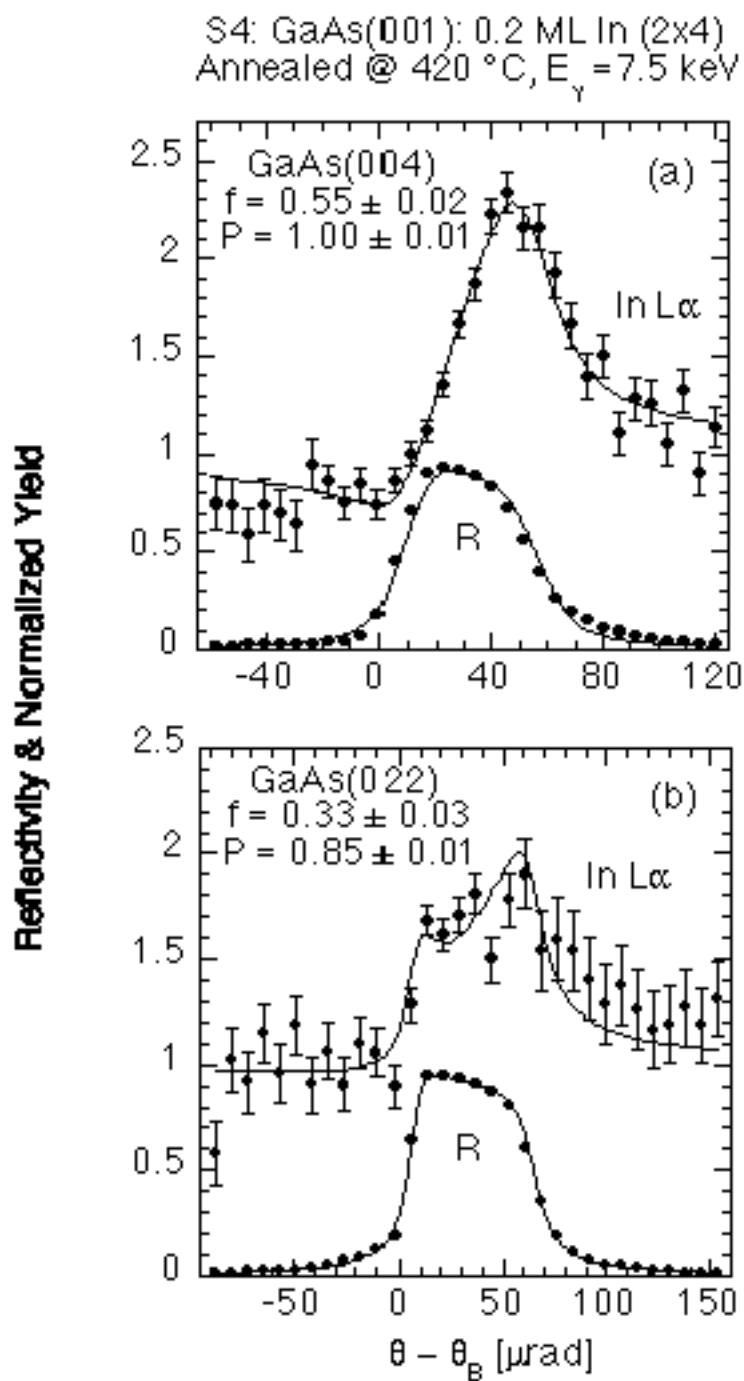


Figure 6.13 The (004) and (022) XSW data and analysis for sample S4 annealed at 420 °C.

S4: GaAs(001): 0.2 ML In Streaky (4x1)
 Annealed @ 450 °C, $E_\gamma = 7.5$ keV

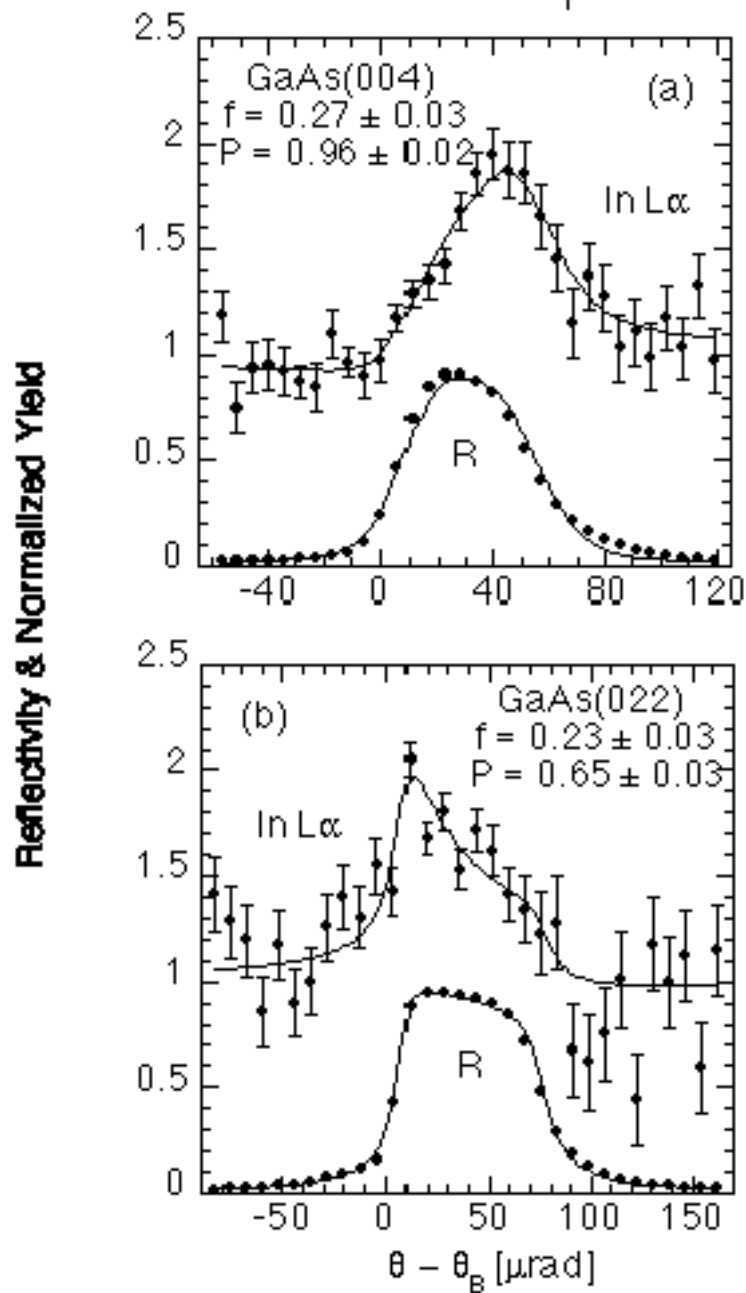


Figure 6.14 The (004) and (022) XSW data and analysis for sample S4 annealed at 450 °C.

results of the XSW analysis. The coherent fractions f_H and the coherent positions P_H were determined by χ^2 fits of Eq. (2.72) to the In $L\alpha$ fluorescent yields. The In surface coverages were estimated from a RBS-calibrated In MNN/Ga LMM Auger peak ratio. This ratio was determined to be approximately 1.3 for a full ML of In adsorbed on the GaAs(001) surface. The annealing temperatures were estimated based on direct temperature measurements using a pyrometer as well as the surface LEED patterns after heat treatments.

6.4 Discussions

6.4.1 XSW analysis: $(4\times 2)/c(8\times 2)$

We first consider samples S1 and S2 (Figures 6.9 and 6.10), both of which were annealed at 480°C and exhibited the sharp $(4\times 2)/c(8\times 2)$ LEED pattern. The coherent positions of the (004), $(\bar{1}11)$ and (111) reflections from S1 and S2 were essentially identical, indicating that the surface structures were similar, regardless of the slight coverage difference between S1 and S2. Since the data set from sample S2 contains one extra measurement at the (022) reflection, which has provided important structural information, the following discussion will be focused on the results of sample S2.

The (004) coherent fraction and the coherent position for sample S2 were determined to be $f_{004} = 0.46 \pm 0.04$ and $P_{004} = 1.14 \pm 0.02$. If we consider symmetric In dimers the major surface structure, as was proposed by Resch-Esser *et al.* for an In-

terminated GaAs(001) surface at $\Theta_{\text{In}} < 0.25$ ML, this measured P_{004} would directly locate the In dimer to be $P_{004}d_{004} = 1.61 \pm 0.03$ Å above the last substrate (004) diffraction plane. This In height is comparable to the bulk In position we reported earlier by XSW for a 1 ML InAs buried in a GaAs(001) matrix [7.10], but much lower than the Sb position measured on the GaAs(001):Sb (2×4) surface by XSW, as discussed in Chapter 5. Other (004) measurements at higher In coverages (data not shown) showed that f_{004} dropped drastically to around 0.15 as the coverage went beyond 0.5 ML, suggesting the development of a second structure. This is consistent with the ladder-type pattern observed by the STM study for $\Theta_{\text{In}} > 0.25$ ML.

Based on the (004) result, it is possible to calculate the coherent positions that would be expected at other Bragg reflections based on a simple structural model. Generally this can be achieved by using symmetry arguments. For the present semiconductor surface, a two-fold symmetry has to be satisfied by the adsorption sites for each surface structure. As a result, the average positions measured at the various Bragg reflections must finally intersect at a point on one of the two-fold axes normal to the surface (this would not be the case if the adsorbate occupies two or more than two non-equivalent two-fold symmetry sites). For example, Figure 6.15(a) shows the [110] projection of a (unreconstructed) GaAs(001) surface, where A, B, C and D are the locations determined by the (004) XSW result of S2 and two vertical mirror planes. For the $(\bar{1}\bar{1}1)$ reflection, the corresponding coherent positions (with $P_{\bar{1}\bar{1}1} = 0$ at the $(\bar{1}\bar{1}1)$ Ga planes) can be related to P_{004} by $P_{\bar{1}\bar{1}1} = (P_{004} + n)/4$, where $n = 3, 2, 1$ and 0 for A, B, C and D, respectively.

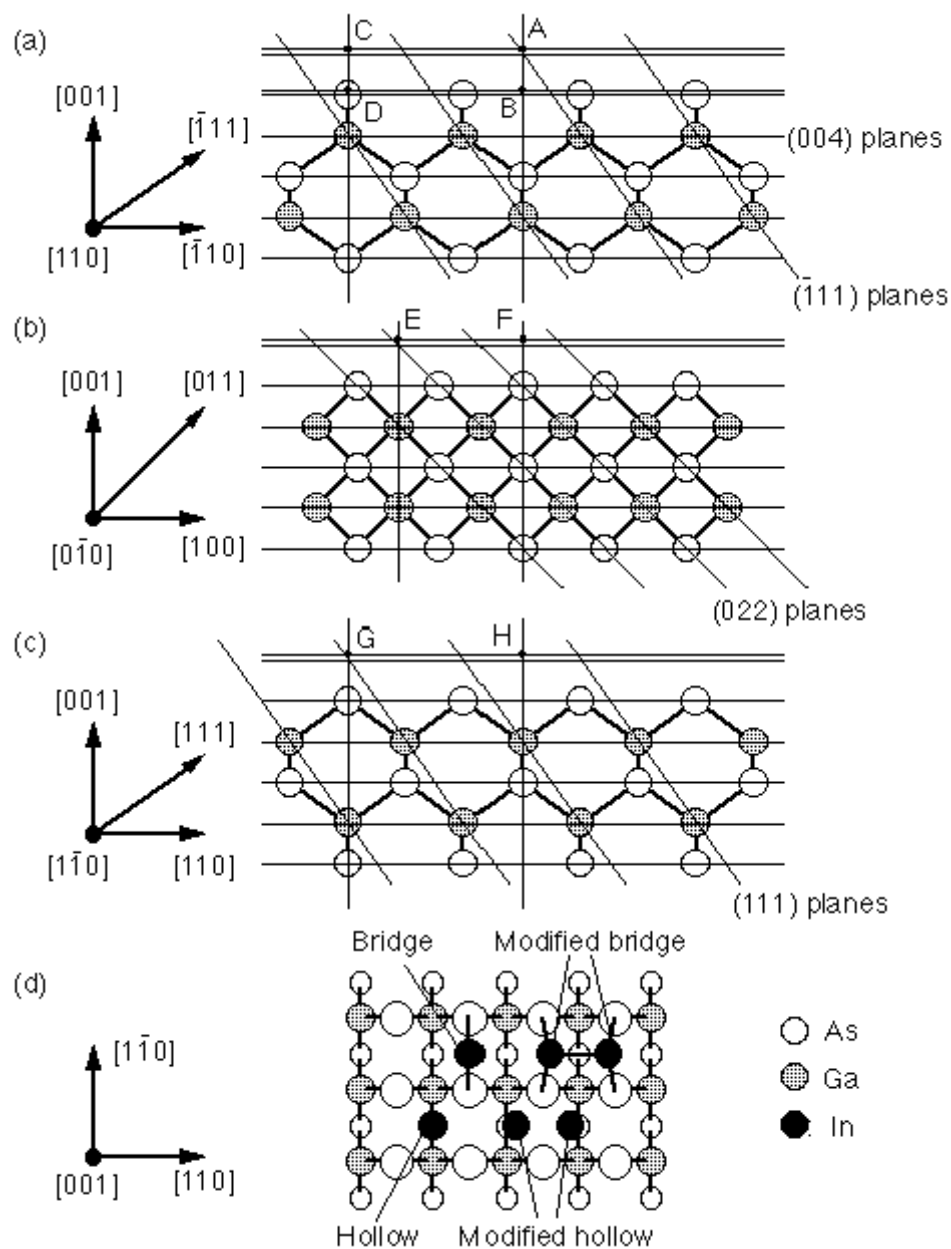


Figure 6.15 (a) - (c) The $[110]$, $[0\bar{1}0]$ and $[\bar{1}\bar{1}0]$ projected views of various symmetric sites (A – H) on the unreconstructed GaAs(001) surface. The vertical and horizontal dashed lines represent the two-fold symmetry axes and the measured In (004) coherent position for S2, respectively. (d) Possible adsorption sites on the GaAs(001) surface.

Therefore, by symmetry P_{111} is expected to be 1.04, 0.79, 0.54 or 0.29. Our $(\bar{1}11)$ measurement [Figure 6.10(b)] showed that $P_{111} = 0.99 \pm 0.02$, which agreed reasonably well with the In position located by site A. This implied that the distribution of the In adatoms, as projected back to a surface unit cell, was symmetric in the $[\bar{1}10]$ direction around the bulk mirror plane indicated by the dashed line through A and B in Figure.6.15(a) This result is consistent with the Resch-Esser's In-dimer model.

Using the same approach, two different sites on the $[0\bar{1}0]$ projection [E and F in Figure 6.15(b)] were considered to be the possible candidates for the average In position which satisfied both the two-fold symmetry and the (004) and $(\bar{1}11)$ measurements. Their (022) coherent positions were calculated to be 1.07 and 0.57 using the geometrical relationship $P_{022} = (P_{004} + m)/2$ with $m = 1$ and 0 for E and F, respectively. Notice that if the In adatoms form dimers as described by the Resch-Esser's model, the (022) XSW would measure the coherent position to be at point E (this includes the consideration of a reasonable In dimer bond length). The calculated In yield for $P_{022} = 1.07$ is plotted as a dash line in Figure 6.16(a). However, the best fit to the fluorescence data [solid line in Figure 6.16(a)] yielded $P_{022} = 0.54 \pm 0.02$, in good agreement with the symmetry site F. The contradiction between the (022) measurement and Resch-Esser's model (dashed line) was evident in Figure 6.16(a), where the modulations of the simulated and the best fit for the measured In yields were almost 180° out of phase with respect to each other. When combined with the $(\bar{1}11)$ result, the (022) measurement suggests that the In distribution is centered at a two-fold symmetry site above the hollow [Figure 6.15(d)]

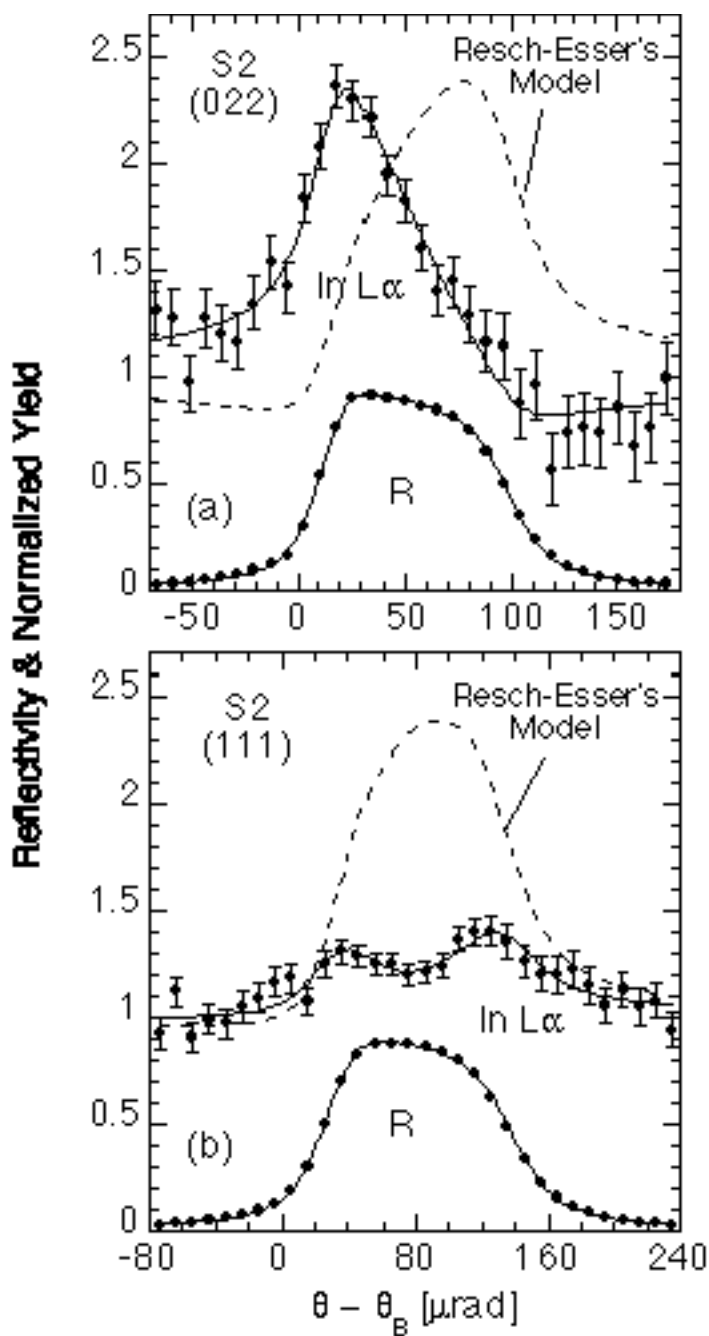


Figure 6.16 Calculated In fluorescence yields (dashed lines) based on Resch-Esser's model [Figure 6.4(a) and Ref. 55] compared with the present XSW measurements for sample S2 for (a) the (022) reflection and (b) the (111) reflection. The (004) coherent position for the model was assumed to be the same as the measured value (1.14).

surrounded by four As atoms in the first layer [B in Figure 6.15(a)], instead of being above the bridge between two neighboring As atoms along the $[\bar{1}10]$ direction [Figure 6.15(d) and A in 6.15(a)], as is the case for the Resch-Esser's model.

These two different local structures, the one observed by XSW and the one proposed based on STM, should also become distinguishable when projected into the (111) plane [Figure 6.15(c)]. Based on the measured P_{004} , P_{111} can be predicted by symmetry to be $P_{111} = (P_{004} + k)/4$ (with $P_{111} = 0$ at the (111) Ga planes) with $k = 3$ or 1 for the two possible two-fold symmetry sites G and H, respectively, in Figure 6.15(c). This simple formula renders $P_{111} = 0.54$ for G and 1.04 for H. It can be shown that the Resch-Esser STM model predicts the In position to be close to site G, while the (022) XSW is consistent with the In location at H. Figure 6.11(b) shows the (111) result and the P_{111} was measured to be 0.66 ± 0.02 . The discrepancy between this value and the estimated (111) position for site G [Figure 6.16(b)], along with the earlier discussion based on the (022) measurement, has led us to the conclusion that the detailed structure of the In-terminated GaAs(001) $(4 \times 2)/c(8 \times 2)$ reconstruction can not be described correctly by the Resch-Esser model. This also implies that the In-induced $(4 \times 2)/c(8 \times 2)$ surface does not form the same structure as the one generally accepted for the Ga-rich (4×2) clean surface. The disagreement between the (111) measurement and the predicted position at H is much smaller, but still exceeds the XSW experimental errors. This suggests that the In structure on the surface was not quite as simple as the single-site model used above.

We compare the calculated coherent positions based on the Resch-Esser's model and the hollow site H in Figure 6.15(c) with the XSW measurements on sample S2 in Table 6.2.

Table 6.2 The calculated coherent positions based on the Resch-Esser's model and the hollow site H in Figure 6.15(c) compared with the XSW results from sample S2. The (004) coherent positions were assumed to be the same as the measured value (1.14) for both calculations.

S2	Measured P	Calculated P (hollow site H)	Calculated P (Resch-Esser's Model)
(004)	1.14	<i>1.14</i>	<i>1.14</i>
(-111)	0.99	1.04	1.04
(111)	0.66	0.54	1.04
(022)	0.54	0.57	1.07

We have qualitatively determined the center of the In distribution based on the coherent positions measured at the various Bragg reflections. The next step would be to examine the distribution width of the In atoms around the center, which is directly related to the coherent fractions. To help the discussion to proceed, we first express the coherent fraction f_H as a product of three factors according to the convolution theorem as $f_H = C a_H D_H$, i.e., the product of the ordered fraction (C), the geometrical factor (a_H) and the Debye-Waller factor (D_H), as discussed in Chapter 5. Here we also use the D_H values of the bulk GaAs for the In adatoms ($D_{004} = 0.86$, $D_{111} = D_{\bar{1}\bar{1}\bar{1}} = 0.97$, and $D_{022} = 0.93$).

Our attention was first drawn to the fact that f_{111} is significantly lower than $f_{\bar{1}\bar{1}\bar{1}}$, and also that f_{022} is smaller than f_{004} . This variation in f_H implies that a_{111} and a_{022} are both less than unity, i.e., multiple positions along the [110] direction are expected for the In. This may be explained if we adopt an In dimer model, as is the case for the Sb-terminated GaAs(001) surface (see Chapter 5). We may assume that an attraction along the [110] direction brings two neighboring In atoms closer together and causes the local symmetry to change from 1×1 to 1×2 [the modified hollow site in Figure 6.15(d)]. We estimated the distance L between two In atoms for this 1×2 structure to be 3.33 \AA using the geometrical relationship $L = \frac{2d_{022}}{\pi} \cos^{-1}\left(-\frac{f_{022}D_{004}}{f_{004}D_{022}}\right)$ (see Chapter 5), assuming a simple dimer model. This large distance, as compared with the In covalent radius ($2r_{\text{In}} = 2.88 \text{ \AA}$), indicates that the dimerization of the In adatoms, if any, is very weak. This finding is consistent with the STM observations at low coverage [55] which showed that the straight lines corresponding to In atoms were formed by oval dots separated by 4 \AA

along the [110] direction, i.e., the local In arrangement had a $\times 1$ symmetry rather than the $\times 2$ period predicted by the Resch-Esser's model.

The above XSW analysis carried out on samples S1 and S2 (annealed at 480 °C) can be summarized as the following. The XSW measured In positions with respect to the substrate lattice showed clear disagreement with the previous $(4\times 2)/c(8\times 2)$ model proposed by Resch-Esser *et al.* [55], which was based on the structural model generally accepted for the GaAs(001) Ga-rich (4×2) reconstruction [74]. In Resch-Esser's model the In adatoms were located at the modified bridge sites (as are the cases for most of the dimerized (001) semiconductor surfaces) forming two In dimers per (4×2) unit cell in the first layer. Our off-normal XSW measurements (particularly the (022) measurement) indicated that for In coverages < 0.25 ML the In adatoms were most likely to occupy the two-fold symmetry site above the hollow among the 4 neighboring surface As atoms. Further analysis of the measured coherent fractions showed evidences that along the [110] direction the adjacent In atoms were either spaced with the 1-fold period or weakly dimerized. This finding was consistent with the high-resolution features revealed by STM.

6.4.2 Structural model for GaAs(001):In $(4\times 2)/c(8\times 2)$

To construct a complete structural model for the $(4\times 2)/c(8\times 2)$ unit cell requires further knowledge of the locations of the As and Ga atoms in the second and third layers,

which are not available from the present XSW studies. However, complementary information may be obtained from the previous STM studies.

Based on the high-resolution STM image shown in Figure 6.3(a), there are at least three features that need to be reasonably explained by the proposed model for a low In coverage. First, the bright straight lines parallel to the $[110]$ direction in the images have been identified indirectly to be In atoms. This was based on the fact that the straight lines were previously broken lines, which turned gradually into complete straight lines as the In coverage increased, and this was the only modification of the surface observed by STM during the sub-ML In deposition [62]. Notice that the surface In atoms showed much higher contrast in these images than the Ga atoms did in the images of the GaAs(001) Ga-rich (4×2) surface [75, 76]. This basically reflects the fundamental difference of the atomic electronic structures between the two elements. This high contrast shown by the In adatoms is consistent with what has been observed on the InAs(001) In-rich (4×2) surface by STM [9]. Furthermore, the local $\times 1$ symmetry exhibited by the oval spots along the In rows resolved in the STM images has to be satisfied by the proposed model. Second, the atomic arrangement of the bare surface in the trench areas for the proposed model needs to be able to yield a reasonable interpretation for the four (virtual) 1×1 faint spots observed in each (4×2) unit cell. Finally, the proposed model has to be successful in explaining the alignment in the $[\bar{1}10]$ direction between the faint spots in the trench areas and the bright oval spots along the In rows.

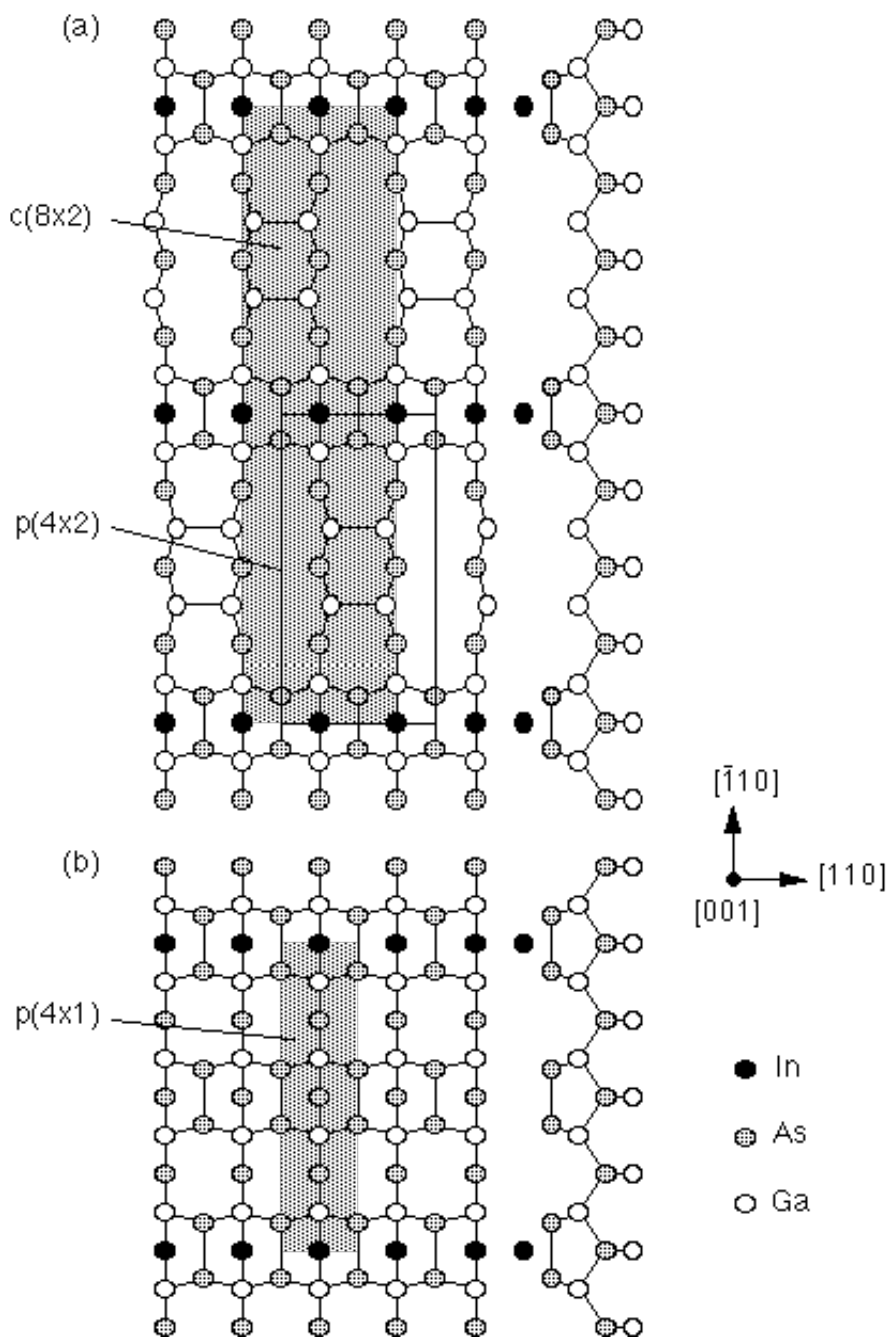


Figure 6.17 (a) The proposed $c(8 \times 2)$ model for the GaAs(001):In surface with an In coverage of 0.25 ML based on the present XSW analysis and the previous STM studies. Also shown is a (4×2) unit cell, which may coexist on the surface with the $c(8 \times 2)$ structure. (b) A (4×1) model constructed by changing the termination of the bare surface in the trenches from Ga dimers in (a) to As dimers (see text).

We now propose a new structural model for the In-induced GaAs(001) $(4\times 2)/c(8\times 2)$ surface for a low In coverage based on our XSW analysis and the previous STM observations. As shown in Figure 6.17(a), a $c(8\times 2)$ unit cell is denoted by the shaded area. It contains four In atoms per $c(8\times 2)$ unit cell in the first layer, corresponding to a coverage of 0.25 ML. The In atoms are located at the hollow sites surrounded by four As atoms in the second layer, consistent with the XSW measurements. In this model the As atoms in the second layer underneath the In rows are considered to be dimerized along the $[\bar{1}10]$ direction based on simple electronic considerations. Whether the In adsorption at the hollow sites will break the underlying As dimers or induce a more complicated local structure is still debatable and requires more experimental evidences. The surface In monomers are separated by 4 \AA and form rows in the $[110]$ direction, which agree with the $\times 1$ symmetry of the oval spots along the straight line observed in the STM images. The four-fold symmetry in LEED pattern corresponds to the 16 \AA spacing between the In rows in the $[\bar{1}10]$ direction. Notice that any model predicting the formation of In dimers is incompatible with the STM observations, as discussed earlier.

In Figure 6.17(a) the trench areas between the In rows are terminated by the Ga dimers in the third layer. The four Ga dimers in the trenches per $c(8\times 2)$ unit cell are considered to be responsible for the virtual 1×1 faint spots resolved in the STM images. It is interesting to notice that in Figure 6.3(a) the faint spots in the image actually appeared as packed in groups of four and exhibited locally a two-fold period along the $[110]$ direction (i.e., not truly 1×1). This is consistent with the dimerization of the Ga

atoms, which is usually expected to occur only in the [110] direction. These Ga dimers also lead to the global $\times 2$ symmetry observed in LEED. Furthermore, this structural model well explains the alignment between the oval dots and the faint spots in the STM images: In Figure 6.17(a) the positions of the In atoms in the [110] direction are in phase with the Ga atoms in the third layer. If the In atoms are removed from the surface, the structure in Figure 6.17(a) becomes the same as the $c(8\times 2)$ model proposed earlier by Skala *et al.* [3.55] for the GaAs(001) Ga-rich surface. It becomes also similar to the model proposed by Torrelles *et al.* [61] for the $\text{In}_{0.04}\text{Ga}_{0.96}\text{As}(001)$ (4×2) surface based on surface x-ray diffraction.

In Figure 6.17(a) a (4×2) unit cell is also shown based on our proposed model. The $c(8\times 2)$ unit cell is constructed by shifting the (4×2) unit cells (or the Ga dimers in the trenches) by 4 \AA along the [110] direction for every other rows. This shift is evident in many areas in the STM image in Figure 6.3(a).

The model in Figure 6.17(a), however, is still not completely satisfactory. One question is whether or not the Ga dimers in the trenches can be resolved in a filled-state STM image [62], as is the case in Figure 6.3(a). This concern arises from the fact that filled-state images are less sensitive to the Ga empty dangling bonds. One plausible solution would be to assume in the model that the trench areas are terminated by As dimers in the second layer [Figure 6.17(b)], whose dangling bonds could be resolved by filled-state STM and contribute to the 1×1 -like faint spots in the images. Nevertheless, this model would render a (4×1) rather than a $c(8\times 2)$ [or a (4×2)] LEED pattern, unless

the In adatoms are fully dimerized in the [110] direction. In addition, the positions of the In atoms are 180° out of phase in the [110] direction with the As dimers in the second layer, inconsistent with the STM results. We therefore concluded with the model shown in Figure 6.17(a).

It is somewhat surprising, in comparison with all the generally accepted models related to the GaAs(001) surface, that the In adatoms adsorb at the hollow sites and do not form In-In dimers. However, it is not unusual for In to form unexpectedly complex structures on semiconductor (001) surfaces. The In-terminated Si(001) and Ge(001) surfaces have been studied by LEED, STM, PES, photoelectron diffraction and surface x-ray diffraction [63 - 67]. It was reported that the Si(001) surface exhibited a (4×3) reconstruction upon the adsorption of 0.5 ML of In at a substrate temperature above 150°C . The structure of this surface has been recently determined by Bunk *et al.* [66] using surface x-ray diffraction and STM. The In adatoms were found all to be three-fold coordinated with the Si atoms, instead of forming In-In dimers. This is in contrast with the structure of the Si(001):Ga (2×2) surface of a similar coverage, which has been showed to form Ga-Ga dimers parallel to the underlying Si dimers [68].

6.4.3 XSW analysis: Streaky (4×1)

For samples S3 and S4, which were annealed at lower temperatures ($\leq 450^\circ\text{C}$), the results of the XSW measurements were less conclusive. The surface of S3 was deposited with 0.4 ML of In and annealed at 450°C . The LEED study afterwards revealed a (4×1)

pattern with short streaks along the [110] direction through the 1×1 spots, indicating the structural transition from the As-rich (2×4) to the In-rich (4×2) was incomplete. The experimental values of f_{004} and P_{004} [Figure 6.12(a)] were reasonably close to the previous results from samples S1 and S2. Interestingly, the (022) coherent fraction was measured to be close to zero. This could be due to the high In coverage and low-temperature annealing, which resulted in a surface structure having two In sites that were 180° out of phase to each other with respect to the (022) planes.

Sample S4 was the only one measured at the 12ID beamline of the BESSRC CAT, after the entire UHV system was relocated from the NSLS to the APS. The In coverage was estimated to be 0.2 ML. The first two XSW measurements (Figure 6.13) were carried out after the surface was annealed at about 420°C . The LEED pattern remained (2×4) at this stage. The sample was then annealed again to about 450°C before the second part of XSW measurements (Figure 6.14). Upon the second annealing the (2×4) pattern vanished and turned into a (4×1) symmetry similar to the one observed on sample S3. The (004) XSW measurements showed a reduction of the coherent fraction after the second annealing, which was consistent with the incomplete (2×4)-(4×2) transition suggested by the streaky (4×1) LEED pattern. It is interesting to notice that the surface structure was able to yield a high In (004) coherent fraction even before the stable (4×2) reconstruction began to develop. More surprisingly, the measured (004) coherent positions of sample S4 were much lower than those from the previous samples. The (022) measurement indicated that the center of the in-plane distribution of the In

atoms was shifting from a bridge-site-like position towards a hollow-site-like position during the (2×4) - (4×2) transition.

The above XSW and LEED studies demonstrated how sensitive the structure of the GaAs(001):In surface was to the overall preparation conditions, in particular the annealing temperature. However, due to the limitation of time, the XSW experimental setup used at the APS for sample S4 was far away from being optimized, particularly for detecting low energy (< 4 keV) fluorescence x-rays from adsorbates of less than 0.5 ML [69]. Further XSW measurements are necessary to confirm the results on sample S4.

6.5 Summary

We have investigated the surface structure of the In-induced GaAs(001) $(4\times 2)/c(8\times 2)$ reconstruction for In coverages < 0.5 ML using LEED, Auger and XSW. Indium was deposited at room temperature onto the GaAs(001) (2×4) surface prepared by thermally desorbing an As protective layer. A sharp $(4\times 2)/c(8\times 2)$ LEED pattern was observed after the substrates were annealed at 480°C . Further annealing at $\geq 500^\circ\text{C}$ resulted in complete desorption of the In adatoms. The XSW analysis on the surfaces terminated with 0.2 – 0.3 ML of In annealed at 480°C showed clear disagreement with the previous model proposed by Resch-Esser *et al.* [55], which was based on the structure widely accepted for the GaAs(001) Ga-rich (4×2) reconstruction. It predicted the formation of two In-In dimers per (4×2) unit cell in the first layer over the modified bridge sites. Surprisingly, we found that the In adatoms were located above the hollow

sites, and the formation of In-In dimers was unlikely. Based on our findings and the previous STM studies we proposed a new $(4\times 2)/c(8\times 2)$ model for this surface. It is characterized by In monomers lining up at the hollow sites above As dimer rows with the trench areas between the In rows terminated with Ga dimers in the third layer. Each $c(8\times 2)$ unit cell contains four In monomers, leading to a coverage of 0.25 ML. The $\times 2$ symmetry is due to the Ga dimerization in the $[110]$ direction. The $8\times$ symmetry is due to the 16 \AA separation in the $[\bar{1}10]$ direction between the In rows as well as the 180° phase shift of the Ga-dimer positions along the $[110]$ direction between the adjacent rows. This model agrees qualitatively with the present XSW results and is able to explain most features observed by STM. However, quantitatively the agreement between the model and the XSW measurements is unsatisfactory. This suggests that the real structure of the surface may be more complicated. Further modification of this model is expected in the future upon the availability of new experimental evidence [70].

Chapter 7 Stains and Lattice Distortions in Buried Heterolayers

7.1 Introduction

X-ray standing wave measurements were used to study the strain in one ML of pseudobinary semiconductor alloys buried in (001) and (111) substrates [1]. For the (001) direction $\text{In}_x\text{Ga}_{1-x}\text{As}$ monolayers were grown in GaAs(001) by molecular beam epitaxy. The measured In position along the [001] direction exhibited a nearly linear dependence on the In concentration x , thus supporting the validity of macroscopic continuum elasticity theory at the one ML limit. A random-cluster calculation using the Keating valence force field was performed to explain microscopically the origin of the vertical expansion of the strained ML observed by the experiment. The calculated As-In-As bond angle and the positions of the first nearest neighbor As atoms of In suggest that the nearly linear dependence of the In height on the alloy composition is a combined result of the As-In-As bond bending and the local lattice distortion at the GaAs/ $\text{In}_x\text{Ga}_{1-x}\text{As}$ interface. The calculated In-As and Ga-As bond lengths were found to depend weakly on the In concentration, consistent with an earlier calculation for the case of a thick $\text{In}_x\text{Ga}_{1-x}\text{As}$ film on GaAs(001) and the available EXAFS data. In addition, we applied the evanescent-wave-emission effect to directly measure the vertical displacement of the GaAs cap induced by the strain in a buried InAs layer. The measured cap displacement showed good agreement with the In position and continuum elasticity theory. Nevertheless, our off-normal {111} XSW measurements revealed an unexpected anisotropic In distribution in the buried layers.

For the (111)-oriented strained layers, InSb(111)/ 1 ML InAs_xSb_{1-x} heterostructures were measured by XSW and EXAFS. The XSW measured As (111) positions in the films showed a strain effect much larger than what was suggested by continuum elasticity theory. However, the EXAFS measurements detected no significant bond length split between the in-plane and out-of-plane In-As bonds, which was predicted by a random cluster calculation using Keating valence force field to be as large as 0.05 Å for x = 1.

7.2 Strains in GaAs(001)/InGaAs

Highly strained III-V semiconductor heterostructures, e.g. InGaAs/GaAs, have been widely investigated and used in devices such as high-speed transistors and quantum-well lasers [2]. Recent studies of monolayer-period strained III-V superlattices have demonstrated great potential in forming a new type of nanostructure with enhanced optical properties [3]. In predicting electronic and optical properties, continuum elasticity theory is used to evaluate the strain state [4]. In a planar pseudomorphically-grown heterostructure, the film is constrained to have the same in-plane lattice parameters as the substrate, while it is free to relax in the growth direction. This results in a distortion of the unit cell of the film. Based on macroscopic continuum elasticity theory, for cubic materials with the film parallel to the (001) plane, the strain normal to the (001) plane (ϵ_{\perp}) is related to the in-plane strain (ϵ_{\parallel}) by (Appendix A):

$$\epsilon_{\perp} = -2 \frac{C_{12}}{C_{11}} \epsilon_{\parallel} , \quad (7.1)$$

where C_{ij} are the bulk elastic constants for the embedded material. For InAs/GaAs, these constants are $C_{11} = 8.329 \times 10^6 \text{ N/cm}^2$ and $C_{12} = 4.526 \times 10^6 \text{ N/cm}^2$ for InAs [5], and the lattice misfit between InAs and GaAs leads to $\varepsilon_{\parallel} = -6.7\%$. Thus, Eq. (7.1) predicts a strain of $\varepsilon_{\perp} = 7.3\%$ for a pseudomorphic InAs layer buried in GaAs(001). Experimental evidence from Brandt et al. [6], based on a high-resolution electron microscopy (HREM) analysis, showed good agreement with Eq. (7.1) for a 3 monolayer (ML) InAs sample, but gave a much larger ε_{\perp} (12.46%) for a sample with one ML of InAs. This discrepancy has drawn attention to the issue of whether macroscopic elasticity theory can correctly describe the strain in an ultra-thin film [7 – 11].

In the present work, we performed an x-ray standing wave (XSW) study to directly measure the strain in one ML of $\text{In}_x\text{Ga}_{1-x}\text{As}$ buried in GaAs(001) by precisely locating the indium position relative to the underlying GaAs substrate unit cell. These results are shown to agree favorably with the macroscopic continuum elasticity theory. In addition, I carried out a random-cluster calculation for a buried ML using the Keating valence-force field to understand the local structural variations in the thin heterolayers. This calculation provides us with more insight into the microscopic behavior of strain in ML-thick films.

The films were grown by conventional molecular-beam epitaxy (MBE) on semi-insulating polished GaAs substrates cut within 0.5° of the (001) plane. The substrates were cleaned with acetone and methanol and mounted using indium on a silicon block that served as a resistive heating element. They were then inserted into the MBE chamber and annealed for 10 minutes at a substrate temperature $T_s = 570^\circ \text{ C}$ in a $2 \times 10^{-3} \text{ Pa As}_4$ overpressure. In situ substrate cleaning was carried out with 1 keV Ar ions impinging at 15° from the surface in the [001] direction up to a dose of $2.3 \times 10^{16} \text{ cm}^{-2}\text{s}^{-1}$ at the same

T_s and As_4 ambient. These bombardment conditions for as-prepared GaAs substrates have been shown to yield smooth, essentially defect-free GaAs surfaces [12]. A 2 μm GaAs buffer layer was first grown on the sputter-cleaned GaAs surface at $T_s = 570^\circ\text{C}$. During the last 1000 \AA of the buffer-layer growth, T_s was ramped down to 500°C . One ML of $\text{In}_x\text{Ga}_{1-x}\text{As}$ was then deposited at 500°C followed by a 100- \AA -thick GaAs capping layer grown at the same T_s . Three samples with different In concentrations were prepared for the XSW measurements.

The chemical composition of each buried layer was measured by fluorescence yield analysis using an In-implanted Si crystal with a concentration calibrated by Rutherford backscattering as the standard. By comparing the fluorescence yields of the samples to those of the standard, the absolute In coverages of samples A, B and C were determined to be 0.4, 0.6 and 1.1 ML, respectively, with an estimated uncertainty of 0.1 ML. By applying Eq. (7.1), and assuming Vegard's law, the macroscopic elasticity theory predicts the perpendicular strains within the $\text{In}_x\text{Ga}_{1-x}\text{As}$ layers of sample A, B and C to be 2.7%, 4.1% and 7.3%, respectively.

The XSW experiments were performed at beamline X15A of the National Synchrotron Light Source (NSLS) [13]. The measurement consists of simultaneously recording the fluorescence spectra and the reflectivity from a sample while scanning a double-crystal Si(004) monochromator in energy through the (004) Bragg reflection of the GaAs substrate [14]. This scan causes the standing wave to phase shift inward by one-half of a d-spacing relative to the hkl diffraction planes, and induces a characteristic modulation of the fluorescence yield. The samples were kept in a helium atmosphere throughout the x-ray measurements in order to eliminate Ar $K\alpha$ from the fluorescence spectrum and to

reduce the attenuation of the low energy fluorescent x-rays. The data were analyzed based on von Laue and Ewald's dynamical-diffraction theory [15] and the procedure described in Section 2.3.

Table 7.1 Results of the (004) XSW measurements. The coherent fractions f_{004} and coherent positions P_{004} were determined by χ^2 fit of Eq. (2.72) to the data. The theoretical values of ε_{\perp} and P_{004} were obtained by applying Eq. (7.1) and Eq. (7.2) for A and B, respectively, using calibrated x values. The ε_{\perp} of C was calculated for 1 ML of buried InAs. The theoretical P_{004} was derived from the (004) Fourier component of 1.1 ML of strained InAs (see text).

Sample	Thickness (ML)	x	f_{004}	P_{004}	ε_{\perp} theory	P_{004} theory
A	1	0.4	0.79 ± 0.02	1.05 ± 0.01	2.7%	1.056
B	1	0.6	0.77 ± 0.02	1.08 ± 0.01	4.1%	1.086
C	1.1	1.0	0.67 ± 0.02	1.165 ± 0.01	7.3%	1.165

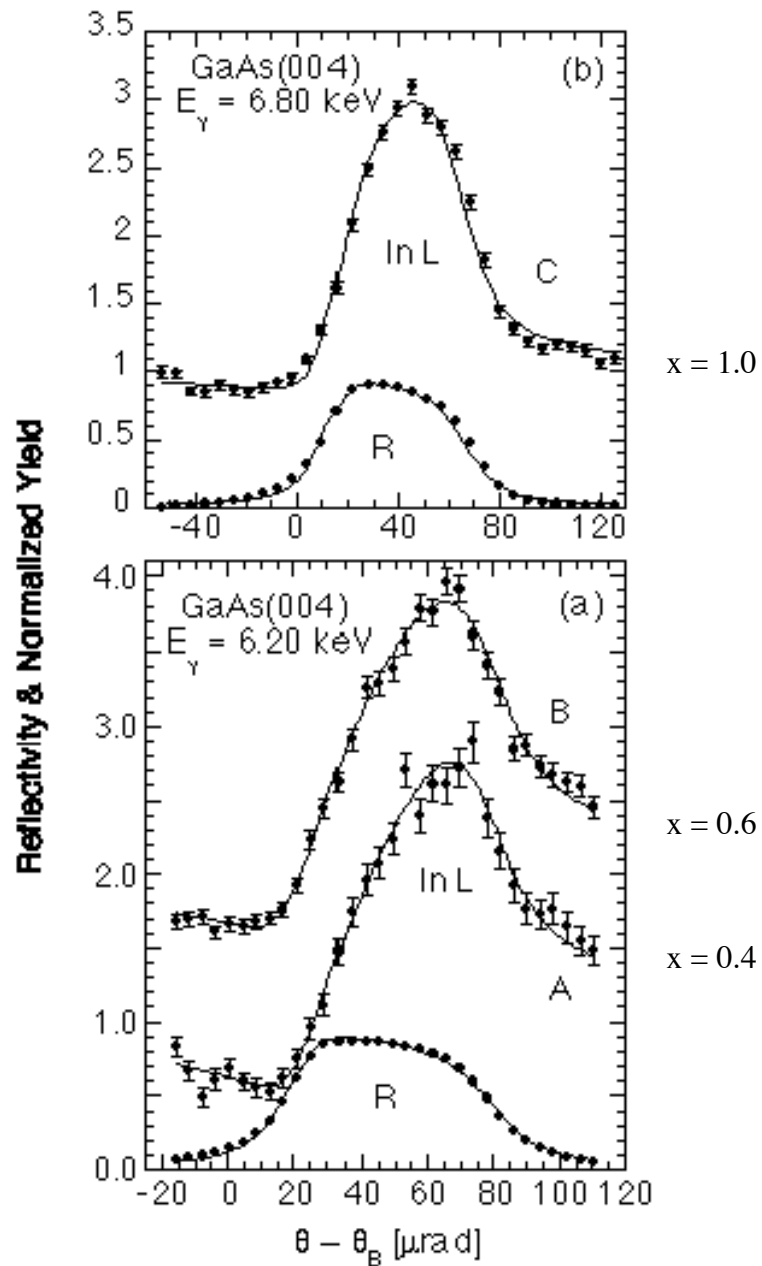


Figure 7.1 The (004) XSW data and the theory (solid lines) for the normalized In L fluorescence yields and the GaAs(004) reflectivity R versus incident angle θ for (a) samples A and B and (b) sample C (see text and Table 7.1). The In L curve for sample B is offset by 1 for the purpose of clarity.

Figure 7.1 shows the In L fluorescence yields as a function of the incident angle θ for samples A, B and C along with the (004) reflectivity R. The parameters of the XSW analysis, determined by the best fits of Eq. (2.72) to our data, are summarized in Table 7.1. For samples A and B, if one assumes that the In occupies only one lattice position when projected along the [004] axis, i.e., $a_{004} = 1$ [16], the In coherent fraction f_{004} should be close to the room-temperature GaAs(004) Debye-Waller factor $D_{004} = 0.86$ [17]. The present measured coherent fractions for A and B, when compared with D_{004} , can be interpreted to mean that 91% ($C = 0.91$) of the In atoms are located at the ordered positions defined by their P_{004} , and the remaining 9% are randomly distributed. The high measured values of f_{004} indicate that under the specified growth condition a buried heterostructure with 1 ML $\text{In}_x\text{Ga}_{1-x}\text{As}$ well confined in a single layer has been achieved.

The In coherent positions determined in Figure 7.1 are $P_{004} = 1.05 \pm 0.01$ for sample A and $P_{004} = 1.08 \pm 0.01$ for sample B, which locate the heights of the In to be $1.48 \pm 0.01 \text{ \AA}$ and $1.53 \pm 0.01 \text{ \AA}$, respectively, above the nearest As plane extrapolated from the substrate (Figure 7.2). Based on Vegard's law, the (004) d-spacing of cubic $\text{In}_x\text{Ga}_{1-x}\text{As}$ is 1.454 \AA for $x = 0.4$ and 1.474 \AA for $x = 0.6$. Therefore, our measurements have detected a vertical expansion of the buried layer due to the lateral compression. The elastic deformation of a unit cell can be, in general, described macroscopically by the continuum elasticity theory. However, when applying the same theory to a one-ML-thick strained film, certain issues must be considered more carefully. First, strain is a relative quantity; therefore, the placement of the boundary of the strain-affected region is more critical for the case of a buried single monolayer. Second, within the strained region, the lattice

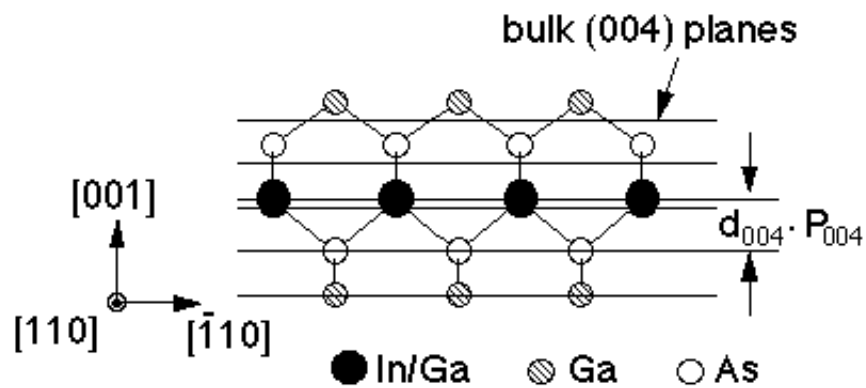


Figure 7.2 The $[110]$ projected side view depiction of a pseudomorphically grown 1 ML $\text{In}_x\text{Ga}_{1-x}\text{As}$ buried heterostructure. The dashed lines represent the (004) Ga and As planes of the GaAs substrate, and the solid line indicates the In/Ga position in the buried film with respect to the (004) planes.

deformation must be uniform to allow the strain calculated in Eq. (7.1) to be used for predicting the position of an atom in the strained layer. For an (001)-oriented film of zinc-blende structure, this uniformity is ensured by the fact that the four different directions along the tetrahedral bonds are all equivalent with respect to the in-plane stress imposed by the substrate. If we assume that the boundary of the strained region is at the nearest As planes above and below the $\text{In}_x\text{Ga}_{1-x}$ layer, the indium (004) coherent position can be related to the vertical strain ε_{\perp} by

$$P_{004} = (1 + \varepsilon_{\perp})a_{f0} / a_{s0} \quad , \quad (7.2)$$

where $a_{s0} = 5.6532 \text{ \AA}$ is the GaAs substrate lattice constant, and a_{f0} is the unstrained bulk lattice constant for the $\text{In}_x\text{Ga}_{1-x}\text{As}$ layer. Therefore, macroscopic continuum elasticity theory [Eq. (7.1)] predicts, through Eq. (7.2) and Vegard's law, that the In height P_{004} increases in a nearly linear manner from 0 to 0.15 as x varies from 0 to 1. In particular, Eq. (7.2) predicts that $P_{004} = 1.056$ for sample A and $P_{004} = 1.086$ for sample B, in good agreement with the present XSW measurements.

For sample C, the geometrical factor a_{004} is expected to be smaller than unity due to the multiple In positions. If we model the buried layer as one full ML of InAs plus 0.1 ML of InAs in the second layer, the In distribution could be characterized by two distinct lattice positions z_1 and z_2 , and the corresponding (004) Fourier component would become $CD_{004}[0.91\exp(2\pi iz_1) + 0.09\exp(2\pi iz_2)]$. The vertical strain of 7.3% for InAs on GaAs(001) suggests that $z_1 = 0.15$ and $z_2 = 0.45$. We can therefore express the coherent

fraction to be $f_{004} = 0.76C$, which estimates $C = 0.88$ as compared with the measured $f_{004} = 0.67$. The coherent position calculated from this simple model is 1.165, in good agreement with the experiment as well.

On a microscopic scale, Woicik et al. recently reported bond length calculations based on a random-cluster approximation for tetragonally distorted $\text{In}_x\text{Ga}_{1-x}\text{As}$ layers on GaAs(001), GaAs(111) [18] and InP(001) [19]. Excellent agreement of these calculations with measurements has been demonstrated by EXAFS [19, 20] and diffraction anomalous fine structure (DAFS) [21]. Their (001) calculations showed that the In-As bond length in the strained film depended very weakly on the In concentration x , in contrast to the monotonous increase of the In height measured in our present work and predicted by macroscopic elasticity theory. The cluster used in Woicik's calculation, however, is for films much thicker than one ML. If the In-As bond length exhibits the same constancy behavior at the one ML limit, mechanisms other than bond stretching must exist to account for the variation of the In positions we measured. To understand microscopically how the lattice of a buried single layer responds to a biaxial stress, and to compare it with the macroscopic description of strain effect discussed above, we performed a similar random-cluster calculation for one ML of $\text{In}_x\text{Ga}_{1-x}\text{As}$ buried in GaAs(001). The results of our calculation agree well with the present XSW measurements as well as the previous theoretical predictions [18, 22] and experimental observations [9, 11, 20, 21] for the local structures of InGaAs strained layers.

Our calculation follows essentially the approach discussed in Ref. 18, which is a simplified version of the quasichemical approximation (QCA) developed by Sher et al. [23]. Figure 7.3 shows the 42-atom cluster together with the 44 medium atoms used in the present calculation. The cluster was constructed from a planar core to account for the

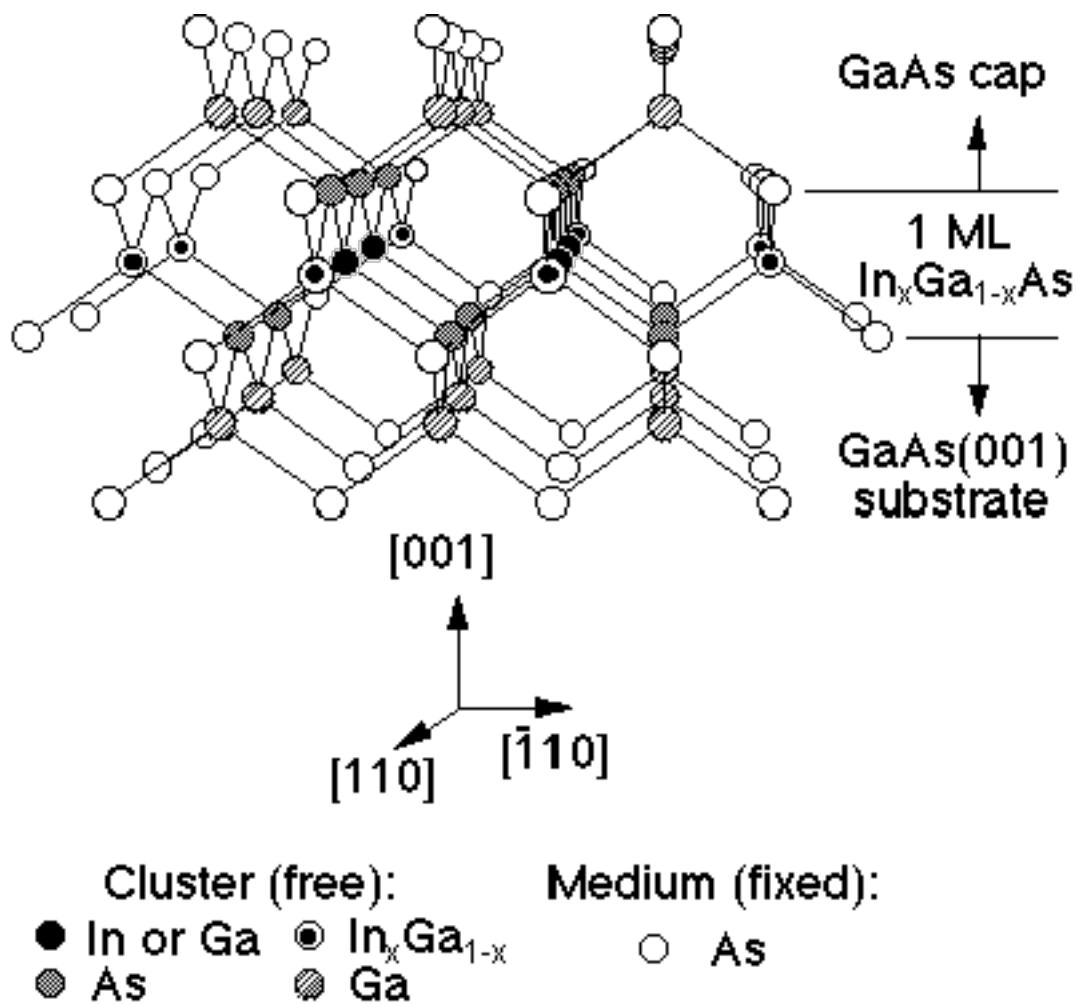


Figure 7.3 The 42-atom cluster and the surrounding 46 medium atoms used in the present calculation for 1ML $\text{In}_x\text{Ga}_{1-x}\text{As}$ buried in GaAs(001). During the energy minimization, only the atoms within the cluster are allowed to relax. The medium atoms are fixed at their tetragonally distorted virtual-crystal sites.

2-dimensional nature of the buried ML. The 4 cation sites at the center of the cluster are occupied randomly by j In atoms and $4-j$ Ga atoms. The 12 anions in the first shell are As atoms. In the second shell, the top and the bottom layers are occupied by 18 Ga atoms, and the middle layer is occupied by $8 \text{In}_x\text{Ga}_{1-x}$ virtual atoms (each one has the properties averaged over In and Ga based on x). Finally, there are 44 As atoms in the third shell. Statistically the QCA method requires the cluster to be independent of the surrounding matrix. To uncouple the cluster from the rest of the lattice, the 44 third-shell As atoms (or the medium atoms) are fixed at their tetragonally distorted virtual-crystal sites.

For the zinc-blende structure, the short-range interaction between atoms can be described by the Keating valence-force field [24] model, where the total strain energy of the system is expressed as a two-force-constant equation

$$E = \sum_i \frac{3}{8} \frac{\alpha_i}{r_{i,0}^2} (r_i^2 - r_{i,0}^2)^2 + \sum_i \sum_{j=1}^3 \sum_{k>j}^4 \frac{3}{8} \frac{\beta_{ijk}}{r_{ij,0} r_{ik,0}} \left(\mathbf{r}_{ij} \cdot \mathbf{r}_{ik} + \frac{r_{ij,0} r_{ik,0}}{3} \right)^2. \quad (7.3)$$

The first term is the strain energy due to bond stretching, characterized by the two-body radial-force constant α and summed over all the bonds within the cluster. The second term accounts for the strain energy due to bond bending, characterized by the three-body angular-force constant β and summed over all the atoms within the cluster [25]. The \mathbf{r} 's are the bond vectors between two neighboring atoms and the subscript 0 denotes a unstrained bond length. The energy due to chemical effects was ignored in this calculation [18]. To correct the overestimation of the strain energy caused by fixing the medium atoms in space [23], we weakened the cluster-medium interaction by setting $\beta = 0$ whenever a Ga-As bond between the third shell and a Ga atom in the top or the bottom layers of the second shell was involved in the calculation of the second term in Eq. (7.3). The third-shell As atoms

were allowed to have three-body angular interaction with the cluster only through the 8 $\text{In}_x\text{Ga}_{1-x}$ virtual atoms in the middle layer of the third shell. This is necessary in providing the rigidity against the lateral expansion of the $\text{In}_x\text{Ga}_{1-x}\text{As}$ ML.

All the atoms were initially located at their tetragonally coordinated virtual-crystal sites, which have the same in-plane coordinates as the GaAs substrate. The vertical initial position of each atomic layer was determined by minimizing the strain energy per $\text{In}_x\text{Ga}_{1-x}$ atom using Eq. (7.3) for an artificially constructed monolayer of $\text{In}_x\text{Ga}_{1-x}$ virtual atoms buried in GaAs(001). The 42 atoms within the cluster were then allowed to move until Eq. (7.3) reached its minimum [26]. For each composition, six different clusters were considered to explore all the possible arrangements for In or Ga to occupy the four cation sites at the center of the clusters. The structural dimensions obtained from the individual clusters were then averaged according to their population, which was determined by the Bernoulli distribution for a given x and the degeneracy of each cluster.

Figure 7.4, 5 and 6 show the results of the calculation averaged over the six clusters as a functions of the In concentration x . In Figure 7.4 we directly related the vertical positions of the atoms in the $\text{In}_x\text{Ga}_{1-x}\text{As}$ layer to the nearest (004) As plane extrapolated from the substrate. This was accomplished by assuming that the bottom As layer in Figure 7.3 is aligned with a substrate (004) plane. Figure 7.4(a) shows the calculated In coherent position P_{004} in unit of the GaAs (004) d-spacing. The cluster calculation predicts a nearly linear dependence of P_{004} on x , which is basically identical to the trend suggested by the macroscopic theory using Eq. (7.1) and (7.2). In Figure 7.4(a), the calculated curve

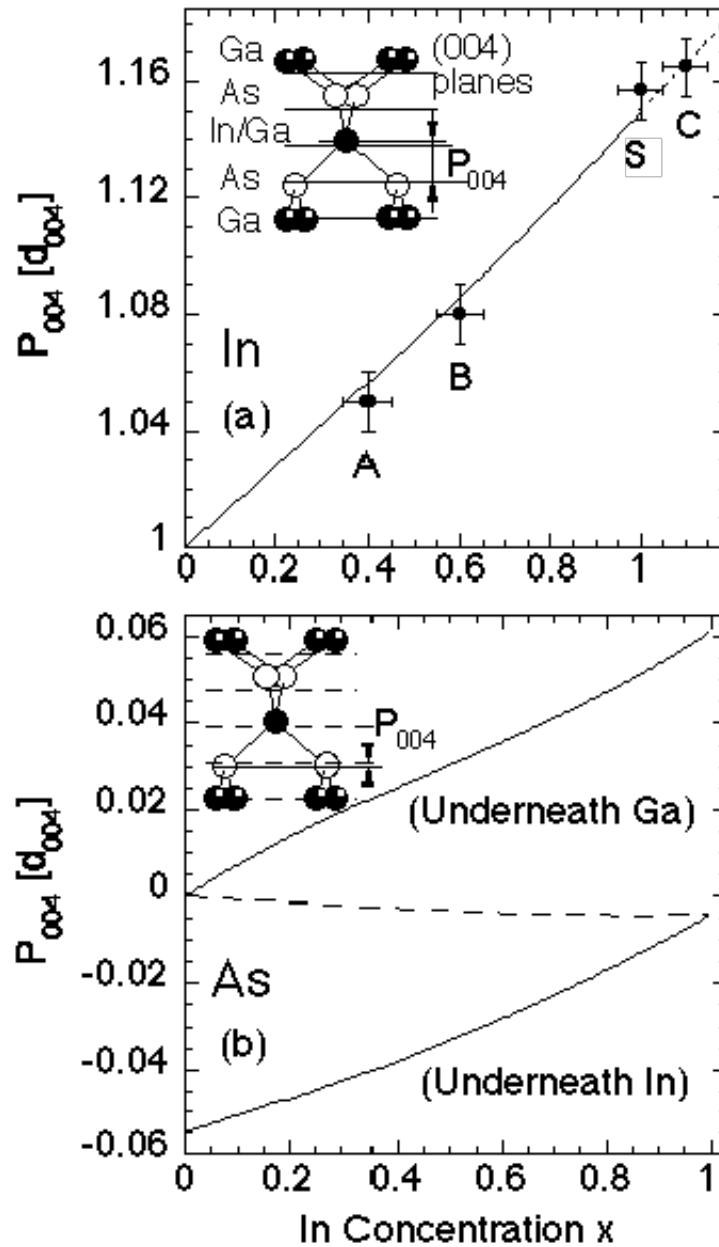


Figure 7.4 The calculated vertical positions with respect to the nearest substrate (004) As plane for (a) the In atoms and (b) the As atoms right below the $\text{In}_x\text{Ga}_{1-x}$ layer. The measured positions A, B and C in (a) are from the present XSW experiment. The data point S is the statistically averaged value of the In P_{004} positions for $x = 1.0$ in Ref. 9, 10, and 11. The dashed line in the $x > 1.0$ region in (a) is calculated assuming a full ML of InAs in the first layer plus a sub-ML of InAs in the second layer. The dashed line in (b) is the population-weighted average over the two solid lines.

agrees not only with the present XSW data (A and B) but also with the statistically averaged In position (1.157 ± 0.01) of three earlier measurements [9 – 11] for $x = 1.0$ (D).

Figure 7.4(b) shows the (004) positions for the As atoms right below the $\text{In}_x\text{Ga}_{1-x}$ layer that form bonds with an In atom (the lower curve) or a Ga atom (the upper curve). For those As atoms underneath In, the theory suggests a vertical deviation from their bulk positions, which can be as large as -5.5% of the GaAs(004) d-spacing at the limit of very dilute In. This is due to the fact that these As atoms are pushed down by the bigger In atoms above, which are held by the surrounding lattice. The lower the In concentration, the more GaAs-like the buried monolayer, and therefore the larger this effect. For $x = 1.0$, the entire heterolayer is covered by In, and thus the As at the interface are free vertically to resume their bulk-like positions [27]. The opposite effect is predicted for the P_{004} of the As underneath Ga.

Figure 7.5(a) and (b) show the change in the second nearest neighbor distances along the $[\bar{1}10]$ direction (d_1) and along the $[101]$ direction (d_2), respectively, between the As atoms right below and above the $\text{In}_x\text{Ga}_{1-x}$ layer. The As-In-As case and the As-Ga-As case were considered separately in each figure. The vertical scale has been normalized to the corresponding distance for the GaAs substrate $d_{s0} = a_{s0} / \sqrt{2} = 3.997 \text{ \AA}$. At the dilute In limit, the As-In-As separation is about 5.3% larger than d_{s0} for both d_1 and d_2 , which is comparable to the lattice mismatch between InAs and GaAs. The similar As-As distance in all directions implies that the InAs tetrahedron remains the three-fold symmetry for small x . As x increases, the lateral compression builds up gradually as a result of increasing lattice mismatch and hence causes both the As-In-As and As-Ga-As separations

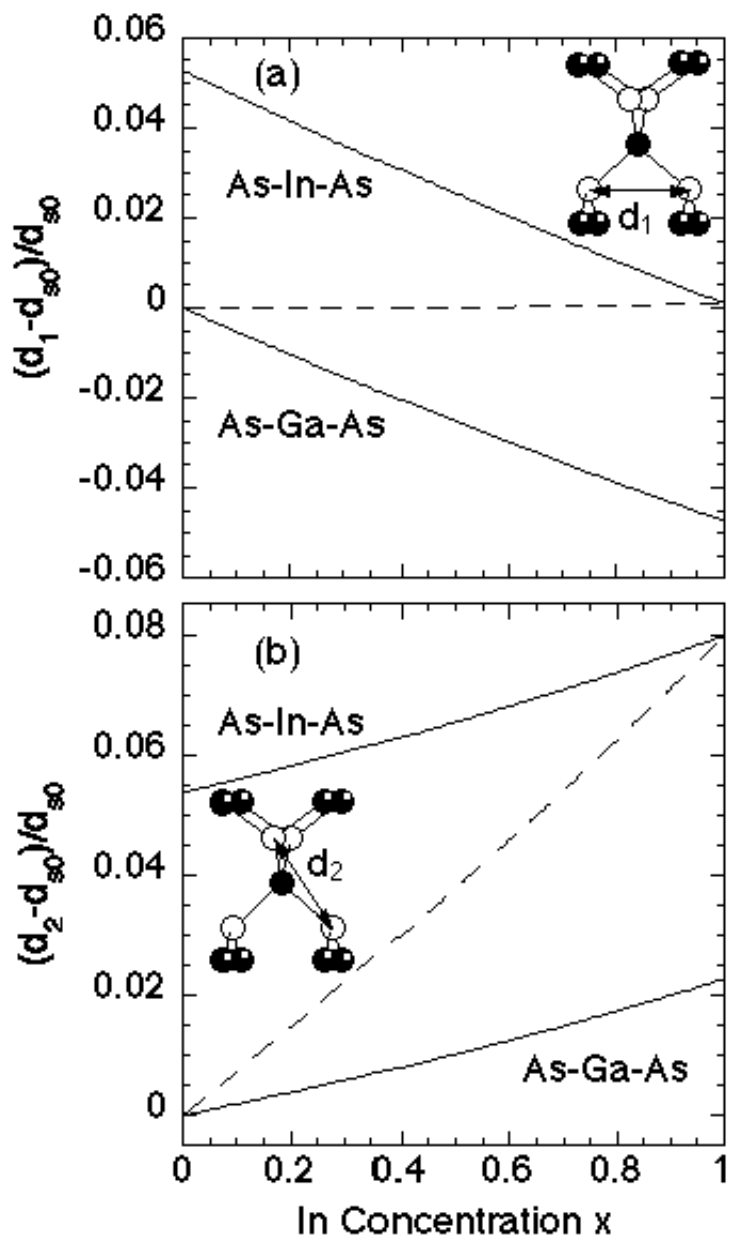


Figure 7.5 The calculated compositional dependence of the variation of the second nearest neighbor As-As distance for the As atoms right below and above the $\text{In}_x\text{Ga}_{1-x}$ layer. The solid lines are the average of the As-As distances along the $[\bar{1}10]$ and $[110]$ directions (a), and the average over the $[011]$, $[101]$, $[0\bar{1}1]$ and $[\bar{1}01]$ directions (b). In each calculation, those As atoms bonding to In and those to Ga in the buried layer are considered separately. The dashed line in each figure is the population-weighted average over the two solid lines.

along the $[\bar{1}10]$ directions to decrease. The former finally approaches to d_{s0} , as required by symmetry, and the latter becomes 4.7% smaller than d_{s0} for $x = 1.0$ due to the local expansion of the InAs tetrahedrons surrounding each Ga atom. Meanwhile, the vertical expansion of the buried layer leads to larger As-In-As and As-Ga-As distances along the $[101]$ direction towards higher x . Therefore, our calculation renders a split between d_1 and d_2 for both the As-In-As and As-Ga-As distances. The same effect has been measured by polarization-dependent EXAFS of the second-shell distance of Ge for a coherently grown GeSi layer on Si(001) [28].

Figure 7.6(a) shows the In-As and the Ga-As bond lengths L (solid lines) in the strained $\text{In}_x\text{Ga}_{1-x}\text{As}$ monolayer. For comparison, we also plotted the bulk-alloy bond lengths calculated for cubic $\text{In}_x\text{Ga}_{1-x}\text{As}$ (long-dashed lines). For the strained bond lengths, our calculation agrees with Woicik's results [18] for a thick $\text{In}_x\text{Ga}_{1-x}\text{As}$ film on GaAs(001). Both the In-As and Ga-As bond lengths are essentially constant over the range of $0 \leq x \leq 1$: the In-As bond stays at about 98% of its natural bond length ($L_{\text{In-As},0} = 2.623 \text{ \AA}$) and the Ga-As bond remains nearly unstrained ($L_{\text{Ga-As},0} = 2.448 \text{ \AA}$). This tendency is the main cause of the local lattice distortion around In atoms at lower x (and around Ga atoms at higher x) suggested in Figure 7.4(b) and 7.5(a). When compared with the bond lengths in cubic $\text{In}_x\text{Ga}_{1-x}\text{As}$, the In-As and Ga-As bonds in a strained ML are equally contracted, as observed and explained by Woicik et al. [20, 21] for a 213 \AA thick $\text{In}_{0.22}\text{Ga}_{0.78}\text{As}$ on GaAs(001). The contraction of the In-As bond length at the one ML limit has been measured by Woicik et al. [9, 11] using EXAFS. They reported an In-As bond length of $2.57 \pm 0.02 \text{ \AA}$ for $x = 1.0$, in good agreement with the present

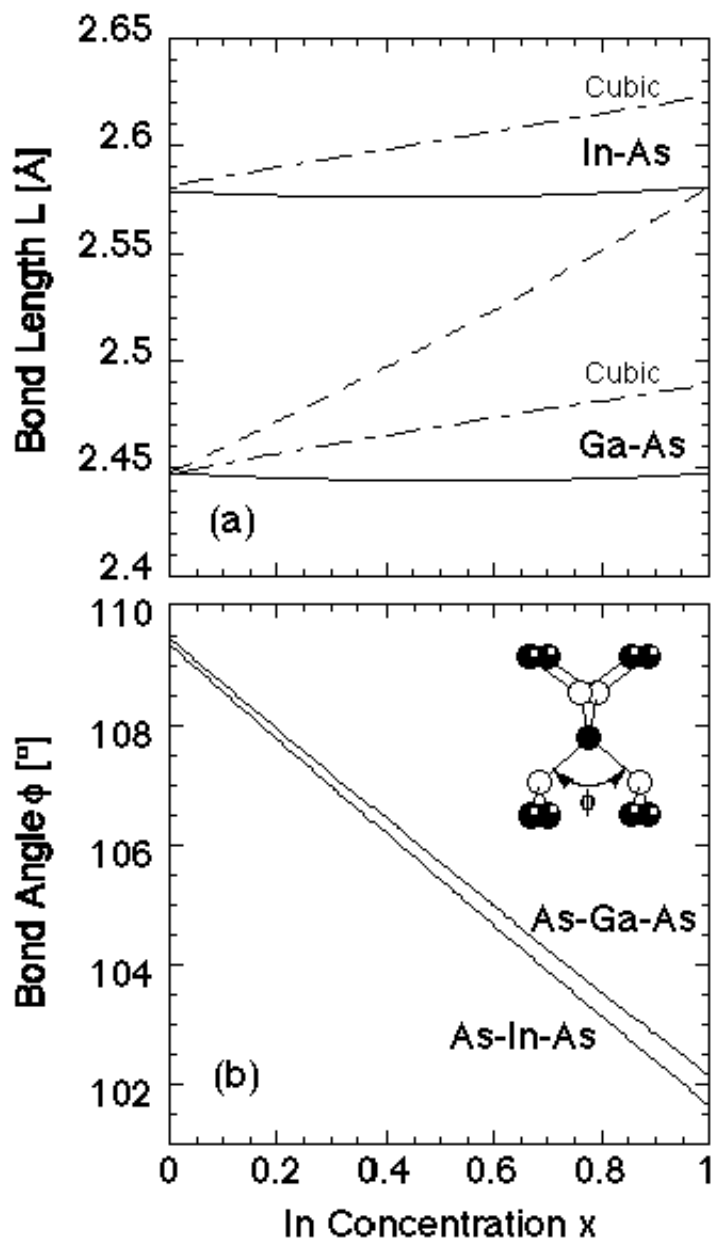


Figure 7.6 The calculated (a) In-As and Ga-As bond lengths L and (b) As-In-As and As-Ga-As bond angles ϕ in the $\text{In}_x\text{Ga}_{1-x}\text{As}$ ML as functions of the In concentration x (solid lines). The long-dashed lines in (a) are the In-As and the Ga-As bond lengths for cubic $\text{In}_x\text{Ga}_{1-x}\text{As}$. The calculation in (b) considers only the bond angle as indicated in the inset. The dashed line in (a) is the population-weighted average over the two solid lines.

calculation. Since the As atoms right below a full ML of In were shown [Figure 7.4(b) and 7.5(a)] to have bulk-like positions, we can also estimate the In-As bond length from the XSW-measured In height through $L_{\text{In-As}} = 0.25a_{s0}\sqrt{P_{004}^2 + 2}$ for a strained, pure InAs monolayer. Using the statistically averaged value of the In P_{004} positions in Ref. 9, 10, and 11 for $x = 1.0$, the above formula renders a bond length $L_{\text{In-As}} = 2.582 \text{ \AA}$, consistent with the present calculation and the EXAFS findings. At the limit of very dilute In, the In-As and Ga-As bond lengths in strained and cubic $\text{In}_x\text{Ga}_{1-x}\text{As}$ should converge to the same values. Our calculated bond lengths at this limit are therefore supported by the measurements reported by Mikkelsen and Boyce [29]. However, our results do not predict the stretched Ga-As bond length observed by Proietti et al. [30, 31] in their EXAFS measurements of InGaAs films on GaAs(001).

Figure 7.6(b) shows the As-In-As and As-Ga-As bond angles ϕ in the heterolayer as defined in the inset. For the sp^3 hybrid orbitals the natural bond angle is $\phi_0 = 109.47^\circ$. Our calculation indicates that the As-In-As and As-Ga-As bond angles are close to ϕ_0 for small x . As x increases, the As-In-As as well as the As-Ga-As bond angles decrease due to the in-plane stress. The total bond bending is about 8° for both InAs and GaAs tetrahedrons over the entire compositional range. Notice that this bond angle adjustment is directly related to the strong x dependence of the As-As distance in Figure 7.5 and the (004) In position in Figure 7.4(a), but not a result of elongation of In-As or Ga-As bond.

The dashed lines in Figure 7.4(b), 7.5 and 7.6(a) were obtained by averaging in each figure the two solid lines after they were properly weighted with either the In or the Ga population in the buried layer. They represent the structural dimensions that would be predicted by the virtual-crystal model [19], which disregards the distinction between In and

Ga and treats each atom in the buried layer as a virtual $\text{In}_x\text{Ga}_{1-x}$ atom. The dashed lines in Figure 7.4(b) and 7.5(a) imply that the average position of the As atoms at the bottom of the GaAs/ $\text{In}_x\text{Ga}_{1-x}$ interface is already bulk-like. Therefore, macroscopically the regions beyond the first nearest neighbor of $\text{In}_x\text{Ga}_{1-x}$ are essentially unstrained. This justifies our earlier assumption in defining the boundary of the strained region for applying the macroscopic elasticity theory to a buried ML.

In contrast to the linearity of the bulk-alloy lattice constants predicted by Vegard's law, the calculated In height, bond lengths and As-As second nearest neighbor distances (d_1 and d_2) exhibit nonlinear behaviors under biaxial stress. This has an origin in the fact that the perpendicular strain (or the lattice constant c) of a tetragonally distorted film is not a linear function of the film composition [Eq. (7.1)]. In Fig 6(a), for example, the effect of the substrate constraint against the film lateral expansion causes the In-As and Ga-As bond lengths to deviate from following the straight lines for the bulk alloy, and the nonlinear nature of the vertical expansion of the film leads to the slight bowing of the theoretically evaluated bond length curves.

Based on our XSW measurements and cluster calculation, we now have a microscopic description of the effect of strain on a ML-thick film. At very low In concentration, the stress around each In atom remains isotropic. Thus, the As-In-As bond angle stays close to its natural value. The incorporation of In atoms causes primarily the four first nearest neighbor As atoms of each In to be pushed away from their bulk positions. As the In concentration rises, the $\text{In}_x\text{Ga}_{1-x}$ layer begins to form and the stress becomes more lateral. This increasing biaxial compression bends the As-In-As and As-Ga-As bond angles, but the more InAs-like environment allows the four nearest neighbor As atoms of each In to

move back to their tetragonally coordinated virtual-crystal positions. As a result, the buried layer expands vertically. Over the entire compositional range, the In-As and Ga-As bonds in the buried layer are equally contracted in such a way that their bond lengths remain constant. Therefore, our calculation suggests that the bond-length strain in a one-ML $\text{In}_x\text{Ga}_{1-x}\text{As}$ film is accommodated through the combination of (a) the As-In-As and As-Ga-As bond bending, (b) the equal contraction of In-As and Ga-As bond lengths, and (c) the local lattice distortion at the GaAs/ $\text{In}_x\text{Ga}_{1-x}\text{As}$ interfaces. Factors (a) and (c) are also responsible for the variation of the In height. Factors (a) and (b) are expected to have larger effect for higher In concentrations, while (c) should become more pronounced near the dilute In or Ga limit. Since our single-ML calculation and the result in Ref. 18 for a thick overlayer predict the same compositional dependence for In-As and Ga-As bond lengths, our above conclusion should also be valid for the case of a thick $\text{In}_x\text{Ga}_{1-x}\text{As}$ layer grown on GaAs(001).

The success of the macroscopic continuum elasticity theory in calculating the position of one ML of $\text{In}_x\text{Ga}_{1-x}$ buried in GaAs(001) can be further appreciated if we consider applying the same theory to a strained film grown along the [111] direction. The complication of the (111) case originates from the fact that the four different directions that the tetrahedral bonds point to in a [111]-oriented film are not all equivalent with respect to the lateral stress. The bond along the [111] direction is expected to be less strained than the bonds parallel to the $[\bar{1}11]$, $[1\bar{1}1]$ and $[11\bar{1}]$ directions [18]. Therefore, the contraction or expansion of the lattice may not be uniform in the [111] direction. We are currently investigating the (111) case and the related issues will be discussed in a separate report.

In summary, x-ray standing wave measurements were carried out to study the strain in pseudobinary $\text{In}_x\text{Ga}_{1-x}\text{As}$ alloys buried in GaAs(001) at the one monolayer limit. The measured In positions along the (001) direction were found in good agreement with the values predicted by macroscopic continuum elasticity theory. A more microscopic description of the strain effect was obtained by performing a random-cluster calculation using the Keating valence-force field. With a cluster specially constructed for a buried, one-ML-thick film, our calculation shows a weak compositional dependence of the In-As and Ga-As bond lengths. This is similar to the results from an earlier calculation for a thick $\text{In}_x\text{Ga}_{1-x}\text{As}$ film on GaAs(001) [18]. In addition, the calculated As-In-As bond angles and the positions of the first nearest neighbor As atoms suggest that the strain in the buried monolayer is accommodated through the combination of the As-In-As and As-Ga-As bond bending, the equal contraction of the In-As and Ga-As bond lengths, and the local lattice distortion at the GaAs/ $\text{In}_x\text{Ga}_{1-x}$ interfaces. The bond bending and the local lattice distortion are also found to be the cause of the vertical expansion we measured in the strained layers.

7.3 In-plane structures of GaAs(001)/InGaAs probed by off-normal XSW measurements

In addition to the studies of the vertical expansion of buried unit cells, we investigated the in-plane structures of the heterolayers by performing (111) and $(\bar{1}11)$ XSW measurements. A Si(111) monochromator was tuned to a photon energy of $E_\gamma = 6.90$ keV for these experiments. Totally 7 samples (labeled A through G) were characterized.

Table 7.2 lists the results of the (004) analysis for sample D through G. The measured In positions for sample E and G showed good agreement with continuum elasticity theory and the calibrated In coverages. Table 7.3 summarizes the off-normal

Table 7.2 XSW results of the (004) measurements on sample D through G ($E_\gamma = 6.8$ keV). All the samples were grown with a 20 Å thick GaAs cap.

Sample	D	E	F	G
$\text{In}_x\text{Ga}_{1-x}\text{As}$ Thickness (ML)	0	1	1	2
x	0	0.41	0.7	0.41
Measured In Coverage (ML)		0.5		0.9
P_{004} calculated		1.071		1.133
P_{004} measured (± 0.02)		1.07		1.12
f_{004} measured (± 0.03)		0.66		0.61

Table 7.3 Results of the off-normal XSW measurements ($E_\gamma = 6.9$ keV).

Sample		A		B		C		E		G	
ML		1		1		1		2		2	
x				1		0.41		0.41		0.41	
H	ϕ	f \pm 0.02	P \pm 0.02	f	P	f	P	f	P	f	P
(111)	0°	0.64	0.98	0.57	0.94	0.61	0.993	0.51	0.926	0.54	0.973
($\bar{1}\bar{1}1$)	180°					0.61	0.992	0.47	0.921	0.58	0.978
($\bar{1}11$)	90°	0.89	0.99	0.96	0.99	0.85	0.998	0.86	0.973	0.86	0.990
(1 $\bar{1}1$)	270°					0.92	1.009	0.88	0.968	0.94	0.998

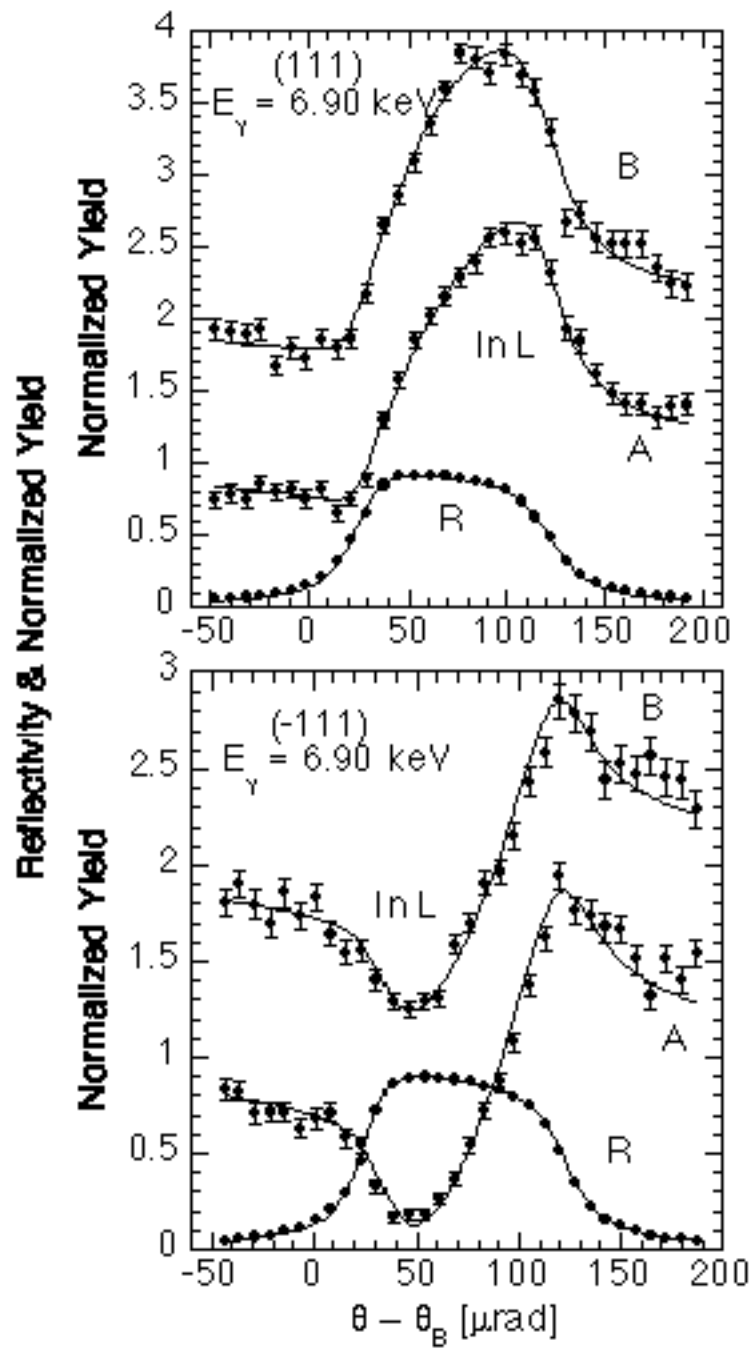


Figure 7.7 The (111) (top) and $\bar{1}\bar{1}1$ (bottom) XSW data and the best fits (solid lines) for the normalized In L fluorescence yields and reflectivity (R) versus the incident angle (θ) for samples A and B.

measurements for all the samples, where the coherent positions $P_{\{111\}}$ have their origins at the substrate Ga lattice position. In Figure 7.7 we showed the typical (111) and $(\bar{1}\bar{1}\bar{1})$ angular dependences of the In yields measured from our samples. Notice that the GaAs $\{111\}$ bilayer polarity is inverted as we switch between the [111] and $[\bar{1}\bar{1}\bar{1}]$ reflections (Figure 7.8). This leads to the dissimilarity in the modulation of the In yield exhibited in Figure 7.7.

By projecting the In position onto the [111] and the $[\bar{1}\bar{1}\bar{1}]$ axes, P_{111} and $P_{\bar{1}\bar{1}\bar{1}}$ can be geometrically related to P_{004} by $P_{111} = P_{\bar{1}\bar{1}\bar{1}} = (P_{004} + 3)/4$, which is similar to the expressions we used in Chapter 5 and 6. This equation assumes that the 2-fold symmetry about the [001] axis is not broken by the formation of the $\text{In}_x\text{Ga}_{1-x}\text{As}$ layer. Based on the XSW (004) results, this symmetry requirement predicts $P_{\{111\}}$ to be slightly greater than unity for all the samples. Our measured In $\{111\}$ coherent positions showed a reasonable agreement with the prediction (see Table 7.3). This consistency confirms that the distributions of the In atoms are symmetrically centered about a 2-fold symmetry axis perpendicular to the (004) plane.

For a pseudomorphically grown $\text{In}_x\text{Ga}_{1-x}\text{As}$ buried layer, as depicted in Figure 7.8, the In has only one $\Delta d/d$ position with respect to the $\{111\}$ planes. Therefore, the geometrical factor is $a_{111} = a_{\bar{1}\bar{1}\bar{1}} = 1$ and a four-fold symmetry is expected in terms of the present XSW measurements. The coherent fractions f_{111} and $f_{\bar{1}\bar{1}\bar{1}}$ should be equal to the product of the RT GaAs(111) Debye-Waller factor $D_{111} = 0.97$ and the order fraction C . Based on the (004) coherent fractions, we estimated that each sample should have the same f_{111} and $f_{\bar{1}\bar{1}\bar{1}}$ and the values should be between 0.7 and 0.9 for all the samples. However, our analysis (Table 7.3) showed that all the $f_{\bar{1}\bar{1}\bar{1}}$'s were measured close to 0.9,

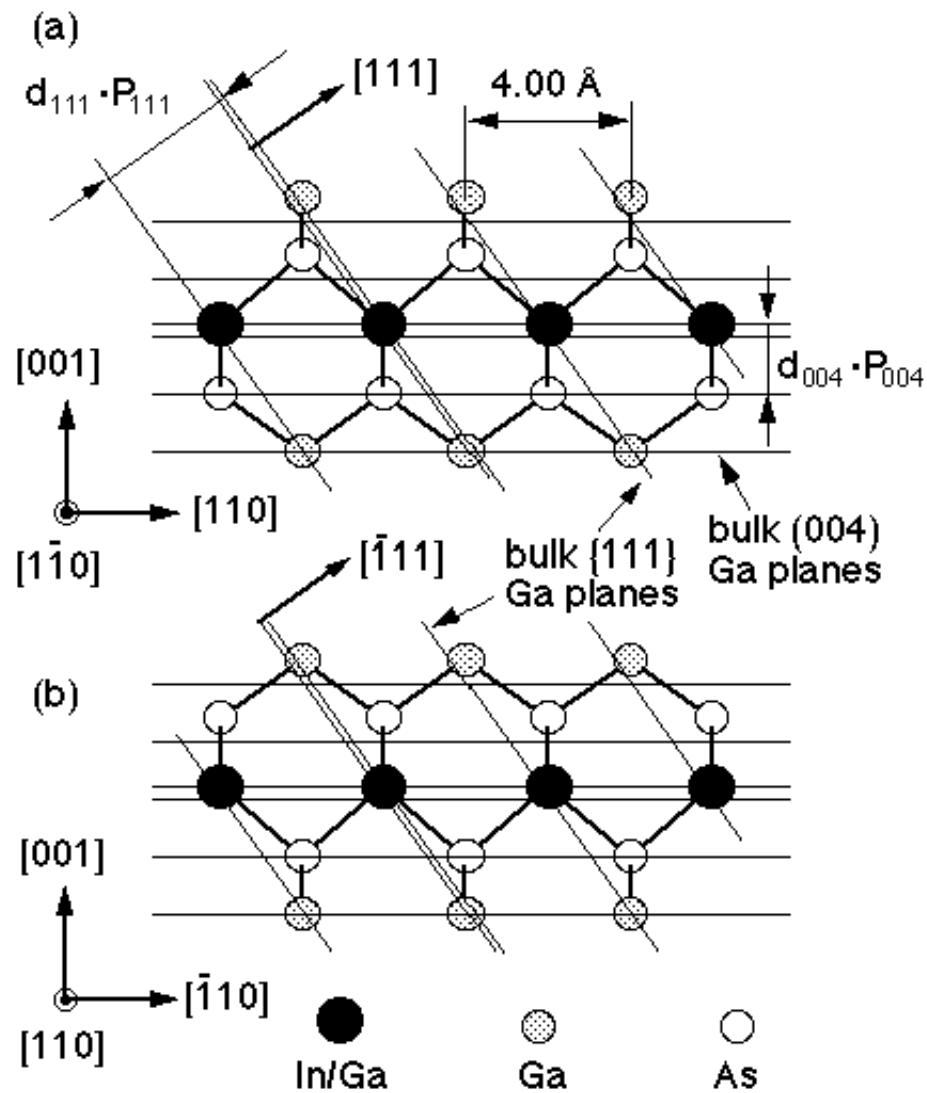


Figure 7.8 (a) $[1\bar{1}0]$ and (b) $[110]$ projected side views of a pseudomorphically grown 1 ML $\text{In}_x\text{Ga}_{1-x}\text{As}$ buried heterostructure. The solid lines represent the (004) diffraction planes and the $\{111\}$ Ga planes of the GaAs substrate, and the dashed lines indicate the In/Ga position in the buried film and the As/Ga positions in the cap.

while all the f_{111} 's were close to 0.6. Similar results were obtained from the $(\bar{1}\bar{1}1)$ and $(1\bar{1}1)$ measurements on sample C, E, and G (Table 7.3). Since the (111) and $(\bar{1}\bar{1}1)$ reflections measured the $[110]$ and $[\bar{1}\bar{1}0]$ components of the in-plane atom distribution (Figure 7.8), this clear discrepancy between the measured f_{111} and $f_{\bar{1}\bar{1}1}$ indicated an anisotropic lateral In distribution along the two orthogonal directions. In other words, the In atoms, as translated back into a substrate 1×1 unit cell, were sharply confined to a symmetric position along the $[\bar{1}\bar{1}0]$ direction, but has a wider spread along the $[110]$ direction.

We attempted to investigate more on this anisotropic In distribution by performing x-ray diffraction on the same samples. The diffraction experiments were carried out at beamline X6B at the NSLS. We first searched for the possible superstructures that may contribute to the asymmetry observed by XSW, but no fractional order reflection was found on any of the samples. We then collected the diffraction intensities along the bulk GaAs 00L, 11L and $\bar{1}\bar{1}$ L rods. Figure 7.9 shows the results of these crystal truncation rod (CTR) scans [32]. It is evident that the distortion of the intensity curve near the strong bulk reflections becomes more pronounced as the total In content in the buried layer increases. This so-called Pendellösung fringes are due to the interference between the diffracted beams from the substrate and from the 20 Å thick displaced cap. However, the measured 11L and $\bar{1}\bar{1}$ L rods are nearly identical and thus reveal no structural anisotropy of these films.

Anisotropy has been reported in previous studies of the initial growth stage and the optical properties [33] of lattice-mismatched III-V heteroepitaxial structures. Using scanning tunneling microscopy (STM), Bressler-Hill *et al.* [42] observed that growing a submonolayer of InAs on a vicinal GaAs(001) surface formed two-dimensional (2D)

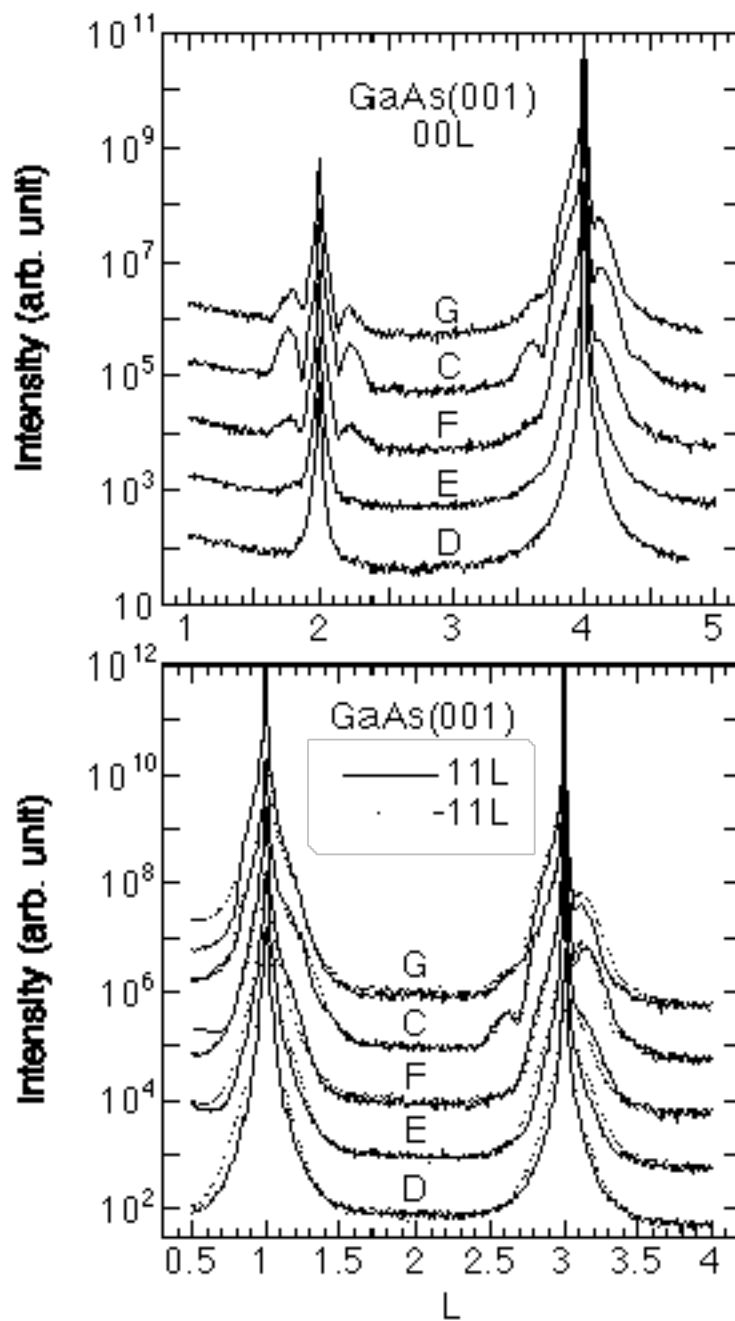


Figure 7.9 00L (top, solid lines), 11L (bottom, solid lines) and $\bar{1}1L$ (bottom, dots) rod scans at 8.00 keV for samples C through G.

islands elongated in the $[\bar{1}10]$ direction. Similar anisotropic morphology has also been observed during the homoepitaxy of GaAs on GaAs(001) [34]. This asymmetric 2D growth is believed to be a result of anisotropic Ga (or In) surface diffusion rates [35] and step edge reactivities [34] along the $[\bar{1}10]$ and the $[110]$ directions. Based on these observations, one possible explanation for our off-normal XSW result would be that during the $\text{In}_x\text{Ga}_{1-x}\text{As}$ monolayer growth, 2D $\text{In}_x\text{Ga}_{1-x}\text{As}$ islands (or steps) were formed and then embedded in the GaAs matrix of the cap. Through a lateral elastic deformation of the step edges toward the GaAs matrix, the biaxial strain experienced by the $\text{In}_x\text{Ga}_{1-x}\text{As}$ islands can be reduced. This is similar to the observation reported by Massies and Grandjean based on their RHEED study of the growth of $\text{In}_x\text{Ga}_{1-x}\text{As}$ on GaAs(001) [36]. Thus, the In atoms near an step edge parallel to the $[\bar{1}10]$ (or $[110]$) axis will have non-ideal in-plane positions along the $[110]$ (or $[\bar{1}10]$) direction. If the $\text{In}_x\text{Ga}_{1-x}\text{As}$ islands were on average much narrower in the $[110]$ direction, and the step density was higher for the steps parallel to the $[\bar{1}10]$ [34], a lower coherent fraction can be therefore expected for the $[111]$ XSW measurement. Based on the present study alone, we were not able to quantitatively determine the origin of this anisotropic broadening of the In distribution. It was also not clear how the vertical distortion of the $\text{In}_x\text{Ga}_{1-x}\text{As}$ lattice was affected by the lateral anisotropy we observed. Further investigations would be necessary to answer these questions.

7.4 Strain-induced cap displacement: An x-ray evanescent-wave emission measurement

Another way to measure the strain in a buried film is to consider the displacement of the cap layer in the growth direction with respect to the ideal lattice of the substrate. A MBE-grown sample with 1 ML of InAs on GaAs(001) capped by a GaAs layer of 25 Å

was prepared at the National Institute of Standards and Technology [10]. In this section we demonstrate that by combining the conventional XSW method and the evanescent-wave-emission effect (see Section 2.4) one can precisely measure the strain-induced cap displacement and examine its homepitaxy, even the cap layer thickness t_c was only 25 Å.

Studying the structural variation in the near-surface region with the XSW method requires an effective way for isolating surface signals from bulk signals. This would typically be accomplished by using photoelectron emission [37]. The conventional fluorescence-based XSW technique, due to its lack of surface sensitivity, presumably would not be considered as an appropriate tool for this kind of measurement. However, one can effectively reduce the depth probed by fluorescence by employing the evanescent-wave-emission effect discussed earlier.

Table 7.4 Result of the (004) XSW measurements and calculated escape depths Z_2 at $\alpha_u = 2^\circ, 3^\circ, 4^\circ$ and 10° . The coherent fractions f and coherent positions P are determined by χ^2 fits of Eq.(2.72) to the data with $L(\theta)$ defined by Eq.(9) for As and with $L(\theta) = 1$ for In.

α_u		10°	4°	3°	2°
Z_2 [Å]		900	330	230	120
As	f	0.81±0.01	0.70±0.01	0.65±0.01	0.48±0.03
	P	1.00±0.01	1.01±0.01	1.024±0.01	1.062±0.01
In	f	0.43±0.03	0.44±0.02	0.42±0.02	0.43±0.02
	P	1.154±0.01	1.151±0.01	1.159±0.01	1.156±0.01

The low-takeoff angle XSW experiments were carried out at $\alpha_u = 4^\circ, 3^\circ$ and 2° , where α_u was the upper limit of the fluorescence takeoff angle defined by the fluorescence slit.

Figure 7.10 shows the As $L\alpha$ fluorescence yields measured at $\alpha_u = 10^\circ$ and 2° . The coherent fractions and coherent positions for arsenic and indium measured at various takeoff angles are tabulated in Table 7.4.

As evident in Figure 7.10, as α_u approaches the critical angle $\alpha_c = 1.5^\circ$, the fluorescence modulation amplitude gradually decreases and the yield maximum is shifted toward the low angle side of the rocking curve. This corresponds to a decrease in the coherent fraction and an increase in the coherent position. This change is due to the significant reduction of the As $L\alpha$ escape depth near the critical angle which makes the As $L\alpha$ signal more sensitive to the cap and less sensitive to the bulk GaAs. In the extreme case, where $\alpha_u = 2^\circ$ and the maximum escape depth is about 120 \AA , over 30% of the As yield is contributed by the cap. The coherent fraction (f_c) and coherent position (P_c) for the arsenic in the cap can therefore be determined quantitatively by fitting the following modified yield equation to the fluorescence data:

$$Y(\theta) = Y_{OB} \left\{ 1 + R(\theta) + 2\sqrt{R(\theta)} \cdot \left[f_s \cos(v(\theta) - 2\pi P_s) \frac{L_s}{L} + f_c \cos(v(\theta) - 2\pi P_c) \left(1 - \frac{L_s}{L}\right) \right] \right\} L. \quad (7.4)$$

The constant L is the effective thickness defined by Eq.(2.79) with $\alpha_1 = 0$ and with $\mu_{z,1}(\theta)$ omitted (since $\mu_{z,1}(\theta) < \mu_{z,2}(\alpha)$ when α is near α_c). The constant L_s has the same

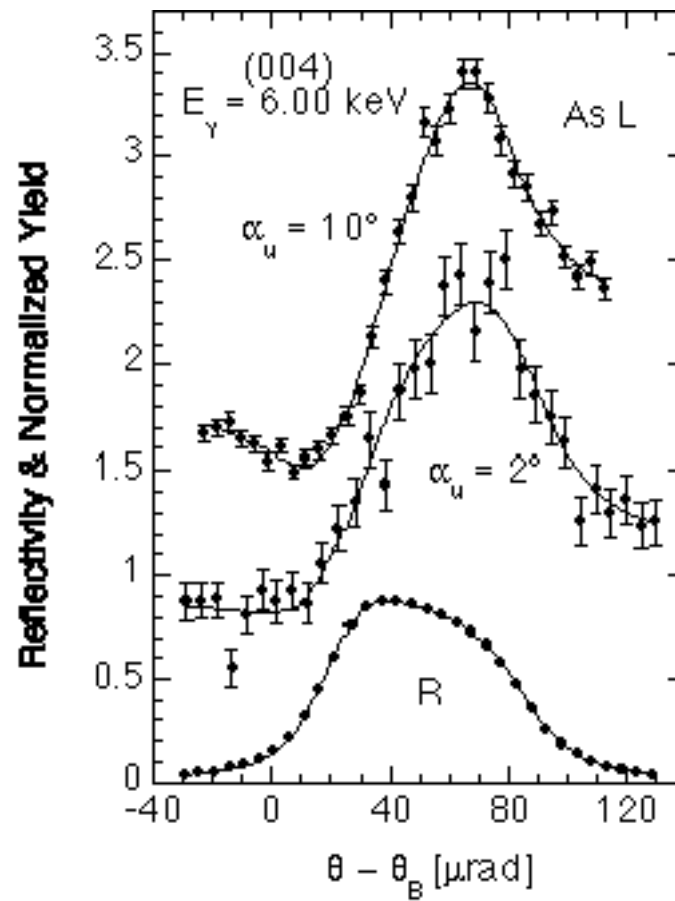


Figure 7.10 The experimental XSW data and the best fits for the normalized As L fluorescence yields at $\alpha_u = 2^\circ$ and 10° and the GaAs(004) reflectivity (R) versus the incident angle (θ). The sample was a ML of InAs grown on a GaAs(001) substrate and capped with 25 Å of GaAs.

definition as L except that the integration over depth starts at $z = t_c$ rather than $z = 0$. This accounts for the arsenic yield contributed by the substrate below the cap.

In Eq.(7.4) f_c and P_c are the substrate arsenic coherent fraction and coherent position. These values were determined to be $f_c = 0.81 \pm 0.01$ and $P_c = 1.00 \pm 0.01$ by the (004) XSW measurement at $\alpha_u = 10^\circ$. In this case the escape depth is significantly larger than the cap thickness t_c and thus the cap contribution is negligible. The reasonably high coherent fraction (in comparison with the 0.86 GaAs(004) Debye-Waller factor) and the ideal bulk coherent position for arsenic at $\alpha_u = 10^\circ$ indicate a highly ordered GaAs buffer layer where 94% of the arsenic atoms register with the bulk GaAs(004) planes.

The χ^2 fit of Eq.(7.4) to the $\alpha_u = 2^\circ$ data with fixed parameters α_u , t_c , f_c and P_c gives $f_c = 0.64 \pm 0.12$ and $P_c = 0.33 \pm 0.03$, corresponding to a 0.47 ± 0.04 Å displacement of the cap layer (h_c) in the growth direction with respect to the bulk (004) planes. This result is in good agreement with our measured indium (004) position, which predicts $h_c = 2h_{In} = 2a_{GaAs}P_{004In} = 0.44$ Å, as depicted by the ball and stick model in Figure 7.8. This consistency between our measurements of the cap displacement and the In position have an important implication with respect to characterizing the overall strain of a buried film which is thicker than 1 ML. In such a case, the multiple positions of the impurity atoms in the strained layer will reduce the coherent fraction and thus obscure the structural information gained from the coherent position of the impurity. However, by measuring the position of the cap layer with XSW, one can obtain the cumulative lattice displacement within the strained layer.

For samples with a thicker (100 ~ 200 Å) cap layer, it is possible to essentially eliminate the substrate signal at $\alpha_u \sim \alpha_c$ and directly measure the positions of the atoms in the cap. Since $\mu_{z,1}(\theta) \ll \mu_{z,2}(\alpha)$ in Eq.(2.79) and only one coherent position needs to be considered in Eq.(7.4), Eq.(2.73) with $L(\theta) = 1$ becomes a proper formula for describing

the fluorescence yield in this case, which implies that atoms distributed within the depth of a few hundred angstroms can be treated as if they were on the surface. Consequently, the uncertainties about the cap layer thickness t_c and the upper limit of the emission takeoff angle α_u can be completely removed from the data interpretation. With these advantages realized, the XSW method can be applied as a highly precise nondestructive probe for studying buried heteroepitaxial structures as well as interfacial segregation.

7.5 Strains in *InSb(111)/InAsSb*

As mentioned earlier at the end of Section , the tetrahedrons in a [111] and [001] oriented semiconductor thin films are expected to respond differently to the substrate-imposed lateral stress due to the different bonding orientations with respect to the growth directions. We therefore carried out high-resolution characterizations of heterostructures composed of ML thick InAsSb films buried in InSb (111) substrates using XSW and EXAFS. In this section we present the experimental results and compare them with continuum elasticity theory and calculations using Keating potential.

The samples (W1 and W2) were grown by metal-organic vapor phase epitaxy (MOVPE) as a single monolayer of $\text{InAs}_x\text{Sb}_{1-x}$ buried in a InSb(111) matrix. The cap thickness was about 25 Å. The As coverage in the buried monolayers was determined by x-ray fluorescence analysis to be 0.23 ML and 0.95 ML for W1 and W2, respectively, using a RBS calibrated As implanted Si standard. Both the XSW and EXAFS measurements were conducted using the 5ID-C undulator station at the DND CAT at the Advanced Photon Source. For the XSW measurements, the APS undulator and the DND liquid N₂ cooled Si(111) monochromator were tuned to an x-ray energy of 12.8 keV to excite the As K fluorescence (no Si channel cut was used). The InSb(111) reflection was employed to directly measure the heights of the As atoms. The InSb(022) reflection of each sample was

also recorded to confirm the pseudomorphic growths of the buried layers. The XSW data were collected using totally two synchrotron runs, which were separated by 14 months. During the second run the XSW measurements were repeated prior to the EXAFS experiment. Figure 7.11 and 7.12 show the XSW data and the results of the analysis using (2.72). The number “-1” and “-2” in the labels denote the first and second synchrotron runs during which the data were measured. The coherent fractions and coherent positions determined by the best fits are summarized in Table 7.5.

The As K EXAFS measurements were carried out to directly determine the In-As bond lengths of the buried layers. Since a strain induced bond length split between the bonds along the [111] direction and the bonds parallel to the $[\bar{1}11]$, $[1\bar{1}1]$ and $[11\bar{1}]$ directions was expected, each sample was measured at two different geometries: the sample surface parallel (in plane) and perpendicular (out of plane) to the polarization of the incident x-ray (Figure 7.13). Since the cross section of photoelectric effect has an angular dependence and is proportional to $(\hat{\mathbf{e}} \cdot \hat{\mathbf{r}}_j)^2$, where $\hat{\mathbf{e}}$ is the polarization vector of the incident x-ray and $\hat{\mathbf{r}}_j$ in the present case is the unit vector pointing from the emitting atom to its j th first-shell atom, the in-plane geometry has made the In-As bonds parallel to the [111] direction completely invisible to the EXAFS measurement. While for the out-of-plane geometry 75% of the EXAFS signals were contributed by the In-As bonds parallel to the [111] direction and 25% by those parallel to the $[\bar{1}11]$, $[1\bar{1}1]$ and $[11\bar{1}]$ directions. The x-ray optics used for the EXAFS experiment was the same as the XSW measurements. The

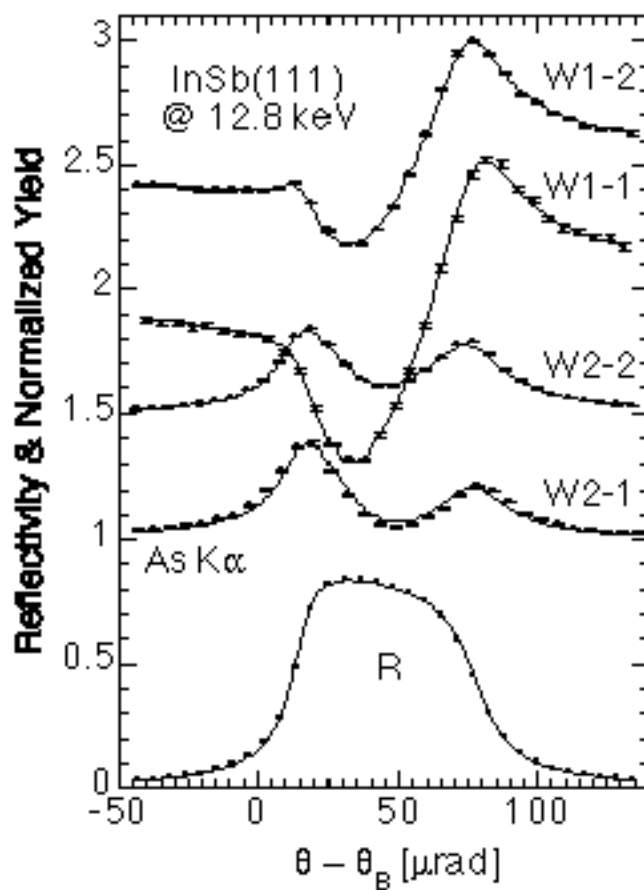


Figure 7.11 The experimental XSW data and the best fits for the normalized As K α fluorescence yields and the InSb(111) reflectivity (R) versus the incident angle (θ) for samples W1 and W2. The labels “-1” and “-2” denote the first and second synchrotron runs during which the data were measured.

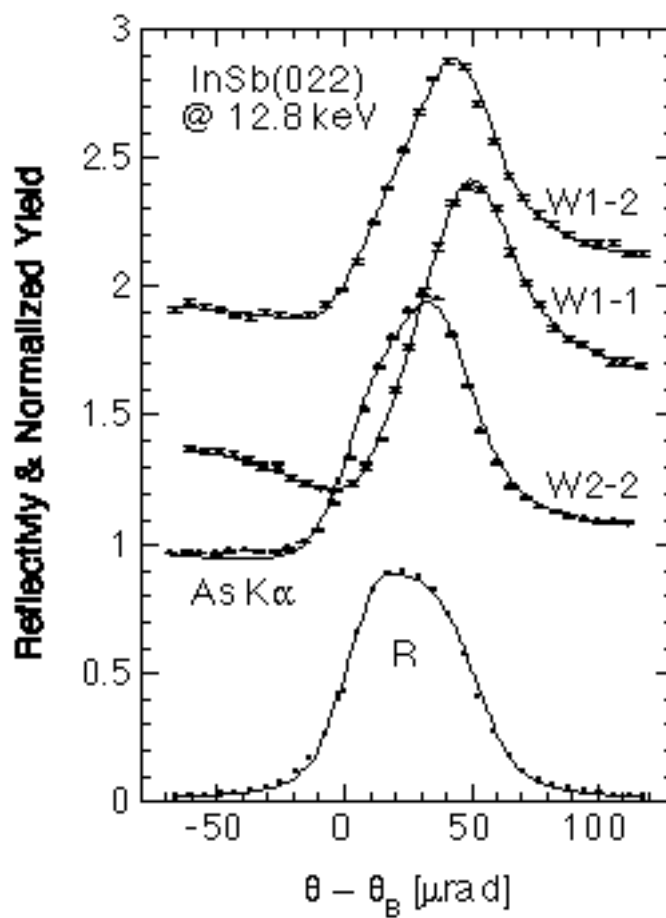


Figure 7.12 The experimental XSW data and the best fits for the normalized As K α fluorescence yields and the InSb(022) reflectivity (R) versus the incident angle (θ) for samples W1 and W2. The labels “-1” and “-2” denote the first and second synchrotron runs during which the data were measured.

energy scans were achieved by scanning simultaneously both the undulator gap and Si(111) monochromator. The As K fluorescence x-ray from the samples were recorded by a solid state detector. The samples were kept spinning at a few hundred rpm to smear out the glitches and spikes in the EXAFS spectra due to Bragg reflections. The incident angles were about 10° for the in-plane geometry and 0.5° for the out-of-plane geometry. An InAs powder sample was measured as the EXAFS standard using a transmission mode. The incident and the transmitted intensities were recorded by a pair of ion chambers about 8” apart filled with He. The measured absorption coefficients $\mu(E)$ for the InAs standard and sample W2 at the in-plane and out-of-plane geometries were plotted in Figure 7.14. The EXAFS measurement of sample W1 did not yield data with enough statistics due to the lower As concentration, small sample size and limited beam time.

Table 7.5 XSW results of the (111) and (022) As K measurements ($E\gamma = 12.8$ keV). The "P₁₁₁ theory" was based on the non-cluster Keating calculation (Figure 7.18).

Sample	x(As) (±5%)	ϵ_{\perp} theory	H	f (±0.01)	P* (±0.01)	P ₁₁₁ * theory	P ₀₂₂ cal.**
W1	0.23	-1.0%	(111)-1	0.85	0.71	0.74	
			(111)-2	0.65	0.70		
			(022)-1	0.62	0.95	0.94	
			(022)-2	0.41	0.95		
W2	0.95	-3.8%	(111)-1	0.41	0.62	0.716	
			(111)-2	0.39	0.64		
			(022)-2	0.29	0.90	0.84	

* P₁₁₁ is the position with respect to an In (111) plane.

** Based on measured P₁₁₁ and symmetry.

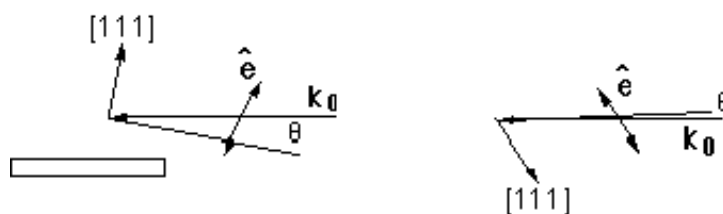


Figure 7.13 The in-plane and out-of-plane geometries for the polarization-dependent EXAFS measurements.

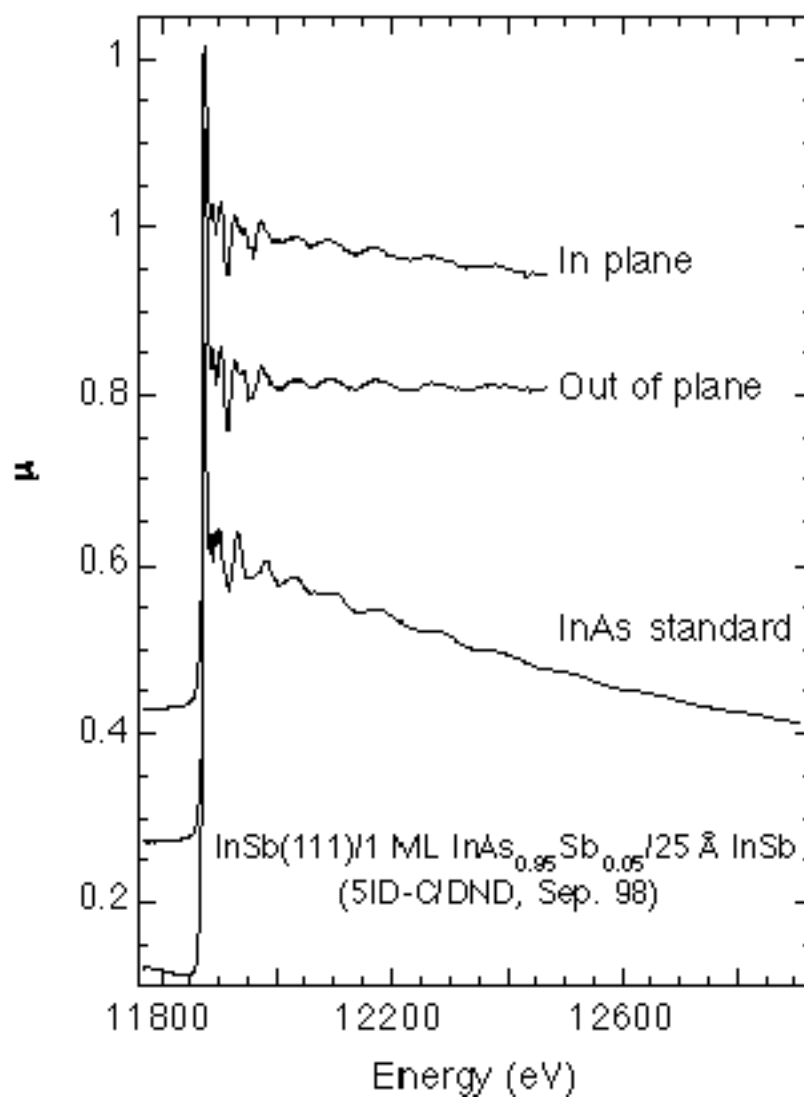


Figure 7.14 EXAFS measured absorption coefficients $\mu(E)$ for the InAs standard and for sample W2-2 at the in-plane and out-of-plane geometries.

The XSW characterizations (see Table 7.5) along the growth direction suggests that a high quality InAsSb buried layer can be grown at low As concentrations. This is based on the high (111) coherent fraction (0.85) measured on sample A. Since the (111) coherent position for the bulk Sb atoms is 0.75 with respect to the In planes, the measured As P_{111} 's for sample W1 (0.71) and W2 (0.63) indicate that the As vertical positions has been strongly affected by the lateral tensions imposed by the substrates. Based on the symmetry of the zinc-blende structure, P_{022} can be related to P_{111} by $P_{022} = 4P_{111}/3$ [Figure 7.15]. Table 7.5 shows that this relationship was perfectly satisfied by sample W1 but not by sample W2. Furthermore, the ratio $f_{022}/f_{111} = (D_{022}/D_{111})(a_{022}/a_{111})$ [see Eq. (5.3)] was measured to be approximately 0.7 for both samples, while an ideal pseudomorphic model ($a_{022} = a_{111} = 1$), as the one depicted in Figure 7.15, would predict $f_{022}/f_{111} = D_{022}/D_{111} \approx 0.9$ [38]. This could imply that a static Debye-Waller factor needs to be considered to account for the local structural disorder of the buried layers. Also notice that the second measurements on sample W1 showed significant reductions in the coherent fractions, indicating a degradation of the film over the 14-month period.

The EXAFS data were analyzed following the standard EXAFS procedures [39]. Figure 7.16 (a) shows the As K EXAFS, $\chi(k)$, after background removed by fitting of splines to the raw data in Figure 7.14 between $(E_0 + 12)$ eV to $(E_0 + 600)$ eV, where E_0 is the energy of the absorption edge, $k = \sqrt{2m(\hbar\omega - E_0)}/\hbar$ is the photoelectron wave number, and $E_\gamma = \hbar\omega$ is the incident photon energy. Figure 7.16(b) shows the magnitudes of the Fourier transform of the k-weighted EXAFS, $k\chi(k)$, between $k = 2 \text{ \AA}^{-1}$ and 12.2 \AA^{-1} . The peaks between $r = 1.5 \text{ \AA}$ and 3.2 \AA correspond to the first-nearest neighbor distances for the As atoms, i.e., the In-As bond lengths. It is already evident in Figure 7.16(b) that the In-As bond lengths in the buried layer are about 0.04 \AA longer than

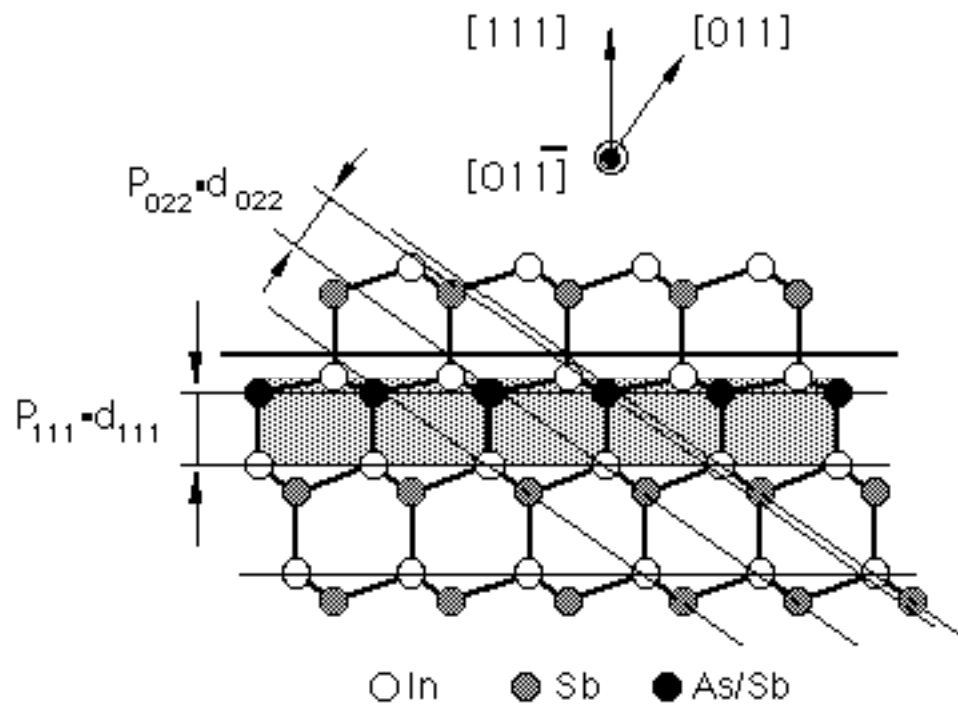


Figure 7.15 The $[01\bar{1}]$ view of an InSb(111)/1 ML InAsSb/InSb heterostructure. The solid lines represent the (111) In planes and the (022) planes. The dashed lines indicate the (111) and (022) positions for the As/Sb atoms in the buried layer.

that of the InAs standard. This is consistent with what is expected for a film under tension. However, no bond length split can be concluded without further analysis. The curves in Figure 7.16(b) between $r = 1.5 \text{ \AA}$ and 3.2 \AA were then back transformed to the k space. These Fourier-filtered first-shell contributions are compared with the $k\chi(k)$ functions in Figure 7.17(a). Finally, the Fourier-filtered first-shell data for the buried layer were fitted by the following function assuming a single bond length [Figure 7.17(b)]

$$\chi(k) = N|f(k)|\sin[2kr_0 + \phi(k)], \quad (7.5)$$

where $f(k)$ is the backscattering amplitude, $\phi(k)$ is the total first-shell phase shift, N is the coordination number for the first shell and r_0 is the averaged In-As bond length. The functions $f(k)$ and $\phi(k)$ were extracted from the InAs standard data with bulk In-As bond length $r_0 = 2.623 \text{ \AA}$ and $N = 4$. Only two free parameters, N and r_0 , in (7.5) were used in fitting the data for the buried layer. For the in-plane measurement N and r_0 were determined to be 3.24 and $2.661 \pm 0.009 \text{ \AA}$, and for the out-of-plane measurement they were determined to be 3.88 and $2.655 \pm 0.008 \text{ \AA}$, respectively. The error bars of r_0 can be further reduced if we model the in-plane data using the out-of-plane data. This rendered a difference $r_{0,IP} - r_{0,OP} = 0.006 \pm 0.006 \text{ \AA}$ and a ratio $N_{IP}/N_{OP} = 0.83$. Since the out-of-plane EXAFS measured an average of the two different In-As bond lengths, the true bond length of the In-As bonds along the [111] direction are expected to be slightly shorter than 2.655 \AA . This leads to a slightly larger bond length split.

We now compare the XSW measurements with continuum elasticity theory. Based on the theory, for a cubic material grown pseudomorphically along the [111] direction, the

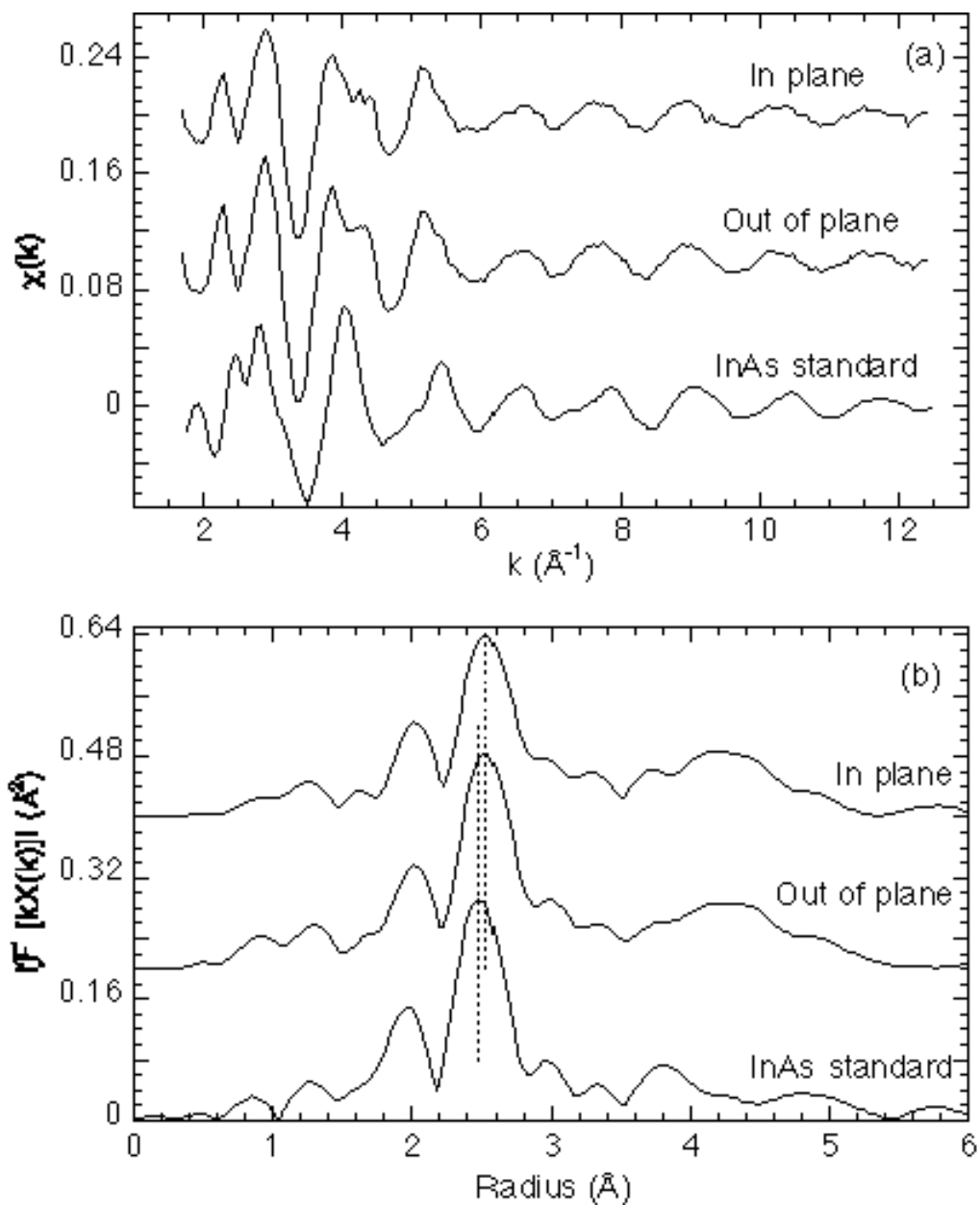


Figure 7.16 (a) The As K EXAFS $\chi(k)$ and (b) the magnitudes of the Fourier transform of the k -weighted EXAFS, $k\chi(k)$, between $k = 2 \text{\AA}^{-1}$ and 12.2\AA^{-1} for the InAs standard and for the in-plane and out-of-plane measurements of sample W2-2.

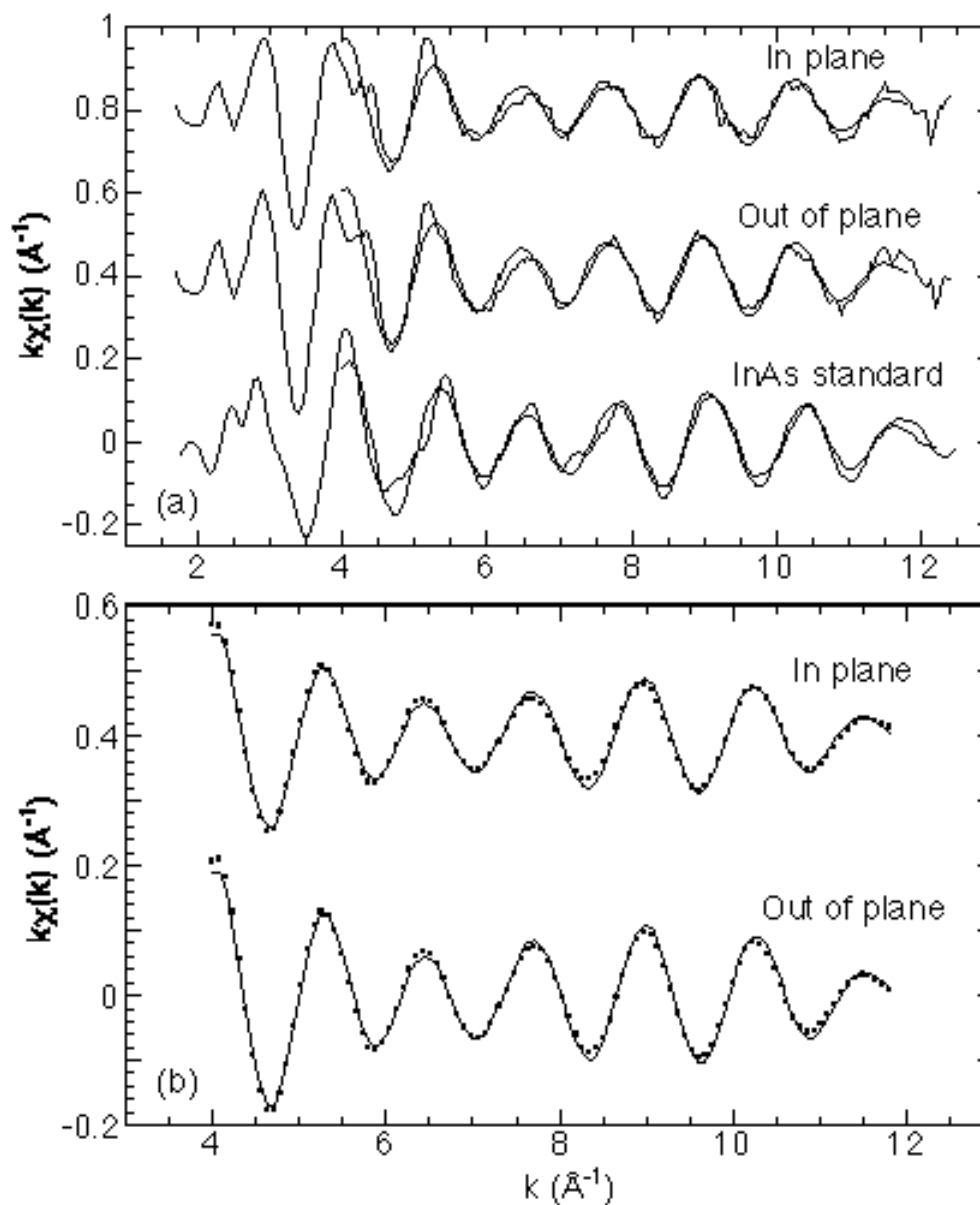


Figure 7.17 (a) Comparisons of the Fourier-filtered first-shell contributions with $k\chi(k)$ and (b) the best fits to the Fourier-filtered first-shell data for the in-plane and out-of-plane measurements of sample W2-2.

vertical strain ε_{\perp} in the film can be related to the in-plane strain ε_{\parallel} imposed by the substrate as (Appendix A)

$$\varepsilon_{\perp} = -\frac{2C_{11} + 4C_{12} - 4C_{44}}{C_{11} + 2C_{12} + 4C_{44}} \varepsilon_{\parallel}, \quad (7.6)$$

where C_{ij} are the bulk elastic constants of the film [5]. The in-plane strain ε_{\parallel} can be estimated by the expression $\varepsilon_{\parallel} = (a_{s0} - a_{f0})/a_{f0}$. For a pure InAs layer on the InSb(111), it renders a strain $\varepsilon_{\parallel} = 7.0\%$ based on the bulk lattice constants $a_{\text{InAs}} = 6.0584 \text{ \AA}$ and $a_{\text{InSb}} = 6.4794 \text{ \AA}$. Therefore Eq. (7.6) predicts a vertical strain ε_{\perp} of -4.0% . For one ML of InAs buried in InSb(111) we can convert this vertical strain to the average (111) coherent position for the As atoms in the film assuming (a) the In atoms at the lower InAs/InSb interface stay at their bulk-like positions and (b) the InAs tetrahedrons in the film deform uniformly in the [111] direction. This leads to the following expression (Figure 7.15)

$$P_{111} = \frac{3(1 + \varepsilon_{\perp})a_{f0}}{4a_{s0}}, \quad (7.7)$$

where a_{f0} and a_{s0} are the bulk lattice constants of the film and substrate, respectively. Eq. (7.7) predicts $P_{111} = 0.67$ for InAs. For one ML of $\text{InAs}_x\text{Sb}_{1-x}$ alloy buried in InSb(111), we can carry out a similar calculation by combining Eq. (7.6) and (7.7) with Vegard's law. We plot out P_{111} for the arsenic as a function of the composition x (the lower dotted line) in Figure 7.18(a). The upper dotted line in Figure 7.18(a) is the (111) position for the In atoms at the upper InAsSb/InSb interface, which should follow $P_{111} = (1 + \varepsilon_{\perp})a_{f0}/a_{s0}$ and approach to one at the dilute As limit.

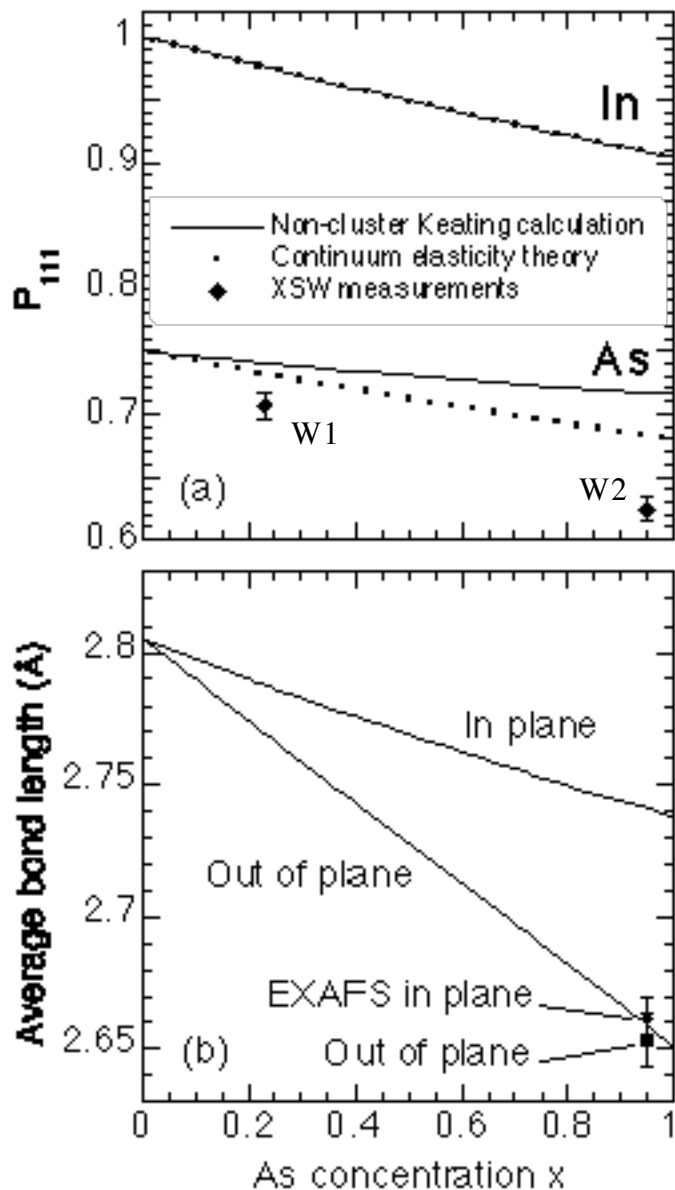


Figure 7.18 (a) Comparison between the P_{111} calculated based on continuum elasticity theory (dots) and the non-cluster Keating calculation (solid lines) for the As in the buried monolayer and the In at the lower InAsSb/InSb interface. Also shown in (a) are the XSW measured P_{111} for W1 and W2. (b) The in-plane and out-of-plane population-weighted average In-As $_x$ Sb $_{1-x}$ bond lengths based on the non-cluster Keating calculation. Also shown are the EXAFS measured In-As bond lengths for sample W2.

We next apply Keating potential to calculate the structure for the same system. This approach allowed us to remove the assumptions of fixed interface position and uniform vertical deformation [see (7.7)]. In the first step we constructed a model containing a ML of $\text{InAs}_x\text{Sb}_{1-x}$ sandwiched between two InSb layers. We replaced the anions in the buried layer with the same $\text{As}_x\text{Sb}_{1-x}$ virtual atoms, which had the average properties of As and Sb. This simplified model did not consider the As and Sb atoms in the buried layer separately, i.e., it can be used to calculate only the average (111) positions and bond lengths, but it provided simple calculations without statistical consideration for the As and Sb distributions in the film. We determined the positions of the atoms by minimizing the Keating energy per $\text{As}_x\text{Sb}_{1-x}$ virtual atom based on (7.3). By symmetry all the atoms were allowed to move only in the [111] direction. In Figure 7.18(a) we plotted the results of this calculation as solid lines for the In atoms at the upper InAsSb/InSb interface and for the $\text{As}_x\text{Sb}_{1-x}$ virtual atoms in the buried layer. For the In (111) position, the present Keating calculation showed excellent agreement with continuum elasticity theory [40]. While it indicated that the average anion vertical position in the film was less affected by the lateral tension, as compared to the continuum elasticity theory. This implies that the uniform vertical deformation of the InAsSb tetrahedrons in a [111]-oriented buried layer may not be a valid assumption. The small reduction of the anion height in the buried layer as x increases is also consistent with the expectation that the In-As bonds parallel to the [111] direction are less strained than those along the other three directions. However, our XSW measured As (111) positions [Figure 7.18(a)] did not follow either of the theoretical trends and showed a much large effect of the lateral strain.

To estimate the bond lengths in the strained $\text{InAs}_x\text{Sb}_{1-x}$ (111) monolayer, we performed a random cluster calculation using the Keating potential (7.3). The cluster and the boundary conditions used in this calculation [Figure 7.19(a)] were similar to the one in

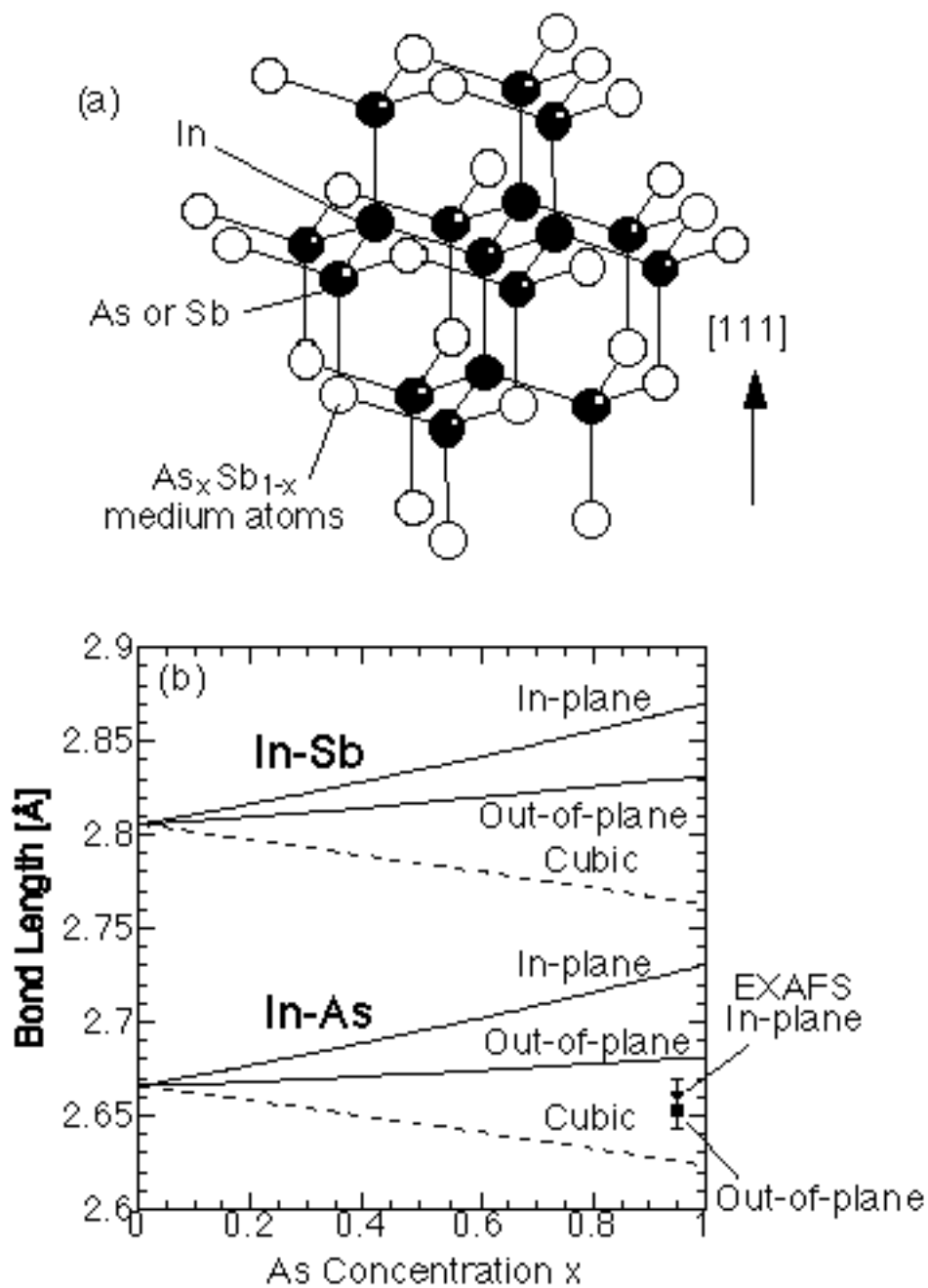


Figure 7.19 (a) The $\text{InAs}_x\text{Sb}_{4-j}$ cluster with the medium atoms used for the present random-cluster calculation. (b) Calculated In-As and In-Sb bond lengths in a strained $\text{InAs}_x\text{Sb}_{1-x}$ layer (solid lines) and unstrained bulk $\text{InAs}_x\text{Sb}_{1-x}$ (dashed lines). Also shown are the EXAFS measured In-As bond lengths for sample W2.

Ref. 18 for a thick (111) film. A cluster with a buried (111) monolayer, perhaps similar to the one introduced in Section 7.2, would be more desirable but will not be considered in this work. Figure 7.19(b) shows the results of the present cluster calculation. The in-plane and out-of-plane In-As and In-Sb bond lengths (solid lines) in the strained layer were calculated as functions of the As concentration x . Also shown for comparison were the In-As and In-Sb bond lengths in bulk $\text{InAs}_x\text{Sb}_{1-x}$ (dashed lines). The cluster calculation predicted a bond length split, which can be as large as 0.05 \AA for $x = 1$, between the in-plane and out-of-plane In-As bonds. The out-of-plane bonds were shown to be less strained and elongate by only a small amount from their natural lengths. In Figure 7.18(b) we have already estimated the average in-plane and out-of-plane bond lengths based on the non-cluster Keating calculation discussed earlier. Interestingly, it suggested an even larger bond length split (0.09 \AA) at $x = 1$ [41]. Our polarization-dependent EXAFS measurements showed, however, a very small ($< 0.01 \text{ \AA}$) bond length difference, and the two In-As bond lengths were both measured to be close to the calculated bond lengths for the out-of-plane In-As bond. Notice that if we assume that the In atoms at the lower InAsSb/InSb interface are bulk-like [40], the XSW measured As P_{111} for sample W2 implies an out-of-plane In-As bond length to be $L = P_{111}a_{\text{InSb}} / \sqrt{3} \approx 2.36 \text{ \AA}$, which is too short to be physical and is inconsistent with the EXAFS data and the calculations.

In summary, we have investigated the strain in one ML of $\text{InAs}_x\text{Sb}_{1-x}$ buried in InSb(111) using XSW, EXAFS and theoretical calculations. The measured As (111) positions in the films showed a strain effect much larger than what was suggested by continuum elasticity theory. While the EXAFS measurements detected no significant bond length split between the in-plane and out-of-plane In-As bonds, which was predicted by a random cluster calculation using Keating valence force field to be as large as 0.05 \AA for $x = 1$. We speculate that the buried layers, particularly the one with the higher As

concentration, were partially relaxed and therefore effects other than elastic stain needed to be considered to properly interpret our experimental observations.

Chapter 8 Summary

In the current studies we explore the surface structures of GaAs(001) induced by the adsorption of Sb and In using the XSW technique. The GaAs(001):Sb-(2×4) surface prepared by MBE was studied by (004), (022) and (111) x-ray standing waves. All three XSW measurements are consistent with the formation of symmetric Sb dimers above the modified bridge site. The Sb dimer height was determined to be $h' = 1.72 \pm 0.02 \text{ \AA}$ above the bulk-like (004) Ga atomic plane. The Sb dimer bond length was measured to be $L = 2.84 \pm 0.05 \text{ \AA}$. Both values are in good agreement with previous theoretical calculations and other related measurements. The Sb coverage of the (2×4) reconstruction was determined by Rutherford backscattering to be 0.48 ML, consistent with surface models having two Sb dimers per (2×4) unit cell, and disagreeing with models (δ_1 , β_2 and β_3) having one and three Sb dimers per unit cell. Finally, the (111) measurement showed no lateral shift of the Sb dimers in the [110] direction. Our analysis strongly favors the (2×4) model with one As dimer in the third layer (the β_2 model) over the α_2 and δ_2 models.

For the investigation of the In-induced GaAs(001) (4×2)/c(8×2) reconstruction, indium was deposited at room temperature onto the GaAs(001) (2×4) surface prepared by thermally desorbing an As protective layer. A sharp (4×2)/c(8×2) LEED pattern was observed after the substrates were annealed at 480°C. Further annealing at $\geq 500 \text{ }^\circ\text{C}$ resulted in complete desorption of the In adatoms. The XSW analysis on the surfaces

terminated with 0.2 – 0.3 ML of In annealed at 480 °C showed clear disagreement with the previous model proposed by Resch-Esser *et al.*, which was based on the structure widely accepted for the GaAs(001) Ga-rich (4×2) reconstruction. It predicted the formation of two In-In dimers per (4×2) unit cell in the first layer over the modified bridge sites. Surprisingly, we found that the In adatoms were located above the hollow sites, and the formation of In-In dimers was unlikely. Based on our findings and the previous STM studies we proposed a new (4×2)/c(8×2) model for this surface. It is characterized by In monomers lining up at the hollow sites above As dimer rows with the trench areas between the In rows terminated with Ga dimers in the third layer. Each c(8×2) unit cell contains four In monomers, leading to a coverage of 0.25 ML. The ×2 symmetry is due to the Ga dimerization in the [110] direction. The 8× symmetry is due to the 16 Å separation in the $[\bar{1}10]$ direction between the In rows as well as the 180° phase shift of the Ga-dimer positions along the [110] direction between the adjacent rows. This model agrees qualitatively with the present XSW results and is able to explain most features observed by STM. However, quantitatively the agreement between the model and the XSW measurements is unsatisfactory. This suggests that the real structure of the surface may be more complicated. Further modification of this model is expected in the future upon the availability of new experimental evidences.

Furthermore, we applied XSW to characterize the strain in one ML of pseudobinary semiconductor alloys buried in (001) and (111) substrates. For the (001) direction $\text{In}_x\text{Ga}_{1-x}\text{As}$ monolayers were grown on GaAs(001) by molecular beam epitaxy. The

measured In position along the [001] direction exhibited a nearly linear dependence on the In concentration x , thus supporting the validity of macroscopic continuum elasticity theory at the one ML limit. A random-cluster calculation using the Keating valence force field was performed to explain microscopically the origin of the vertical expansion of the strained ML observed by the experiment. The calculated As-In-As bond angle and the positions of the first nearest neighbor As atoms of In suggest that the nearly linear dependence of the In height on the alloy composition is a combined result of the As-In-As bond bending and the local lattice distortion at the GaAs/ $\text{In}_x\text{Ga}_{1-x}\text{As}$ interface. The calculated In-As and Ga-As bond lengths were found to depend weakly on the In concentration, consistent with an earlier calculation for the case of a thick $\text{In}_x\text{Ga}_{1-x}\text{As}$ film on GaAs(001) and the available EXAFS data. In addition, we applied the evanescent-wave-emission effect to directly measure the vertical displacement of the GaAs cap induced by the strain in a buried InAs layer. The measured cap displacement showed good agreement with the In position and continuum elasticity theory. Nevertheless, our off-normal {111} XSW measurements revealed an unexpected anisotropic In distribution in the buried layers. For the (111)-oriented strained layers, $\text{InSb}(111)/1 \text{ ML } \text{InAs}_x\text{Sb}_{1-x}$ heterostructures were measured by XSW and EXAFS. The XSW measured As (111) positions in the films showed a strain effect much larger than what was suggested by continuum elasticity theory. However, the EXAFS measurements detected no significant bond length split between the in-plane and out-of-plane In-As

bonds, which was predicted by a random cluster calculation using Keating valence force field to be as large as 0.05 \AA for $x = 1$.

In addition, we describe the theoretical background for calculating the total internal x-ray field near a Bragg reflection of a thin film based on the Takagi-Taupin dynamical theory. This leads to the possibility of using the standing waves generated by a thin film as a structural prob. We tested our theory by studying the polarization states of a PbTiO_3 thin film grown on a $\text{SrTiO}_3(001)$ structure. It was found that the 400 \AA as-grown PbTiO_3 film was in a single up polarization state

REFERENCES

Chapter 2

- [1] S. Takagi, *Acta Cryst.* 15, 1311 (1962).
- [2] D. Taupin, *Bull. Soc. Fr. Miner. Crist.* 87, 469 (1964).
- [3] M.V. Koval'chuk, V.G. Kon, and E.F. Lobanovich, *Sov. Phys. Solid State* 27, 2034 (1985); A.Yu. Kazimirov, M.V. Kovalchuk, and V.G. Kohn, *Sov. Tech. Phys. Lett.* 14, 587 (1988); P. Novak, J. Kub, M. Marysko, A.Yu. Kazimirov, A.N. Sosphenov, and M.V. Kovalchuk, *J. Mag. Mat.* 101, 155 (1991); A.Yu. Kazimirov, M.V. Kovalchuk, A.N. Sosphenov, V.G. Kohn, J. Kub, P. Novak, and M. Nerviva, *Acta. Cryst.* B48, 577 (1992).
- [4] A. Authier, J. Gronkowski, and C. Malgrange, *Acta, Cryst.* A45, 432 (1989).
- [5] M. Schuster, A. Lessmann, A. Munkholm, S. Brennan, G. Materlik, and H. Riechert, *J. Phys. D: Appl. Phys.* 28, A206 (1995).
- [6] A. Lessmann, S. Brennan, A. Munkholm, M. Schuster, H. Riechert, and G. Materlik, *Phys. Rev. B* 59, 10801 (1999).
- [7] A. Kazimirov A, T. Haage, L. Ortega, A. Stierle, F. Comin, and J. Zegenhagen, *Solid State Commun.* 104, 347 (1997).
- [8] G. Scherb, A. Kazimirov, J. Zegenhagen, T.-L. Lee, M.J. Bedzyk, H. Noguchi, and K. Uosaki, *Phys. Rev. B* 58, 10800 (1998).
- [9] M.J. Bedzyk, A. Kazimirov, D.L. Marasco, T.-L. Lee, C.M. Foster, G.-R. Bai, P.F. Lyman, and D.T. Keane, to be published.
- [10] J. Zegenhagen, *Surf. Sci. Rep.* 18, 199 (1993).
- [11] B.W. Batterman and H. Cole, *Rev. Mod. Phys.* 36, 681 (1964).
- [12] Z.G. Pinsker, *Dynamical Scattering of X-rays in Crystals*, Springer-Verlag, Berlin (1978).
- [13] R.W. James, *The Optical Principles of the Diffraction in Crystals*, G. Bell and Sons, London, 1950.

- [14] W.H. Zachariasen, *Theory of X-Ray Diffraction in Crystals*, John Wiley and Sons, New York, 1945.
- [15] P. P. Ewald and his *Dynamical Theory of X-ray Diffraction*, edited by D. W. J. Cruickshank, H.J. Juretschke, and N. Kato, Oxford University Press, England, 1992.
- [16] Y. Qian, Ph.D. thesis, Northwestern University, Evanston, 1995.
- [17] W.J. Bartels, J. Hornstra, and D.J. W. Lobeek, *Acta. Cryst.* A42, 539 (1986).
- [18] P.P. Ewald, *Ann. Physik* 49, 1 (1916); 54, 519 (1917).
- [19] M. von Laue, *Ergeb. Exakt. Naturw.* 10, 133 (1931).
- [20] S. Takagi, *J. Phys. Soc. Japan* 26, 1239 (1969).
- [21] A. Authier and D. Simon, *Acta. Cryst.* A24, 517 (1968).
- [22] T. Uragami, *J. Phys. Soc. Japan* 27, 147 (1969).
- [23] A.M. Afanas'ev and V.G. Kohn, *Acta. Cryst.* A27, 421 (1971).
- [24] T. Saka, T. Katagawa, and N. Kato, *Acta. Cryst.* A29, 192 (1973).
- [25] J.D. Jackson, *Classical Electrodynamics*, 3rd Ed., John Wiley and Sons, New York, 1998.
- [26] The 0th order term of κ corresponds to the average value of the dielectric constant of the material. So the average refractive index is $n = k_i / k_e = \sqrt{\kappa_0}$
 $= \sqrt{1 + \chi_0} = \sqrt{1 - \Gamma F_0} \approx 1 - \frac{1}{2} \Gamma F_0$.
- [27] $\mathbf{E} = (1 + \chi)^{-1} \mathbf{D} \approx (1 - \chi) \mathbf{D}$ and $\nabla \times \nabla \times \mathbf{D} = \nabla(\nabla \cdot \mathbf{D}) - \nabla^2 \mathbf{D} = -\nabla^2 \mathbf{D}$. Notice that since χ is very small in the wavelength range of x-ray, there is essentially no difference between using \mathbf{D} and \mathbf{E} field in deriving the theory. However, it is less problematic in discussing the cases for the different polarization states by using \mathbf{D} field.
- [28] We omit the high-order terms containing $\frac{\partial^2 \mathbf{D}_g}{\partial x^2}$ and $\frac{\partial^2 (\mathbf{g} \cdot \mathbf{u})}{\partial x^2}$ in (2.20) and the terms containing $\nabla \times \mathbf{D}_q$ and $\nabla \times (\mathbf{k}_g' \times \mathbf{D}_q)$ in (2.22).

- [29] $\hat{\mathbf{s}}_{\mathbf{g}_0} \cdot \hat{\mathbf{e}}_{\mathbf{g}_0} = 0$ for a perfect lattice. For a deformed lattice we assume that the deformation is so small that $\hat{\mathbf{s}}_{\mathbf{g}} \cdot \hat{\mathbf{e}}_{\mathbf{g}_0} \approx 0$.
- [30] Since $\mathbf{a} \times (\mathbf{b} \times \mathbf{c}) = (\mathbf{a} \cdot \mathbf{c})\mathbf{b} - (\mathbf{a} \cdot \mathbf{b})\mathbf{c}$, $\mathbf{k}_g' \times (\mathbf{k}_g' \times \mathbf{D}_q) = (\mathbf{D}_q \cdot \mathbf{k}_g')\mathbf{k}_g' - (\mathbf{k}_g' \cdot \mathbf{k}_g')\mathbf{D}_q$.
- [31] The approximation in (2.27) holds not because $|\mathbf{k}_0|^2 \approx k^2$ but because Γ is a very small number. Notice that $|\mathbf{k}_0|^2 \neq k^2$ in the vicinity of a Bragg reflection. See Section 2.2.4.
- [32] More than one tie point are usually selected by the boundary conditions. See the discussion in Ref. 2.11.
- [33] R.S. Becker, J.A. Golovchenko, and J.R. Patel, Phys. Rev. Lett. 50, 153 (1983).
- [34] For example, M. Born and E. Wolf, Principles of Optics, 6th edition, Pergamon Press, New York, 1993.
- [35] B.W. Batterman, Phys. Rev. 133, A759 (1964).
- [36] T. -L. Lee, Y. Qian, P. F. Lyman, J. C. Woicik, J. G. Pellegrino, and M. J. Bedzyk, Physica B 221, 437 (1996).

Chapter 3

- [1] J. Zegenhagen, Surf. Sci. Rep. 18, 199 (1993).
- [2] Y. Qian, Ph.D. thesis, Northwestern University, Evanston, 1995.

Chapter 4

- [1] W. Monch, Semiconductor Surfaces and Interfaces, 2nd Ed., Springer-Verlag, Berlin (1995).
- [2] J. Singh, Semiconductor Optoelectronics: Physics and Technology, International Ed., McGraw-Hill, Singapore (1995).
- [3] For example, A. Kahn, Surf. Sci. Rep. 3, 193 (1983); J. Fritsch, P. Pavone, and U. Schroder, Phys. Rev. Lett. 71, 4194 (1993).

- [4] C.B. Duke, *Chem. Rev.* 96, 1237 (1996).
- [5] W.A. Harrison, *Surf. Sci.* 55, 1 (1976).
- [6] W.A. Harrison, *J. Vac. Sci. Technol.* 16, 1492 (1979).
- [7] M.D. Pashley, *Phys. Rev. B* 40, 10481 (1989).
- [8] J.E. Northrup and S. Froyen, *Phys. Rev. B* 50, 2015 (1994).
- [9] S. Mirbt, N. Moll, A. Kley, and J.D. Joannopoulos, *Surf. Sci.* 422, L177 (1999).
- [10] W.A. Harrison, *Electronic Structure and the Properties of Solids*, Dover, New York (1989).
- [11] R.E. Peierls, *Quantum Theory of Solids*, Oxford University Press, New York (1955), and see Ref. 4.4 for the application of the theory to semiconductor surfaces.
- [12] A.Y. Cho, *J. Appl. Phys.* 42, 2074 (1971).
- [13] J.R. Arthur, *Surf. Sci.* 43, 449 (1974).
- [14] A.Y. Cho, *J. Appl. Phys.* 47, 2841 (1976).
- [15] A.J. Van Bommel and J.E. Crombeen, *Surf. Sci.* 57, 437 (1976).
- [16] J.H. Neave and B.A. Joyce, *J. Crys. Growth* 44, 387 (1978).
- [17] P. Drathen, W. Ranke, and K. Jacobi, *Surf. Sci.* 77, L162 (1978).
- [18] A.J. Van Bommel, J.E. Crombeen, and T.G.J. Van Oirschot, *Surf. Sci.* 72, 95 (1978).
- [19] J. Massies, P. Etienne, F. Dezaly, and N.T. Linh, *Surf. Sci.* 99, 121 (1980).
- [20] R.Z. Bachrach, R.S. Bauer, P. Chiaradia, and G.V. Hansson, *J. Vac. Sci. Technol.* 18, 797 (1981).
- [21] R.Z. Bachrach, R.S. Bauer, P. Chiaradia, and G.V. Hansson, *J. Vac. Sci. Technol.* 19, 335 (1981).

- [22] T.-C. Chiang, R. Ludeke, M. Aono, G. Landgren, F.J. Himpsel, and D.E. Eastman, *Phys. Rev. B* 27, 4770 (1983).
- [23] D.J. Frankel, C. Yu, J.P. Harbison, and H.H. Farrell, *J. Vac. Sci. Technol. B* 5, 1113 (1987).
- [24] R. Ludeke and L. Esaki, *Phys. Rev. Lett.* 33, 653 (1974).
- [25] R. Ludeke and A. Koma, *J. Vac. Sci. Technol.* 13, 241 (1976).
- [26] T.G. Andersson and S.P. Svensson, *Surf. Sci.* 110, L578 (1981).
- [27] P.K. Larsen, J.F. van der Veen, A. Mazur, J. Pollmann, J.H. Neave, and B.A. Joyce, *Phys. Rev. B* 26, 3222 (1982).
- [28] J.A. Appelbaum, G.A. Baraff, and D.R. Hamann, *Phys. Rev. B* 14, 1623 (1976).
- [29] J. Pollmann and S.T. Pantelides, *Phys. Rev. B* 18, 5524 (1978).
- [30] I. Ivanov, A. Mazur, and J. Pollmann, *Surf. Sci.* 92, 365 (1980).
- [31] D.J. Chadi, C. Tanner, and J. Ihm, *Surf. Sci.* 120, L425 (1982).
- [32] J. Ihm, D.J. Chadi, and J.D. Joannopoulos, *Phys. Rev. B* 27, 5119 (1983).
- [33] D.J. Chadi, *J. Vac. Sci. Technol. A* 5, 834 (1987); see also G.-X. Qian, R.M. Martin, and D.J. Chadi, *Phys. Rev. B* 38, 7649 (1988).
- [34] M.D. Pashley, K.W. Haberern, W. Friday, J.M. Woodall, and P.D. Kirchner, *Phys. Rev. Lett.* 60, 2176 (1988).
- [35] M.D. Pashley, K.W. Haberern, and J.M. Woodall, *J. Vac. Sci. Technol. B* 6, 1468 (1988).
- [36] D.K. Biegelsen, R.D. Bringans, J.E. Northrup, and L.-E. Swartz, *Phys. Rev. B* 41, 5701 (1990).
- [37] H.H. Farrell and C.J. Palmstrøm, *J. Vac. Sci. Technol. B* 8, 903 (1990).
- [38] J.P. Harbison and H.H. Farrell, *J. Vac. Sci. Technol. B* 6, 733 (1988).
- [39] T. Ohno, *Phys. Rev. Lett.* 70, 631 (1993).

- [40] J.E. Northrup and S. Froyen, *Phys. Rev. Lett.* 71, 2276 (1993).
- [41] M.D. Pashley, K.W. Haberern, and R.M. Feenstra, *J. Vac. Sci. Technol. B* 10, 1874 (1992).
- [42] V. Bressler-Hill, M. Wassermeier, K. Pond, R. Maboudian, G.A.D. Briggs, P.M. Petroff, and W.H. Weinberg, *J. Vac. Sci. Technol. B* 10, 1881 (1992).
- [43] T. Hashizume, Q.K. Xue, J. Zhou, A. Ichimiya, and T. Sakurai, *Phys. Rev. Lett.* 73, 2208 (1994).
- [44] T. Hashizume, Q.K. Xue, A. Ichimiya, and T. Sakurai, *Phys. Rev. B* 51, 4200 (1995).
- [45] Y. Garreau, M. Sauvage-Simkin, N. Jedrecy, R. Pinchaux, and M.B. Veron, *Phys. Rev. B* 54, 17638 (1996).
- [46] J.M. McCoy, U. Korte, and P.A. Maksym, *Surf. Sci.* 418, 273 (1998).
- [47] G.P. Srivastava and S.J. Jenkins, *Phys. Rev. B* 53, 12589 (1995).
- [48] W.G. Schmidt and F. Bechstedt, *Phys. Rev. B* 54, 16742 (1996).
- [49] Other recent theoretical calculations of the clean GaAs(001) surface without giving detailed structural parameters are: S.B. Zhang and A. Zunger, *Phys. Rev. B* 53, 1343 (1996); C.M. Goringe, L.J. Clark, M.H. Lee, M.C. Payne, I. Stich, J.A. White, M.J. Gillan, and A.P. Sutton, *J. Phys. Chem. B* 101, 1498 (1997).
- [50] A comprehensible explanation can be also found in *Concepts in Surface Physics* by M.C. Desjonqueres and D. Spanjaard, 2nd Ed., Springer-Verlag, Berlin (1996).
- [51] C. Kress, M. Fiedler, W.G. Schmidt, and F. Bechstedt, *Phys. Rev. B* 50, 17697 (1994).
- [52] M.D. Pashley and K.W. Haberern, *Phys. Rev. Lett.* 67, 2697 (1991).
- [53] M.D. Pashley, K.W. Haberern, R.M. Feenstra, and P.D. Kirchner, *Phys. Rev. B* 48, 4612 (1993).
- [54] U. Resch-Esser, N. Esser, J. Zegenhagen, W. Richter, M. Cardona, and B.O. Fimland, *J. Vac. Sci. Technol. B* 13, 1672 (1995).

- [55] S.L. Skala, J.S. Hubacek, J.R. Tucker, J.W. Lyding, S.T. Chou, and K.-Y. Cheng, *Phys. Rev. B* 48, 9138 (1993).
- [56] Q. Xue, T. Hashizume, J.M. Zhou, T. Sakata, T. Ohno, and T. Sakurai, *Phys. Rev. Lett.* 74, 3177 (1995).
- [57] T. Ohno, *Surf. Sci.* 357 - 358, 265 (1996).
- [58] J. Cerda, F.J. Palomares, and F. Soria, *Phys. Rev. Lett.* 75, 665 (1995).
- [59] P. Moriaty, P.H. Beton, Y.-R. Ma, A.W. Dunn, M. Henini, and D.A. Woolf, *J. Vac. Sci. Technol. B* 14, 943 (1996).
- [60] P.L. Larsen, J.H. Neave, J.F. van der Veen, P.J. Dobson, and B.A. Joyce, *Phys. Rev. B* 27, 4966 (1983).
- [61] C. Sasaoka, Y. Kato, and A. Usui, *Surf. Sci. Lett.* 265, L239 (1992).
- [62] M. Sauvage-Simkin, R. Pinchaux, J. Massies, P. Calverie, N. Jedrecy, J. Bonnet, and I.K. Robinson, *Phys. Rev. Lett.* 62, 563 (1989).
- [63] A.P. Payne, P.H. Fuoss, D.W. Kisker, G.B. Stephenson, and S. Brennan, *Phys. Rev. B* 49, 14427 (1994).
- [64] V.H. Etgens, M. Sauvage-Simkin, R. Pinchaux, J. Massies, N. Jedrecy, A. Waldhauer, and N. Greiser, *Surf. Sci.* 320, 252 (1994).
- [65] C. Xu, J.S. Burnham, R.M. Braun, S.H. Goss, and N. Winograd, *Phys. Rev. B* 52, 5172 (1995).
- [66] A.R. Avery, D.M. Holmes, J.Sudijono, T.S. Jones, and B.A. Joyce, *Surf. Sci.* 323, 91 (1995).
- [67] C.W. Snyder, J.Sudijono, C.-H. Lam, M.D. Johnson, and B.G. Orr, *Phys. Rev. B* 50, 18194 (1994).
- [68] M. Kuball, D.T. Wang, N. Esser, M. Cardona, J. Zegenhagen, and B.O. Fimland, *Phys. Rev. B* 51, 13880 (1995).
- [69] I. Chizhov, G. Lee, R.F. Willis, D. Lubyshev, D.L. Miller, *Surf. Sci.* 419, 1 (1998).

- [70] J.G. McLean, P. Kruse, A.C. Kummel, *Surf. Sci.* 424, 206 (1999).
- [71] For example, Q.-K. Xue, T. Hashizume, and T. Sakurai, *Appl. Surf. Sci.* 141, 244 (1999).
- [72] L. Daweritz and R. Hey, *Surf. Sci.* 236, 15 (1990).
- [73] S.P. Kowalczyk, D.L. Miller, J.R. Waldrop, P.G. Newman, and R.W. Grant, *J. Vac. Sci. Technol.* 19, 255 (1981).
- [74] S.A. Clark, C.J. Dunscombe, D.A. Woolf, S.P. Wilks, and R.H. Williams, *J. Vac. Sci. Technol. B* 12, 551 (1994).
- [75] Private communication with J. Zegenhagen (Max-Planck-Institut, Stuttgart, Germany).
- [76] U. Resch-Esser, N. Esser, D.T. Wang, M. Kuball, J. Zegenhagen, B.O. Fimland, and W. Richter, *Surf. Sci.* 352-354, 71 (1996).
- [77] U. Resch, N. Esser, Y.S. Raptis, W. Richter, J. Wasserfall, A. Forster, and D.I. Westwood, *Surf. Sci.* 269/270, 797 (1992).
- [78] M.C. Gallagher, R.H. Prince, and R.F. Willis, *Surf. Sci.* 275, 31 (1992).

Chapter 5

- [1] F. Maeda, Y. Watanabe, and M. Oshima, *Phys. Rev. B* 48, 14733 (1993).
- [2] N. Esser, A.I. Shkrebtii, U. Resch-Esser, C. Springer, W. Richter, W.G. Schmidt, F. Bechstedt, and R. Del Sole, *Phys. Rev. Lett.* 77, 4402 (1996).
- [3] P. Moriarty, P.H. Beton, Y.-R. Ma, and M. Henini, *Phys. Rev. B* 53, R16148 (1996).
- [4] M. Sugiyama, S. Maeyama, F. Maeda, and M. Oshima, *Phys. Rev. B* 52, 2678 (1995).
- [5] Y. Qian, P.F. Lyman, T.-L. Lee, and M.J. Bedzyk, *Physica B* 221, 430 (1996).

- [6] M. Lohmeier, H.A. van der Vegt, R.G. van Silfhout, E. Vlieg, J.M.C. Thornton, J.E. Macdonald, and P.M.L.O. Scholte, *Surf. Sci.* 275, 190 (1992).
- [7] M.G. Betti, C. Mariani, N. Jedrecy, R. Pinchaux, A. Ruocco, and M. Sauvage-Simkin, *Phys. Rev. B* 50, 14336 (1994).
- [8] G.P. Srivastava, S.J. Jenkins, *Surf. Sci.* 377 - 379, 23 (1997).
- [9] W.G. Schmidt and F. Bechstedt, *Phys. Rev. B* 55, 13051 (1997).
- [10] W.G. Schmidt and F. Bechstedt, *Surf. Sci.* 377 - 379, 11 (1997).
- [11] W.F.J. Slijkerman, P.M. Zagwijn, J.F. van der Veen, D.J. Gravesteijn, and G.F.A. van de Walle, *Surf. Sci.* 262, 25 (1992).
- [12] M.W. Grant, P.F. Lyman, J.H. Hoogenraad, and L.E. Seiberling, *Surf. Sci.* 279, L180 (1992).
- [13] M.J. Bedzyk and G. Materlik, *Phys. Rev. B* 31, 4110 (1985).
- [14] T. Matsushita and H. Hayashi, *Phys. Stat. Sol. (a)* 41, 139 (1997); *International Tables for X-Ray Crystallography*, edited by C.H. MacGillavry *et al.*, (The Kynoch Press, Birmingham, England, 1962) Vol. III.
- [15] G.E. Franklin, E. Fontes, Y. Qian, M.J. Bedzyk, J.A. Golovchenko and J.R. Patel, *Phys. Rev. B* 50, 7483 (1994).
- [16] P.F. Lyman, Y. Qian, T.-L. Lee and M.J. Bedzyk, *Physica B* 221, 426 (1996).
- [17] H.H. Farrell and C.J. Palmstrøm, *J. Vac. Sci. Technol. B* 8, 903 (1990).
- [18] D.J. Chadi, *J. Vac. Sci. Technol. A* 5, 834 (1987); see also G.-X. Qian, R.M. Martin, and D.J. Chadi, *Phys. Rev. B* 38, 7649 (1988).
- [19] J.E. Northrup and S. Froyen, *Phys. Rev. Lett.* 71, 2276 (1993).

Chapter 6

- [1] C. Ohler, C. Daniels, A. Forster, and H. Luth, *J. Vac. Sci. Technol. B* 15, 702 (1997).
- [2] H. Yamaguchi and Y. Horikoshi, *Phys. Rev. B* 45, 1511 (1992).

- [3] H. Yamaguchi and Y. Horikoshi, *Phys. Rev. B* 48, 2807 (1993).
- [4] H. Yamaguchi and Y. Horikoshi, *Jpn. J. Appl. Phys.* 33, L1423 (1994).
- [5] H. Yamaguchi and Y. Horikoshi, *Phys. Rev. B* 51, 9836 (1995).
- [6] H. Yamaguchi and Y. Horikoshi, *J. Cryst. Growth* 150, 148 (1995).
- [7] S. Ohkouchi and N. Ikoma, *Jpn. J. Appl. Phys.* 33, L1770 (1994).
- [8] M. Gothelid, Y. Garreau, M. Sauvage-Simkin, R. Pinchaux, A. Cricenti, and G. Le Lay, *Phys. Rev. B* 59, 15285 (1999).
- [9] C. Kendrick, G. LeLay, and A. Kahn, *Phys. Rev. B* 54, 17877 (1996).
- [10] M. Noguchi, K. Hirakawa, and T. Ikoma, *Phys. Rev. Lett.* 66, 2243 (1991).
- [11] L.O. Olsson, C.B.M. Andersson, M.C. Hakansson, J. Kanski, L. Ilver, and U.O. Karlsson, *Phys. Rev. Lett.* 76, 3626 (1996).
- [12] C. Ohler, C. Daniels, A. Forster, and H. Luth, *J. Vac. Sci. Technol. B* 15, 702 (1997).
- [13] J. Tersoff, *Phys. Rev. B* 32, 6968 (1985).
- [14] A.G. Milnes, A.Y. Polyakov, *Mat. Sci. Eng. B* 18, 237 (1993).
- [15] J.M. Moison, C. Guille, and M. Bensoussan, *Phys. Rev. Lett.* 58, 2555 (1987).
- [16] H. Yamaguchi and Y. Horikoshi, *Phys. Rev. Lett.* 70, 1299 (1993).
- [17] J.N. Stranski and L. Krastanov, *Ber. Akad. Wiss. Wien.* 146, 797 (1938).
- [18] D. Leonard, K. Pond, and P.M. Petroff, *Phys. Rev. B* 50, 11687 (1994).
- [19] T.R. Ramachandran, R. Heitz, P. Chen, and A. Madhukar, *Appl. Phys. Lett.* 70, 640 (1997).
- [20] T.R. Ramachandran, R. Heitz, N.P. Kobayashi, A. Kalburge, W. Yu, P. Chen, and A. Madhukar, *J. Cryst. Growth* 175/176, 216 (1997).
- [21] J.G. Belk, J.L. Sudijono, D.M. Holmes, C.F. McConville, , T.S. Jones, and B.A. Joyce, *Surf. Sci.* 365, 735 (1996).

- [22] J.G. Belk, C.F. McConville, J.L. Sudijono, T.S. Jones, and B.A. Joyce, *Surf. Sci.* 387, 213 (1997).
- [23] S.M. Scholz, A.B. Muller, W. Richter, D.R.T. Zahn, D.I. Westwood, D.A. Woolf, and R.H. Williams, *J. Vac. Sci. Technol. B* 10, 1710 (1992).
- [24] V. Bressler-Hill, A. Lorke, A. Varma, P.M. Petroff, K. Pond, and W.H. Weinberg, *Phys. Rev. B* 50, 8479 (1994).
- [25] V. Bressler-Hill, A. Varma, A. Lorke, B.Z. Nosho, P.M. Petroff, K. Pond, and W.H. Weinberg, *Phys. Rev. Lett.* 74, 3209 (1995).
- [26] C.W. Snyder, B.G. Orr, D. Kessler, and L.M. Sander, *Phys. Rev. Lett.* 66, 3032 (1991).
- [27] C. Ratsch and A. Zangwill, *Surf. Sci.* 293, 123 (1993).
- [28] P.B. Joyce, T.J. Krzyzewski, G.R. Bell, B.A. Joyce, and T.S. Jones, *Phys. Rev. B* 58, R15981 (1998).
- [29] K. Brunner, U. Bockelmann, G. Abstreiter, M. Walther, G. Bohm, G. Trankle, and G. Weimann, *Phys. Rev. Lett.* 69, 3216 (1992).
- [30] J.-Y. Marzin, J.-M. Gerard, A. Izrael, D. Barrier, and G. Bastard, *Phys. Rev. Lett.* 73, 716 (1994).
- [31] M.V. Belousov, N.N. Ledentsov, M.V. Maximov, P.D. Wang, I.N. Yasievich, N.N. Faleev, I.A. Kozin, V.M. Ustinov, P.S. Kop'ev, and C.M. Sotomayor Torres, *Phys. Rev. B* 51, 14346 (1995).
- [32] M Grundmann, N.N. Ledentsov, O. Stier, J. Bohrer, D. Bimberg, V.M. Ustinov, P.S. Kop'ev, and Zh. I. Alferov, *Phys. Rev. B* 53, R10509 (1996).
- [33] K.H. Schmidt, G. Medeiros-Ribeiro, U. Kunze, G. Abstreiter, M. Hagn, and P.M. Petroff, *J. Appl. Phys.* 84, 4268 (1998).
- [34] M. Grundmann, O. Stier, and D. Bimberg, *Phys. Rev. B* 52, 11969 (1995).
- [35] J. Kim, L.-W. Wang, and A. Zunger, *Phys. Rev. B* 57, R9408 (1998).
- [36] L. Harris, D.J. Mowbray, M.S. Skolnick, M. Hopkinson, and G. Hill, *Appl. Phys. Lett.* 73, 969 (1998).
- [37] V.M. Ustinov *et al.*, *Appl. Phys. Lett.* 74, 2815 (1999).

- [38] L.F. Lester, A. Stintz, H. Li, T.C. Newell, E.A. Pease, B.A. Fuchs, and K.J. Malloy, *IEEE Photon. Technol. Lett.* 11, 931 (1999).
- [39] J. Phillips, K. Kamath, T. Brock, and P. Bhattacharya, *Appl. Phys. Lett.* 72, 3509 (1998).
- [40] G. Yusa and H. Sakaki, *Superlatt. Microstruct.* 25, 247 (1999).
- [41] J. Phillips, P. Bhattacharya, S.W. Kennerly, D.W. Beekman, and M. Dutta, *IEEE J. Quantum Elect.* 35, 936 (1999).
- [42] R.M. Tromp and M.C. Reuter, *Phys. Rev. Lett.* 68, 954 (1992).
- [43] J. Massies and N. Grandjean, *Phys. Rev. B* 48, 8502 (1993).
- [44] E. Tournie, N. Grandjean, A. Trampert, J. Massies, and K.H. Ploog, *J. Cryst. Growth* 150, 460 (1995).
- [45] M. Copel, M.C. Reuter, E. Kaxiras, and R.M. Tromp, *Phys. Rev. Lett.* 63, 632 (1989).
- [46] K. Sakamoto, K. Miki, T. Sakamoto, H. Yamaguchi, H. Oyanagi, H. Matsuhata, and K. Kyoya, *Thin Solid Films* 222, 112 (1992).
- [47] T. Schmidt, J. Falta, G. Materlik, J. Zeysing, G. Falkenberg, and R.L. Johnson, *Appl. Phys. Lett.* 74, 1392 (1999).
- [48] J. Tersoff, *Phys. Rev. B* 43, 9377 (1991).
- [49] W.J. Schaffer, M.D. Lind, S.P. Kowalczyk, and R.W. Grant, *J. Vac. Sci. Technol. B* 1, 688 (1983).
- [50] H. Munekata, L.L. Chang, S.C. Woronick, and Y.H. Kao, *J. Cryst. Growth* 81, 237 (1987).
- [51] E. Tournie and K.H. Ploog, *Appl. Phys. Lett.* 62, 858 (1993).
- [52] A. Trampert, E. Tournie, and K.H. Ploog, *J. Cryst. Growth* 146, 368 (1995).
- [53] E. Tournie, O. Brandt, and K.H. Ploog, *Appl. Phys. Lett.* 60, 2877 (1992).

- [54] E. Tournie, O. Brandt, K.H. Ploog, and M. Hohenstein, *Appl. Phys. A* 56, 91 (1993).
- [55] U. Resch-Esser, N. Esser, C. Springer, J. Zegenhagen, W. Richter, M. Cardona, and B.O. Fimland, *J. Vac. Sci. Technol. B* 13, 1672 (1995).
- [56] C. Springer, U. Resch-Esser, C. Goletti, W. Richter, and B.O. Fimland, *Surf. Sci.* 377 – 379, 404 (1997).
- [57] Q. Xue, Y. Hasegawa, T. Ogino, H. Kiyama, and T. Sakurai, *J. Vac. Sci. Technol. B* 15, 1270 (1997).
- [58] Q. Xue, T. Ogino, H. Kiyama, Y. Hasegawa, and T. Sakurai, *J. Cryst. Growth* 175/176, 174 (1997).
- [59] J. Behrend, M. Wassermeier, and K.H. Ploog, *J. Cryst. Growth* 167, 440 (1996).
- [60] See Yonglin Qian's Ph.D. thesis, page 67.
- [61] X. Torrelles, J. Rius, F. Boscherini, S. Heun, B.H. Mueller, S. Ferrer, J. Alvarez, and C. Miravittles, *Phys. Rev. B* 57, R4281 (1998).
- [62] Private communication with J. Zegenhagen (Max-Planck-Institut, Stuttgart, Germany).
- [63] D.H. Rich, A. Samsavar, T. Miller, H.F. Lin, T.-C. Chiang, J.-E. Sundgren, and J.E. Greene, *Phys. Rev. Lett.* 58, 579 (1987).
- [64] A.A. Baski, J. Nogami, and C.F. Quate, *Phys. Phys. B* 43, 9316 (1991).
- [65] H.W. Yeom, T. Abukawa, M. Nakamura, X. Chen, S. Suzuki, S. Sato, K. Sakamoto, T. Sakamoto, and S. Kono, *Surf. Sci.* 340, L983 (1995).
- [66] G. Falkenberg, L. Seehofer, and R.L. Johnson, *Surf. Sci.* 371, 86 (1997).
- [67] O. Bunk, G. Falkenberg, L. Seehofer, J.H. Zeysing, R.L. Johnson, M. Nielsen, R. Feidenhans'l, and E. Landemark, *Appl. Surf. Sci.* 123/124, 104 (1998).
- [68] Y. Qian, M.J. Bedzyk, S. Tang, A.J. Freeman, and G.E. Franklin, *Phys. Rev. Lett.* 73, 1521 (1994).

- [69] A UHV compatible, single-element Ge solid-state detector with a 1 mil Be window was used to collect the fluorescence spectra for the XSW measurements on sample S4 at the BESSRC CAT (APS). The detector was pointed at the sample at an angle of about 40° away from the polarization direction of the incident x-ray beam due to the geometry of the existing XSW chamber. This detector angle increased the contribution of Compton scattering to the fluorescence background. The total fluorescence count rate was limited to about 15000 cps by the detector system (with energy resolutions better than 200 eV). All the other UHV XSW measurements presented in Chapter 5 and 6 were carried out using a non-UHV Si(Li) solid-state detector, which can be pointed at the samples along the polarization direction. However, the thick Be window between the samples and the detector was undesirable for low-energy fluorescence measurements (see Yonlin Qian's Ph.D. thesis for the details).
- [70] J. Zegenhagen and his co-workers have conducted surface x-ray diffraction on the GaAs(001):0.3 ML In (4x2)/c(8x2) surface. They are currently collaborating with X. Torrelles using the direct method to solve the surface structure and meanwhile planning to acquire more fractional-order rod data of this surface.
- [71] D.J. Chadi, *J. Vac. Sci. Technol. A* 5, 834 (1987); see also G.-X. Qian, R.M. Martin, and D.J. Chadi, *Phys. Rev. B* 38, 7649 (1988).
- [72] P. Moriaty, P.H. Beton, Y.-R. Ma, A.W. Dunn, M. Henini, and D.A. Woolf, *J. Vac. Sci. Technol. B* 14, 943 (1996).
- [73] J. Singh, *Semiconductor Optoelectronics: Physics and Technology*, International Ed., McGraw-Hill, Singapore (1995).
- [74] D.K. Biegelsen, R.D. Bringans, J.E. Northrup, and L.-E. Swartz, *Phys. Rev. B* 41, 5701 (1990).
- [75] S.L. Skala, J.S. Hubacek, J.R. Tucker, J.W. Lyding, S.T. Chou, and K.-Y. Cheng, *Phys. Rev. B* 48, 9138 (1993).
- [76] Q. Xue, T. Hashizume, J.M. Zhou, T. Sakata, T. Ohno, and T. Sakurai, *Phys. Rev. Lett.* 74, 3177 (1995).

Chapter 7

- [1] Samples A through G (Section 7.2 and 7.3) were grown by Prof. Barnett's

group at NU. Sample W1 and W2 (Section 7.5) were prepared by Prof. Wessels' group at NU. The sample used for the evanescent-wave emission measurements in Section 7.4 was grown by J.G. Pellegrino at NIST.

- [2] For example, F. Martelli, A. Polimeni, A. Patane, M. Capizzi, P. Borri, M. Gurioli, and M. Colocci, A. Bosacchi, and S. Franchi, *Phys. Rev. B* 53, 7421 (1996); W. E. Hoke, P. S. Lyman, J. J. Mosca, H. T. Hendriks, A. Torabi, W. A. Bonner, B. Lent, L.-J. Chou, and K. C. Hsieh, *J. Appl. Phys.* 81, 968 (1997).
- [3] S.T. Chou, K.Y. Cheng, L.J. Chou, and K.C. Hsieh, *Appl. Phys. Lett.* 66, 2220 (1995).; T. Mattila, L. Bellaiche, L.-W. Wang, and A. Zunger, *Appl. Phys. Lett.* 72, 2144 (1998).
- [4] For example, S. Picozzi, A. Continenza, and A.J. Freeman, *Phys. Rev. B* 52, 5247 (1995).
- [5] *Semiconductors : Group IV Elements and III-V Compounds*, Edited by O. Madelung (Springer-Verlag, Berlin, 1991).
- [6] O. Brandt, K. Ploog, R. Bierwolf, and M. Hohenstein, *Phys. Rev. Lett.* 68, 1339 (1992).
- [7] C. Giannini, L. Tapfer, S. Lagomarsino, J. C. Boulliard, A. Taccoen, B. Capelle, M. Ilg, O. Brandt, and K. H. Ploog, *Phys. Rev. B* 48, 11496 (1993).
- [8] J. E. Bernard and A. Zunger, *Appl. Phys. Lett.* 65, 165 (1994).
- [9] J. C. Woicik, J. G. Pelligrino, S. H. Southworth, P. S. Shaw, B. A. Karlin, and C. E. Bouldin, *Phys. Rev. B* 52, R2281 (1995).
- [10] T. -L. Lee, Y. Qian, P. F. Lyman, J. C. Woicik, J. G. Pellegrino, and M. J. Bedzyk, *Physica B* 221, 437 (1996).
- [11] J.C. Woicik, K.E. Miyano, J.G. Pellegrino, P.S. Shaw, S.H. Southworth, and B.A. Karlin, *Appl. Phys. Lett.* 68, 3010 (1996).
- [12] J. G. C. Labanda, S. A. Barnett, and L. Hultman, *Appl. Phys. Lett.* 66, 3114 (1995).
- [13] Y. Qian, N. Sturchio, R. Chiarello, P. F. Lyman, T. -L. Lee, and M. J. Bedzyk, *Science* 265, 1555 (1994).
- [14] This energy scan is equivalent to scanning the angle of the sample substrate

about the Bragg angle, and the abscissas of the XSW data will be expressed as angular deflections for convenience.

- [15] See Eq. (2.60) and (2.72).
- [16] See Eq. (5.) and the discussion there.
- [17] $D_{004} = \exp(-B/2d_{004}^2)$, where $B = 0.59 \text{ \AA}^2$ is from T. Matsushita and H. Hayashi, Phys. Stat. Sol. (a) 41, 139 (1997); International Tables for X-Ray Crystallography, edited by C.H. MacGillavry et al. (The Kynoch Press, Birmingham, England, 1962), Vol. III.
- [18] J.C. Woicik, Phys. Rev. B 57, 6266 (1998).
- [19] J.C. Woicik, J.A. Gupta, S.P. Watkins, and E.D. Crozier, Appl. Phys. Lett. 73, 1269 (1998).
- [20] J.C. Woicik, J.G. Pellegrino, B. Steiner, K.E. Miyano, S.G. Bompadre, L.B. Sorensen, T.-L. Lee, and S. Khalid, Phys. Rev. Lett. 79, 5026 (1997).
- [21] J.C. Woicik, J.O. Cross, C.E. Bouldin, B. Ravel, J.G. Pellegrino, B. Steiner, S.G. Bompadre, L.B. Sorensen, K.E. Miyano, and J.P. Kirkland, Phys. Rev. B 58, R4215 (1998).
- [22] A. Amore Bonapasta and G. Scavia, Phys. Rev. B 50, 2671 (1994).
- [23] A. Sher, Mark van Schilfgaarde, An-Ban Chen, and W. Chen, Phys. Rev. B 36, 4279 (1987).
- [24] P.N. Keating, Phys. Rev. 145, 637 (1966).
- [25] The values of the constants α and β for InAs and GaAs used in this calculation were taken from R.M. Martin, Phys. Rev. B 1, 4005 (1970).
- [26] The energy minimization process followed the conjugate gradient method described in W.H. Press et al., Numerical Recipes in Fortran, Second Edition (Cambridge University Press, 1994).
- [27] For $x = 1.0$, the vertical position of the As underneath In is about 0.4% of d_{004} lower than the bulk As position. This can be understood from the fact that, under the same strain condition, the Ga-As bond length is expected to be shorter if the As atom bonds to Ga and In atoms simultaneously (see discussion

in Ref. 7.18).

- [28] J.C. Woicik, C.E. Bouldin, K.E. Miyano, and C.A. King, *Phys. Rev. B* 55, 15386 (1997).
- [29] J.C. Mikkelsen, Jr. and J.B. Boyce, *Phys. Rev. Lett.* 49, 1412 (1982), and *Phys. Rev. B* 28, 7130 (1983).
- [30] M.G. Proietti, F. Martelli, S. Turchini, L. Alagna, M.R. Bruni, T. Prospero, M.G. Simeone, and J. Garcia, *J. Cryst. Growth* 127, 592 (1993).
- [31] M.G. Proietti, S. Turchini, J. Garcia, G. Lamble, F. Martelli, and T. Prospero, *J. Appl. Phys.* 78, 6574 (1995).
- [32] For example, R. Feidenhans'l, *Surf. Sci. Rep.* 10, 105 (1989).
- [33] For example, M.V. Belousov et al, *Phys. Rev. B* 51, 14346 (1995).
- [34] V. Bressler-Hill, R. Maboudian, M. Wassermeier, X.-S. Wang, K. Pond, P.M. Petroff and W.H. Weinberg, *Surf. Sci.* 287/288, 514 (1993).
- [35] K. Ohta, T. Kojima and T. Nakagawa, *J. Cryst. Growth* 95, 71 (1989).
- [36] J. Massies and N. Grandjean, *Phys. Rev. Lett.* 71, 1411 (1993).
- [37] T. Takahashi and S. Kikuta, *J. Phys. Soc. Jpn.* 47 (1979), 620; M.J. Bedzyk, Materlik and M.V. Kovalchuk, *Phys. Rev. B* 30, 4881 (1984).
- [38] This was estimated based on the RT Debye-Waller factor for GaAs.
- [39] For example, P.A. Lee, P.H. Citrin, P. Eisenberger, and B.M. Kincaid, *Rev. Modern Phys.* 53, 769 (1981). The EXAFS data were analyzed by J.C. Woicik (NIST) using a personal EXAFS program. Figure 7.16 and 7.17(a) are the results of a re-analysis of the data by the author using MacXAFS based the parameters provided by Woicik.
- [40] The present non-cluster Keating calculation showed that the In atoms at the lower InAsSb/InSb interface were slightly above the ideal bulk position. The maximum deviation was about 0.025 Å at $x=1$. This was due to the fact that InAs has larger β than InSb, i.e., it is easier to compress a Sb-In-Sb bond angle than a Sb-In-As bond angle. In Figure 18 this deviation of the In position has been added to the dashed lines.

- [41] This discrepancy indicates that the (001) and (111) cluster calculations may require different boundary conditions for reducing the excess rigidity imposed by the statistical constraint. See Ref. 7.18.
- [42] V. Bressler-Hill, A. Lorke, A. Varma, P.M. Petroff, K. Pond, and W.H. Weinberg, *Phys. Rev. B* 50, 8479 (1994).

Appendix A

- [1] J.F. Nye, *Physical Properties of Crystals*, 1st Ed., Oxford University Press, London, 1985.

Appendix A Strains in Pseudomorphic Heterolayers of Cubic Materials

Based on Hook's law, the relationship between the stress (σ) and strain (ϵ) in a solid can be described by

$$\sigma_{ij} = C_{ijkl} \epsilon_{kl} \quad i, j, k, \text{ and } l = 1, 2, \text{ or } 3, \quad (\text{A.1})$$

where the fourth-rank tensor C_{ijkl} contains the 81 stiffness constants (or elastic constants) of the solid. σ and ϵ are both second-rank tensors with their first index representing the directions of the stress and strain fields and their second index the normal directions of the surfaces that the fields are applied to, as illustrated in Figure. Due to symmetry of C_{ijkl} Eq. (A.1) can be simplified into a matrix form [1]

$$\sigma_i = C_{ij} \epsilon_j \quad i \text{ and } j = 1, 2, \dots, 6. \quad (\text{A.2})$$

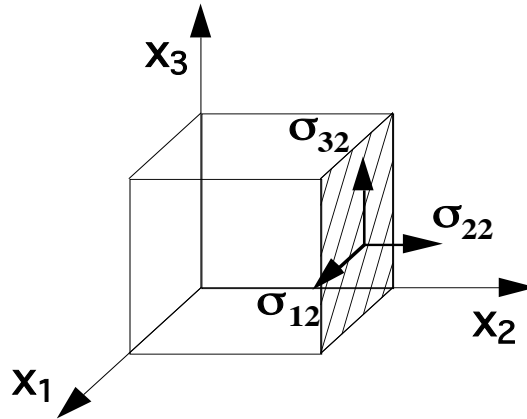


Figure A.1 The stress tensor notation.

In this matrix notation the single index 1 through 6 denote 11, 22, 33, 23/32, 31/13 and 12/21 in the original tensor notation. It can be shown that for cubic materials with the coordinate system \mathbf{x}_1 , \mathbf{x}_2 and \mathbf{x}_3 chosen to be along \mathbf{a} , \mathbf{b} and \mathbf{c} of the unit cell, most of the elements of the matrix C_{ij} vanish and $C_{11} = C_{22} = C_{33}$, $C_{12} = C_{13} = C_{23}$ and $C_{44} = C_{55} = C_{66}$,

$$\begin{pmatrix} \sigma_1 \\ \sigma_2 \\ \sigma_3 \\ \sigma_4 \\ \sigma_5 \\ \sigma_6 \end{pmatrix} = \begin{pmatrix} C_{11} & C_{12} & C_{12} & 0 & 0 & 0 \\ C_{12} & C_{11} & C_{12} & 0 & 0 & 0 \\ C_{12} & C_{12} & C_{11} & 0 & 0 & 0 \\ 0 & 0 & 0 & C_{44} & 0 & 0 \\ 0 & 0 & 0 & 0 & C_{44} & 0 \\ 0 & 0 & 0 & 0 & 0 & C_{44} \end{pmatrix} \begin{pmatrix} \varepsilon_1 \\ \varepsilon_2 \\ \varepsilon_3 \\ \varepsilon_4 \\ \varepsilon_5 \\ \varepsilon_6 \end{pmatrix}. \quad (\text{A.3})$$

This leads to

$$\sigma_3 = C_{12}(\varepsilon_1 + \varepsilon_2) + C_{11}\varepsilon_3. \quad (\text{A.4})$$

For a heterostructure pseudomorphically grown along the \mathbf{c} axis, the film is constrained to have the same in-plane lattice parameters as the substrate, while it is free to relax in the growth direction, i.e.,

$$\sigma_3 = 0 \text{ and } \varepsilon_1 = \varepsilon_2 = \varepsilon_{\parallel}. \quad (\text{A.5})$$

(A.4) and (A.5) suggest that

$$\varepsilon_{\perp} = \varepsilon_3 = -2 \frac{C_{12}}{C_{11}} \varepsilon_{\parallel}. \quad (\text{A.6})$$

To apply (A.2) to a strained film grown along the (111) direction, we need to redefine the coordinate system so \mathbf{x}_3' is parallel to the (111). This can be achieved by applying the transformation matrix

$$a_{ij} = \frac{1}{\sqrt{6}} \begin{pmatrix} \cos\theta - \sqrt{3}\sin\theta & \cos\theta + \sqrt{3}\sin\theta & -2\cos\theta \\ -\sin\theta - \sqrt{3}\cos\theta & -\sin\theta + \sqrt{3}\cos\theta & 2\sin\theta \\ \sqrt{2} & \sqrt{2} & \sqrt{2} \end{pmatrix} \quad (\text{A.7})$$

which transforms an old coordinate \mathbf{r}_j to its new coordinate \mathbf{r}_i' through $\mathbf{r}_i' = a_{ij}\mathbf{r}_j$. The angle θ is an azimuthal angle about the (111) direction which defines the directions of \mathbf{x}_1' and \mathbf{x}_2' . It will be shown that how to choose θ does not affect the formula we are deriving here. The transformation (A.7) can be applied only to the tensor notation [1] using

$$C_{ijkl}' = a_{im}a_{jn}a_{kp}a_{lq}C_{mnpq}, \quad (\text{A.8})$$

i.e.,

$$\sigma_{ij}' = a_{im}a_{jn}a_{kp}a_{lq}C_{mnpq}\varepsilon_{kl}' \quad (\text{A.9})$$

where C_{ijkl}' is stiffness tensor under the new coordinate system. After converting Eq. (A.9) to the matrix notation, it can be shown that

$$\sigma'_3 = \frac{1}{3}[(c_{11} + 2c_{12} - 2c_{44})\varepsilon'_1 + (c_{11} + 2c_{12} - 2c_{44})\varepsilon'_2 + (c_{11} + 2c_{12} + 4c_{44})\varepsilon'_3]. \quad (\text{A.10})$$

The same pseudomorphic growth condition as (A.5) therefore requires

$$\varepsilon_{\perp} = -\left(\frac{2C_{11} + 4C_{12} - 4C_{44}}{C_{11} + 2C_{12} + 4C_{44}}\right)\varepsilon_{\parallel} \quad (\text{A.11})$$

for (111)-oriented heterolayers.